Diss. ETH No. 26277

Aerothermal Effects of High-Pressure Turbine Rim Seals and Blade Tip Geometries in the Presence of Cooling Flows

A thesis submitted to attain the degree of

DOCTOR OF SCIENCES of ETH ZURICH

(Dr. sc. ETH Zurich)

presented by

Rainer Schädler

Master of Science ETH in Mechanical Engineering
born on 10.01.1987
citizen of Liechtenstein

accepted on the recommendation of
Prof. Dr. Reza S. Abhari, examiner
Prof. Dr. Francesca di Mare, co-examiner
Dr. Anestis I. Kalfas, co-examiner

2019

Acknowledgements

The present thesis is the outcome of five years of work at the Laboratory for Energy Conversion at ETH Zurich and more. Work was supported by two joint industrial and academic research programs between the Laboratory for Energy Conversion and Siemens AG and MTU Aero Engines AG. The programs were associated with "Luftforschungsprogramm LuFo V" supported by the German Federal Ministry of Economics and Technology.

I want to express my gratitude to the head of the Laboratory for Energy Conversion, Prof. Dr. Reza S. Abhari, for his guidance and support throughout my time in the laboratory. His profound knowledge and experience in the turbomachinery sector helped me to extend my technical background in the field and beyond. Most of all, I would like to thank Prof. Abhari for placing his trust in me to operate and manage the sophisticated test rig "LISA", which is truly a unique experience.

I want to thank Dr. Anestis I. Kalfas for all the support during my time at ETH Zurich, not only at a technical but also on a personal level. Without his commitment, the integration and operation of the rotor onboard telemetry system would not have been possible. I will never forget the support he provided me for my first publication; it was and still is highly appreciated.

Prof. Dr. Francesca di Mare honors me by co-examining my work. I am deeply thankful for her time and effort reviewing the present thesis.

This research project was made possible by the technical and financial support of two industrial partners, Siemens AG and MTU Aero Engines AG. I want specifically acknowledge the constructive contributions of Dr. Gregor Schmid, Dr. Tilman auf dem Kampe, Dr. Ewald Lutum, Dr. Jochen Gier, and Dr. Carsten Schneider.

I also want to thank the Gas Turbine Laboratory (GTL) of The Ohio State University for the high-quality thin-film double-sided heat flux gauges which were pivotal for the heat transfer part of this work.

It is very important to me to express my deepest gratitude to my predecessors. Dr. Kai Regina introduced me to the test rig and always found time to answer my questions. His systematic thinking also shaped my perception of how to tackle technical issues. I will never forget his outstanding support for the assembly of my first turbine configuration. I am very thankful for the useful advice and help provided by Dr. Patrick Rebholz—without him, the challenging rotating frame of reference measurements would have never

been possible. I also want to acknowledge the valuable input from Dr. Benoit Laveau, especially at the beginning of the project.

I was blessed to work with two exceptional people who covered the heat transfer part of the research project. It goes without saying that this work would not have been possible without the help of Dr. Sebastiano Lazzi Gazzini. Sebastiano is one of the kindest and most honest persons I know and was a loyal and true friend throughout the occasionally difficult times during the project. Grazie di tutto, Sebastiano.
I would like to express my deepest gratitude to Dominic Hänni who was not just a project partner but became a very good friend. Thank you for sharing the load and nearly endless days in the LISA control room as well as for the enjoyable time outside of the lab.

I want to thank Dr. Carsten Degendorfer and Vahid Iranidokht for making our office a warmer place with their presence and for the discussions we had about work and life in general. Without the competent help of Dr. Ilias Papagiannis, Dr. Asad Raheem, and Andrea Mazzetti, the extensive numerical part of this work would not have been possible. I also owe deep gratitude to them for co-supervising the student projects.

The former members of the instrumentation group, namely Dr. Michel Mansour and Dr. Ilias Bosdas, have been my two mentors since I was a master's degree student in the laboratory. I owe deep gratitude to both of them for thoroughly teaching me the essential installation steps for the various instrumentation types that were pivotal to this work. In that context, I'm thankful for the help provided by Alexandros Chasoglou with the fast-response probes toward the end of the project.

Most of the essential electrical components required for this work were designed and implemented by Flori Alickaj. His technical support was always of the highest quality and I want to thank him for his efforts throughout the challenging project.

Ein herzliches Dankeschön geht an Thomas Künzle und Rolf Rüttimann von der Laborwerkstatt, welche mit grosser technischer Finesse und Flexibilität die anspruchsvollsten Miniatur-Bauteile hergestellt haben und mir dabei stets mit hilfreichen Verbesserungsvorschlägen zur Seite standen.

Special thanks also go to former students of the laboratory, namely Moritz Schauer, Elia Iseli, Dominic Hänni, Stefan Hiltbrand, Marco Lang, Riccardo Bagnara, and Samuel Rechsteiner, who all contributed to this thesis one way or another with exceptional work.

A big thank you also goes to Marlene Hegner for the highly efficient help with numerous administrative issues and for always finding the right words in the challenging times of the project. Thank you also to Polat Mevluet and Ben

Newton for their prompt help with IT and website issues.

I also want to express my gratitude to present and former members of the Laboratory for Energy Conversion for their assistance and for fruitful discussions. Specifically, I acknowledge Markus Brandstätter and Marco Weber for their technical expertise, and Dr. Ndaona Chokani for his encouraging words and teaching us how to present our research appropriately. I thank Dr. Jeremy Nickol for his help with the double-sided heat flux gauges and humorous discussions about my home country. To Dr. Patrick Eser, I give my regards for his help organizing and handling student projects. I thank Artemis Ioannou and Janis Vinklers for all the pleasant conversations, especially during the first year of my PhD. I thank Alissa Brenn and Katharina Hoheneck for the memorable coffee breaks and discussions we had.

Finally, I would like to thank my family for their continuous support and understanding. Liebe Mama, Papa und Corina, ihr seid die grosse Stütze in meinem Leben und ohne euch wäre diese Arbeit nicht möglich gewesen. Vielen Dank, dass ihr immer an mich geglaubt habt, besonders in schweren Zeiten. Diese Arbeit ist euch gewidmet.

Zurich, June 2019
Rainer Schädler

Abstract

The primary scope of this thesis is to contribute to improving the aerothermal performance of turbine sections in modern gas turbines for electricity production and aircraft propulsion in aero engines. The high-pressure turbine components in such machines are typically subjected to significant thermal loads induced by the continuously increasing turbine entry temperatures. Sensitive components, such as rotor disks and blades, are consequently supplied with cooling flows that, in turn, tend to have a detrimental impact on the aerodynamic performance of the turbine. In that context, geometrical features, like the rim seals and the rotor blade tips, bear great potential for optimization. Furthermore, the designers aim to reduce the number of turbine blades to cut the cooling requirements. Within that design space, this work targets providing guidelines for optimizing the rim seal space and rotor blade tips to efficiently use and reduce the expensive cooling flows while maintaining high aerodynamic performance levels. Potential unfavorable concomitant effects on the turbine characteristics (such as turbine noise) are elucidated in the context of the optimization process.

The present work was carried out within the scope of a joint academic and industrial research effort to improve the aerothermal performance of high-pressure turbines by integrating novel geometrical features such as advanced rim seal designs and rotor blade tips in combination with non-axisymmetric end wall contouring. In total, three different 1.5-stage turbine configurations with multiple sub-assemblies, each consisting of specific rim seal and tip designs, were probed for different cooling flow rates in the axial turbine facility "LISA" at ETH Zurich. A unique experimental dataset is presented consisting of inter-row pneumatic and fast-response probes as well as cavity wall-mounted pressure and temperature measurements. The unsteady flow perturbations inside the delicate rim seal space were resolved using miniature-sized, piezo-resistive pressure transducers installed both on the stator- and rotor-sided hub cavity walls. A purpose-made hub cavity heat transfer setup consisting of thin-film heater and double-sided heat flux gauges allowed for changes in the thermal boundary conditions during turbine operation and thereby offered the determination of heat transfer and ingestion quantities. A modular multipurpose rotor onboard telemetry system was used, enabling the acquisition and subsequent transfer of pressure and temperature data from the rotor relative frame of reference. The test rig capabilities were extended by a low-temperature bypass flow system, which facilitated increasing the

temperature difference between cavity fluid and main annulus flow. A modular, bladed-disk design was introduced to allow for a rainbow rotor setup featuring different blade tip designs for the same test run. The experimental work was complemented by extensive unsteady computational fluid dynamics simulations using the in-house developed explicit solver MULTI3.

The complex flow field in the rim seal space was traced by fast-response instrumentation and unsteady calculations. The significance of specific non-synchronous low-frequency flow perturbations (cavity modes) for the aerothermal turbine design was elaborated, indicating that the main annulus ingestion behavior, as well as the turbine noise emissions, are directly affected by these flow structures. Transient full-annular numerical modeling presented a reasonable prediction of the low-frequency modes. The extensive probing of different turbine operating conditions and rim seal designs provides measures to attenuate the hub cavity asynchronous flow excitation.

A novel rim seal design concept, termed as "purge control features," is proposed, which was found to improve the aerodynamic performance for an already optimized turbine stage in the presence of rim seal purge flow. In comparison to a baseline case, the absolute stage efficiency increase were experimentally determined to be 0.4 % points. Complementary beneficial effects on the ingestion behavior and the attenuation of low-frequency cavity modes were experimentally and computationally quantified.

A unique experimental dataset for a combined study of turbine ingestion and hub cavity convective heat transfer is provided for a systematic variation of rim seal purge flow rates. The sensitivity analysis of the ingestion and heat transfer with respect to purge air highlights the importance of cooling flow rates to the overall improvement of the aerothermal performance of a turbine stage. An increase in the local convective heat transfer coefficient by a factor of 2–3 on the rotor-sided hub cavity wall was detected for a 1 % increase in purge flow injection rate. The resultant heat transfer coefficients were compared to existing empirical correlations, indicating the limitations of such approaches in providing accurate predictions.

Extensive probing of a substantially reduced blade count rotor featuring an optimized blade and end wall design revealed the potential to improve the turbine stage performance by 0.4 % points. However, the achievements were compromised by a significant increase in turbine tonal noise emissions by up to 13 dB. An additional absolute performance gain, up to 0.1 % points, was seen by integrating a set of advanced blade tip geometries that were experimentally cross-compared using a rainbow rotor setup. The combined absolute stage performance gain was found to be 0.5 % points for a 22 % reduction in rotor blade count, resulting in an overall higher aerothermal performance.

Kurzfassung

Das Hauptaugenmerk dieser Arbeit ist es zur Verbesserung der aerothermischen Leistung von Turbinenabschnitte für moderne Gasturbinen beizutragen, welche zur Stromerzeugung und zum Antrieb von Flugzeugen eingesetzt werden. Die Hochdruckturbinen in solchen Maschinen sind typischerweise erheblichen thermischen Belastungen ausgesetzt, die durch die ständig steigenden Turbineneintrittstemperaturen hervorgerufen werden. Sensible Komponenten, wie beispielsweise die Rotorscheiben und Schaufeln, werden deshalb mit Kühlluft versorgt, deren Einsatz sich wiederum nachteilig auf die aerodynamische Leistung der Turbine auswirkt. Geometrische Merkmale, wie etwa die Nabendichtungen und Rotorspitzen, bergen in diesem Zusammenhang ein grosses Optimierungspotenzial. Darüber hinaus ist es das Ziel der Ingenieure, die Anzahl der Turbinenschaufeln zu reduzieren, um den Kühlluftbedarf zu senken. Innerhalb dieses Auslegungsspielraums zielt diese Arbeit darauf ab, Richtlinien zur Optimierung der Nabendichtungen und der Rotorspitzen bereitzustellen, um kostspieligen Kühlluftströme effizient zu nutzen und zu reduzieren und um gleichzeitig eine hohe aerodynamische Leistung zu gewährleisten. Eventuelle unvorteilhafte Begleiterscheinungen bezüglich der Turbinencharakteristiken (wie etwa der Turbinenlärm) werden im Rahmen des Optimierungsprozesses erläutert.

Die bereitgestellte Forschungsarbeit wurde Zusammenarbeit mit der Industrie durchgeführt, um die aero-thermische Leistung von Hochdruckturbinen durch die Integration neuartiger geometrischer Merkmale, wie zum Beispiel durch hochentwickelte Nabendichtungen und Rotorspitzen in Kombination mit nicht-rotationssymmetrischer Seitenwandkonturierung, zu verbessern. Insgesamt wurden drei verschiedene 1.5-stufige Turbinenkonfigurationen mit mehreren Unterbaugruppen, die jeweils spezifische Nabendichtungen und Rotorspitzen enthalten, für unterschiedliche Kühlluftraten in der axialen Forschungsturbine „LISA“ an der ETH Zürich untersucht. Ein einzigartiger experimenteller Datensatz ist in der Arbeit präsentiert, welcher pneumatische und schnell ansprechende Sondenmessungen, sowie Druck- und Temperaturemessungen an den Kavitätswänden beinhaltet. Die instantionären Strömungseffekte innerhalb des komplexen Nabendichtungsraumes wurden mit piezo-resistiven, miniatur Druckaufnehmern aufgelöst, die sowohl an der statoral als auch an der rotorseitigen Kavitätswand installiert wurden. Eine speziell angefertigte Kavitäts-Wärmeübertragungsinstrumentation, bestehend aus einem Dünnschicht-Heizelement und doppelseitigen Wärmestromdichte-Streifen,

ermöglichte es, die thermischen Randbedingungen während des Turbinenbetriebs zu ändern und damit die Wärmeübertragungs- und Heissgaseinzugseigenschaften zu bestimmen. Ein modulares Mehrzweckdatenerfassungssystem wurde verwendet, welches die Erfassung und die anschliessende Übertragung von Druck- und Temperaturdaten im und aus dem rotor-relativen Bezugssystems ermöglicht. Die Prüfstandsfunktionen wurden durch ein Niedertemperatur-Rotorscheibenkühlluftsystem erweitert, welches ermöglichte, die Temperaturdifferenz zwischen der Kavitätsströmung und des Hauptturbinenstroms zu erhöhen. Zudem wurde ein modulares Laufraddesign eingeführt, um einen Regenbogenaufbau des Rotors und dessen Test mit unterschiedlichen Schaufelspitzendesigns für den gleichen Testlauf zu ermöglichen. Ergänzt wurde die experimentelle Arbeit durch umfangreiche instationäre numerische Strömungssimulationen mit dem intern entwickelten expliziten Berechnungsprogramm MULTI3.

Das komplexe Strömungsfeld im Nabendichtungsraum wurde durch schnell ansprechende Instrumentierung und instationäre Berechnungen aufgelöst. Die Bedeutung spezifischer asynchroner und niederfrequenter Strömungseffekte (Naben-Kavitätsmoden) für das aero-thermische Turbinendesign wurde herausgearbeitet, durch die Analyse wird darauf hingedeutet, dass der Heissgaseinzug sowie die Turbinenschallemissionen direkt von diesen spezifischen Strömungsstrukturen beeinflusst werden. Transiente Simulationen, welche die gesamten Schaufelringe modellieren (360° Domäne), lieferten eine akzeptable Vorhersage der tief-frequenten Kavitätsmoden. Die umfangreiche Überprüfung verschiedener Turbinenbetriebsbedingungen und Nabendichtungsdesigns legt Massnahmen zur Dämpfung der asynchroner Strömungseffekte des Nabendichtungsraum offen.

Ein neuartiges Konzept für das Design der Nabendichtung wird vorgeschlagen, welches als „purge control features“ bezeichnet wird und dessen Integration die aerodynamische Leistung für eine bereits optimierte Turbinenstufe, in der Präsenz von Rotorscheibenkühlluft, verbessert. Mit Bezug auf eine Referenzturbinenkonfiguration wurde eine Verbesserung des Stufenwirkungsgrades für nominale und hohe Rotorscheibenkühlluftraten experimentell auf 0.4 %-Punkte bestimmt. Ergänzende positive Effekte auf das Heissgaseinzugsverhalten und die Dämpfung von niederfrequenten Kavitätsmoden wurden experimentell und numerisch quantifiziert.

Ein einzigartiger experimenteller Datensatz wird bereitgestellt für eine kombinierte Studie des Heissgaseinzugs und der konvektive Wärmeübertragung im Nabendichtungsraum für eine systematische Variation der Rotorscheibenkühlluft. Die Sensitivitätsanalyse des Heissgaseinzugs und des Wärmeübergangs in Bezug auf die Rotorscheibenkühlluft unterstreicht die Bedeutung von Kühlluftraten für die Gesamtverbesserung der aerothermischen Leistung einer Turbinenstufe. Ein Anstieg des lokalen konvektiven

Wärmeübertragungskoeffizienten um den Faktor 2–3 an der rotorseitigen Kavitätswand wurde für eine 1 % Erhöhung der Rotorscheibenkühlluftrate gemessen. Die resultierenden Wärmeübertragungskoeffizienten wurden mit bestehenden empirischen Korrelationen verglichen. Basierend auf diesem Vergleich werden die Grenzen solcher Ansätze aufgezeigt, um präzise Vorhersagen zu treffen.

Die umfangreiche Sondierung eines Rotors, welcher mit beträchtlich reduzierter Schaufelzahl und einem optimierten Schaufel- und Seitenwand-Design ausgestattet wurde, zeigt das Potenzial die Leistung der Turbinenstufe um 0.4 %-Punkte zu steigern. Die ermutigenden Ergebnisse wurden jedoch durch einen signifikanten Anstieg der tonalen Schallemissionen der Turbine um bis zu 13 dB beeinträchtigt. Ein zusätzlicher absoluter Leistungsgewinn, von bis zu 0.1 %-Punkten, wurde durch die Integration einer Reihe von fortschrittlichen Schaufelspitzengeometrien erzielt, welche experimentell mit einem Regenbogenrotor-Setup quer verglichen wurden. Die kombinierte absolute Leistungssteigerung der Stufe betrug 0.5 %-Punkte für eine 22 %ige Reduktion der Schaufelzahl, was zu einer insgesamt höheren aero-thermischen Leistung führte.

Contents

1. Introduction

1.1. Motivation

Human society in the 21st century faces inevitable challenges in the electricity and transportation sector that are posed by the rapidly increasing world population. Even with substantial technological advances in many fields over the last decades, hundreds of millions of people in emerging countries remain without access to electricity or basic infrastructure. A recent scenario [70] forecasts a 1.7 billion-person global population increase by 2040, which will spike energy demand by more than a quarter, mostly in urban areas in developing economies. Consequently, the focus of a transforming energy strategy needs to be on main pillars such as affordability, reliability, and sustainability.

In the electricity sector, the penetration of renewable energy sources, for instance, solar and wind energy, offers the advantage of providing sustainable and more affordable electricity. The share of renewables covering global energy demand is expected to increase approximately 20 % by 2023, and the fastest growth is expected to take place in the electricity sector [69]. Nevertheless, the availability and stability of these resources typically depend on environmental aspects such as weather fluctuations. Electricity production needs to be reliably provided at all times; therefore, the level between production and consumption must be balanced. Conventional energy sources are still necessary to level out the expected fluctuations in electricity production. In that context, gas turbines offer appropriate flexibility combined with lower carbon emissions (e.g., compared to coal-fired power plants). Both aspects are addressed in Figure 1.1. Projections done by BP [18] anticipate that the global share of total power generation in 2040 would be characterized by significant renewable energy sources (around 25 %). However, gas turbines are still expected to have a significant contribution in 2040, about 20 % (Figure 1.1, left). The generation of electricity in power stations faces public scrutiny as it is associated with greenhouse gas emissions and rising global temperatures. Breaking down the shares, electricity production by power plants contributes to approximately one-quarter of global warming. This is a lower percentage than that perceived by the public, who see power plants as having a far greater role in global warming than they do. Contributions from fossil-fuel related industries and agriculture are typically forgotten as greenhouse gas emitters, even though

they dominate the CH_4 and N_2O emissions in the form of strong greenhouse gases. Despite progress in renewables, projections by the International Energy Agency (IEA) [68], anticipate a non-negligible contribution of coal, gas, and oil to the total CO_2 greenhouse gas emissions in the power generation sector in the year 2040. Coal, however, takes a factor of 2.5 larger share in total carbon emissions from power generation than gas and oil (Figure 1.1, right). This underlines the statement that gas turbines provide a lower negative environmental footprint than coal. Since the amount of emissions CO_2 are typically linked to the installed capacity and efficiency of power plants, there is still a profound need to improve the performance of gas turbines to further contribute to decarbonization in the electricity sector. Such advances are typically attempted in the thermal cycle efficiency of the gas turbine.

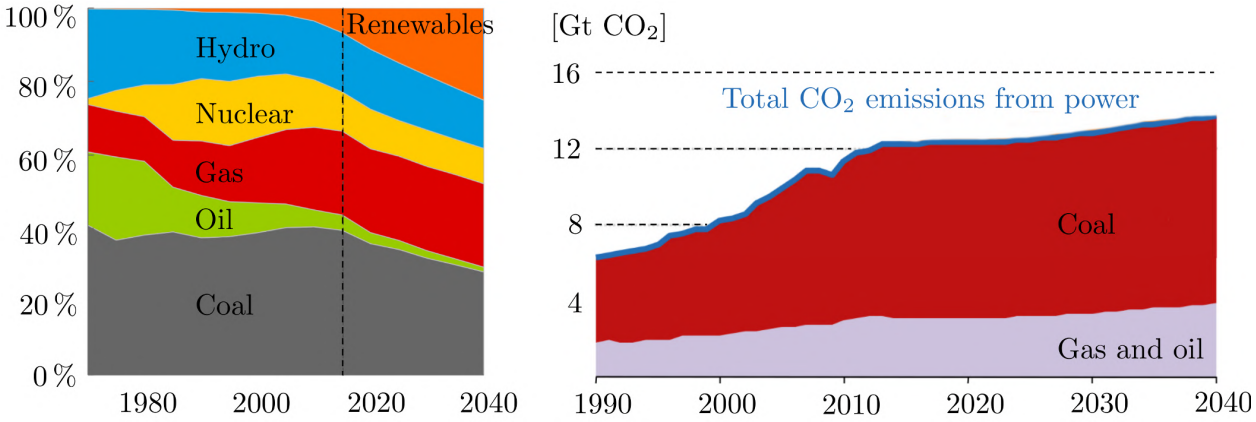

Figure 1.1.: Historical trends and projections in global share of total power generation (left, adapted from [18]) and CO_2 emissions by fuel (right, modified from [68]) until year 2040

Air transportation faces similar challenges to the electricity sector. Over the last four decades, the flight traffic volume and number of carried air passengers have increased globally. Figures from 2017 show that annual passenger volume is approaching 4 billion [194]. Substantial economic growth in East Asia is partly behind the significant increase in air passengers. In Figure 1.2, the total number of air passengers per country is displayed for 2017. Clearly, China and North America have a large share of the total passengers. Relatively stable kerosene prices between 2011 and 2016 [4] helped sustain the air transportation growth rate in recent years. Increasing greenhouse gas emissions are one of the main drawbacks in the growing air transportation sector due to the absence of alternative propulsion systems to gas turbines. The annual CO_2 emissions from air transportation are approximately 2 % of the total carbon dioxide emissions (2010, [21]).

To counteract human-induced climate change and implement carbon offsetting and reduction strategies, the International Air Transportation Association suggested a road map [71] based on target emissions communicated in the "Flightpath 2050" to the European Commission. In this road map, about 30 %

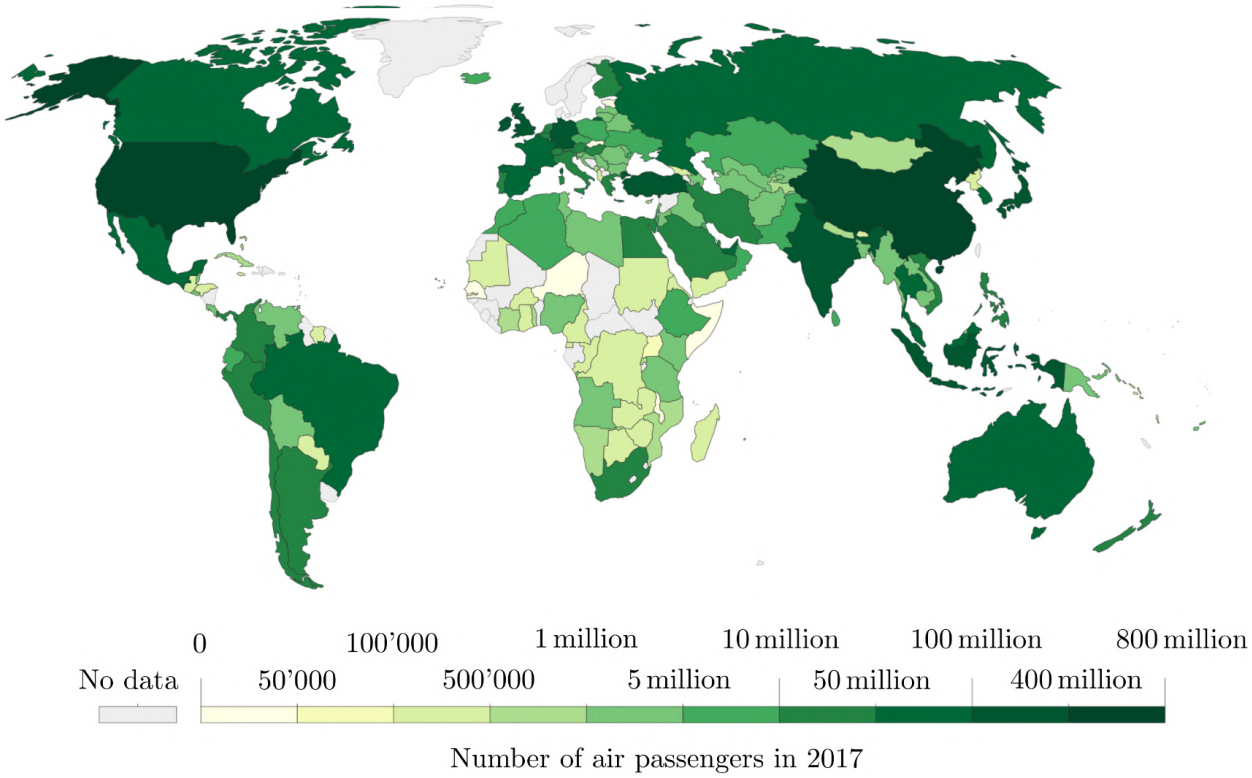

Figure 1.2.: Total number of air passengers carried in the year 2017 including domestic and international aircraft passengers [194]

of the targeted emission reduction is anticipated to be achieved by increasing fuel efficiency as well as the weight of existing technologies such as engines and airframes. Further reductions in emissions are expected to be reached by air traffic optimization and airport procedures. Individual suppliers of aircraft components are therefore improving existing technologies to achieve carbon-neutral growth by 2030. One of the major components in this optimization attempt is the aircraft engine itself, which is typically a gas turbine-based turbofan. Summarizing the last four decades of improvements related to the turbofan engine, major contributions were made to thermodynamic cycle efficiency and propulsive efficiency. Cycle efficiency, in particular, has been boosted in recent years by increasing the combustor exit temperature and reducing the aerodynamic losses of the components. These advances are also reflected in the power plants of the stationary gas turbine sector.

The Flightpath 2050 roadmap [71] also incorporates a substantial reduction in perceived noise emissions (65 %) generated from aircraft. Higher bypass ratios in recent years significantly reduced jet noise, which was the dominant source of emissions on the engine side. Fan-induced noise then became more prominent, which was tackled by the implementation of a geared turbofan concept. Both technological advances—high bypass ratios and the geared turbofan concept—lead to an increase in the importance of turbine noise to the designers.

Both the power generation and aviation sectors seek to improve thermodynamic cycle efficiency motivated by the aforementioned increased demand and the implementation of strict regulations. Increasing the turbine inlet temperature requires advanced cooling methods and materials since the fluid temperature (>1800 K) exceeds the melting temperature of the turbine components, especially in the first stage of the high-pressure turbine section. This trend is well captured by the projections of Kyprianidis [90] and illustrated in Figure 1.3 (a). It is expected that the increase of the peak turbine inlet temperature is in the order of 10 K per year. On the materials side, nickel-based superalloys such as INCONEL are typically used in combination with a ceramic-based thermal barrier coating to follow this drive for higher inlet temperatures. Even though the advances in materials science are substantial, the need for highly evolved cooling strategies is still growing as the vane and blades in the first stage of the high-pressure turbine cannot withstand the enormous thermal loads without active cooling. In Figure 1.3 (b), a fully cooled high-pressure turbine vane segment and blade of the GP7000 engine is shown where specific attention should be given to the density of the cooling hole patterns on the airfoil surface and platform. State-of-the-art thermal management in gas turbines also includes sealant and purge flows to cool not only the blade platform but especially the rotor disk. This provides active blockage against hot gas ingress from the main flow path into the disk cavities. In that context, the combination of hub sealing and purge flows, as well as well-designed rim seals, becomes increasingly important in the design space of evolved turbine stages.

On the other hand, the continuous drive for higher aerodynamic efficiency of the turbine section is spurred by an increase in computational power, which has enabled the design and optimization of highly three-dimensional shaped airfoils, non-axisymmetric end wall contouring, and advanced blade tip and seal geometries. The need for detailed validation of optimization and prediction tools is pivotal for complex designs that are expected to reduce aerodynamic efficiency deterioration due to the formation of secondary flows. Wisler [193], for example, showed that an improvement of high-pressure turbine aerodynamic performance by 1 %, results in a 0.82 % improvement of an aero engine's thrust-specific fuel consumption (TSFC). Also, engine suppliers aim to reduce the number of components (e.g., number of stages, airfoils per stage) to reduce weight (aviation) and cut down on maintenance and manufacturing costs. However, reducing aerodynamic components typically is accompanied by an increase in the blade loading and lift coefficients, which benefits the formation of high-strength secondary flow structures [47], especially in low aspect-ratio turbine stages. Since cooling requirements grow as the turbine inlet temperature increases, aerodynamic performance of turbine stages is

typically reduced due to the injection of cooling flows. Therefore, turbine research needs to operate right at the interface of thermal management and aerodynamic performance, with a view toward component reduction. Additionally, research should comply with strict emissions regulations for greenhouse gases, pollutants, and noise.

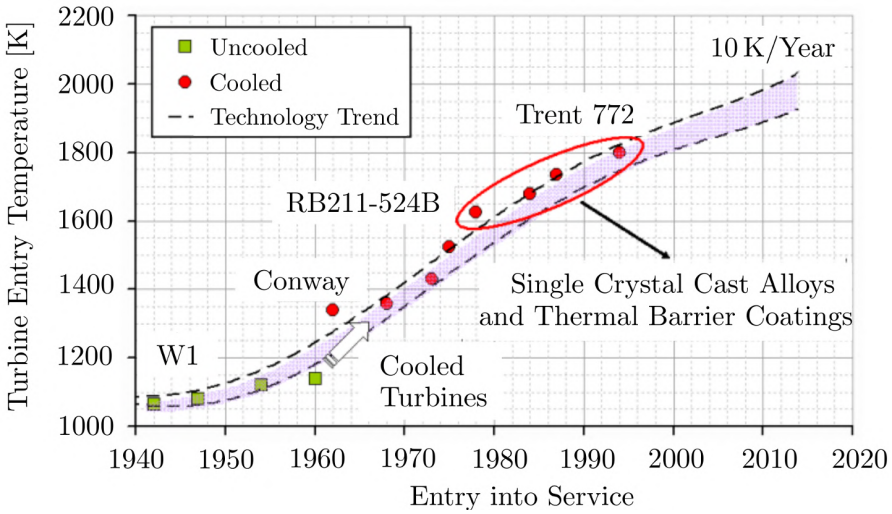

(a) History and projections of turbine entry temperature [90]

(b) Fully cooled high-pressure turbine vane and blade of the GP7000 equipped with thermal barrier coating [121]

Figure 1.3.: Thermodynamic cycle efficiency improvement by aiming for higher turbine inlet temperatures in combination with advanced cooling strategies

Therefore, the main purpose of this work is to contribute to the aerothermal optimization of high-pressure turbines. This consists of reducing cooling requirements by advanced rim seal arrangements and lowering blade count while improving aerodynamic performance of the turbine section using advanced geometrical features. Within this improvement process, potential concomitant effects on the turbine characteristics (such as turbine noise) are aimed to be included.

1.2. Literature Review

The design considerations for state-of-the-art turbines are diverse as not only aerodynamic aspects must be assessed but also thermal-structural and aeroacoustic issues need to be addressed to cope with the harsh environment. This literature review aims to provide an overview of the individual aerodynamic pillars, as well as works that include thermal management aspects. Since part of the present work also includes novel geometrical features that help to reduce the efficiency penalties partly associated with the secondary flow formation, work from other researchers shall be reviewed in that regard.

1.2.1. Loss Generation Mechanisms in Turbomachinery

When it comes to losses, different definitions can be found in open literature. Denton [39] provides a clear and compact formulation of losses which emphasizes that any flow feature that reduces the efficiency of a turbomachine and contributes to the entropy production introduces losses. Entropy itself is claimed to be the only reliable measure of loss in turbomachinery. It is found to be independent of the frame of reference and is determined by temperature and pressure. Furthermore, Denton [39] identified three processes that contribute to entropy production:

- Viscous friction and mixing
- Heat transfer
- Non-equilibrium processes

Additionally, Denton [39] differentiated between three different sources of losses in turbomachinery which are, however, not fully independent of each other:

- **Profile losses**: are associated with the development of boundary layers on the blade surface. The main driver for loss production is the viscous dissipation inside the blade boundary layer, which can be laminar, transitional, or turbulent [107].
- **End wall losses or secondary losses**: are provoked by secondary flow structures formed in the blade passage. The velocity non-uniformity (e.g., boundary layers) at the start of the blade row provokes the formation of these flow structures. Furthermore, the interaction of the secondary flows with the adjacent blade rows contributes to this loss source, which also was anticipated by Hawthorne [63].

- **Leakage losses**: are attributed to the viscous dissipation induced by the mixing of the leakage flows (e.g., tip leakage flows and rim seal leakage flows) with the main annulus flow, which was investigated in detail by Bindon [13] for tip clearance flows.

Denton stated that each of these loss sources contributes to approximately one-third to the overall losses in turbomachines. Traupel [185] investigated different loss sources in axial turbines and elaborated various correlations to quantify those losses. Sharma et al. [181], Moore et al. [119], and Harrison [58] investigated loss generation in turbomachines. A major part of this work also discussed the formation and interaction of secondary flows with the main annulus flow. Secondary flows, as well as flow unsteadiness, cannot be directly translated to losses. Nevertheless, the spatial velocity gradients in secondary flows cause secondary kinetic energy to be converted by viscous dissipation, mixing, and unsteady chopping by adjacent blade rows, which leads to losses. In a highly unsteady flow, additional production of shear forces occurs, which in turn can provoke losses from mixing and viscous dissipation [75].

Secondary Flows The presence of blade rows and end walls in turbomachinery intrinsically provokes the formation of viscous boundary layers, which are typically accumulated in the wake of the blade as low-momentum fluid or rolled up as horseshoe vortices around the vane and blade profiles. Squire and Winter [184] proposed the classical secondary flow theory in 1951, where they described the conversion of the tangential vorticity in the inlet boundary layers into streamwise vorticity at the exit of blade rows using vorticity transport equations. Hawthorne [62, 63] confirmed the flow phenomena for a linear cascade by experimental evidence. Vortex lines, which can be similarly defined as streamlines, cannot be disrupted according to the inviscid theory. Therefore, the vorticity in the inlet boundary layer wraps around the blade or vane and provokes velocity components normal to the dominating flow direction. Cumpsty [33] proposed this process as a general definition for the secondary flow formation.
Due to the inherent cross-passage pressure gradient between the blade pressure and suction side, the pressure-side leg of the rolled-up vortex (pressure-side leg of horseshoe vortex) migrates to the adjacent suction side. Once the vortex makes contact with the blade suction side, it tends to lift off the end wall and becomes the passage vortex. The passage vortices are usually one of the largest secondary flow structures (besides the tip leakage vortex) in unshrouded turbines and their strength and extent depend on the blade solidity, the aspect ratio, and the blade turning. Many publications related to loss generation associated with the passage vortex formation can be found. Among the first researchers, Moore et al. [119] and Moustapha et al. [120] described the flow phenomena. Walsh and Gregory-Smith [188] furthermore highlighted that in

rotating machinery, the secondary flow effects are even more pronounced as the boundary layers of the stationary frame of reference appear skewed in the consecutive downstream rotating row. The interaction of the migrating vortex to the suction side and its interaction with the blade surface, as well as with the suction-side leg of the horseshoe vortex, promotes the radial migration of the passage vortex. Sieverding and Van den Bosche [183] concluded that the position of the suction-side leg of the horseshoe depends on the strength and extent of the passage vortex. According to Gregory-Smith et al. [53], the suction-side leg can even mix out and is, therefore, hard to detect. The presence of a corner vortex, as described by Sieverding [182] and Yamamoto [195, 196], forms between the passage vortex, the blade surface, and the end wall of the adjacent blade and is characterized by an opposite sense of rotation compared to the passage vortex. A comprehensive flow model and detailed explanations were provided in the work of Langston [91], which is also illustrated in Figure 1.4 (a). Schlienger et al. [171] detailed the complex interaction of the horseshoe vortex legs with the blade wake (Figure 1.4 (b)) and the blade itself via probe measurements in a continuous running model turbine.

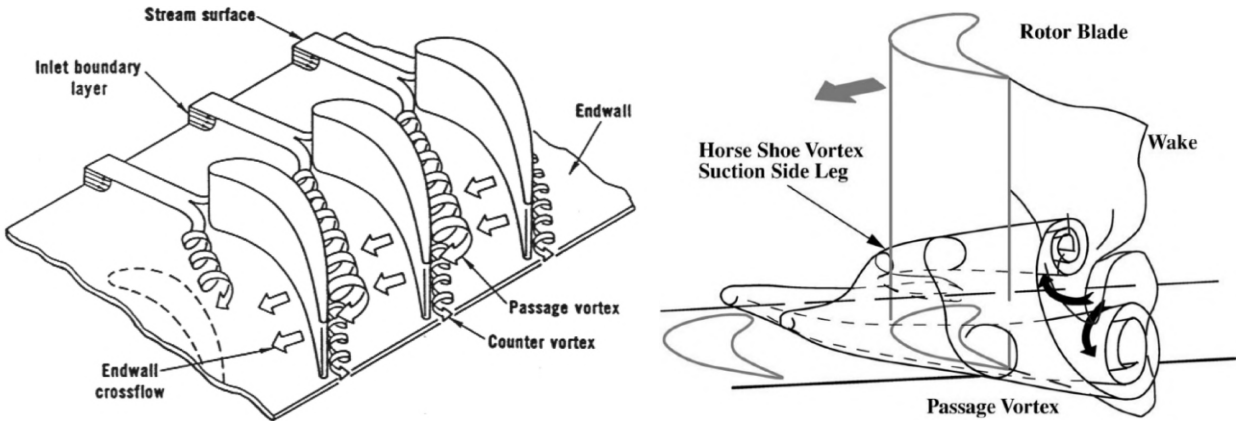

(a) Secondary flow model by Langston [91] **(b)** Blade-wake-vortex interaction [171]

Figure 1.4.: Comprehensive secondary flow models

Tip Leakage Flows and Blade Tip Designs When addressing losses in a turbine stage, the inevitable presence of gaps between stationary and rotating parts plays an important role. The design of tip clearance, for example, requires detailed knowledge of the centrifugal loads, thermal expansion, and axial thrust. In high-pressure turbines, which feature low aspect ratio unshrouded blades, the loss contribution of the tip leakage flows is judged to be up to 30 % of the total aerodynamic losses [15, 20]. Obviously a shroud, as found in the low-pressure turbines, would contribute to reducing the negative impact of the over-tip flow. In high-pressure turbines, however, the significant centrifugal load combined with the huge thermal loads complicates the integration of a shroud, as the blade root stress would go up as mass is added at the tip.

Furthermore, extensive cooling would be required to cover the larger surface areas at the tip and deal with the flow recirculation in the tip cavities. In the lecture provided by Harvey [59], a detailed overview of different blade tip concepts was shown. He estimated that shroudless turbines have a higher sensitivity to tip clearance variations than shrouded ones, in the sense that unshrouded high-pressure turbines create twice as many losses as a two-finned shroud configuration. A vast amount of publications can be found that investigate different blade tip geometries to reduce tip leakage flow. The most common concept to be found is a squealer-type tip geometry that enables reduction of the tip gap. The potential contact area between the blade tip and the casing is reduced so damage can be minimized in case of rubbing, which not only causes damage due to the bare contact with the casing but also potentially clogs the cooling holes at the tip so that the blade tip remains with reduced coolant. A squealer tip, therefore, provides an appropriate solution. Many studies show the beneficial impact of a well-designed squealer tip, such as Kaiser and Bindon [81], Camci et al. [20] and recently by Cernat et al. [23] and Pátý et al. [133]. Mischo et al. [115, 116] conducted an extensive numerical study on squealer tip geometries and visualized the complex tip leakage flow which is shown in Figure 1.5. They found an aerothermal-optimized squealer tip geometry with a non-uniform squealer fence thickness which favorably modulates the tip leakage vortices formation (Figure 1.5 (b)).

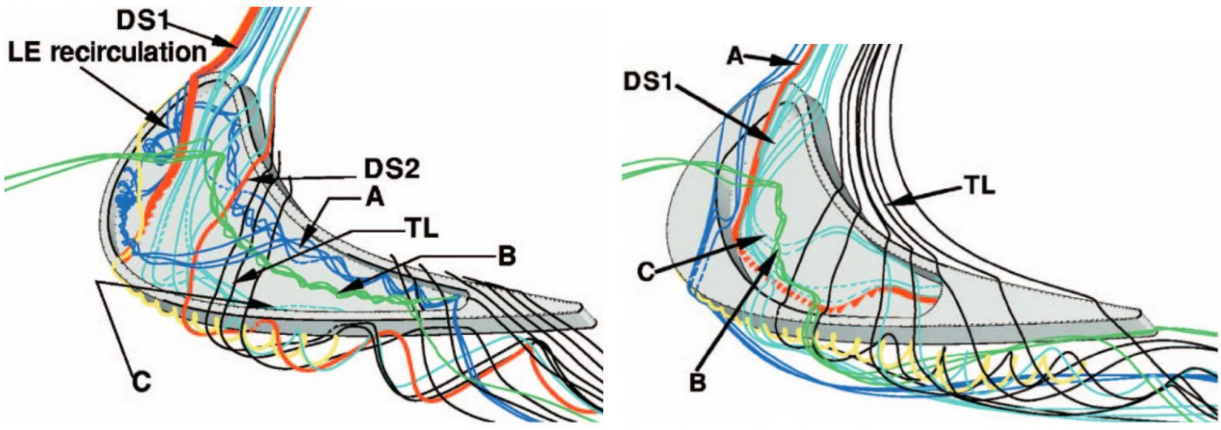

(a) Baseline squealer tip **(b)** Optimized squealer tip

Figure 1.5.: Tip leakage flow visualization over two shroudless turbine blade tips suggested by Mischo et al. [116]

Other blade tip concepts such as winglets, in combination with local geometrical features, were described and investigated by Dey and Camci [41], Zhou et al. [198], and Harvey and Ramsden [60]. Furthermore, contoured and carved blade tips can be found in recent studies. Lavagnoli et al. [92] and De Maesschalck et al. [37] presented such designs in their work. Since part of these concepts is designed and optimized using numerical tools, the need for experimental data is still enormous in order to validate the predictions. A cost-effective

and relatively fast way of testing various tip designs is to equip sectors of a turbine rotor with different designs, typically termed a "rainbow rotor." In recent publications, rainbow rotor testing can be found in [23], [92] as well as in [159].

Cooling Flows The continuous drive to increase the turbine inlet temperature challenges the aerothermal design of the turbine, especially the first stage of the high-pressure turbine. To protect the turbine components from overheating and disintegration from elevated temperatures, active and passive cooling strategies are required. Active cooling is typically achieved by internal and film cooling, which also includes rim seal purge flow, blade tip coolant ejection as well as casing injection. The necessary cooling air is drawn from the compressor section of the engine, although it should be emphasized that the coolant still has a temperature in the order of 950 K (enough to melt most of the aluminum alloys). The complex internal cooling flow paths of an actual aeronautical high-pressure turbine section are comprehensibly illustrated in Figure 1.6.

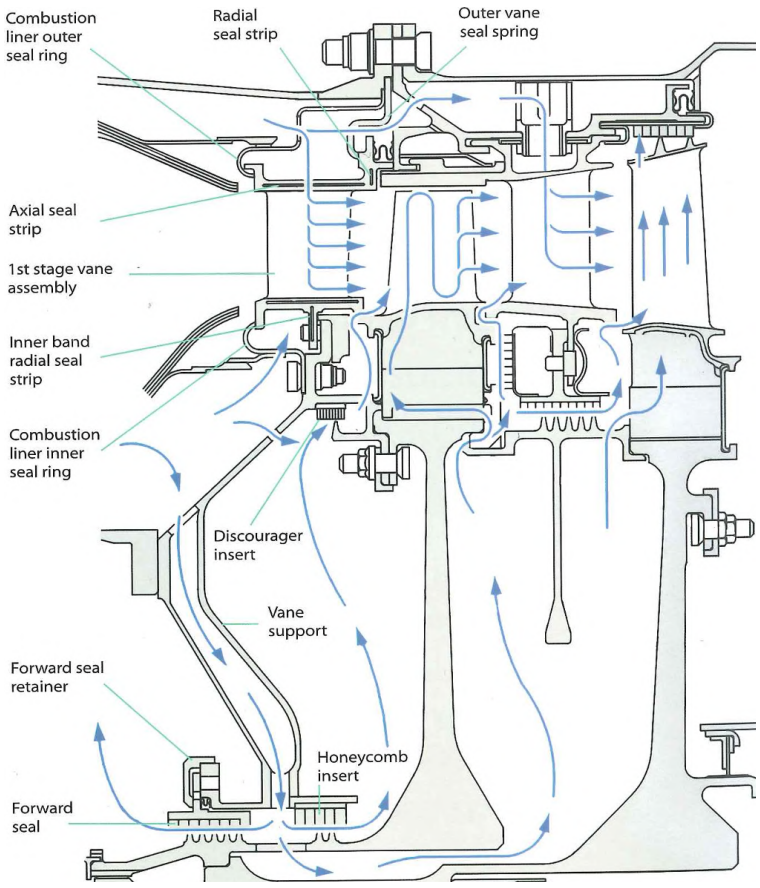

Figure 1.6.: Turbine cooling circuit in the AE 3007 [160], blue arrows schematically indicate the hypothetical cooling flow paths

Two types of cooling flow injection are detailed in this work. The flow that is bled from the upstream compressor and fed to the rotor drum to be leaked

through the hub rim seals is commonly termed as the "rim seal purge flow" (see Figure 1.6). The objective of this practice is to (1). actively cool the rotor disk and (2). prevent hot gas ingress from the main annulus flow into the hub cavities, which has the potential to reach sensitive components such as the bearings and the shaft.
The downside of the cooling injection is a reduction of the effective mass flow upstream of its injection location in the turbine section. Furthermore, the mixing between the colder fluid with the main flow gas is a potential source of losses. Additional blockage, and consequently a redistribution of the streamlines, was found to alter the aerodynamics of a turbine stage [75, 173]. From an aerodynamic point of view, the design intent is to reduce the amount of rim seal purge mass flow and, therefore, aerodynamic losses associated with the cooling injection to improve aerodynamic performance. The hot gas ingress is anticipated to be driven by disk pumping and the non-axisymmetric, external pressure field in the main annulus [175, 176]. Kobayashi et al. [86] investigated the minimum required coolant mass flow and found that the pressure difference criterion tends to underestimate the requirements. Different rim seal designs were investigated by Chew et al. [28] and Dadkhah et al. [36] regarding the minimum required rim seal coolant mass flow. Roy et al. [168] highlighted the importance of the pronounced unsteady pressure field inside the hub cavity in relation to ingress and egress. Even at flow rates slightly above the minimum injection rate, Mirzamoghadam et al. [113, 114] detected minor ingress into the rim seal space.
Many researchers have investigated the effect of cooling injection on the formation of secondary flows. McLean et al. [108, 109] experimentally assessed the potential of novel injection concepts in the rim seal, such as "radial and impingement cooling" as well as "root injection." They found that the secondary flow structures and the stage performance depend significantly on the cooling mass flow rate, and that stage efficiency improvements in the order of 1.5 % points were achieved. A comparison of radial to compound injection was provided by Girgis [49], where the latter was shown to improve aerodynamic performance. Ong et al. [127] highlighted that pre-swirling the coolant jet has a beneficial impact on performance due to the reduction of viscous dissipation and secondary flow strength. The injection of rim seal flow promotes an intensification and enhanced radial migration of the rotor hub passage vortex, according to Paniagua et al. [130]. Reid et al. [157] showed that the aerodynamic performance penalty is about 0.56 % points per percent of injected rim seal flow. Marini and Girgis [102] elaborated a blade leading edge platform design that improves aerodynamic efficiency by 0.07 % points and additionally reduces sensitivity to the rim seal purge flow injection. Schuepbach et al. [175] documented a 0.6 % points efficiency drop for a 0.9 % purge flow injection. They associated both the strengthening of

the rotor hub passage vortex and the higher radial migration of the vortex to the presence of the purge flow. Regina et al. [155] measured a higher sensitivity of the performance to purge flow for a turbine configuration with increased axial spacing between the blade rows compared to the one described by Schuepbach [175]. Jenny et al. [75, 76] found similar effects of the purge fluid for a low-pressure turbine representative configuration and reported an up to 1.3 % points efficiency drop per percent of injected purge mass flow.

In the present work, the near tip flow field was studied when coolant was ejected at the rotor blade tip. The blade tips are typically subjected to high thermal loads in high-pressure turbines and are therefore susceptible to material failure. Additionally, the effective cooling of this part of the blade is particularly challenging due to the complex flow structures that are formed within the tip gap between the blade and casing. Kim et al. [84] noted that the thermal performance of the blade tip region can be enhanced with tip coolant ejection. Using a two-dimensional model of the tip cooling, they found that the ejection of coolant through discrete slots provides a protective coolant layer. Kwak et al. [89] investigated both a flat tip and a cavity tip in a linear cascade in terms of film cooling. The authors concluded that the ejection of tip coolant on the pressure side of the blade led to a further reduction of the blade-tip heat transfer coefficient. Regarding thermal performance, they showed that a cooled cavity tip performed better than a cooled flat tip. The effect of blowing from dust or dirt purge holes was addressed by Hohlfeld et al. [67] and Couch et al. [32]. Dust holes were manufactured in the blade tip to get rid of dirt from the coolant flow through centrifugal forces, such that these large dirt particles do not clog the smaller-diameter film-cooling holes. Both papers described a blockage effect of the ejected flow on the tip leakage flow. The effect was even more pronounced as the tip gap was reduced. Chen et al. [26] studied the aerodynamic implications of the blade tip coolant ejection using a two-dimensional model. The authors concluded that when the tip coolant flow was ejected normal to the tip leakage flow, it blocked the tip leakage flow.

There is limited research published that addresses the aerodynamic effects of tip coolant on a large-scale rotating rig. One of those few was Dey [40], who investigated the aerodynamics of a flat tip under tip ejection. The coolant mass flow ratio was 0.3 % of the inlet mass flow rate, and the author concluded that this rate was too low to induce a substantial reduction in the tip leakage loss. Using the same test facility, Rao and Camci [149] stated that a cooling mass flow ratio between 0.41 % and 0.72 % was beneficial for the aerodynamic performance in a rig with tip gaps between 0.7 % and 1.4 % of the blade height. Furthermore, Rao and Camci [150] complemented their extensive study with

an investigation of the cooling hole positions. The locations of the cooling holes were at 61 %, 71 %, 81 % and 91 % of the blade axial chord in the tip trench of the flat tip. The tip gap was 1.4 % of the blade height. The size of the tip leakage vortex was found to be reduced when mass flow ratios between 0.2 % and 0.45 % were ejected at 61 % and 71 % axial chord. The most pronounced loss reduction was achieved when coolant was ejected at 81 % axial chord, whereas no substantial effect on the tip leakage vortex formation was observed at 91 % axial chord. Zhou and Hodson [197] provided an extensive experimental, analytical, and numerical study wherein the aerodynamic performance of four different cooled tips with coolant mass flow ratios between 0 % and 1.2 % and different tip gap sizes were studied. They found that for a cooled flat tip, the tip leakage losses first decreased and then increased again as the coolant mass flow ratio was increased. Furthermore, they pointed out that for the cavity tip, the blockage effect of the coolant was not as pronounced as for the cooled flat tip. As the coolant mass flow ratio was increased, the tip leakage losses also increased. In sum, available research demonstrated that the impact of the tip coolant ejection on aerodynamic performance was sensitive to the coolant mass flow ratio, the tip gap size, the location of ejection, and the tip geometry itself.

1.2.2. Unsteady Turbine Aerodynamics

The inherent change of the frame of reference from stationary to rotating in turbomachines results in a typically highly unsteady nature of the flow physics. In general, the flow unsteadiness caused by the blade row interaction can be divided into a deterministic and non-deterministic contribution. The deterministic unsteadiness is driven by the blade passing frequency or its harmonics. The non-deterministic part of the total flow unsteadiness is found to be high at locations characterized by high turbulence levels, eddy shedding, and boundary layer transition. The interaction between the blade rows results in alternating patterns of the flow field. Sharma et al. [181] distinguished between two major events for the flow downstream of a stator vane. The maximum interaction occurred when the flow structures of the stator were modulated by the rotor leading edge. The flow structures were typically chopped by the leading edge and their remnants interacted with the rotor passage structures and became part of the wake and secondary flow structures. The turbulence levels were found to be low when the maximum interaction took place. On the other hand, the minimum interaction was detected when the stator flow structures were convected into the rotor passage without considerably interacting with the rotor leading edge. In this instance, the turbulence level in the free stream was enhanced. One other aspect of the unsteady flow behavior in a turbine is the formation of shocks, but since the

test rig that is used in the present work is operated under sub-sonic flow conditions, the topic is not addressed in this section.

Potential Flow Interaction The potential field in a turbine blade row refers to the static-pressure field around a stationary or rotating blade, which can be seen by neighboring blade rows. The potential interaction between vanes and blades provokes a fluctuating pressure field. In the work of Dean [38], the author pointed out that the temporal change in the static-pressure field is a work process that causes a modulation of the total pressure field driven by the potential field effect. A detailed investigation of the potential field effect was carried out by Parker and Watson [132], in which they found that it exponentially decayed with increasing distance to the blade. Kachel and Denton [80] provided a detailed description of the unsteady interaction mechanisms, and Matsunuma [105] reported a strong interaction between a nozzle guide vane and the downstream rotor.

Wake-Blade Interaction The wake of a turbine blade is formed due to the merging of the pressure- and suction-side boundary layer downstream of the trailing edge and is characterized by a velocity deficit. When interacting with the downstream blade rows, wakes tend to be cut into lumps of low-momentum fluid. Meyer [112] introduced a wake-blade interaction concept, which is termed as "negative jet." As described by Meyer, the negative jet provokes an accumulation of the wake fluid on the blade suction side that causes a removal on the pressure side. Hodson and Dawes [66] provided a complementary explanation of the negative jet effect. According to the authors, the wake is "bowed" before it enters the downstream blade passage due to the higher velocities in the center of the passage. The higher velocities incite wake fluid shearing on the blade suction side, whereas the wake is stretched on the pressure side. Therefore, the authors pointed out that most of the wake fluid leaves the passage at the suction side with a limb across the blade passage which reaches the pressure side. Furthermore, Hodson and Dawes [66] described an unsteady recirculation when the wake fluid impinges onto the suction side of the downstream blade row. Unsteady surface pressure and lift variation resulted from this recirculation. Convection of the wake fluid causes temporal pressure gradients, which in turn represent a work mechanism as suggested by Dean [38]. It was found that this work mechanism provoked fluctuations of the stagnation temperature which were more pronounced than the deficit of stagnation temperature in the wake at the inlet of the blade row. In the work of Rose and Harvey [163], the concept of "Differential Work" was introduced. The concept states that in a turbine, less work extraction takes place from the wake than from the free stream. In an extensive experimental and numerical study, Rose et al. [161] confirmed this concept. The authors

observed that wakes become hotter due to intra-fluid heat transfer, which results in a drop in the entropy levels within the wake by four times the average entropy increase during the expansion of the main flow. Furthermore, Rose [162] estimated that the mixing losses associated with the wake of a high-pressure turbine are about 1 % points of the stage efficiency.

Vortex-Blade Interaction Binder et al. [12] were among the first ones who studied vortex-blade interaction mechanisms. The authors explained that vane passage vortices are cut into fragments by the downstream rotor blades and that the vortex is broken down during the process. Chaluvadi et al. [24] and Behr [8] objected that the vortex is not chopped by the rotor blade but bent around the leading edge such that a pressure and suction side limb of the incoming vortex is formed. Additionally, Chaluvadi et al. [24] observed that the suction-side leg of the upstream vane passage vortex was convected through the passage above the passage vortex of the downstream blade row. In a complementing study by Chaluvadi et al. [25], the authors found a 21 % increase of the total pressure losses in the stator secondary flows due to the interaction with the upstream rotor vortices. The pressure-side limb of the upstream vane passage vortex was found to be merged with the forming rotor passage vortex. In the work of Behr et al. [10], it was reported that the suction side limb of the vane passage vortex was convected below the forming rotor passage vortex in contrast to the visualizations provided by Chaluvadi et al. [24]. Schneider et al. [172] provided a comprehensive insight into the multi-stage vortex-blade interaction using experimental and computational data, highlighting the complex convection process of vane passage vortices throughout the downstream rotor passage. Kasper et al. [82] visualized the vortex instability at the rotor inlet and showed that the vortex was breaking down in a spiral mode due to the blade row interaction.

Non-Synchronous Flow Excitation in Cavities - Cavity Modes In recent experimental and computational studies, the existence of large-scale, non-synchronous flow structures inside turbine rim cavities was indicated. It was found that these modes could have a phase speed that was different from the rotor speed (typically less than the rotational speed of the rotor). Abrahamson et al. [3] were among the first ones who reported on the presence of such large-scale vortical structures in their experimental and computational work. In the work of Czarny et al. [35], the existence of large flow structures in the rotor-stator cavities was shown, indicating that their characteristics depended on the rotational speed of the rotor and the aspect ratio of the specific cavity. In a rotor-stator configuration featuring a cylindrical cavity, unsteady vortical structures were indicated by direct numerical simulations [180]. A representative turbine rim seal cavity was modeled by O'Mahoney et al. [126], showing

low-frequency flow excitation in the rim seal space as a result of an extensive large eddy simulation.

Rotating large-scale flow structures have also been computationally identified by Cao et al. [22]. The authors further observed that the structures provoke zones of purging and ingestion around the circumference. They evaluated the phase speed of the rotating flow structures to be lower than the phase speed of the rotor. This concurred well with the fast-response pressure measurements in the respective test rig. Based on measurements conducted by Roy et al. [166], even the rotational speed was well predicted by the computations (90–97 % of the rotor speed). Flow structures that rotate within the rim seal space at sub blade passing frequency were also presented by Hills et al. [64] and Julien et al. [79]. Jakoby et al. [73] indicated the existence of large-scale rotating flow structures through experimental and computational evidence (Figure 1.7 (left)). The authors stated that these structures rotate at a fraction of the rotor speed (80 % of the rotor speed) and anticipated that they significantly contribute to hot gas ingestion. In a recent full-annular computational study, Wang et al. [189] highlighted the formation of low-frequency structures (Figure 1.7 (right)) that are not linked to the blade passing. Boudet et al. [17] showed the existence of cells inside the rim seal that were characterized by a frequency of 12 % of the blade passing frequency; instabilities were also found around 50 % of the blade passing frequency.

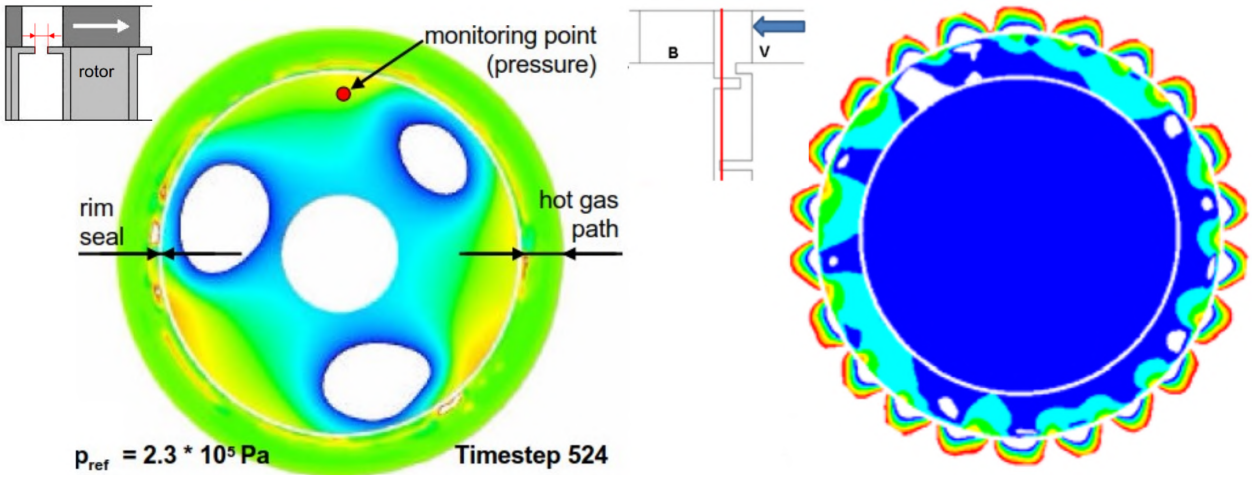

Figure 1.7.: Large-scale, low-frequency flow structures inside the rim seal space represented by alternating pressure patterns by Jakoby et al. [73] (left) and Wang et al. [189] (right)

Schuepbach et al. [175] conducted time-resolved pressure measurements at the rotor exit of a 1.5-stage highly loaded axial turbine for two different rim seal purge flow rates. Spectral analysis of the pressure signal for purge flow injection revealed a band of elevated pressure fluctuations at around half of the rotor blade passing frequency, whereas the low-frequency content vanished

by changing to nominal sucking. The authors associated the pronounced low-frequency pressure fluctuations to a nonlinear interaction with cavity instabilities. Chilla et al. [30] performed extensive numerical investigations of different overlap-type rim seal geometries and related the pronounced low-frequency pressure fluctuations at the rim seal interface to a vortex shedding process of the flow structures into the rotor hub end wall. The circumferential non-uniform pressure field provoked by the rotor-stator interaction, the purge flow rate, the circumferential velocity difference between cavity flow and main annulus flow, as well as the geometry were identified as main drivers for the instabilities found at the rim seal interface. Berg et al. [11] recently presented a study where the authors systematically changed the cavity aspect ratio, the purge flow ratio, and the flow direction (defined by the ratio of primary tangential to axial velocity) to see the effect on the cavity modal response. Most of the open literature is dedicated to the nature of the hub cavity flow structures themselves, with a primary focus on the detrimental effects of these rotating structures on hot gas ingestion.

Aeroacoustics and Noise Emissions Recent technological advances for aircraft engines reduce what originally was the primary source of noise emissions—jet noise—of a turbofan engine. High bypass ratios facilitated substantially reducing jet noise as it scales to the eighth power of the exhaust velocity [19]. Also, the signature of the fan noise was improved due to achievements in the geared turbofan concept. Consequently, the importance of turbine noise has significantly increased. For example, the tonal noise emitted by the blade rows is still a critical quantity, especially during take-off and landing when the engines face toward the ground. Furthermore, the presence of highly unsteady flows can trigger instabilities that were analyzed by various researchers such as Blackburn and Lopez [14] and Globulev and Atassi [50]. Such instabilities can be induced by cavities leading to non-synchronous rotating flow structures, as previously described. The contribution of such non-synchronous structures to the acoustic field of a turbine is rarely discussed in open literature. Rebholz et al. [152, 153] performed a combined study of noise emissions and aerodynamic performance assessment in a 1.5-stage low-pressure turbine representative turbine configuration. The work provides information on the benefit of using a rotor shroud trailing-edge cutback geometry to suppress non-synchronous low-frequency oscillation in the context of turbine noise. Furthermore, the authors stated the complexity of numerically modeling such flow perturbations. Further research was provided on the aeroacoustic aspects of turbines. A fundamental work was provided by Warren and Strahle [190]. Knobloch et al. [85] focused their study on the propagation of direct and indirect combustion noise through a transonic high-pressure turbine stage. By a modal decomposition of the acoustic field, they found other excitation modes than

the anticipated rotor-stator interaction. Faustmann et al. [46] performed a study on the impact of axial spacing and a novel embedded design (additional splitter blades integrated into the nozzle guide vane) in a transonic turbine facility. They reported a considerable reduction in turbine tonal noise due to the increase of axial distance and the embedded design concept. The fundamental work by Tyler and Sofrin [186] described the noise generating and propagating mechanisms using spinning modes and modal decomposition for axial flow compressors, which is also applicable to the turbine acoustic field.

1.2.3. Turbine Rim Seals and Cavity Designs

The rim seal space was found to be a complex flow field region that exhibits specific structures with their own characteristic time scale. As the design of the rim seal and the shape of the cavities bear the potential to control and manipulate the sealing flows, the interest of researchers in that topic has increased in recent years. The overall design goal is to offer geometrical solutions that mitigate the aerodynamic performance penalties associated with the injection of purge flow and at the same time discourage the ingestion of hot gas into the hub cavity. Several interesting publications can be found in open literature that investigated different rim seal design options. Popović and Hodson [143, 144] studied the effect of an extensive range of different overlap-type rim seals in a low-speed turbine cascade. Specifically, the authors found that the integration of a blended forward-facing step in the hub end wall lowers the aerodynamic losses associated with the rim seal flows by one-third in relation to a baseline configuration. They suggested that the overlap between rotor sealing arm and stator hub platform is as large as possible. Schuler et al. [177, 178] conducted a geometrical sensitivity study in a low-pressure turbine cascade for an axial gap rim seal against a compound overlap rim seal that features rounded corners. The work highlighted that the overlap-type seal with rounded corners attenuates the passage vortex strength due to reduced disturbances of the incoming end wall boundary layer. Marini and Girgis [102] performed numerical simulations for a single-stage transonic high-pressure turbine where they compared a rim seal design with a raised leading-edge platform to one with a recessed one. The authors found that the extent and location of the hub passage vortex was altered by the different designs and reported a 0.07 % points higher stage efficiency for the raised leading-edge platform. In a recent study, Chilla et al. [31] investigated the potential of axisymmetric and non-axisymmetric shapes that were integrated into the rotor-sided sealing arm upstream of the leading edge for an overlap-type rim seal. Through extensive computations, it was found that both concepts reduced the main annulus flow ingestion and increased the stage performance

of the turbine. Similar studies can also be found for the tip shroud cavities of low-pressure turbines, which bear similar potential to reduce leakage flow losses. Rosić et al. [164, 165] showed the potential for significant efficiency gains by well-designed shroud cavity geometries. Moreover, Pfau et al. [137] and Gier et al. [48] underlined the importance of the exit shroud cavity geometry on the interaction of shroud leakage flows and the main annulus flow.

1.2.4. Hot Gas Ingestion and Hub Cavity Heat Transfer

The continuous drive to improve gas turbine efficiency using an enhanced turbine inlet temperature places increased significance on the efficient usage of the expensive cooling flows. An important aspect of cooling flow management is the reduction of the ingestion of hot main annulus gas into the stator-rotor rim seal space. The ingestion mechanisms are commonly subdivided into three different effects. The rotating fluid in the rim seal space creates a radial pressure gradient, which can cause the static pressure in the rotor-stator hub cavity to drop below the one in the main annulus. Typically, egress or purging occurs near the rotating disk where the centrifugal effect is most pronounced, which is commonly termed as the "disk-pumping effect." To conserve the radial mass flow, ingestion takes place toward the stator-side of the rim seal cavity. This category of ingestion is typically termed as "rotationally driven ingestion." In that context, Chew et al. [27, 28] provided an elementary model to determine the minimum purge or sealing flow requirements to prevent hot gas ingestion for a simple rim seal geometry. Graber et al. [52] derived an ingestion model based on the turbulent transport and stated that for radial clearance seals with overlapping stationary and rotating parts, the ingestion dynamics are driven by the rim seal geometry rather than by the disk boundary layer. An additional model for rotationally induced ingress was provided in the work of Owen [128], where the author assumed axisymmetric flow and made use of the radial equilibrium equation.

The second ingestion mechanism is induced by the external non-uniform and unsteady circumferential pressure distribution in the main annulus provoked by the presence of the stator vanes and rotor blades. Ingestion takes place when the external pressure (in the main annulus) exceeds the static pressure in the hub cavity and vice versa, egress or purging occurs when the external pressure is lower. This ingestion type is commonly termed as "externally induced ingestion" or "pressure-driven ingestion." Some interesting studies can be found that experimentally underline the described ingestion mechanism, for example, by Kobayashi et al. [86], Phadke and Owen [138], [139] and [140], as well as by Dadkhah et al. [36]. If both rotationally and externally induced

ingestion occurs, literature refers to it by stating "combined ingress" takes place. In recent years, the combined assessment has become more attractive as the complexity of the rim seal designs has increased. Hamabe and Ishida [55] and Chew et al. [29] reported an order of magnitude estimation for the combination of rotationally and externally induced ingestion.
To provide the most efficient use of cooling air, the ingestion of hot gas from the main annulus into the rim seal cavity must be assessed and quantified. Also, detailed knowledge of the convective heat transfer characteristics in hub cavities is required. Specifically, the temperature distribution on the rotor disks is necessary to predict stresses and durability. Open literature mainly addresses the ingestion mechanisms through experimental and computational studies. Scant publications can be found that investigate the convective heat transfer quantities, such as the heat transfer coefficient and adiabatic wall temperature. Experimental studies that address the topic are typically conducted in rotating disk facilities without stator vanes and rotor blades. One example was provided by Owen and Rogers [97], where rotor-averaged heat transfer levels were provided. Metzger et al. [111] provided in their early work a more localized consideration of the heat transfer quantities where jet impingement onto the rim of a free rotating disk was experimentally investigated. Qureshi et al. [147] measured local rotor disk heat transfer coefficients for a model turbine disk geometry portion. Metzger et al. [110] obtained detailed radial distributions of both stator and rotor heat transfer coefficients using a transient experimental method. The method included a thin coating of visually indicating material applied to the surface section of interest. Using optical data acquisition facilitated obtaining the surface temperatures, which were used to derive the heat transfer coefficients with consistent thermal boundary conditions. One of the few publications that involved the evaluation of heat transfer quantities in conjunction with a bladed main annulus was provided by Roy et al. [167]. The authors presented both computational and experimental data. The rotational Reynolds number and the secondary flow rate were changed to provide an extensive sensitivity study. The work concluded that the secondary flow rate dominated heat transfer in the source region (radially inside of the rim seal space), whereas rotational movement of the fluid relative to the rotor disk drove the convective heat transfer coefficient in the core region (closer to the effective rim seal). In addition, an empirical correlation was provided for the Nusselt number distribution on the rotor disk surface.

1.3. Research Objectives

The global objective of this work is to contribute to optimizing the aerothermal performance of advanced high-pressure turbines. Through integrating novel design concepts, aerodynamic performance is improved by reducing cooling

requirements (using advanced rim seal arrangements) and lowering blade count (coupled with specific blade tip designs). This improvement process also intends to quantify potential concomitant effects on turbine characteristics, such as turbine noise.

The following research objectives are addressed in this work, using accurate experimental techniques and extensive numerical modeling of three different engine-representative turbine configurations equipped with advanced geometrical features:

(1) Elaborate the significance of low-frequency, non-synchronous flow structures within the rim seal space for different aerothermal design aspects and assess the capability of numerical tools to predict them accurately.

(2) Derive measures to attenuate the signature of the hub cavity asynchronous flow perturbations by extensively probing different turbine operating conditions and geometrical variations of the rim seal.

(3) Quantify and reduce the sensitivity of different rotor performance parameters to the injected purge flow using novel geometrical features installed at the rim seal exit.

(4) Experimentally determine the ingestion and heat transfer quantities for different sealing flow rates in a high-pressure turbine representative rim seal arrangement and assess the capability of existing empirical correlations to predict the heat transfer levels inside the hub cavity.

(5) Describe and quantify the performance and aeroacoustic implications of a pronounced blade count reduction for a high-pressure turbine rotor and provide blade tip design concepts to diminish the provoked additional tip losses due to the enhanced blade loading.

1.4. Thesis Outline

The present work provides an experimental and computational investigation of the aerothermal effects related to high-pressure turbine rim seals and rotor blade tip geometries. Three different turbine configurations, with various individual variations, were extensively probed in the context of this thesis using purpose-made instrumentation and unsteady numerical modeling. The thesis content includes explanations of the specific unsteady nature of rim seals and highlights the impact on the characteristics of a turbine stage (Chapter 3). The detrimental effects of hub cavities and injected rim seal purge flow are elaborated, and a novel rim seal design is proposed to improve the aerothermal

performance of an already optimized turbine configuration (Chapter 4). The rim seal content of the thesis is complemented by an investigation of the heat transfer quantities inside the hub cavity under different purge flow rates (Chapter 5). Different rotor blade tip designs were tested to reduce the detrimental effect of the leakage and secondary flows near the tip for a reduced blade count rotor configuration (Chapter 6). Hence, this thesis is structured as follows:

Chapter 1 At the beginning of the thesis, the underlying motivation of the work is described. The need for improved aerodynamic and thermal performance of high-pressure turbines in compliance with strict emission regulations for the stationary gas turbine and aviation sector is discussed. In that context, the integration of well-designed rim seals and blade tip geometries bear great potential to advance the respective technological field. Accordingly, the literature review presents a detailed overview of the unsteady aerodynamics and thermal characteristics of a turbine stage such that a solid base is given for the discussion of the major findings of the present thesis.

Chapter 2 The Methods chapter introduces the experimental and numerical methods that were used in the course of this work. The axial turbine facility is detailed, and the different turbine configurations, various instrumentation types, and data acquisition systems are described. The modified rim seal purge flow injection system that allows for cooling down the coolant flow is described. A purpose-made rainbow rotor setup that features coolant air ejection at the blade tip is introduced. Furthermore, the data post-processing of the acquired experimental data is explained, and the measurement uncertainty for all measurement techniques is discussed. The description of the numerical setups for the unsteady calculations is given in the last section of the chapter.

Chapter 3 The flow field in turbine cavities is found to have characteristic dynamics. This chapter specifically discusses the nature of non-synchronous flow perturbations in the rim seal space, termed as "hub cavity modes," and their modulation by the injected rim seal purge flow. The convection of the signature of the formed hub cavity structures is investigated. The impact of the modes on the characteristics of a turbine stage is addressed. The capability of unsteady computations to model the cavity dynamics is investigated. The numerical results were used to reveal the source of the specific flow perturbations and quantify their impact on the turbine ingestion behavior.

Chapter 4 The second chapter, related to turbine rim seals, dedicates its focus to the aerodynamic effects of novel geometrical features installed at the

interface between the hub cavity and the main annulus flow to mitigate the detrimental impact of rim seal purge flow injection on the stage performance. Fast-response and pneumatic probe measurements reveal the beneficial impact of the geometrical features on the aerodynamic performance characteristics of an already optimized turbine stage. A qualitative assessment of the change in hot gas ingestion levels is provided by inter-row probe measurements complemented by unsteady computational fluid dynamics (CFD) calculations.

Chapter 5 The quantification and investigation of the convective heat transfer and main annulus ingestion in an engine-representative overlap-type rim seal are presented in this part of the work. The major dynamics in the hub cavity are investigated by an array of unsteady pressure transducers installed on the first stator- and rotor-sided cavity wall. A purpose-made heat transfer setup allows for determination of the cavity wall temperatures and convective heat transfer quantities by modifying thermal boundary conditions. The integration of a cold purge flow secondary air system enables enhancement of the temperature difference between the main annulus and cavity flow such that ingestion characteristics can be derived. The influence of different rim seal purge flow rates on specific quantities is defined, which enables the generation of a unique dataset.

Chapter 6 This chapter addresses the potential to diminish tip leakage and secondary flow losses by employing geometrically altered rotor-blade tip designs for an unshrouded turbine configuration with a substantially reduced blade count. The aerodynamic and aeroacoustic implications of the blade count reduction are detailed with respect to a baseline design. The performance quantities of the different tip designs are assessed with fast-response pressure measurements in combination with a rainbow rotor design featuring five-blade tip designs. The sensitivity of the designs to tip coolant ejection is addressed. Based on aerodynamic performance parameters, the most favorable design is elaborated.

Chapter 7 The concluding chapter presents summaries and conclusions from the individual chapters and offers guidelines for the aerothermal design of high-pressure turbine stages. An outlook for future investigations is given to the interested reader.

2. Experimental and Numerical Methods

2.1. Experimental Test Facility

The experimental investigations were performed in the research axial turbine facility "LISA" at the Laboratory for Energy Conversion at ETH Zurich. The test facility is a continuously running system operated at moderate rotational speeds and low flow temperatures. It was designed to accommodate axial turbine configurations, ranging from 1-stage up to 2-stages, which are tested under engine-representative operating conditions. In the context of this thesis, the test rig was assembled with multiple 1.5-stage, high-pressure turbine representative configurations. A schematic view of the facility is provided in Figure 2.1.

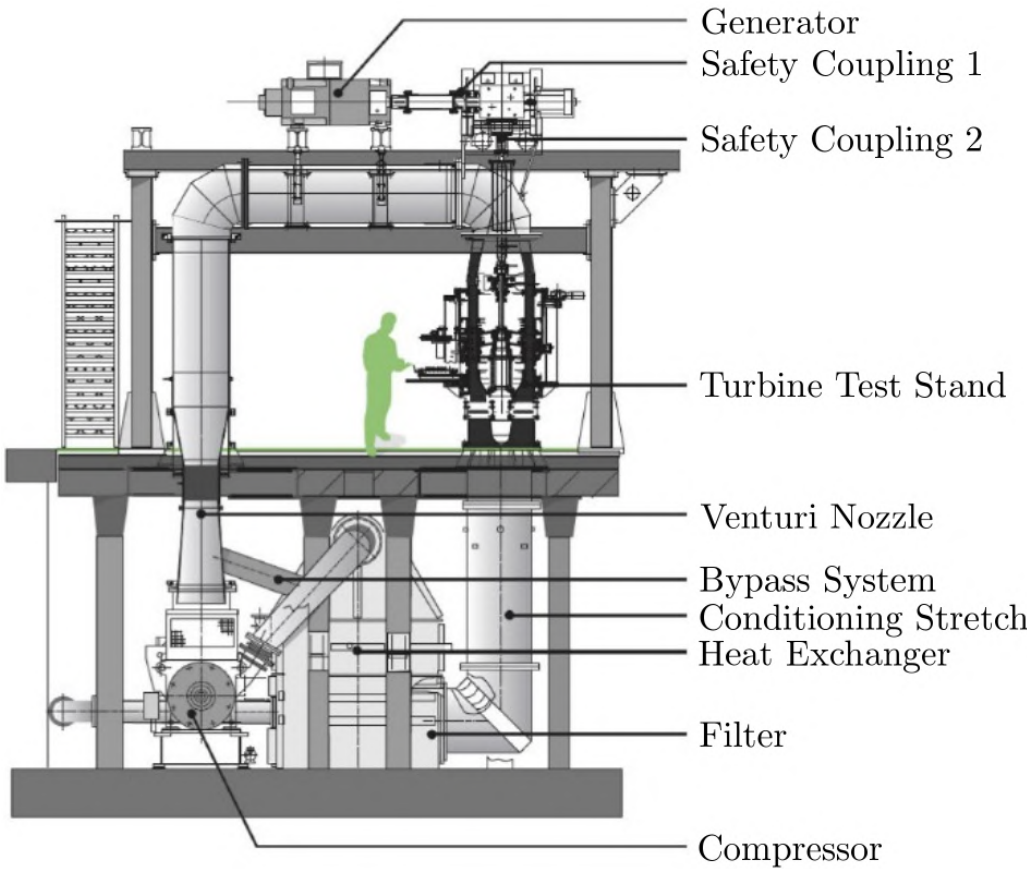

Figure 2.1.: Schematic view of the "LISA" research axial turbine facility

The flow path of the test facility is quasi-closed and opens to atmosphere downstream of the turbine test section. The working fluid for the experiments

is air. The facility extends over three floors and features a 750 kW radial compressor that achieves a maximum compressor pressure ratio of $\Pi_{\text{max}} = 1.5$ at a mass flow rate of approximately 12 kg/s. The turbine inlet total temperature $T_{\text{t,in}}$ is controlled with a two-stage water-to-air heat exchanger to an accuracy of $\pm 0.3\,\%$. In order to account for varying atmospheric pressures, the total-to-static pressure ratio over the test section is kept constant by adjusting the variable inlet guide vanes of the compressor at constant rotational speed. A calibrated Venturi nozzle measures the total mass flow upstream of the compressor inlet. The 3 m long flow conditioning stretch homogenizes the flow before entering the turbine test section. Additionally, a flow path contraction is installed to further reduce the flow non-uniformity and brings the air to a turbine inlet Mach number of $M = 0.14$. Three main struts in the nose cone region (upstream of the flow contraction) support the shaft train. The turbine inlet total pressure is measured with Pitot probes installed on additional thin struts located approximately three axial chords upstream of the test section. The rotational speed of the turbine is kept constant and is controlled to an accuracy of $\pm 0.02\,\%$ (± 0.5 rpm) by a DC generator. The torque of the turbine is measured with a custom-made torque meter, which is installed on the vertical shaft between the turbine test section and the gearbox. An angular gearbox with gear ratio 1:2 is installed and couples the vertical shaft train to the horizontal one. In case of a gearbox failure, the safety couplings decouple the gearbox from the turbine and the generator, respectively. The generated power by the turbine is fed back into the electricity grid.

2.1.1. Turbine Operating Point

The turbine design operating conditions indicated in Table 2.1 are kept the same for all turbine configurations and measurements presented in this work. The total-to-static pressure ratio over the 1.5-stage configurations is kept constant at $\Pi_{1.5} = 1.65$ and is determined from the turbine total inlet pressure at 36 % span and the static pressure at the hub at the exit of the second stator. Given the maximum compressor pressure ratio of $\Pi_{\text{max}} = 1.5$, a tandem de-swirl vane arrangement is integrated to recover the static pressure at the exit of the second stator back to ambient conditions, which enables reaching the intended design turbine total-to-static pressure ratio. The turbine total inlet temperature is controlled to be stable at $T_{\text{t,in}} = 328$ K. The flow at the exit of the first stator is compressible with a peak Mach number of 0.55 in close vicinity to the hub. Since the facility is open to atmosphere at the exit of the turbine section, the pressure information is typically non-dimensionalized by the turbine inlet total pressure, which permits accurate comparisons between different measurement days.

Table 2.1.: Turbine design operating conditions

$\Pi_{1.5}$	$1.65 \pm 0.4\,\%$
$T_{\mathrm{t,in}}$	$328 \pm 0.3\,\mathrm{K}$
$\frac{\dot{m}\sqrt{T_{\mathrm{t,in}}}}{p_{\mathrm{t,in}}}$	$151.8 \pm 0.2\,\% \frac{\mathrm{kg}\sqrt{\mathrm{K}}}{\mathrm{s \cdot bar}}$
$\frac{N}{\sqrt{T_{\mathrm{t,in}}}}$	$2.48 \pm 0.05 \frac{\mathrm{rps}}{\sqrt{\mathrm{K}}}$
M (S1ex/Rex/S2ex)	0.53/0.27/0.48
Re (S1/R/S2)	$7.1/3.8/5.1 \cdot 10^5$

2.1.2. Aerodynamic Probe Measurement Planes and Grid

The aerodynamic results presented in this work were obtained from measurements using miniature pneumatic and fast-response probes. Typically, measurements at four different measurement planes were performed for most of the considered 1.5-stage turbine configurations. Depending on the subject of interest and the turbine configuration, the measurement grid was moderately changed with respect to the number of radial grid points. The detailed description of the measurement grid is given in the subsequent paragraphs, and a schematic representation of the measurement locations is shown in Figure 2.2.

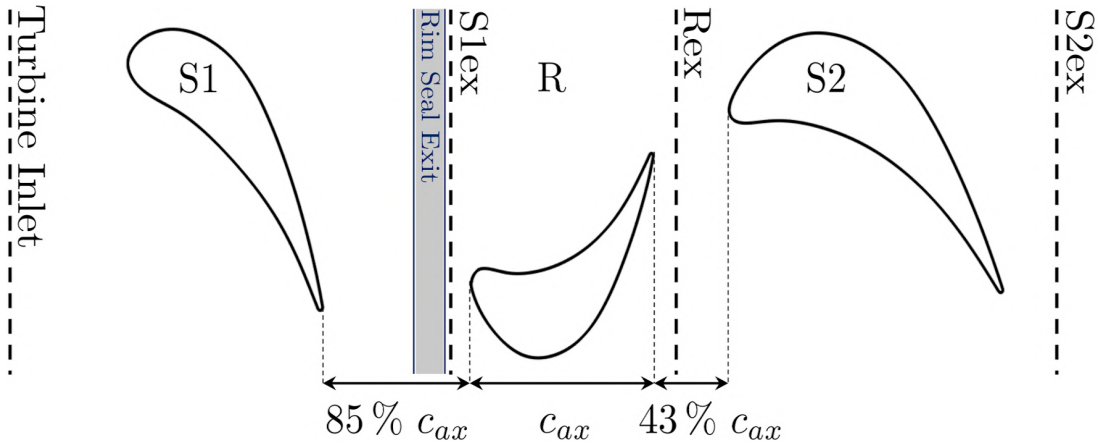

Figure 2.2.: Representation of probe measurement planes with respect to the vane and blade positions at mid-span (not to scale). Axial spacing between the blade rows in percentage of the rotor axial chord c_{ax} as well as the rim seal exit is depicted.

Measurement Plane at Turbine Inlet Probe measurements at the inlet of the turbine configuration were conducted to determine the inlet total pressure profile and the turbulence intensity which were later used as boundary

conditions for the numerical predictions. Pneumatic five-hole probe (5HP) and fast-response probe (FRAP) measurements were performed about 60 % of the first stator axial chord upstream of the test section. The 5HP grid consists of 11 equidistant points in the circumferential direction covering one first stator pitch and 39 points in the radial direction, which were clustered toward the end walls. The FRAP grid is defined identically as the 5HP one except the most inner grid point is left out in order to provide a larger safety distance of the probe head toward the hub end wall.

Measurement Plane S1ex The rotor inlet flow field is experimentally examined by using a miniature pneumatic four-hole probe (4HP) and the FRAP at the measurement plane S1ex. At this plane, the 4HP is used instead of the 5HP due to its probe tip shape, which allows the probe to traverse into the rim seal space. The measurement plane is located about 11 % of the rotor axial chord at mid-span upstream of the rotor leading edge. The measurement grid includes initially 39 (38) radial points for the 4HP (FRAP) and 41 equidistant points in circumferential direction covering one first stator pitch with a resolution of 0.25°. The radial traversing features a clustering toward the end walls.
For the rim seal investigations (provided in Chapter 3 and 4), the measurement plane was modified by tilting the radial axis of the probe traversing by 7° toward the first stator. Depending on the rim seal design, this permits immersing the probe head into the rim seal hub cavity down to −20 % span without risking the mechanical integrity of the probe. The most extended measurement grid includes 49 radial points with fine clustering at the interface between the rim seal and the main annulus. This provides an appropriate spatial resolution to resolve the pronounced velocity gradients in this region. The circumferential grid resolution remains unchanged with respect to the traditional measurement plane.

Measurement Plane Rex The rotor exit flow field is investigated at the measurement plane Rex which is located about 12 % of the rotor axial chord downstream of the rotor trailing edge at mid-span. For an accurate assessment of the turbine stage efficiency, 5HP measurements were conducted. In order to determine the underlying unsteady flow mechanisms associated with the change in efficiency, fast-response probes were used to complement the studies. The measurement grid for the 5HP and fast-response probes covers in the circumferential direction one-second stator pitch with a total number of 41 equidistant grid points providing a resolution of 0.25°. The radial traversing features 39 (38) grid points for the 5HP (FRAP), and a fine clustering of the measurement points toward the end walls were applied. To provide sufficient safety distance of the probe tip toward the rotor hub end wall, the most inner measurement point of the probe is at about 6 % blade span.

Measurement Plane S2ex The turbine exit measurement plane is located about 20 % of the second stator axial chord downstream of the second stator trailing edge at mid-span. The spatial resolution of the measurement grid is identical to the rotor exit one. In Table 2.2, a summary of the different probes which were used for the specific measurement planes is provided.

Table 2.2.: Overview of the aerodynamic probes used at different measurement planes

Measurement plane	Probes
Turbine inlet	5HP, FRAP
S1ex	4HP, FRAP
Rex	5HP, FRAP, FENT
S2ex	5HP, FRAP, FENT

2.1.3. Rim Seal Purge Flow Injection System

In the scope of this work, the different turbine configurations were operated in the presence of cooling flows. One of these cooling flows is the air injected between the first stator and the rotor, which is termed as "rim seal purge flow" or simply "purge flow" throughout this thesis.
To provide the turbine with purge flow, mass flow from the primary air loop was bled off upstream of the main flow conditioning stretch, which is termed "bypass mass flow" $\dot{m}_{\mathrm{bypass}}$ and measured with a standard Venturi nozzle. After passing an auxiliary distributor (Octopus), the air was fed into the rim seal hub cavity through 10 tunnels inside the first stator. One sector, including three vanes, features one tunnel whereas two sectors are missing one. In Figure 2.3, a schematic view on the leakage flows in the 1.5-stage turbine configuration is illustrated. Inside the rim seal hub cavity, two leakage paths are indicated with two dotted arrows. One of them is through the rotor upstream seal into the main annulus flow, $\dot{m}_{\mathrm{purge}}$. The effective leakage flow, $\dot{m}_{\mathrm{drum}}$, is ejected through the drum to the atmosphere after being measured with an additional standard Venturi nozzle. The drum plenum pressure level can be adjusted by a vacuum pump in combination with a manually operated valve. The pressure inside the drum is therefore controlled such that the pressure difference Δp across the rotor downstream seal is about zero. Under these conditions, the mass flow through the rotor downstream seal is assumed to be zero, which facilitates an accurate determination of the drum leakage flow. Subsequently, the injected rim seal purge flow can be calculated as the difference between the bypass mass flow and the drum leakage mass flow.
The turbine operating parameter of interest with respect to the purge flow is the rim seal purge flow injection rate IR, which is the ratio between the

injected mass flow and the main turbine mass flow. This quantity is defined in Equation 2.1.

$$IR = \frac{\dot{m}_{\text{purge}}}{\dot{m}_{\text{main}}} = \frac{\dot{m}_{\text{bypass}} - \dot{m}_{\text{drum}}}{\dot{m}_{\text{main}}} \tag{2.1}$$

The measurement and computational results presented in this work were conducted for various injection rates ranging from $IR = 0.0\,\%$ up to a maximum of $IR = 1.2\,\%$. The nominal purge flow injection rate was chosen to be $IR = 0.8\,\%$. The initial rim seal purge flow studies were conducted with a temperature ratio close to unity between the total temperature of the purge flow and the turbine inlet total temperature. The typical variation of the purge flow injection rate throughout a measurement day was within $\pm 0.02\,\%$, and the measurement uncertainty was evaluated to be $\pm 0.01\,\%$.

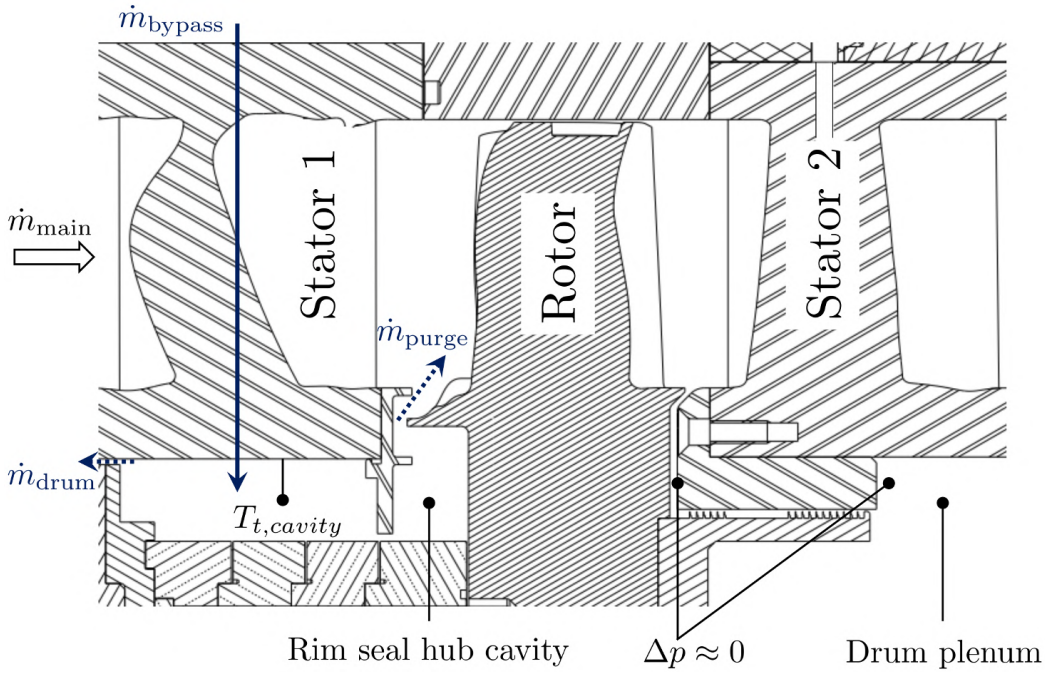

Figure 2.3.: Illustration of leakage flows in one of the 1.5-stage configurations

2.1.4. Turbine Auxiliary Air System Modification: Cold Bypass Flow Setup

To increase the temperature difference between the injected rim seal purge flow and the main annulus flow, the auxiliary air system of the test rig was modified. The modified system was specifically integrated for the rim seal hub cavity heat transfer investigations and was also used for the rotor tip geometry study in combination with blade tip coolant ejection. A comprehensible schematic of the modified auxiliary airflow path is depicted in Figure 2.4. The basic concept of the modification includes the integration of a separate compressed air flow

path (dashed blue arrow), which is fed by the ETH shop air reservoir. The dew point of the compressed air (6 bar at source) is, in a first step, reduced to about 223 K (−50 °C) by a regenerating adsorption dehumidifier. The setting of the supplied air mass flow is enabled by a control valve, which is located between the dehumidifier and the chiller. The chiller is a single cycle cooler that is specified to be capable of reducing the air mass flow down to 210 K (−63 °C) without a stated corresponding mass flow and temperature stability indication. Therefore, detailed testing of the system during standstill and turbine operation was undertaken. The two components were initially used for LEC's high-speed wind tunnel LAVAL. More detailed information on the dehumidifier and chiller can be found in the work of Vipluv [187]. The piping toward the experimental facility had to be modified to provide cooled air mass flow to the test section and accurately measure the mass flow by means of an orifice plate measurement section. The airflow path from the chiller toward the turbine test section was thermally insulated to reduce heat pickup along the way and avoid condensation effects.

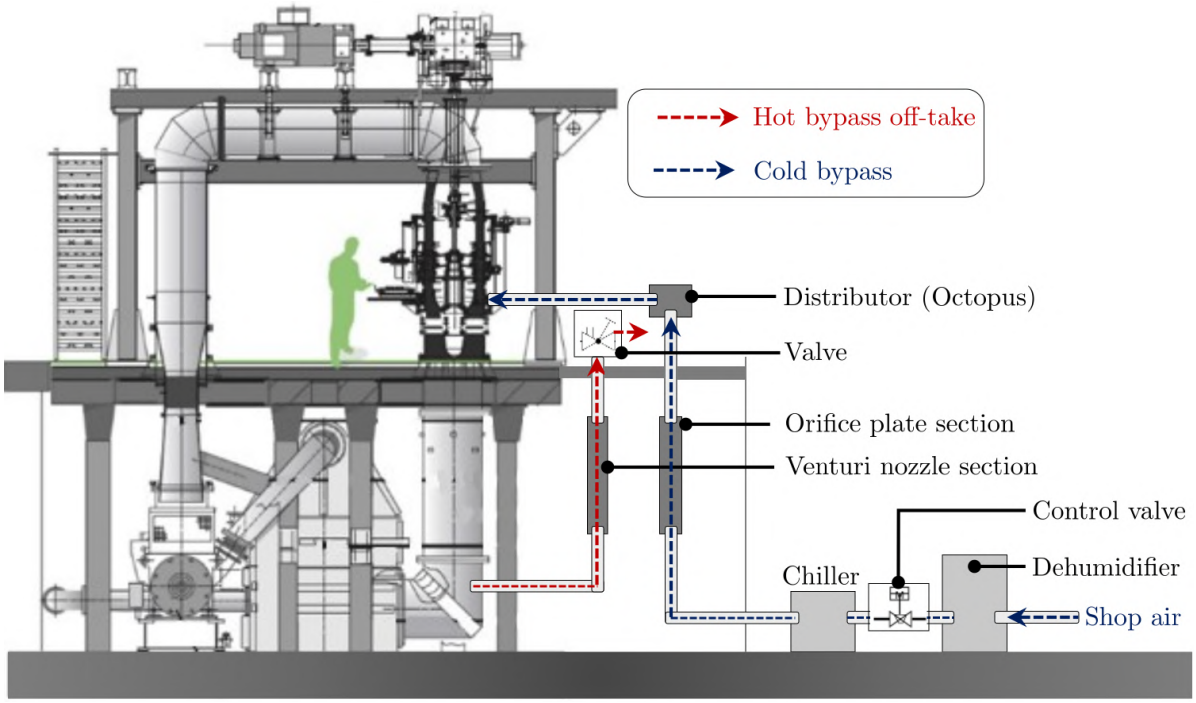

Figure 2.4.: Schematic of cold bypass air path (dashed blue arrow) and balancing hot bypass offtake (dashed red arrow)

Different flow quantities were measured within the flow path. First, the cold bypass mass flow was accurately determined using an ISA standard orifice plate with the mass flow calculation provided by the ISO 5176-2 norm. The required pressure data was recorded by a difference PSI module, which is introduced in the subsequent section 2.1.6. A PT100 resistance thermometer was installed in the external distributor (Octopus) to provide temperature information on the incoming airflow and heat pickup of the flow along the piping. Additionally, a

humidity sensor was installed in the distributor to track a possible malfunction of the dehumidifier and avoid potential condensation effects inside the turbine test section. The mass flow was split into 10 tunnels in the distributor, identical to the previously introduced purge flow injection system, and fed into the rim seal hub cavity. Inside the hub cavity, the temperature of the injected cold bypass flow was measured using two miniature temperature probes that were displaced in circumference and provided the temperature boundary conditions for future numerical predictions. The measurement location of the cavity temperature probes is schematically shown in Figure 2.3. The temperature probes were equipped with miniature PT100 sensors, which were installed on a polyetheretherketone (PEEK) shaft that reduces the effect of thermal conduction of the hotter first stator platform on the sensor due to its low thermal conductivity. Having a small size temperature sensor increases the accuracy of the total temperature measurements of the cavity fluid [61].
Since a separate source was feeding the cold bypass flow to the turbine test section, the injected mass flow needed to be balanced not to constantly add mass flow to the quasi-closed loop system, which would change the turbine operating point over time. Therefore, an offtake of the primary air loop upstream of the main flow conditioning stretch was integrated (dashed red arrow, Figure 2.4). The mass flow that was bled off was measured with a standard Venturi nozzle that was previously used for the original rim seal purge flow injection system and afterward vented to atmosphere. A control valve permits regulation of the mass flow such that the mass flow difference between the cold bypass mass flow and the hot offtake is close to zero.
The characteristics of the modified auxiliary air system were tested in terms of different settings for the single-cycle cooler and their impact on the cold bypass mass flow stability, the temperature stability in the rim seal hub cavity, and the humidity levels in the auxiliary distributor. The main objective was to provide stable conditions of the air supply for a measurement time of at least 10 hours. A chiller temperature set point of 253 K (−20 °C) was found to be appropriate to provide stable conditions for a maximum cold bypass mass flow rate of 175 g/s, which led to a purge flow injection rate of $IR = 1.2\,\%$. The temperature in the rim seal hub cavity significantly depended on the amount of injected cold bypass air. A maximum temperature difference between the turbine inlet total temperature and the cavity total temperature of 35 K was found, which resulted in a temperature ratio of 0.89 for a rim seal purge flow injection rate $IR = 1.2\,\%$. More data with respect to the total temperature ratios can be found in Table 2.3. The cavity temperature variation during one measurement day was typically ±0.3 K. The variation of the cold rim seal purge flow injection rate over one measurement day was within $\pm 0.02\,\%$ (e.g., $IR = 0.8\,\% \pm 0.02\,\%$).

Table 2.3.: Total temperature ratios for different rim seal purge flow injection rates (IR)

IR [%]	$T_{t,cavity}/T_{t,in}$ [-]
0.0	0.963
0.4	0.917
0.8	0.901
1.2	0.893

2.1.5. Tip Coolant Ejection and Rainbow Rotor Design

Blade tip designs and tip leakage and cooling flows are crucial aspects of state-of-the-art gas turbines. To test all these effects in a cost- and time-effective way, the test rig was upgraded. This study's tasks include extending the turbine rig capabilities to provide coolant flow to the blade tips and testing different blade tip geometries during the same run. The new design was operated in conjunction with the previously introduced cold bypass flow setup (section 2.1.4) and was integrated for the reduced blade count rotor configuration described in section 2.2.3. The setup was expected to provide a safe upgrade to the test rig, which permits study of the aerodynamics and blade tip heat transfer patterns (not covered in this work) associated with tip coolant ejection. A modular design is therefore introduced in this section, which allowed for the installation of different blade tip designs on the same rotor as well as measurement of the supplied tip coolant flow.

Tip Coolant Setup and Mechanical Integrity The main objectives for the design of the blade tip coolant and rainbow rotor configuration were the safe operation, the ejection of coolant at the blade tip as well as the ability to install and, if necessary, exchange different blade tip geometries. Since the turbine rig was designed to feature blade integrated disks (blisks), the design space was also limited by manufacturing capabilities. A viable solution that allowed for the combination of all the design requests was a blade tip cap approach, where the blade is separated into a cap and a blade root section. This provides the advantages that a blade internal coolant supply path can be manufactured by conventional manufacturing processes and allow for modular installation of different blade tip geometries. In Figure 2.5, a conceptual representation of the blade cap approach is depicted. Three pitch-wise consecutive blades of the blisk are machined down to about 75 % blade span, and two rib-type roots for fixation are left toward the leading and trailing edge of the chopped blade. In the center of the two ribs, the tip coolant supply borehole is drilled, which provides the internal tip coolant flow to the blade cap plenum. The blade caps are manufactured out of PEEK, a thermoplastic polymer which

provides a low density combined with a high mechanical strength (tensile strength: 90–100 MPa) for a temperature up to 140 °C. Additionally, the material electrically and thermally insulates appropriately such that a special heat transfer setup also could be implemented on the blade tip (not covered in this work). It is convenient to use the blade cap approach for instrumentation on the blade tip because temperature and pressure sensors, which are installed in the blade cap plenum, can be installed and calibrated independently of the rotor blisk. The blade caps typically feature cooling and dust holes inside the squealer geometries and on the blade-pressure side. More details can be found in section 2.2.3, where the different tip designs and cooling hole patterns are introduced. A tight fit of the blade caps, combined with two pins, provides the mechanical fixation of the tip caps.

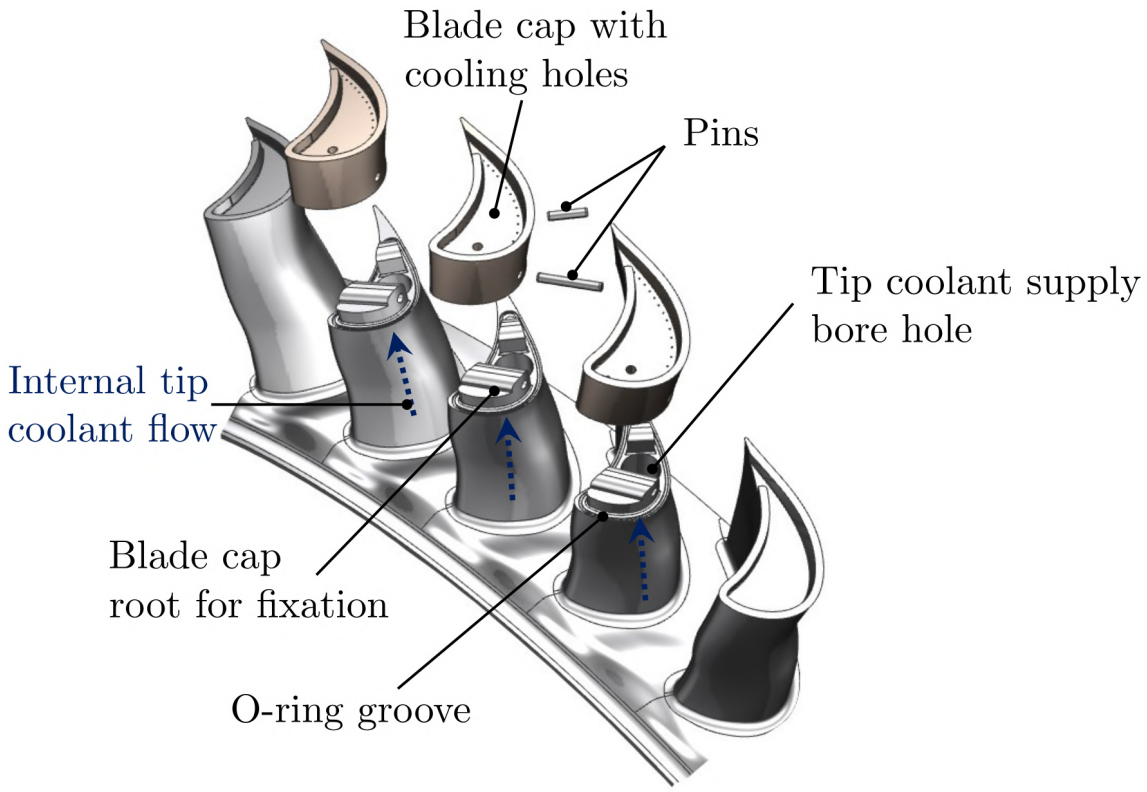

Figure 2.5.: Representation of modular tip coolant ejection rotor design for different blade tip geometries

For the preliminary design of the setup, a finite element structural analysis was conducted using ANSYS Workbench. Since the mechanical integrity of the concept had to be guaranteed, experiments were employed before proceeding with the final manufacturing of the components. The expected centrifugal load on the fixation was calculated to be 410 N, also considering an overshoot speed of the turbine during the startup sequence. To investigate the mechanical robustness of the design, a blade cap dummy was built in-house, which is shown in Figure 2.6 (left). An upper and lower rib allows for clamping the assembly in a tensile test machine. The boreholes in the upper clamping rib

were initially designed to conduct an additional structural test by attaching weights using fishing lines. The Institute of Virtual Manufacturing (IVP) at ETH Zurich permitted the performance of static tensile tests on their apparatus (Figure 2.6, right) which also provides a thermal chamber. Details of the tensile test machines can be found in [125]. Short-time tests were conducted at two different chamber temperatures (room temperature and 55 °C), which were representative of the temperatures throughout the first stage of the turbine test section. The test assembly was ramped up to a load of 1000 N at two different rates (2 N/s and 5 N/s). Consecutively, a long-term test over six hours at a load of 1'000 N was conducted that showed excellent robustness and reliability of the setup. The design was therefore examined experimentally and provided a safety factor of at least 2.4. Experimental testing in the turbine rig proofed reliable operation for over 500 operating hours.

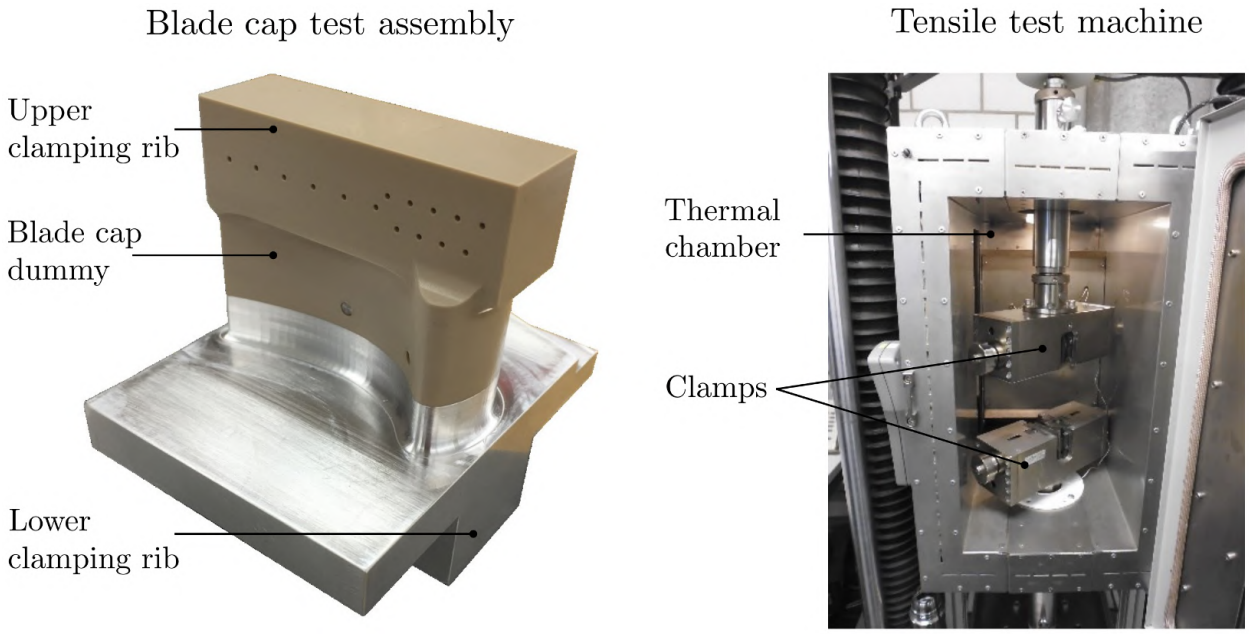

Figure 2.6.: Blade tip cap dummy setup for mechanical integrity tests: tip cap dummy (left) and tensile test machine (right, IVP ETH Zurich [125])

To avoid leakage flows in or out of the blade cap plenum, the final design included an O-ring at the interface between the blade cap and blade root. After installation of the blade caps, the recess areas (due to pin boreholes and instrumentation pockets) were properly filled with high-strength epoxy. The surfaces were carefully polished to avoid flow disturbances.

Tip Coolant Flow Path and Measurement (Miniature Venturi Tube)
The mass flow provided to the blade tip established out of a pressure difference between the rim seal hub cavity and the blade tip as well as an anticipated pumping effect due to the rotation of the rotor. The internal cooling path in the blisk is schematically shown in Figure 2.7 (left). The tip coolant flow is

drawn from the rim seal hub cavity (recalling Figure 2.3). The rotor assembly on the rotor-sided hub cavity wall is equipped with a plate that has access holes such that the coolant flow enters the internal cooling path. These access holes are not axially manufactured but are aligned with the local relative flow yaw angle, which was extracted out of a steady-state computational fluid dynamics (CFD) simulation. The presence of the access plate allows for sealing the internal cooling path from the hub cavity so that the tip coolant mass flow is reduced to close to zero. The coolant is then guided radially outwards and enters the miniature Venturi tube, which measures the tip coolant mass flow based on the pressure difference achieved by the flow acceleration in the contraction section. Details on the rotor pressure sensors and calibration that were used to equip the Venturi tube can be found in section 2.4. A picture of the raw (not instrumented) Venturi tube out of aluminum is provided in Figure 2.7 (right). The internal shape of the Venturi was achieved by 3D printing (selective laser melting, SLM), whereas the outer shape and features were manufactured by conventional processes. To withstand the centrifugal load, an outer thread was manufactured so that the front part of the Venturi tube could be screwed to the rotor blisk. Pockets for the micro-electro-mechanical systems (MEMS) pressure sensor housing were manufactured. The slots and borehole at the rear part of the tube were designed to distribute coolant inside the blade cap plenum and reduce the impingement on the internal lower squealer surface. The tip coolant was ejected through the cooling and dust holes to the main annulus flow. Additional instrumentation inside the blade cap plenum, such as resistance temperature sensors, as well as MEMS pressure sensors, helped to determine the fluid properties inside the plenum.

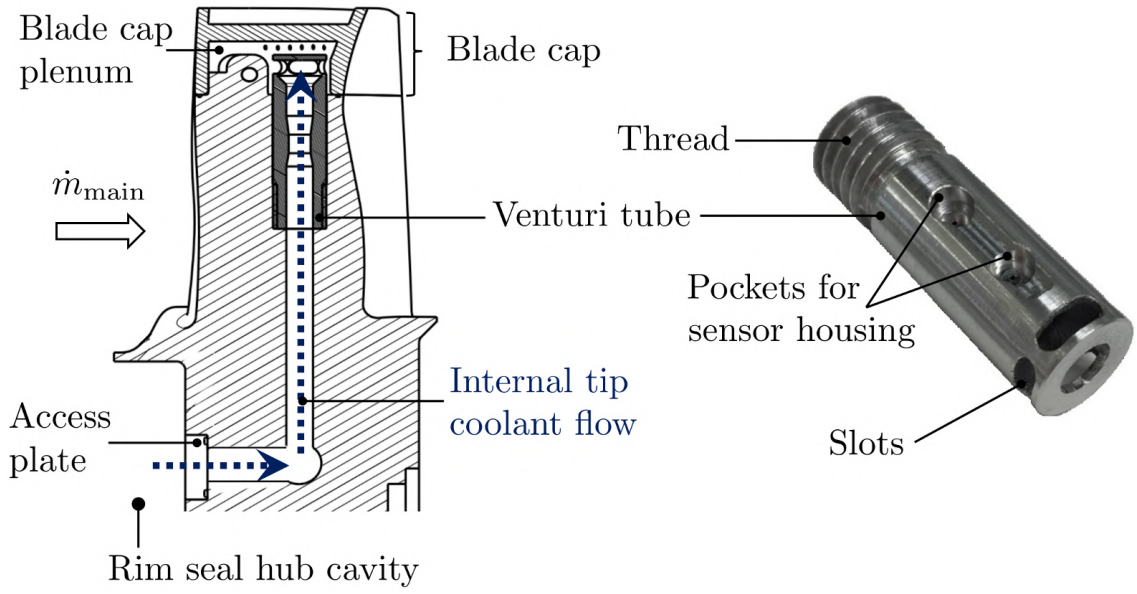

Figure 2.7.: Blade tip coolant flow path (left) and miniature Venturi tube for coolant mass flow measurements (right)

Blade Tip Ejection Operating Conditions The previously introduced blade cap and tip coolant ejection setup was tested during several runs of the test rig. Specifically, the behavior of the ejected tip mass flow is of importance. By means of the miniature Venturi tube which is installed as part of the internal rotor tip coolant path, the mass flow was measured for the turbine design operating conditions and part-load conditions. In Figure 2.8 (left), the tip coolant mass flow ratio TR is depicted for two different rotational speeds of the rotor and various rim seal purge flow injection rates. The tip mass flow ratio is given in percentage of the main turbine mass flow (note that the stated value needs to be interpreted with respect to one rotor passage). For the design rotational speed, a tip coolant mass flow ratio of around 0.4 % was measured. The original intent was to change the tip coolant mass flow by changing the injected amount of rim seal purge flow. As indicated in the figure, the tip coolant mass flow increased by only 3.5 % when increasing the purge flow from $IR = 0.0\,\%$ to the design condition of $IR = 0.8\,\%$. Only a moderate change can therefore be achieved when changing the purge flow. This suggests that the main driver for the tip ejection is the rotational speed and the associated pumping effect. The pressure sensor installed in the blade cap plenum underlines the behavior in the tip coolant mass flow. In Figure 2.8 (right), the normalized cap plenum pressure (normalized by the turbine inlet total pressure) is provided for different purge flow injection rates and two rotational speeds. At design rotational speed, the plenum pressure changes only by about 1.4 %. Such measurements were performed for the Optimized Squealer and the Trench concept. Both measurements agree with each other within 1.5 %.

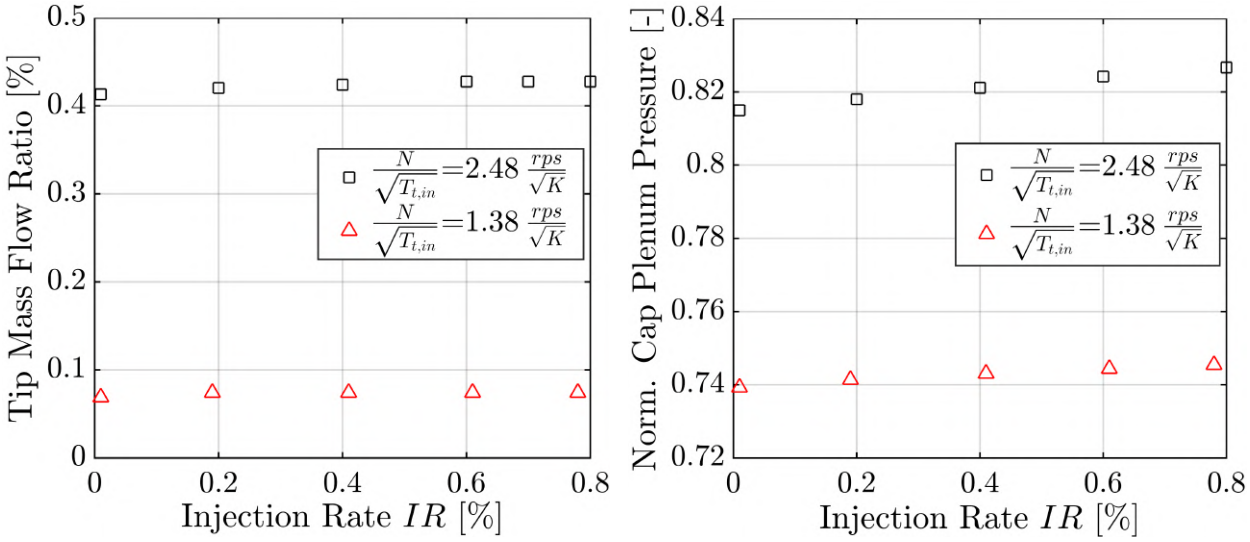

Figure 2.8.: Dependency of the tip coolant mass flow ratio TR (left) and the blade cap plenum pressure (right) with respect to the turbine rotational speed

Based on the presented coolant mass flow rates and the plenum pressure, the

non-dimensional quantities for the tip coolant ejection study can be estimated. In Table 2.4, the widely used quantities are shown. The subscript "c" refers to the coolant quantities, whereas the subscript "∞" is related to the main flow or free stream quantities. The blowing ratio BR was calculated out of the main turbine mass flow and the tip coolant mass flow, by dividing their respective values by the corresponding area. For the coolant, this would be the total area provided by the cooling holes and dust holes. Since it is not feasible to provide accurate information on where most of the coolant mass flow is leaving the plenum, the aforementioned approach was used to calculate the blowing ratio. The density ratio DR was evaluated using the aerodynamic probe data at stator 1 exit and rotor exit. The static pressure and static temperature at 93 % span at both locations were extracted and averaged to get a mean static pressure and temperature, and consequently a mean density ρ_∞. The coolant density was evaluated by the blade cap plenum pressure and temperature measurements. For a purge flow injection rate of $IR = 0.8\,\%$, the measurements in the plenum revealed a temperature of about 304 K. The momentum flux ratio I was simply calculated out of the blowing ratio and the density ratio.

Table 2.4.: Non-dimensional quantities for rotor tip coolant ejection at turbine design condition

Quantities	Definition	Estimated values
Tip mass flow ratio	$TR = \frac{\dot{m}_c}{\dot{m}_{main}}$	0.4 %
Blowing ratio	$BR = \frac{\rho_c U_c}{\rho_\infty U_\infty}$	1.2
Density ratio	$DR = \frac{\rho_c}{\rho_\infty}$	1.1
Momentum flux ratio	$I = \frac{\rho_c U_c^2}{\rho_\infty U_\infty^2} = \frac{BR^2}{DR}$	1.3

Rainbow Rotor Configuration Given the modular rotor tip cap approach, the rotor blisk was modified such that on specific pitch-wise sectors of the rotor, one of the total five tip designs could be installed and supplied with tip coolant. The representative distribution of the different tip geometries is depicted in Figure 2.9. Each sector consisted of three blades that featured the same design. The outer two tip caps should act as guardians to the center one to reduce the impact of the consecutive, non-conform blade tip designs. The non-uniform pitch-wise distribution of the designs was due to balancing reasons that also were induced by the vast amount of other instrumentation components on the rotor blisk. The five different designs were: the Baseline Squealer (uncooled, silver gray), the Baseline Squealer cooled (blue), the

Optimized Squealer (brown), the Trench (dark brown), and the Notch concept (red). Each of these designs was manufactured in a blade cap approach, as described in this section. More details on the specific designs can be found in section 2.2.3. Note that only the Notch concept and the uncooled Baseline Squealer did not have tip coolant ejection. The complete rotor assembly was balanced dynamically after installing and instrumenting the blade caps to comply with the ISO 1940-1 standards for gas turbines.
To study the aerodynamics of each individual tip design, fast-response probe measurements combined with a trigger signal were required that were able to lock the measurement data to the respective rotor blade. Therefore, throughout this work, FRAP and fast-response entropy probes (FENT) were used to provide inter-blade row measurements capable of resolving each individual blade flow field. An overview and detailed information on the probes are provided in sections 2.3.1.3 and 2.3.1.4, respectively.

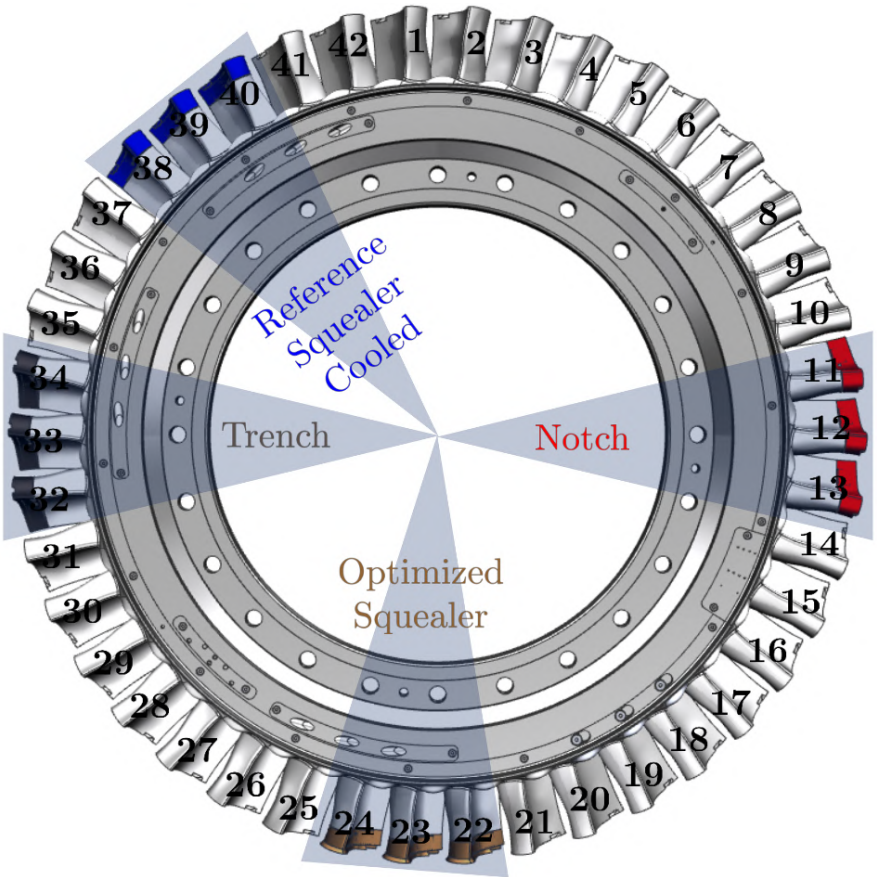

Figure 2.9.: Representation of rainbow rotor configuration featuring different rotor tip designs

Blade Tip Gap Variation Assessment and Blade-to-Blade Variations The tip gap is an important design parameter when it comes to the assessment of aerodynamic performance. The turbine components (rotor blisk and rotor casing) were therefore manufactured with tight dimensional tolerances. The rotor casing inner radius was manufactured with a tolerance of $\pm 25\,\mu$m. The

rotor tip surface shape was manufactured within $\pm 25\,\mu$m and could be kept for all considered rotor designs. Further measurements of the manufacturer using a ZEISS UMC 850 (measurement accuracy for this radius level $\pm 5\,\mu$m) showed that the tip surface radius was typically in the range of +20 to $+23\,\mu$m above the target radius. The overall accuracy of the rotor tip surface radius was then the one of the measurement tools ($\pm 5\,\mu$m). The rotor carrier disk, where the rotor was fixed to, lay within $\pm 20\,\mu$m along the radial coordinate. Therefore, the cumulative dimensional tolerance on the installed tip gap is $\pm 50\,\mu$m ($\pm 0.07\,\%$ span). Furthermore, the rotor-bearing arrangement of the turbine was designed to keep the temporal change of the tip gap as low as possible (within 0.15 % of the blade span [170]) with typical vibrational velocity levels of 0.4–0.6 mm/s at turbine design conditions.

Besides the tip gap uncertainty, the impact of the installed blade tip caps on the flow field against the integral metal blade tips had to be assessed. Such a study was performed without having the other blade tip geometries (Optimized Squealer, Trench, and Notch) included on the rotor. In order to exclude the impact of the blade tip ejection, the coolant access in the rotor upstream hub cavity was closed by exchanging the access plate (Figure 2.7 (left)) with a sealing plate. A first indication that the blade tip caps had a moderate impact on the aerodynamic flow field is provided in Figure 2.10 by means of FRAP data. The time, mass- and circumferentially averaged normalized relative total pressure at rotor exit for the center blade with tip cap is shown relative to the minimum and maximum relative total pressure distribution. The envelope consisting of the minimum and maximum levels for each span-wise coordinate was extracted out of 39 blade passing events (full revolution−3 blade caps) of the integral metal blade tips and provided an assessment of the blade-to-blade variation. Considering the blade-to-blade variation, the measurement uncertainty of the normalized relative total pressure and the radial distribution of the blade cap, one can conclude that the changes induced by the caps are within the uncertainty and the blade-to-blade variation.
To resolve the flow field downstream of the blade caps, FRAP measurements were used. In Figure 2.11, the time-space diagrams of the normalized relative total pressure at rotor exit are shown for the blade passing events with and without blade caps. The comparison was chosen such that the blade caps and three metal blades were about half a rotor revolution apart from each other. The secondary flow structures associated with the rotor caused the drop in relative total pressure at various span positions. Of specific interest is the top 20 % span, where the impact of the blade caps was anticipated. Examining these span-wise positions for the time-series with and without blade caps, the extent of the tip secondary flows and the respective losses were comparable.

Based on that, the three blade caps did not specifically stand out, which highlights the appropriate quality of the manufacturing and installation.

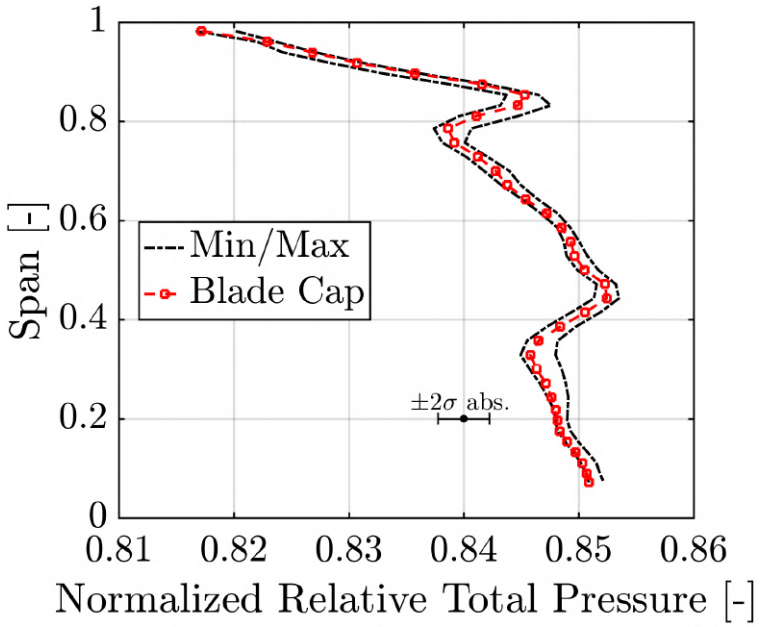

Figure 2.10.: Mass- and circumferentially averaged normalized relative total pressure (FRAP) at rotor exit for blade with tip cap and minimum/maximum distribution along the span extracted from 39 blade passing events

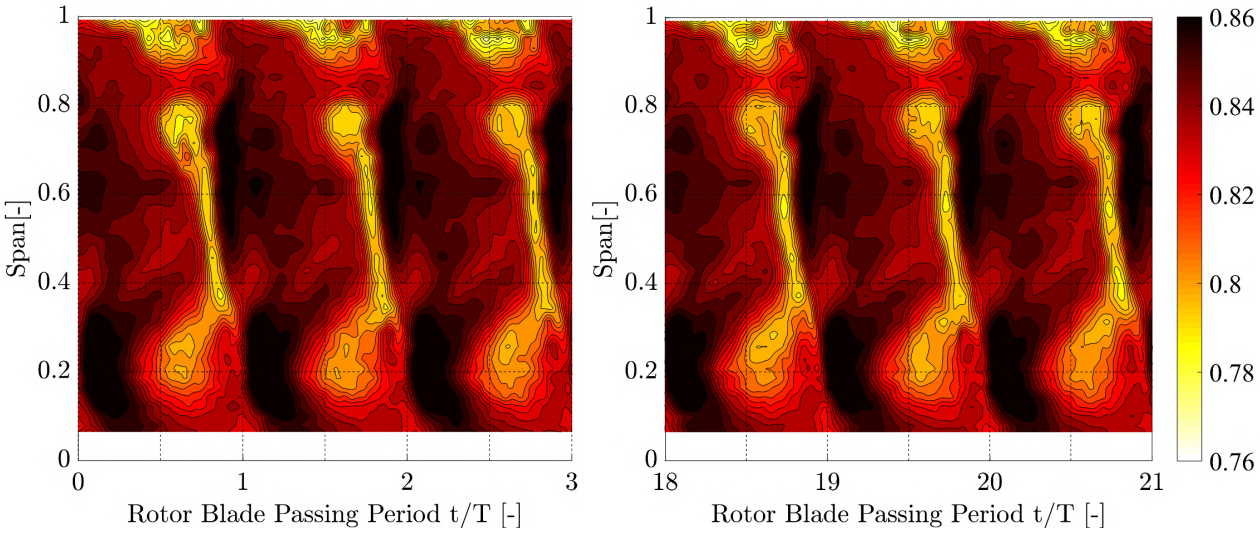

(a) Without blade tip caps **(b)** With blade tip caps

Figure 2.11.: Time-space diagram of the normalized relative total pressure [-] at rotor exit for blade passing events without blade caps (a) and with blade caps (b) for the Baseline Squealer tip geometry (FRAP)

2.1.6. Rig Monitoring and Data Acquisition Systems

To provide high accuracy measurement data and allow for safe operation of the turbine rig, a sophisticated data acquisition and rig monitoring system was part

of the test facility. Specifically, in the presence of sensitive instrumentation and rotor onboard data acquisition systems, the knowledge of the stability and state of the rig is of the highest importance.

2.1.6.1. Rig Surveillance and Safety

The most relevant test facility components were connected to a hardwired safety system which instantly triggers a rig emergency shutdown in case of exceeded limit values or incidences that cause a malfunction of the rig. In such a case, the compressor is switched off and the pressurized air is bypassed as the fast-acting valves are triggered and thereby the turbine runs out. The main facility components and their auxiliary systems are connected interdependently, which prevents the compressor from being started if, for example, the cooling of the gearbox is not operational, or the DC generator is inactive.

The absolute vibration levels of the rotating components, such as the turbine bearings, the gearbox, and the generator were measured with a commercial vibration diagnostic system (VibroControl 4000), which is widely used in industrial applications. The system received signals from two displacement sensors and eight acceleration sensors in total, which were installed at the corresponding locations. The two displacement sensors measured the axial displacement of the rotor disk. At the main turbine bearings, four of the acceleration sensors were installed in orthogonal pairs. The gearbox was equipped with three orthogonally distributed acceleration sensors. One acceleration sensor was fixed to the generator. The data was displayed on two independent systems and logged onto a personal computer. If the predefined vibration and displacement limits were exceeded, an emergency shutdown of the test rig was automatically initiated. The surveillance of the long-term evolution and stability of the vibrations is crucial since the gearbox is operated, critically, during the startup and shutdown of the rig due to resonance crossing.

2.1.6.2. Data Acquisition of Operating Parameters

The data acquisition of the turbine consisted of three independent acquisition systems that real-time monitored, displayed, and logged all relevant turbine operating parameters. To provide accurate measurements, a stable turbine operating point over a long-running period is essential. The only parameter that needs to be adjusted without the help of a sophisticated automatic controlling system is the compressor power (to account for the change in the atmospheric pressure and provide a stable turbine pressure ratio). In that the change of the atmospheric pressure is a slow process and the compressor is the most powerful component of the test rig, an operation without an automatic controlling system was chosen. The power of the compressor, the turbine

pressure ratio, and the turbine mass flow can only be controlled by adjusting the variable inlet guide vanes of the compressor because the exit pressure of the turbine is at atmospheric conditions and the compressor is operated under constant rotational speed. In sum, the turbine operating condition was mainly determined by rotational speed, inlet total temperature, and total-to-static pressure ratio.

Pressure The pressure data of the rig were gained from multiple wall-mounted pneumatic pressure tappings (static pressure) as well as Pitot probes (total pressure) distributed across the turbine test section. The leakage flows are typically controlled by setting the pressure difference across the seals to zero. The turbine inlet total pressure was measured by such Pitot probes, mounted on thin struts at mid-height of the channel. The thin struts were circumferentially displaced to the probe traverse area. The leakage mass flows were determined by the pressure ratio and temperature of standardized nozzles, which are described in more detail in the upcoming paragraph. The pressure was measured by two 16 channels difference pressure PSI modules, which have a pressure range of 34.5 kPa and 5.0 kPa, respectively. The atmospheric pressure was measured by an absolute Keller X33 module.

Temperature and Humidity To measure the turbine inlet total temperature, four calibrated PT100 resistance thermometers were installed upstream of the turbine test section. The inlet temperature was controlled by the input of two additional PT100 sensors, which were installed at the exit of the two-stage heat exchanger. Further temperature data were needed for the mass flow calculation of the various mass flow measurement devices. Inside the rim seal hub cavity, two additional PT100 sensors were installed to determine the temperature of the injected purge flow. In the context of this work, these sensors were replaced with two miniature temperature probes that provided higher accuracy for the purge flow temperature, specifically for the hub cavity heat transfer assessment. Humidity sensors were installed to correct the air density, which resulted in a higher accuracy of the measured turbine mass flow. The test rig consisted of an additional humidity sensor at the turbine exit to avoid condensation effects for certain turbine configurations and operating conditions. For the latest integration of a cold bypass flow injection system, a humidity sensor was installed in the external distributor (Octopus) to check for condensation. Further details are provided in the cold bypass system description.

Mass Flow Measurement Three mass flow measurement devices were installed in the initial turbine test setup to measure the primary, bypass, and drum leakage mass flow, which subsequently allowed for determination of the

purge mass flow. The accurate determination of these mass flows was essential for the turbine efficiency calculation.
The primary mass flow was measured with a calibrated Venturi nozzle, which was located upstream of the inlet to the compressor. The upstream length of the Venturi nozzle setup did not comply with the minimum length specified by the ISO 5167-3 norm. Therefore, the Venturi nozzle—including the two upstream bends—was calibrated at Delft Hydraulics on a certified calibration rig for flow measurement devices. The nozzle discharge coefficient (with respect to the Reynolds number) was calculated based on the measurement of the nozzle's inlet and throat pressure levels, temperature, and humidity.
The leakage mass flow ($\dot{m}_{\mathrm{drum}}$, Figure 2.3), which was vented from the drum plenum to the atmosphere, was measured with an ISA 1932 standard nozzle. The mass flow calculation agrees with the ISO 5167-3 norm. Similar to the primary mass flow calculation, the calculation requires determination of the absolute inlet pressure, temperature, and humidity of the flow at the exit of the nozzle and the pressure difference across the nozzle contraction.
The injected amount of rim seal purge flow was calculated based on the difference of the bypass mass flow ($\dot{m}_{\mathrm{bypass}}$, Figure 2.3) and the vented leakage mass flow. The bypass mass flow is an offtake of the primary air loop, downstream of the heat exchanger, and injected in the rim seal hub cavity beneath the first stator. Again, the bypass mass flow was measured with a standard Venturi nozzle with the mass flow calculation provided by the ISO 5167-3 norm. In the modified auxiliary air flow path, which permits the injection of cold bypass air into the rim seal hub cavity, an ISA standard orifice plate measurement section was integrated. The mass flow determination of the orifice plate followed the ISO 5167-2 norm.

Torque and Rotational Speed The torque meter, which was installed below the gearbox, is a custom-made component and specifically calibrated by Torquemeters Ltd. It provides highly accurate and time-resolved measurements of the torque exerted by the turbine rotor and the rotational speed. The phase shift of two cogwheels located at both ends of the shafts was measured, which enabled determination of the angular deflection associated with the twist of the turbine shaft under load, and subsequently, the torque. The torque meter is able to cope with a peak load of 1'500 Nm.

Aerodynamic Probe System The traversing and acquisition of the aerodynamic probe setup was controlled with an independent personal computer. The probes were moved automatically by a 3-axis traversing system and the data of each measurement point of the grid was saved. The system was used for all presented probe types in this work. Furthermore, the system automatically set the reference pressure and applied the offset and gain calibrations for

the fast-response probes. More details of the traversing and measurement characteristics of the different probes can be found in Lenherr [95].

2.2. Turbine Configurations

The initial design of the turbine configuration was a two-stage shrouded axial turbine, representative of a steam turbine [179]. Behr et al. [8, 9] redesigned the two-stage setup as a 1.5-stage, low aspect ratio, high work, high-pressure gas turbine representative configuration with unshrouded rotors and compressibility effects occurring at the exit of the stators. The presence of a second stator in the 1.5-stage setup results in a more representative rotor exit flow field including rotor-stator interaction phenomena. In the present work, three different 1.5-stage high-pressure turbine representative configurations were tested. Most of the considered configurations featured advanced airfoils and specific geometrical features, such as non-axisymmetric end wall profiling, rim seal features as well as modified blade tips.
The unsteady cavity flow configuration is extensively discussed in Chapter 3, where non-synchronous, low-frequency hub cavity modes are investigated. The rim seal purge flow control feature configuration, analyzed in Chapter 4, provides a design suggestion to overcome the detrimental effects of purge flow injection on the aerodynamic performance. The reduced blade count configuration, featuring a new rim seal design and advanced blade tip designs, builds the geometrical basis for the cavity heat transfer investigations (Chapter 5) and the rotor blade tip study (Chapter 6).

2.2.1. Unsteady Cavity Flow Configuration

The fundamentals of the turbine configuration are in the design space of the extensively investigated turbine design presented by Behr [8]. To proceed to a design that is closer to those in real engines, two specific differences from the design investigated by Behr [8] were implemented. First, the axial distance between the first stator and the rotor was increased by 16 % of the first stator's axial chord at mid-span. Second, the axial gap at the exit of the rim seal hub cavity was increased by the same amount as the axial distance between the first stator and rotor.

Airfoil and End Wall Design On the vane and blade side, a redesign of the airfoils was executed by Siemens using commercially available meshing tools but with CFD and optimization codes with Siemens proprietary scripting. The optimization used steady-state CFD simulations with block-structured meshes and the total-to-total efficiency as the target function. Detailed information on the design changes compared to the vanes and blades described by Behr [8]

can be found in the work of Regina et al. [154, 156], together with an extensive inter-stage flow-field analysis. An illustration of the airfoils is depicted in Figure 2.12. The blade rows feature cylindrical end walls at the hub and tip.

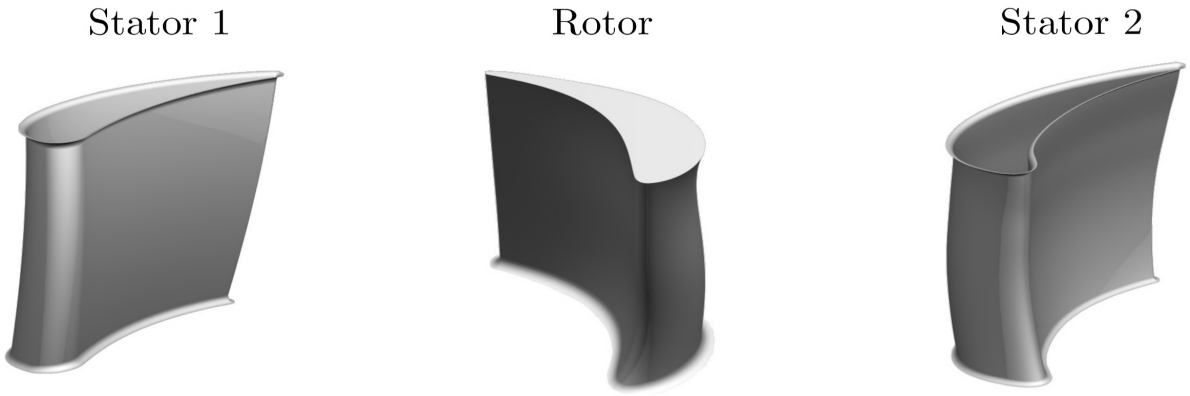

Figure 2.12.: Illustration of airfoils for the unsteady cavity flow configuration (not to scale)

A summary of the basic geometrical details referenced to the blade mid-span position is given in Table 2.5. The vane count for both stators was the same, and together with the number of blades of the rotor, a blade count ratio of 2 / 3 / 2 for the 1.5-stage was given. The nominal tip gap for the unshrouded rotor was 1 % of the blade span. The corresponding turbine operating point and flow field characteristics, such as Mach number and Reynolds number regimes, are presented in Table 2.1. The configuration was operated under rim seal purge flow, as introduced in section 2.1.3.

Table 2.5.: Geometrical details of the airfoils referenced to mid-span

	S1	Rotor	S2
Vane & blade count	36	54	36
Aspect ratio	0.89	1.21	0.83
Solidity	1.23	1.36	1.33

Rim Seal and Hub Cavity Design The hub cavity design for the unsteady cavity flow investigation was characterized by an angel-wing rim seal arrangement as schematically introduced in Figure 2.13. The respective geometrical details are the rim seal interface gap width of 20 % of the first stator axial chord $c_{ax,S1}$ and a platform chamfer angle of 45° which builds an angel wing on the rotor-sided rim seal geometry. A buffer arm was integrated, the design intention of which is to study the effects of an overlap-type rim seal configuration that is representative of real engines. In order not to alter the rotor

dynamics of the test rig, the buffer arm was integrated on the first stator platform [154]. The interesting aspect of the buffer arm was the separation of the hub cavity into two volumes by a sealing gap size of 4 % of the first stator axial chord. The volume ratio between the upper and lower hub cavity section was about 1:8. It is expected that the most pronounced interaction between the hub cavity fluid and the main annulus flow will occur in the smaller upper section.

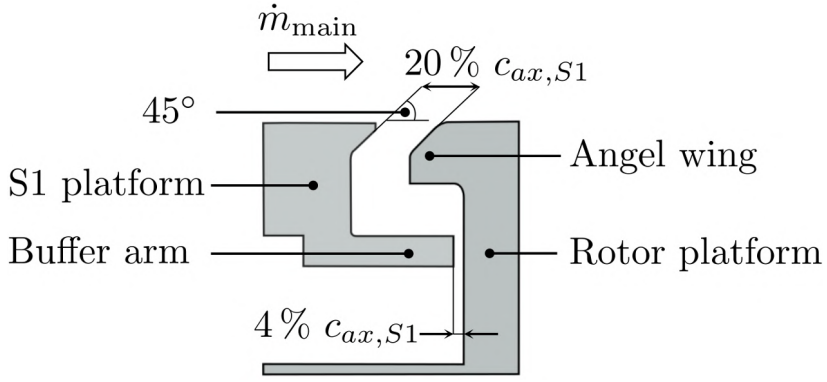

Figure 2.13.: Details of the rim seal and hub cavity design for the unsteady cavity flow configuration

2.2.2. Rim Seal Purge Flow Control Configuration

For the study of novel design features to improve the interaction of the rim seal purge flow with the main annulus flow, a redesigned 1.5-stage turbine configuration was considered with respect to the previously introduced design in section 2.2.1. The overall goal was to achieve higher aerodynamic efficiency by means of optimized airfoils and end wall profiling for all three blade rows. The axial distances between the blade rows were kept similar to the unsteady cavity flow configuration and only marginally altered due to the change in blade and vane sweep. For this configuration, two sub-configurations were considered, where one featured a baseline cavity design and the other novel rim seal features at the interface between the hub cavity and the main annulus flow. These features are presented later in this section, including the design intentions.

Airfoil and End Wall Design The purge flow control configuration featured completely new airfoil designs, which were a result of a CFD optimization process conducted by Siemens to achieve higher aerodynamic performance. The most pronounced changes compared to the previously introduced configuration in section 2.2.1 were particularly found in the first vane design (Figure 2.14), which included pronounced upstream sweep around mid-span and compound bow and lean. The vane count was not altered. The vane aspect ratio and

solidity referenced to mid-span were not changed for the first stator vane. The fillet radii were the same as for the previous design and provided a smooth transition from the vane to the non-axisymmetric end wall contouring. Both hub and shroud end walls featured end wall contouring with a radial deviation Δr to the nominal hub (shroud) radius between $-3\,\%$ ($-1.5\,\%$) and $+2.5\,\%$ ($+3.5\,\%$) of the span. The stator 1 hub and shroud end wall design are depicted in Figure 2.15 (a).

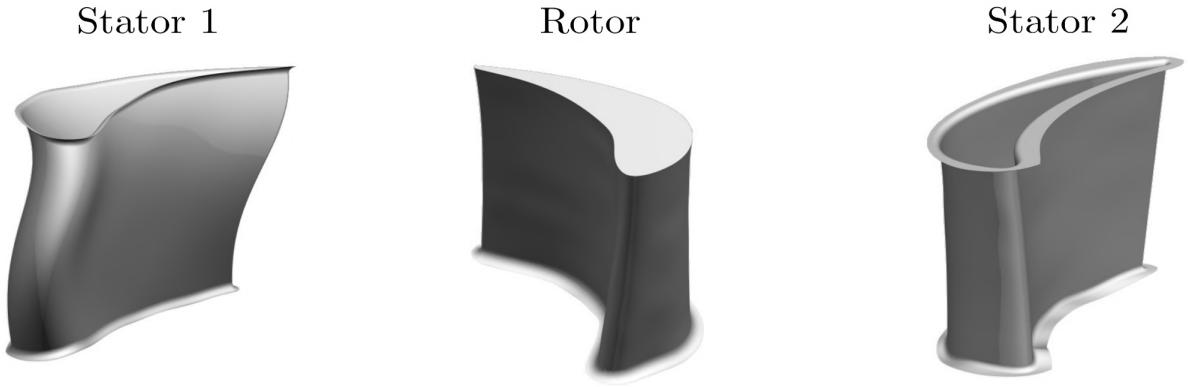

Figure 2.14.: Representation of airfoils for the purge flow control configurations (not to scale)

The profiles of the rotor airfoil resemble the previous design (section 2.2.1); however, the profiles were optimized on five radial sections. The nominal tip gap was not changed and amounted to $1\,\%$ of the blade span. The rotor blade count was kept at 54 blades, and the blade aspect ratio and solidity referenced to mid-span were unaltered. A representation of the rotor airfoil is provided in Figure 2.14. The aerodynamic performance of the rotor is supported by non-axisymmetric end wall contouring at the hub, which is presented in Figure 2.15 (b). The profiling is mild, with a radial deviation of Δr to the nominal hub radius between $-1.6\,\%$ and $+0.8\,\%$ of the span.

Table 2.6.: Airfoil specifications for the purge control configuration referenced to mid-span

	S1	Rotor	S2
Vane & blade count	36	54	36
Aspect ratio	0.89	1.21	0.83
Solidity	1.23	1.36	1.33

The second stator vane, as presented in Figure 2.14, was a CFD-optimized design featuring less-pronounced lean, sweep, and bow portions compared to the first stator vane. The vane count was identical to the first stator. The non-axisymmetric end wall contouring was limited to the hub section, and the shroud end wall was purely cylindrical. The hub end wall profiling was

characterized by a radial deviation to the nominal hub radius between −4 % and +3 % of the span, which is a more aggressive design.
Overall, the turbine configuration showed very comparable Mach numbers and Reynolds numbers throughout the 1.5-stage compared to the previous design. The turbine capacity was unchanged compared to the design introduced in section 2.2.1 and was operated under the same range of rim seal purge flow. The geometrical characteristics of the airfoils are summarized in Table 2.6.

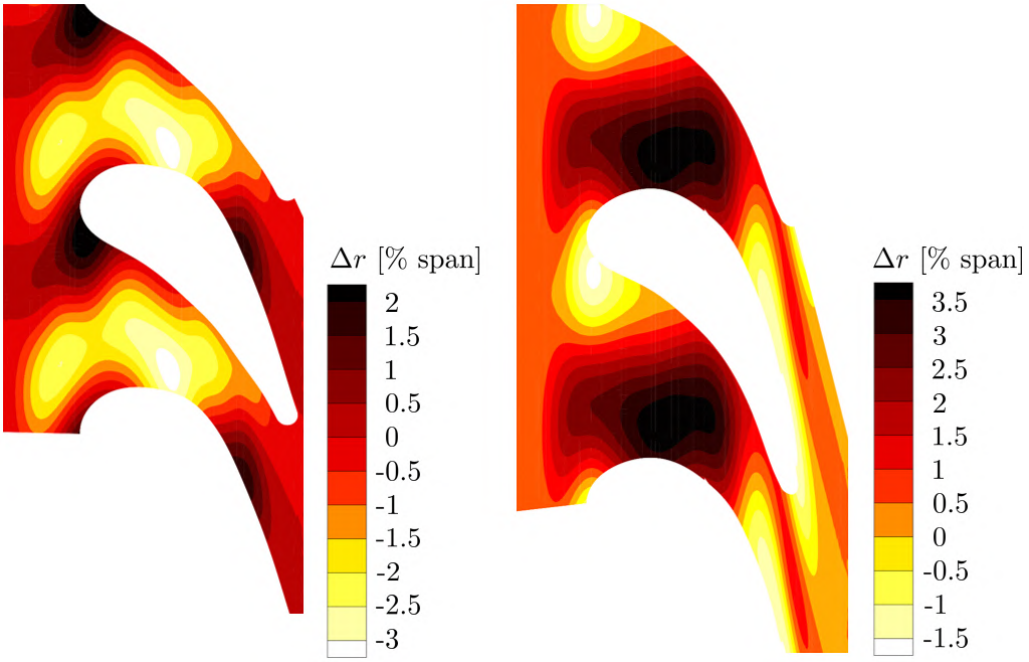

(a) Stator 1 end wall contouring at hub (left) and shroud (right)

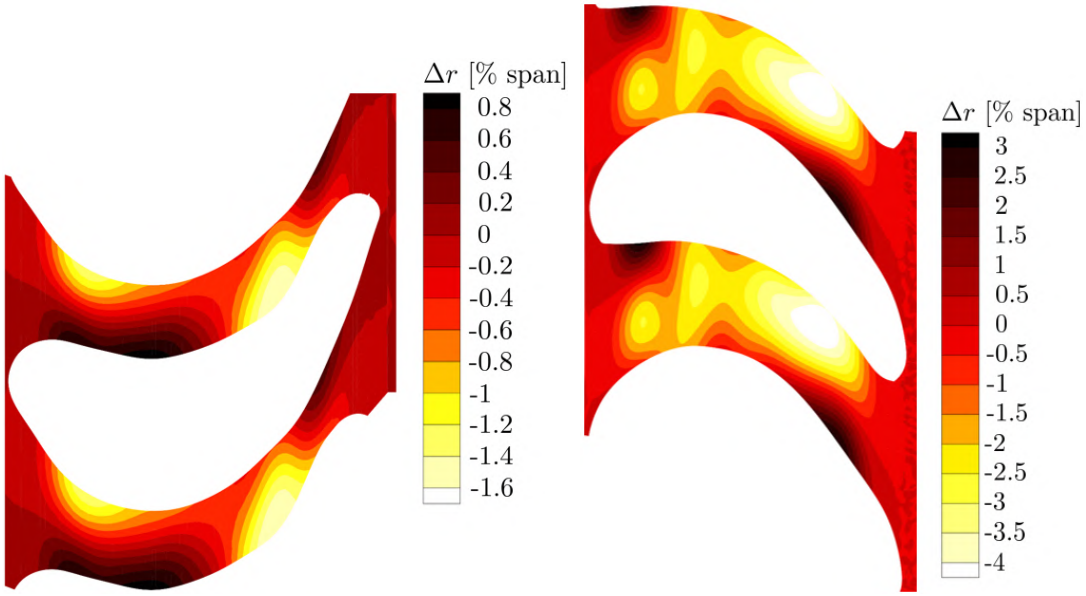

(b) Rotor end wall contouring at hub **(c)** Stator 2 hub end wall contouring

Figure 2.15.: End wall contouring featured in purge flow control turbine configuration (excluding blade fillet portion)

Rim Seal Designs: Purge Control Features (PCF) The main focus of the present turbine configuration is to assess the potential to improve the aerodynamic performance of an already optimized configuration by reducing the detrimental effect of rim seal purge flow injection. The objective was to install advanced geometrical features at the interface between the hub cavity and main annulus flow to modulate the purge flow injection into the main annulus. The rim seal design introduced in Figure 2.13 built the baseline rim seal design. The novel features (termed as "purge control features" (PCF) below) were integrated on the inclined surface at the hub cavity exit neck, which is shown in Figure 2.16. The features were characterized by highly three-dimensional shaped, nozzle-like pockets (stator 1), and advanced grooves (rotor). For the stator-sided design, seven features per stator pitch were installed, which resulted in 252 features in total around the circumference. Within the stator pitch, the features were distributed equidistantly. On the rotor-side, two features per rotor pitch were installed, resulting in 108 features around the circumference. The concept and design of the purge control features were elaborated by Siemens.
The proper installation of these features on the first stator and rotor was enabled by exchangeable rings, which were fixed by screws. The exchangeable rings were pinned to the respective component to provide an accurate relative position of the stator 1 and rotor features relative to the first stator trailing edge (TE) and rotor leading edge (LE).

Prior to detailed investigation of a novel concept, it is crucial to state the design goals. The respective design intentions for the rim seal purge flow control features were formulated as follows and should be read in reference to Figure 2.16:

(1) **Stator-sided purge control features**: the primary issue on the stator side is the hot gas ingestion due to the circumferential pressure distribution caused by the first stator wake. Design features target the guidance and alignment of the purge flow with the main annulus flow exiting the first stator and regulating the static pressure at the rim seal exit. The feature was designed so the depth of the nozzle-like pocket (**a**) is reduced toward the main annulus flow, which induces an acceleration of the purge flow.

(2) **Rotor-sided purge control features**: the intention was to increase the momentum of the rim seal fluid, thereby altering the circumferential and radial velocity components. The groove (**b**) imparts an increased circumferential velocity, thereby adjusting the low-momentum fluid to match closer to the main annulus flow. The angled surface (**c**) supports by imparting a radial component to the purge flow, which targets reducing the high amount of hot gas ingestion.

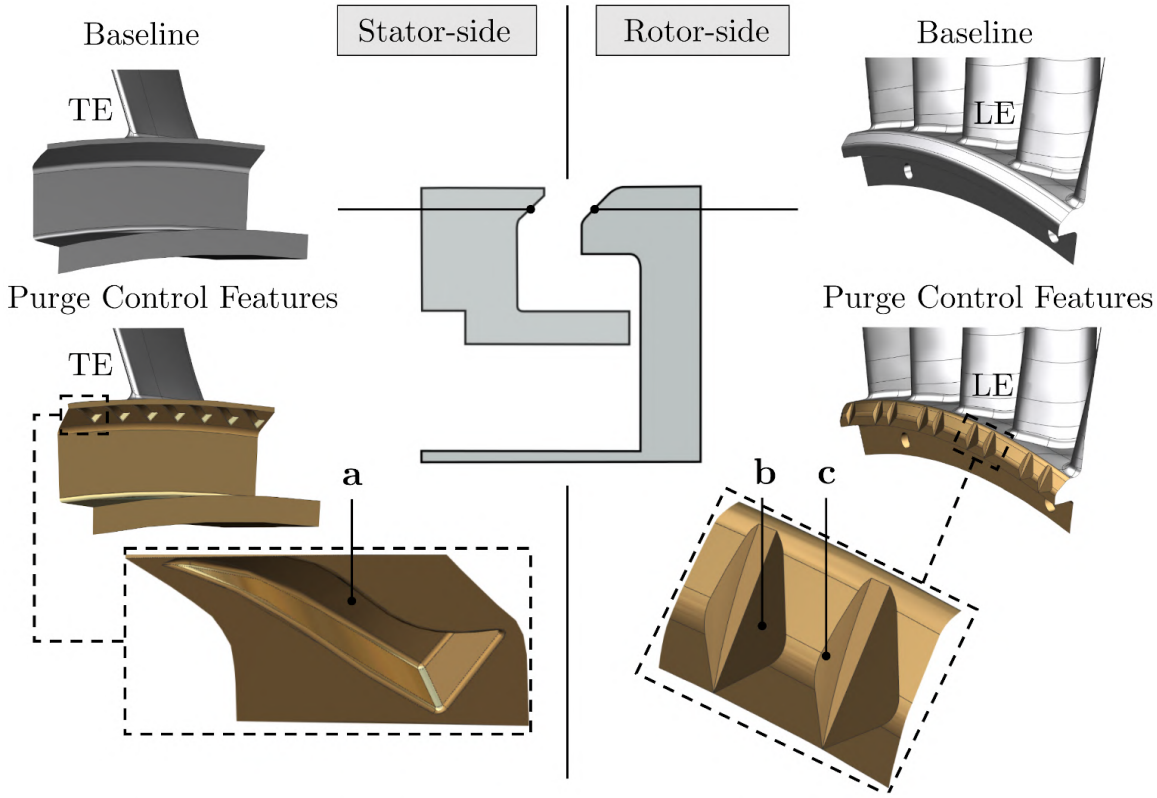

Figure 2.16.: rim seal designs: baseline (top row) and purge control features (bottom row) for stator 1 and rotor. Close-up view of the features (bottom center).

2.2.3. Rotor Tip Variation and Cavity Heat Transfer Configuration featuring a Reduced Blade Count Rotor

The design intention of the rotor tip variation and cavity heat transfer configuration originally focused on the potential to improve aerodynamic efficiency for a significant reduction in rotor blade count. A rotor design was therefore considered with new airfoils and optimized hub end wall contouring. Additionally, the rim seal was changed toward a more engine-representative design. The modular design of the rotor blisk allows for changing the rotor blade tip design with specially designed tip caps in a rainbow rotor setup (section 2.1.5). The individual blade tip designs are introduced in this section.

Airfoil and End Wall Design For this 1.5-stage configuration, only the rotor airfoil was changed, in combination with a blade count reduction from the original 54 to 42 blades. Accordingly, the blade loading increased from a Zweifel coefficient of 1.0 to 1.3. The rotor airfoil was optimized on five radial sections through a profile optimization executed by Siemens. A representation of the airfoil is provided in Figure 2.17. To reflect real engine designs and cope with increased blade loading, the airfoil was equipped with a baseline squealer tip geometry. The nominal tip gap was 1 % of the blade span and

therefore not altered compared to the other designs. The squealer rim had a uniform thickness. Furthermore, the squealer was opened on the pressure side and was therefore characterized by a rim cutback. The present squealer design builds the datum design for further comparisons with more advanced blade tip geometries.
To compensate for additional secondary flow losses due to increased blade loading, the rotor was equipped with a more advanced, non-axisymmetric end wall contouring. The end wall design is shown in Figure 2.17. Compared to the other end wall designs shown in this work, this optimized design was extended upstream into the rotor sealing arm arrangement, which is reflected in the relatively strong radial deviation of −7 % of the span with respect to the nominal hub radius. The contouring started at about 23 % of the rotor axial chord, upstream of the rotor leading edge. Most of the end wall contouring was focused on the section upstream of the rotor leading edge toward about 50 % chord. A pronounced hill was located toward the pressure side, in close vicinity to the rotor leading edge. The corresponding trough was positioned toward the suction side, close to the leading edge. Considering the radial deviation to the nominal hub radius between about −7 % and +4 % of the span, the contouring can be classified as aggressive.

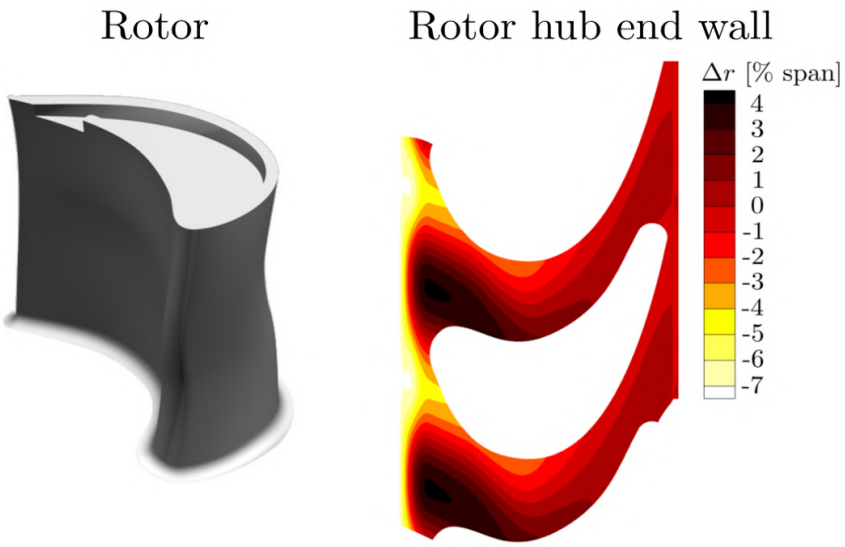

Figure 2.17.: Illustration of rotor airfoil and rotor hub end wall contouring for the rotor tip and cavity heat transfer configuration (not to scale)

The first and second stator were identical to the previously introduced rim seal purge flow control configuration (section 2.2.2). The axial spacing between the blade rows was similar to the other considered turbine configurations and only moderately changed by the rotor blade sweep. The airfoil specifications can be found in Table 2.7.

Rim Seal and Hub Cavity Design The rim seal design for the rotor tip variation and hub cavity heat transfer configuration was significantly changed

Table 2.7.: Airfoil specifications for rotor tip variation and cavity heat transfer configuration referenced to mid-span

	S1	Rotor	S2
Vane & blade count	36	42	36
Aspect ratio	0.89	1.21	0.83
Solidity	1.23	1.06	1.33

compared to the previous angel-wing-type seal. The design was characterized by a S-type and overlapping rotor sealing arm, as depicted in Figure 2.18. As previously mentioned, the rotor hub end wall contouring was extended into the rotor-sided sealing arrangement (dashed blue line in Figure 2.18). Overlap between the rotor sealing arm and the outer stator sealing arm was 2 % of the first stator axial chord. The arrangement of the sealing arm was to provide sealing against hot gas ingress at a larger radius compared to the angel-wing-type seal depicted in Figure 2.13. The axial distance between the rotor sealing arm and the S1 platform wall was 8 % of the first stator axial chord. Additionally, a radial sealing arm was included in the rim seal arrangement (with a radial gap of 4 % of the S1 axial chord) that separates the larger cavity from the smaller hub cavity. The volume ratio between the smaller and larger hub cavity section was determined to be about 1:3 and was, therefore, increased due to the integration of a radial sealing arm compared to the angel-wing-type sealing configuration. Due to the overlapping between the rotor and outer stator sealing arm, a slot was formed that provides space for interesting interactions between the hub cavity and main annulus flow.

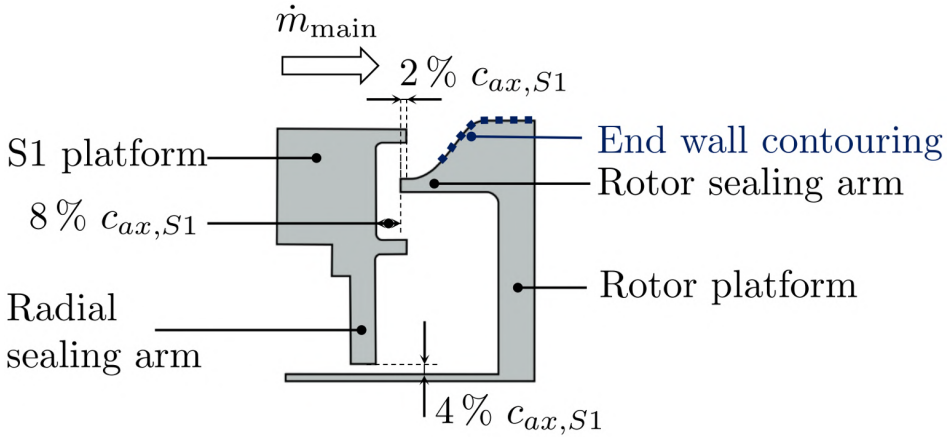

Figure 2.18.: Details of the rim seal and hub cavity design for the rotor tip and cavity heat transfer configuration

Rotor Blade Tip Designs The rotor blade tip variation study conducted in this work focused on five different blade tip geometries. The modification of the blade integrated disk enabled the modular integration of various tip designs in a rainbow rotor setup, as described in section 2.1.5. Additionally, most of the designs were equipped with cylindrical cooling holes on the blade-pressure side as well as in the squealer cavity, which vented cooling air supplied from the rotor upstream hub cavity (section 2.1.5). Dust holes in the squealer cavity were included to be more engine-representative.

(a) **Reference Squealer Uncooled**: The baseline squealer (Figure 2.19 (a)), which already was introduced in the airfoil description of this section, provides the reference geometry to the study that does not feature cooling holes and is a purely metal tip (no blade cap).

(b) **Reference Squealer Cooled**: The same baseline squealer design was equipped with cooling hole patterns (Figure 2.19 (b)) and two dust holes. Thirteen cylindrical cooling holes were located inside the squealer cavity and on the blade-pressure side. The cooling holes inside the squealer cavity started at about 48 % rotor axial chord and were equidistantly positioned along the blade chord, in close vicinity to the suction-side squealer rim. The pressure-side cooling holes started at 31 % rotor axial chord and were located at about 93 % span. For all cooled blade tip designs, the cooling and dust hole diameters were unchanged. In Figure 2.20, the geometrical specifications of the cooling hole arrangement in the squealer cavity and the blade-pressure side are depicted.

(c) **Optimized Squealer**: The optimized squealer is a more advanced blade tip geometry, which was optimized by CFD. The characteristics of the design were a non-uniform thickness and shape of the squealer rim, which can be seen in Figure 2.19 (c). The squealer rim at the blade leading edge was extended upstream. The nominal tip gap was kept the same as for all other designs. The squealer cavity depth was identical to the baseline squealer designs. Due to the advanced squealer rim shape, the squealer rim cutback was increased by about 9 % compared to the baseline squealer. Thirteen cooling holes in the squealer cavity and at the blade-pressure side were manufactured with similar positioning as for the cooled baseline squealer. The two dust holes were considered as well, which had the same position as the previously introduced squealer design. Regarding tip design, the intention was to reduce aerodynamic losses associated with the formation of the tip leakage and tip passage vortices.

(d) **Trench**: The trench concept is a quasi-squealer-type tip geometry, which features a slot (trench) from leading to trailing edge (Figure 2.19 (c)). The nominal tip gap was not changed and the trench had a constant width

along the chord. Within the trench, the thirteen cooling holes were pitch-wise centered and equidistantly positioned, starting from 37 % rotor axial chord. The two dust holes were located at the same axial position as for the other squealer designs, but pitch-wise centered inside the trench. The cooling holes, as well as the dust holes, were conventionally drilled along the radial axis in contrast to the other designs. The thirteen pressure-side cooling holes were identically positioned as for the baseline and optimized squealer. The cooling holes' geometrical specifications agreed with the ones presented in Figure 2.20.

(e) **Notch**: The notch-tip geometry is a flat tip-based design with material removed on the blade tip suction side, which forms a notch. The tip design is uncooled and does not, therefore, feature any cooling or dust holes. The nominal tip gap remained at 1 % of the blade span. The design intention focused on the loss redistribution in the near-tip region in combination with a loss reduction in the tip passage vortices.

(a) Reference squealer without cooling holes

(b) Reference squealer with cooling holes

(c) Optimized Squealer

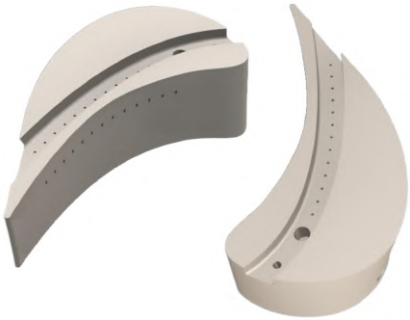

(d) Trench

(e) Notch

Figure 2.19.: Leading and trailing edge view on the rotor blade tip designs (not to scale)

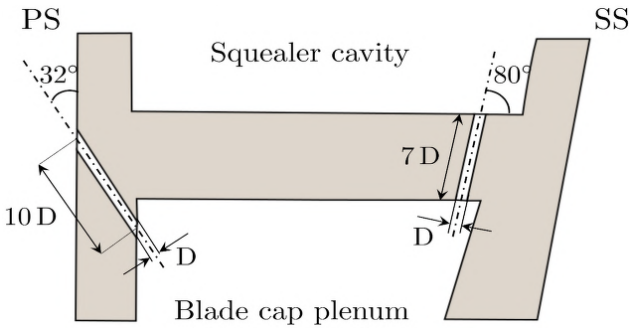

Figure 2.20.: Geometrical specifications of the cooling holes inside the squealer cavity and at the blade pressure side (PS) highlighted by an axial cut through the baseline squealer blade cap (not to scale)

2.3. Aerodynamic Probe Technology

The flow field in turbomachines is of a highly unsteady and three-dimensional nature. To aerodynamically improve the engines, detailed knowledge of the unsteady mechanisms present in the flow is of highest importance. Intrusive measurement techniques, such as pneumatic and fast-response probes or hot-wire anemometry, can provide highly accurate measurements of total and static pressure as well as temperature and flow angles. Although non-intrusive techniques such as laser Doppler anemometry (LDA) and particle image velocimetry (PIV) do not disturb the flow field, they cannot accurately determine unsteady pressure and temperature in the engine. The investigation of the inter-stage flow field in this work was undertaken using miniature pneumatic and fast-response probes, which have a probe tip diameter as small as 1.3 % and 2.6 % of the blade span.

2.3.1. Probe Types

In the context of this work, the pneumatic probes were used to provide time (pneumatically)-averaged flow field data and derive the aerodynamic efficiency of the individual turbine configurations. Due to their reduced complexity, these probes allow a higher degree of miniaturization and typically are characterized by a lower measurement uncertainty compared to fast-response probes. The unsteady flow field was investigated using fast-response probes. All probes used were built and calibrated in-house, and an overview of them is presented in Figure 2.21. The associated measurement uncertainties can be found in section 2.6.1.

2.3.1.1. Pneumatic Four-Hole Probe (4HP)

The shape of the 4HP is characterized by a cylindrical probe tip with an inclined curved surface for the pitch pressure access hole (Figure 2.21 (a)). The probe tip diameter is as small as 1.8 mm, and the tip shape is derived from the one of the fast-response aerodynamic probe (FRAP). The benefit of using a 4HP as compared to a pneumatic five-hole probe is a reduced axial space requirement, which allows the probe to intrude into cavities. Consequently, at stator 1 exit (S1ex), only the 4HP was used in order to be able to take measurements inside the rim seal cavity.

2.3.1.2. Pneumatic Five-Hole Probe (5HP)

The probe tip diameter of the 5HP is as small as 0.9 mm, which provides the smallest size out of the available probes for this work. Its small size minimizes the blockage effect of the probe head on the flow field (Figure 2.21 (b)). The

highest measurement accuracy is achieved with this probe, and therefore it was used for efficiency measurements. The probe head is cobra-shaped and has the advantage of allowing a relatively large distance between the shaft and the effective measurement location. The normal distance between the pressure tappings at the probe head is only 0.3 mm, which provides a high spatial resolution. A 45° angle between the center hole and the surrounding pressure access holes was machined. Due to the symmetry of the pressure access holes, the 5HP was less affected by compressibility effects of the flow (reduced down-wash effects).

2.3.1.3. Fast-Response Aerodynamic Probe (FRAP)

FRAP technology is the result of development and improvement over the last two decades at the Laboratory for Energy Conversion (LEC) at ETH Zurich. The work of Gossweiler [51] and Kupferschmied [88] includes detailed information on the fundamentals of the measurement technique and first measurement results. Further information on the latest design of the standard 2-sensor FRAP is seen in Schlienger [170] and Pfau [135, 136].
The FRAP were designed as stem probes that have a tip diameter of 1.8 mm (Figure 2.21 (c)). Inside the probe tip, two miniature piezo-resistive pressure transducers (MEMS sensors) were encapsulated. Comparable to the introduced 4HP, the probe head shape is characterized by an inclined, curved surface where the pitch pressure access hole is located. The inclination increases the pitch sensitivity of the pressure signal. The yaw pressure access hole is located on the purely cylindrical part of the probe tip shaft and 2.2 mm away from the pitch access hole. Based on shock tube tests, the frequency bandwidth for the total- and static-pressure measurements, as well as the flow yaw and pitch angle, was 48 kHz. The limiting factor for the frequency bandwidth of the probe was the pneumatic cavity between the sensor membrane and the probe access hole surface which had a resonance frequency of about 75 kHz. The standard 2-sensor FRAP is able to withstand temperatures up to 120 °C. The temperature bandwidth was limited to 10 Hz, again provoked by the encapsulation of the sensor inside the probe tip. Within the test rig, the temperature fluctuations were relatively small compared to the pressure fluctuations, which therefore only moderately affected the calculated flow velocities. The data was acquired with a sampling rate of 200 kHz for typically 2 s, resulting in a frequency resolution of 0.5 Hz. At nominal rotational speed of the turbine and a blade count of 54 (42), this resulted in a temporal resolution of 247 (317) samples for three rotor blade passing events.
To determine the total and static pressure as well as the flow yaw and pitch angle, the 2-sensor FRAP was operated in the virtual 4-sensor mode. The concept is schematically introduced in Figure 2.22. The flow field data of each measurement grid point was the result out of three measurements where

(a) Pneumatic four-hole probe

(b) Pneumatic five-hole probe

(c) Fast-response aerodynamic probe

(d) Fast-response entropy probe

Figure 2.21.: Pneumatic and fast-response probes compared to match for scale comparison

the probe was rotated to different angular positions. The center position measurement (yaw sensor p_1, pitch sensor p_4) was enabled by using the flow yaw angle data from the pneumatic probe measurements as probe set angles. The probe was aligned with the mean flow direction, and therefore the yaw sensor provided data that resembles the total pressure. Additionally, in this position, the yaw sensor captures the full frequency spectrum of the flow, which is beneficial for flow excitation studies as provided in this work. The yaw sensor positions p_2 and p_3 provide measurement data when the probe is rotated by $\pm 42°$ with respect to the center position. The angle of rotation of the probe was chosen so that the measurements in the p_2 and p_3 positions were not conducted in the flow separation zone of the probe where the pressure signal would be insensitive to flow angle variations.
The FRAP, in combination with an optical shaft trigger, allowed for synchronizing the three separate measurements. In order to temporarily resolve the flow dynamics with respect to multiples of the rotational speed (e.g., rotor blade passing frequency), the acquired data was phase-lock averaged. Typically, 85 revolutions were used for phase-lock averaging for a measurement time of 2 s, and three consecutive rotor blade passing events were extracted when phase-locking was applied. It is convenient to lock the measurement data to specific rotor blades, which is applied in this work for the rotor blade tip study.

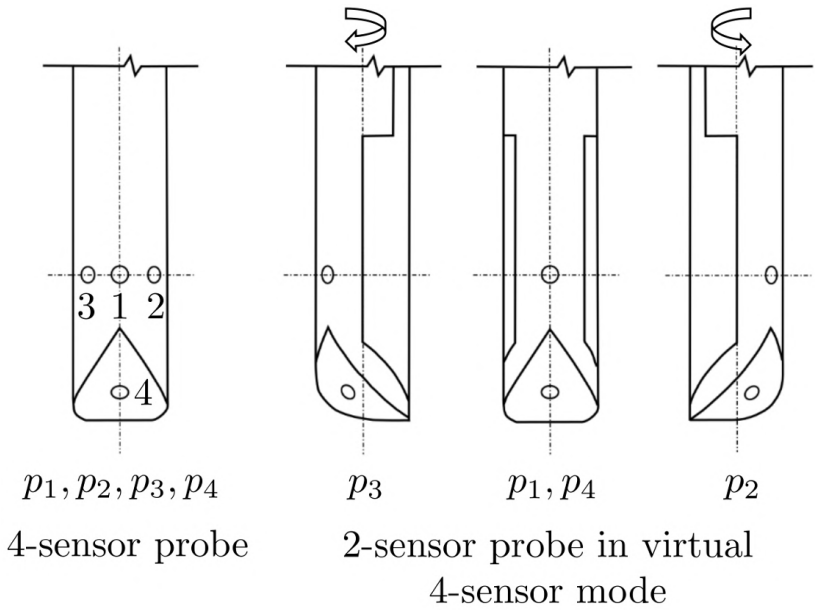

Figure 2.22.: Virtual 4-sensor mode concept for FRAP (modified from [95])

2.3.1.4. Fast-Response Entropy Probe (FENT)

The determination of time-resolved entropy levels in turbomachinery flows is a desirable goal for designers. Based on that, a FENT was developed at ETH Zurich by Mansour [98], and a picture of the probe can be found in Figure 2.21 (d). Mansour et al. [99, 100] demonstrated the capabilities of the probe in different flow regimes and test rigs. Similar to the FRAP, the probe had a probe tip diameter of 1.8 mm and included a miniature piezo-resistive pressure transducer for time-resolved total pressure measurements. A pair of thin-film gauges, with a thickness of only 200 nm, were used as resistance thermometers at two different thin-film temperatures to measure the unsteady total temperature. The area covered by the serpentine shape thin-film gauges was 1.77 mm x 0.85 mm. Therefore, a minimum spatial resolution in the radial direction of 2.5 % of the blade span was achieved. Simultaneous measurement of the unsteady total pressure and total temperature facilitated derivation of the time-resolved entropy rise referenced to the turbine inlet. Similar to the FRAP, a measurement bandwidth of 48 kHz was achieved and data were acquired at a sampling rate of 200 kHz over 2 s. The virtual 4-sensor measurement concept was also applied for the FENT probe.

2.3.2. Probe Traversing System

The test rig was equipped with a fully automated, three-axis probe traversing system. The radial movement, as well as the rotation of the probe around its axis, was enabled by two stepper motors. A third motor, which could circumferentially displace the outer casing of the test rig (to which the rotor casing is mechanically connected), permitted pitch-wise traversing of the probe.

The motor was connected to a Heidenhain encoder. The movable casing rings were all equipped with dynamic radial seals, such that no leakage was caused by the sliding rings (as explained by Schlienger [170]). The concept allowed for continuous area traversing in one plane. A probe access hole of only 10 mm minimized flow disturbances. In Table 2.8, the ranges and accuracy of the individual axes are presented.

Table 2.8.: Probe traversing system range and accuracy

	Range	Accuracy
Yaw axis	360°	0.003°
Radial axis	150 mm	0.1 mm
Circumferential axis	35°	0.002°

2.3.3. Calibration of Aerodynamic Probes

An accurate calibration methodology is key to providing high-quality measurement data. Typically, the probes were calibrated before and after each measurement campaign. The pneumatic and fast-probes were aerodynamically calibrated as a function of the flow yaw and pitch angle as well as total and static pressure for different Mach numbers in LEC's freejet facility. In order to derive the three-dimensional flow field, a multi-dimensional calibration model was calculated based on the aerodynamic calibration of the probes. A static sensor calibration (pressure and temperature) additionally was required for the fast-response probes due to the MEMS sensor technology that was integrated into the probe tips. Two specific calibration facilities were used to perform the probe calibrations.

2.3.3.1. Freejet Facility and Probe Aerocalibration

The facility provided an axisymmetric freejet with a uniform velocity profile at a turbulence level of about 0.3 %. A detailed description of the facility can be found in the work of Kupferschmied [88]. For different Mach number conditions, the probes were calibrated for different flow yaw and pitch angles as well as for total and static pressure. The Mach number conditions were chosen based on the determined turbine inter-stage conditions. For the nominal operating point of the turbine, the Mach number for the turbine inlet was set to $M = 0.14$, for stator 1 exit to $M = 0.56$, for rotor exit to $M = 0.25$, and for stator 2 exit to $M = 0.50$. The probes were calibrated for a yaw angle range of $\pm 24°$ and a pitch angle range of $\pm 20°$ in steps of 2°. The maximum stable Mach number condition that can be achieved in the facility is around 0.8.

Four-Hole Probe The data out of the 4HP aerodynamic calibration were used to define a set of sensitivity coefficients. The data out of the center yaw pressure tapping (p_1) resembled the total pressure of the flow and showed the most pronounced sensitivity to changes in the dynamic head. A difference between yaw pressure tappings (p_2, p_3) was included in the yaw sensitivity coefficient and normalized with an estimation of the dynamic head q. Similarly, the pitch sensitivity coefficient was formulated based on the difference between the center yaw pressure tapping (p_1) and the pitch pressure tapping (p_4). The set of 4HP sensitivity coefficients K_i is shown in Equation 2.2. More precisely, K_t is the total pressure sensitivity coefficient, K_s the static pressure coefficient, K_φ the flow yaw angle coefficient, and K_γ the flow pitch angle coefficient.

$$K_\mathrm{t} = \frac{p_\mathrm{t} - p_1}{q}, \quad K_\mathrm{s} = \frac{p_\mathrm{t} - p_\mathrm{s}}{q}, \quad K_\varphi = \frac{p_2 - p_3}{q}, \quad K_\gamma = \frac{p_1 - p_4}{q} \tag{2.2}$$

with

$$q = p_1 - \frac{p_2 + p_3}{2}$$

Five-Hole Probe Based on the aerodynamic calibration, sensitivity coefficients for the 5HP were defined wherein the center hole (p_1) showed the highest sensitivity to changes of the dynamic head of the flow. In addition, the difference of the yaw pressure tappings (p_2, p_3) and the pitch pressure tappings (p_4, p_5) were used for sensitivity coefficients normalized by an approximation of the dynamic head q. A summary of the 5HP sensitivity coefficients K_i is given in Equation 2.3.

$$K_\mathrm{t} = \frac{p_\mathrm{t} - p_1}{q}, \quad K_\mathrm{s} = \frac{p_\mathrm{t} - p_\mathrm{s}}{q}, \quad K_\varphi = \frac{p_2 - p_3}{q}, \quad K_\gamma = \frac{p_4 - p_5}{q} \tag{2.3}$$

with

$$q = p_1 - \frac{1}{4}\sum_{i=2}^{5} p_i$$

FRAP Since the FRAP was used in a virtual 4-sensor mode, the yaw angle calibration range was increased to ±72°. As introduced in Figure 2.22, the targeted yaw angle calibration range was achieved by combining the data points out of a ±42° rotation of the probe, which reconstructed the p_2 and p_3 positions. Like the 4HP, the pitch sensitivity coefficient was given by the normalized difference of the center yaw hole position p_1 and the pitch pressure hole position p_4. The FRAP sensitivity coefficients were identical to the 4HP coefficients described in Equation 2.2.

FENT Analogous to the FRAP, the FENT probe was used in a virtual 3-sensor mode and also required the extended yaw angle calibration. Due to

the lack of the pitch pressure sensor, the probe did not provide information on the flow pitch angle. Accordingly, the sensitivity coefficients were adapted to the definitions provided in Equation 2.4.

$$K_{\mathrm{t}} = \frac{p_{\mathrm{t}} - p_1}{q}, \quad K_{\mathrm{s}} = \frac{p_{\mathrm{t}} - p_{\mathrm{s}}}{q}, \quad K_{\varphi} = \frac{p_2 - p_3}{q} \tag{2.4}$$

with

$$q = p_1 - \frac{p_2 + p_3}{2}$$

2.3.3.2. Static Sensor Calibration Facility

A fully automated calibration facility, in which the pressure and temperature levels could be controlled individually, built the basis for the static MEMS sensor calibration encapsulated in the fast-response probes. A differential pressure controller (DPI 520), with a relative pressure range of ±1 bar relative to the atmospheric pressure, controlled the back pressure to the probe pressure sensors. The applied pressure was measured with an absolute pressure transducer (Keller PA-33X). The FRAP used for the current turbine configuration was typically calibrated for a pressure range from 50 mbar to 700 mbar (relative to atmosphere) with 27 pressure steps. The temperature calibration range was chosen from 5 °C to 70 °C with steps of 5 °C. The probes were thermally cycled to check for non-repeatable behavior of the sensor sensitivity. After amplification of the signals, a pressure sensitivity of 9.5 mV/mbar and a temperature sensitivity of 17 mV/K were achieved. The FENT probe pressure sensor was calibrated similarly to the FRAP. The temperature calibration of the thin-film gauges was performed by Mansour [98] over a range from 30 °C to 130 °C in steps of 10 °C.

2.4. Complementary Fast-Response Turbine Instrumentation

One of the objectives of the present work was to study the complex aerodynamic and heat transfer patterns in regions of the test turbine that are hard to access with stem probes, for example, the hub cavity. To accurately determine the flow physics, a high temporal resolution for the measurements was required to capture the unsteady nature. Due to the lack of optical accessibility, harsh environment, and limited space, as well as the requirements for a large frequency bandwidth, most of the measurement techniques exclusively relied on fast-response wall-mounted pressure transducers and thin-film gauges. Additionally, to derive the heat transfer quantities in the hub cavity, specially designed heat transfer inserts were developed in combination with double-

sided thin-film heat flux gauges. To determine the relevant quantities for the rotor blade tip coolant ejection, fast-response pressure sensors and resistance temperature sensors were integrated into the blade cap (section 2.1.5) in combination with a miniature Venturi tube. Typically, the fast-response instrumentation was used in the stationary and rotating frame of reference, whereas the rotor onboard measurements required the use of a modular, multipurpose, telemetry, and power supply system. In the following sections, the individual instrumentation types are described in more detail.

2.4.1. Fast-Response Wall-Mounted Hub Cavity Pressure Instrumentation

To study the aerodynamic peculiarities of the hub cavity flows, miniature unsteady pressure transducers were installed on the first stator and rotor cavity wall. Depending on the rim seal design, the aerodynamic probes were not always able to penetrate into the whole cavity so that a wall-mounted approach of pressure sensors was an appropriate option to capture the cavity dynamics at different radial positions. In Figure 2.23 (left), a meridional view on the two rim seal designs is provided, including the radial positions of the pressure transducers on the stator 1 and rotor cavity wall. The angel-wing-type rim seal was equipped with two pressure transducers on the first stator and rotor cavity wall. The integration of the sensors for this rim seal design was originally considered as a preliminary test of the pressure sensors in the stationary and rotating frame of reference, such that a limited number of sensors were installed. Nevertheless, encouraging results were derived from this study as presented in Chapter 3.
For the overlap-type rim seal, a total of 12 unsteady pressure sensors were installed where they were equally split between the first stator- and rotor-sided hub cavity wall. Their specific radial positions are indicated in Figure 2.23. Additionally, the pitch-wise alteration of the pressure field was probed by different circumferential sensor positions. Specifically, the stator-sided hub cavity wall is addressed in the current work. The sensor positions, labeled with **(1)** in Figure 2.23 (bottom left), axially followed the first stator trailing edge to the end of the hub platform and were then projected to the stator hub cavity wall. The positions indicated with **(2)** were defined by following the mid-passage of the first stator streamwise until the end of the hub platform and were then projected on the cavity wall. Position **(3)** was constructed by following the first stator trailing edge until the end of the platform. The rotor sensor positions were defined at two radial positions and pitch-wise distributed so that the angular distance was not matching the rotor pitch.

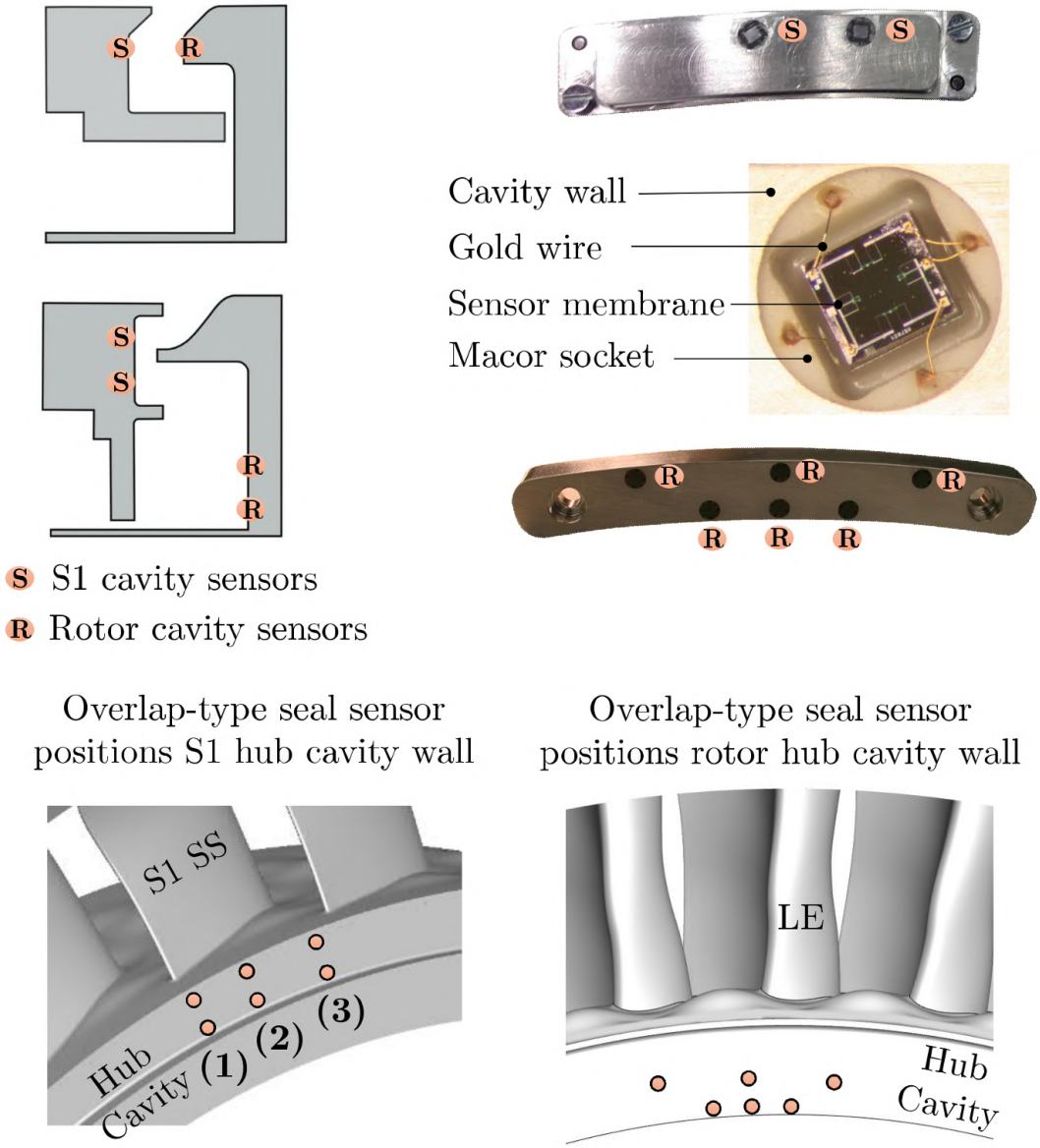

Figure 2.23.: Fast-response pressure sensors in the rotor upstream hub cavity: view on pressure sensor location (left and bottom) and sample pictures of instrumented stator and rotor inserts and non-coated pressure transducer (right)

In that the unsteady pressure sensor measurements were conducted in the stationary and rotating frame of reference, specific requirements arose with respect to the sensor installation and packaging. For the integration of the instrumentation in the axial turbine rig, the size of the packaging had to be as small as possible to have a minimally invasive measurement setup. The measurement bandwidth was specified to be at least 10 kHz in order to resolve the maximum blade passing frequency and at least three harmonics of it. The sensor packaging robustness was to be able to cope with centrifugal accelerations up to $2{\cdot}10^6\, m/s^2$. The signal-to-noise ratio was to allow resolution of pressure oscillations down to at least 100 Pa (about 0.07 % of the turbine inlet total pressure) in order to examine sensitive flow perturbations in the hub cavity.

To achieve these requirements, a set of new hardware was used, including a miniature piezo-resistive absolute pressure die (Measurement Specialties MS7801) with dimensions as small as 1.98 mm x 1.84 mm x 0.89 mm, a modular multipurpose telemetry system for the rotor relative frame, and an in-house developed, two-channel power transfer slip ring. (A description of the sensor packaging and installation follows in the subsequent section.) The telemetry system and power transfer system are introduced in section 2.4.4. The described pressure sensors were also used to equip the Venturi tube used for the rotor blade tip study to quantify the ejected tip coolant flow rate. The concept was introduced in section 2.1.5.

2.4.1.1. Packaging and Installation of Pressure Sensors

The installation and packaging of the miniature pressure sensors were done identically for the stator- and rotor-sided measurement setup. The basic approach included the installation of pressure sensor assemblies into carrier inserts that enabled performance of the static sensor calibration and test measurements independently from the blade rows. Sample pictures of such inserts can be found in Figure 2.23 (top right), where a fully instrumented first stator- and rotor-sided insert is shown. The sensor packaging was supported by a machinable glass ceramic (MACOR) sensor-housing, which provided electrical insulation and appropriate thermal properties to reduce thermal gradients of the packaging. The MACOR socket is visible in Figure 2.23. The pressure sensor membrane was typically protected by a mixture of adhesive and silicone gel. The adhesive was applied to prevent deformation and delamination of the silicone. The silicone had the same thermal expansion coefficient as the pressure sensors, and the adhesive enhanced the coupling of the pressure signal with the applied temperature, which can be observed in the static calibration map of the sensors (section 2.4.1.4). The following installation steps are provided for the interested reader:

(1) **First bonding step of pressure die.** The raw pressure sensor die was temporarily fixed on a carrier jig. To establish electrical connection to the sensor die, a delicate thermos-sonic gold-wire bonding was performed that proved to be robust enough to carry the centrifugal load under rotation. The completed first bonding step facilitated early quality control of the pressure die by bridge-resistance measurements.

(2) **Preparation of ceramic sensor-housing.** The MACOR-based sensor-housing was properly cleaned, and four small-diameter wires were installed from the backside of the socket so that they moderately exceeded the socket surface on the front side. The wires were fixed in place using high-strength epoxy resin and polished such that a flush connecting pad was formed at the top surface of the socket.

(3) **Sensor installation and second bonding step.** The bonded pressure sensor die was installed in the ceramic sensor-housing by using a mixture of specific adhesive and silicone gel. The mixture provided appropriate fixture of the sensor die and offered damping of the mechanical excitation due to the turbine vibrations. After the fixation of the sensor, a second thermos-sonic bonding step was performed where the pressure die was connected to the sensor-housing pad. The quality of both bonding steps was carefully assessed by measuring the bridge resistance. The connection to the sensor-housing pad was supported by a small amount of epoxy resin. In Figure 2.23, a sample picture of the completed step is provided.

(4) **Installation in carrier insert and surface finishing.** The sub-assembly, consisting of the installed and bonded pressure die on the ceramic housing, was carefully installed in the carrier insert and fixed in place with high-strength epoxy resin. The design of the insert provided a small distance between the top surface of the pressure sensor membrane and the carrier insert to protect the sensor with a silicone coating. Accordingly, the open space between sensor die and housing was filled with an adhesive-silicone mixture. The surface finishing was achieved by filling up the space iteratively with small amounts of the mixture. Before each curing step, the assembly was placed in a vacuum oven to remove any trapped air bubbles that could deteriorate the sensor characteristics. The final thickness of the silicone layer was estimated to be approximately within 0.1–0.2 mm.

2.4.1.2. Data Acquisition of Pressure Sensors

For the unsteady pressure measurements, two data acquisition systems were used. The stator-sided pressure data were simultaneously acquired using a 16-channel measurement system with 16 bit resolution. The unsteady surface pressure was recorded with a sampling rate of 200 kHz for typically 4 seconds and phase-locked with the dominating flow field frequency (blade passing or non-synchronous low-frequency modes) in an equivalent way to the FRAP data. The respective synchronization signal was provided by a shaft trigger identical to the FRAP and FENT measurements.
The rotor-sided pressure information was acquired using a purpose-made WiFi telemetry system as described in section 2.4.4. The data were recorded with a sampling rate of 200 kHz for typically 4 seconds. Phase-locking and subsequent averaging were typically done for the vane passing frequency. The synchronization of the data was offered using an infrared laser installed in the turbine drum, which triggered the microcontroller of the telemetry module through a phototransistor.

2.4.1.3. Pressure Sensor Frequency Bandwidth

The added protective silicone layer on top of the sensor membrane was anticipated to reduce the bandwidth of the setup in response to changes in the eigenfrequency of the pressure sensor assembly. For a similar pressure sensor assembly with a comparable silicone layer thickness, Rebholz [151] performed shock-tube tests and compared them with the results of a non-coated reference sensor (as introduced by Mansour et al. [101]). The obtained transfer function of the coated sensor showed a pressure signal amplification which exceeded +3 dB at 210 kHz, which would, in principle, set the natural measurement bandwidth. However, this frequency was higher than the sampling frequency and was therefore cut off. Accordingly, the application of the silicone layer did not limit the original frequency bandwidth of the measurement setup.

2.4.1.4. Calibration of Hub Cavity Pressure Sensors

After the installation of the miniature pressure sensors in the carrier inserts, the assemblies for the stator- and rotor-sided hub cavity wall were calibrated in a fully automated and temperature-controlled pressure chamber. The applied pressure and temperature were controlled in the same way as for the FRAP, using a DPI 520 pressure controller combined with Keller PA-33X transducers. The temperature inside the oven was monitored using two high-accuracy PT100 temperature sensors (±0.05 K for the given temperature range). The respective data acquisition modules for the stator- and rotor-sided setup were used for the calibration to provide a measurement-representative calibration environment. For the rotor-sided sensors, the onboard telemetry modules were put in a separate oven (heated to about 40 °C with air ventilation), which were to emulate the temperature of the turbine drum plenum.

The pressure sensors were calibrated over an absolute pressure and temperature range of 800–1400 mbar in steps of 50 mbar and 40–60 °C in steps of 5 °C. In Figure 2.24, examples of the resulting calibration maps are illustrated for both a stator- and rotor-sided setup. The pressure signal calibrations depicted in Figure 2.24 (a) and (c) reveal the appropriate sensitivity of the voltage signal to changes in the applied absolute pressure. The slight inclination of the vertical lines indicates a moderate dependency of the pressure signal to the temperature which is expected to be chiefly related to the application of the protective adhesive-silicone layer. The temperature calibration similarly shows good sensitivity to the applied temperature, which can be seen by the stability of the horizontal lines in the calibration map (Figure 2.24 (b) and (d)). Typical pressure sensitivity levels for the stator-sided sensors were in the order of 4.9 mV/mbar and for the rotor-sided setup, 4.2 mV/mbar, respectively. The determined bivariable calibration polynomials were of the fourth order for

both pressure and temperature. Typical standard deviations of the pressure calibration model were ±10 Pa for the stator setup and ±45 Pa for the rotor setup. Temperature deviations in the temperature calibration model were ±0.02 K for the stator setup and ±0.1 K for the rotor setup, respectively.

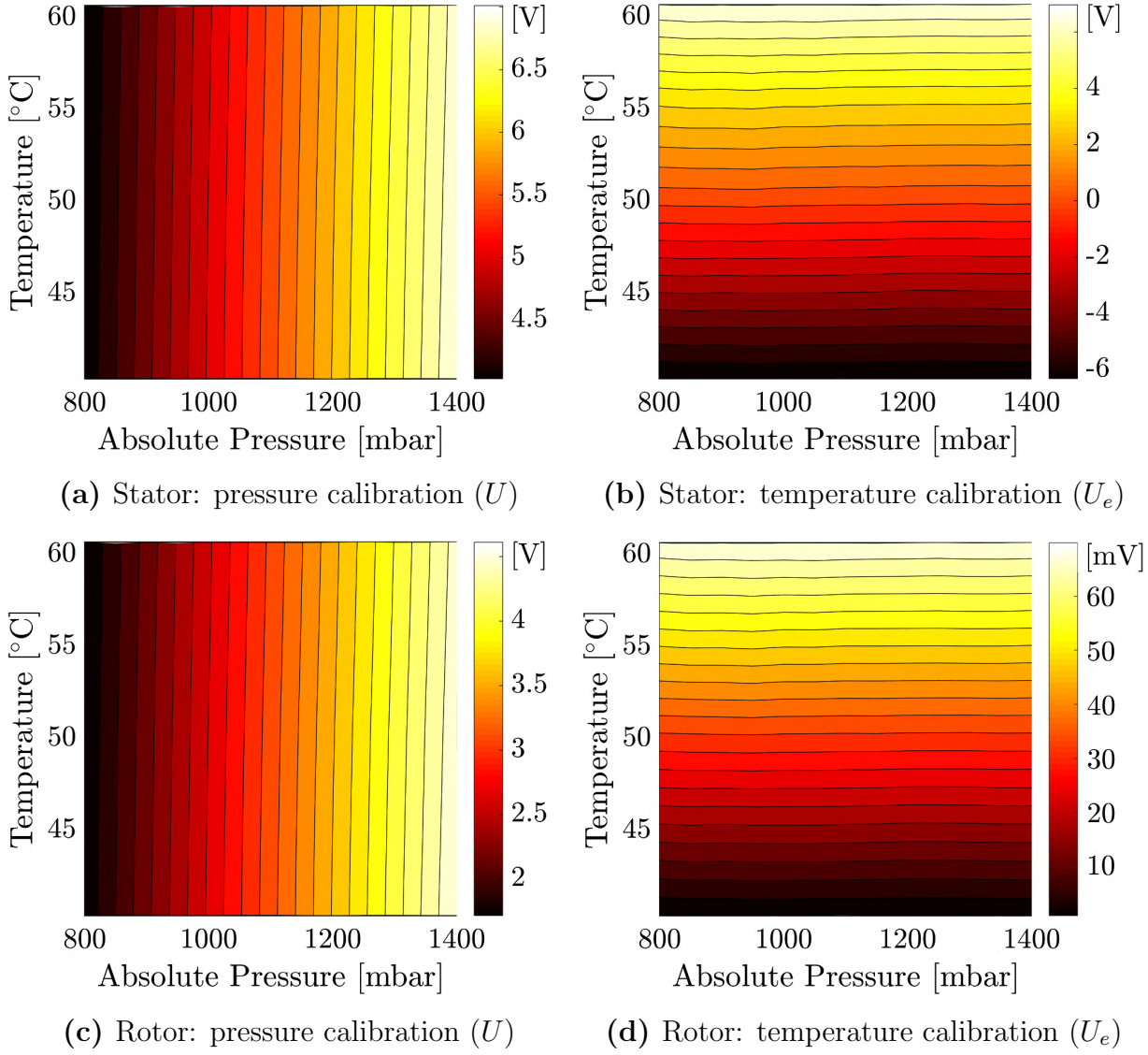

(a) Stator: pressure calibration (U)

(b) Stator: temperature calibration (U_e)

(c) Rotor: pressure calibration (U)

(d) Rotor: temperature calibration (U_e)

Figure 2.24.: Exemplary pressure sensor calibration maps for stator- and rotor-sided hub cavity wall instrumentation

2.4.1.5. Signal-to-Noise Ratio

The pressure signals were recorded with high amplification factors, which resulted in typical signal-to-noise ratios of at least 10 and reaching up to 20 for both the stator and rotor setups. The ratios were calculated based on measurements for nominal operating conditions wherein the square of the dominant peak pressure amplitude (and its harmonics) and the square of the standard deviation of the remaining signal components were related to each other. As the stochastic fluctuations were not entirely provoked by the

signal noise but also contained fluctuations induced by turbulence effects, the approach was judged to be conservative.

2.4.1.6. Centrifugal Effects on the Rotor Hub Cavity Wall Pressure Measurements

Due to the application of a protective adhesive-silicone layer to avoid deterioration of the sensor membrane, the mass associated with the layer provoked a certain straining of the silicone under centrifugal acceleration. The direction of the centrifugal acceleration can be decomposed into a normal and a transversal component to the sensor membrane. In that the rotor hub cavity wall pressure sensors were flush mounted with respect to the rotating walls, the main contributor to the pressure signal came from the transversal acceleration component. In a combined investigation conducted by Matter [106] and Rebholz [151] in a high-speed centrifugal compressor facility (RIGI) at ETH Zurich, they found that specifically the transversal sensitivity to the centrifugal acceleration of a similar pressure assembly was close to zero on average but showed substantial variations for different sensor samples. For the LISA nominal turbine design speed, Rebholz [151] estimated the resulting uncertainty ($2\,\sigma$) of the mean pressure to be around 600–1000 Pa for the transversal component. This contribution is included in the rotor mean pressure uncertainty analysis as presented in section 2.6.5.

2.4.2. Instrumentation for Rotor Tip Study

To assess the tip coolant flow quantities presented in Table 2.4, the rotor blade tip cap and the internal cooling flow path (Figure 2.7) were equipped with pressure and temperature sensors that were recorded by the onboard telemetry system. The pressure transducers were of identical type to the ones used for the hub cavity unsteadiness investigation described in section 2.4.1. The sensors presented a similar quality of the calibration map as the ones illustrated in Figure 2.24. The pressure sensors were used to determine the internal blade cap pressure levels as well as the differential and absolute pressure for the miniature Venturi tube to calculate the tip coolant mass flow (Figure 2.8).

The miniature Venturi tube was calibrated using a mass flow meter (Bronkhorst, F-201AC-FAC), which was used to measure methane mass flow rates up to 50 ln/min. Because the working fluid was air and not methane, the manufacturer offered transformation coefficients to be able to translate the measured values to the air mass flow. The reference values provided by the flow meter allowed for determination of the discharge coefficient for each Venturi tube at different flow rates or throat Reynolds numbers. The characteristic Venturi tube curves are shown in Figure 2.25 (left) where the measured mass flow rate

is correlated to the square root of the pressure drop across the contraction. A typical discharge coefficient trend within the calibrated throat Reynolds number range is provided in the same figure.

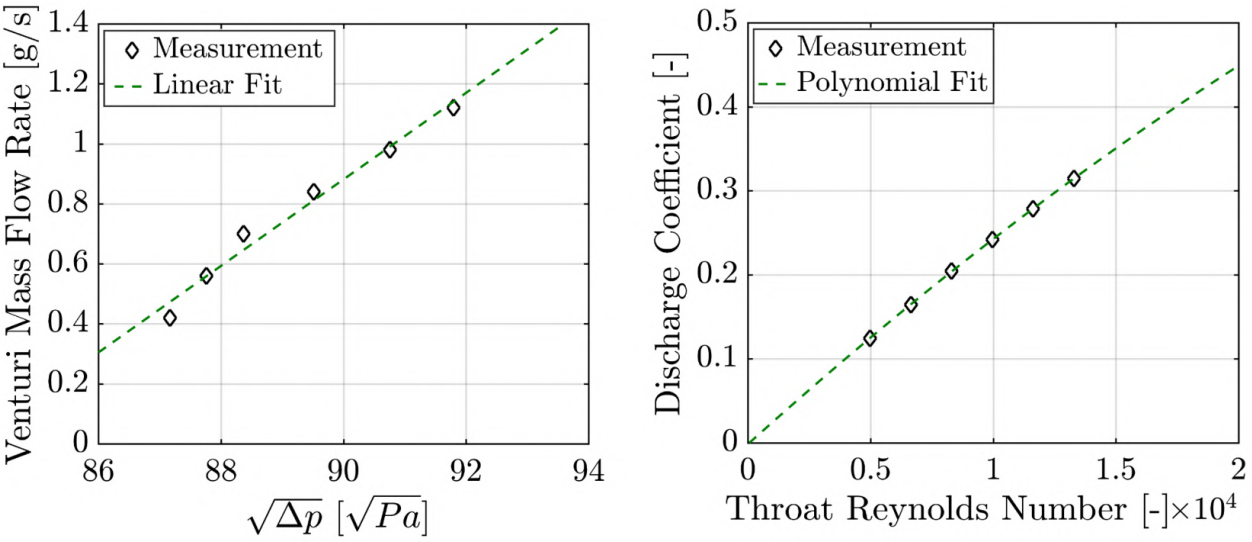

Figure 2.25.: Typical characteristic curves of the miniature Venturi tube calibration indicating the correlation between mass flow rate and pressure drop (left) and discharge coefficient against throat Reynolds number (right)

2.4.3. Hub Cavity Heat Transfer Measurement Setup

The importance of having detailed knowledge of the heat transfer quantities in the rim seal space has been previously highlighted. The convective heat flux $\dot{q}''_{conv}$ from a fluid to a surface is expressed as a function of the temperature gradient normal to the wall, which is indicated in Equation 2.5.

$$\dot{q}''_{conv} = -k_{fluid} \frac{\partial T}{\partial n} \tag{2.5}$$

Where k_{fluid} is the thermal conductivity of the fluid, T the temperature and n the normal to the surface. Due to the complexity of experimentally determining the temperature gradient at the wall, the definition for the convective heat flux at the wall is commonly expressed using a convective heat transfer coefficient h and the temperature difference between the wall and a driving temperature. The driving temperature is typically a point of discussion, but the extensive work provided by Moffat [118] suggests using the adiabatic wall temperature T_{ad} in the definition of the convective heat flux (Equation 2.6).

$$\dot{q}''_{conv} = h\,(T_w - T_{ad}) \tag{2.6}$$

The current study seeks to determine the convective heat transfer coefficient and the adiabatic wall temperature. The measurement of the convective heat transfer coefficient is usually conducted by setting the wall temperature at a

non-equilibrium state compared to the flow and measuring its temperature. Knowing the wall temperature and the heat flux, the heat transfer coefficient can be derived if the adiabatic wall temperature is known. The adiabatic wall temperature can, for example, be directly obtained by measuring the wall temperature of a sufficiently well-insulated wall. Measuring both quantities often requires two separate setups with identical geometries but different materials. Hence, it is favorable to make use of the linear relationship between the convective heat flux and the wall temperature. The linearity and independence of the convective heat transfer coefficient with respect to thermal boundary conditions enables designing an experimental setup that can deduce heat transfer quantities within the same test run. The setup therefore underlies the following energy balance:

$$\dot{q}''_{cond} + \dot{q}''_{conv} + \dot{q}''_{rad} = 0 \tag{2.7}$$

which includes the conductive heat flux $\dot{q}''_{cond}$ as well as the radiation contribution $\dot{q}''_{rad}$. For the turbine environment, the radiation part is not included as the temperature difference from the ambient is small. Consequently, the convective heat flux can indirectly be measured via the conductive heat flux. By using at least two boundary conditions, two sets of wall temperatures and convective/conductive heat fluxes (T_w, $\dot{q}''_{conv}$) were obtained, which were used in combination with Equation 2.6 to deduce the heat transfer quantities (h, T_{ad}). At least two points were required to calculate the parameters of the linear fit, but typically more points were used. The slope of the linear fit, which correlates the heat flux to the wall temperature, represents the convective heat transfer coefficient wherein the intercept with the abscissa defines the adiabatic wall temperature.

Based on these introductory principles, the measurement strategy included a setup able to change thermal boundary conditions inside the hub cavity by means of a heated platform that can vary the wall temperature. The purpose-made measurement instrument included three main components: Kapton based double-sided thin-film heat flux gauges, a high strength and low conductive carrier platform, and a thin-film heater. Since the setup needs to be able to cope with the centrifugal forces induced by the rotation of the rotor, the robustness of the instrumentation is of the highest importance. The individual components are described in more detail in the subsequent sections.

2.4.3.1. Double-Sided Thin-Film Heat Flux Gauges

The convective and conductive heat fluxes, respectively, needed to derive the linear relationship and subsequently deduce the convective heat transfer coefficients were measured using double-sided Kapton thin-film heat flux

gauges. Epstein et al. [45] intensively developed the two-layer thin-film gauge technique, and Abhari et al. [1, 2] successfully integrated the instrumentation on a rotor blade in a blow-down turbine facility in order to measure the time-resolved heat transfer for a cooled and uncooled rotor blade.

For the current work, similar types of thin-film double-sided Kapton heat flux gauges were used that were provided by the Gas Turbine Laboratory of The Ohio State University. Extensive usage was made and significant work was published by the group using the gauges to derive the time-resolved heat transfer on turbine components. Among others, the work of Dunn et al. [42, 43], Mathison et al. [103, 104], Nickol et al. [123, 124] provide interesting datasets. The provided gauges consisted of two temperature-sensing elements (thin films) on either side of the insulating polyimide substrate (Kapton, 51 μm). The temperature-sensitive thin films were typically as small as 1.0 by 1.1 mm. The insulator was adhesively bonded to the test article. A schematic illustration of the multi-layer assembly is provided in Figure 2.26, also including the thin-film heater, which is introduced in the subsequent section 2.4.3.2.

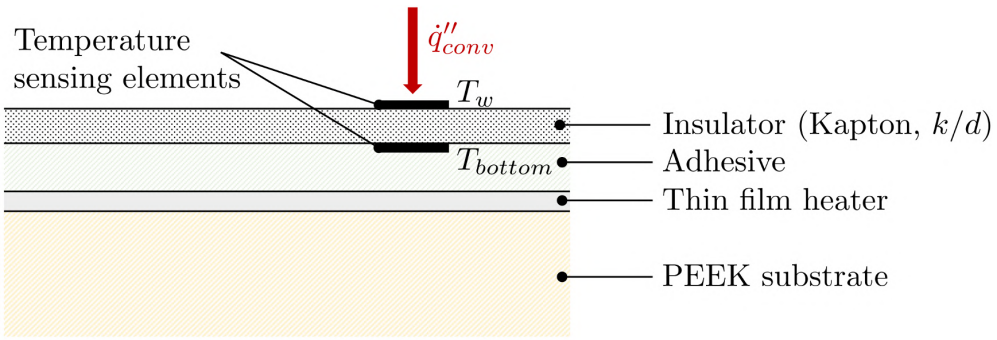

Figure 2.26.: Schematic of double-sided heat flux gauges and multi-layer assembly of the heat transfer setup (not to scale)

As the boundary conditions on each side of the Kapton sheet were known by resistance temperature measurements, only the thermal properties (thermal conductivity, thermal effusivity) and the thickness of the insulator foil were required to derive the time-averaged and time-resolved heat flux. The gauge response was typically separated according to the frequency of the applied wall heat flux. At low frequencies, the temperature difference between the top and bottom thin film was a direct measure of the heat flux to the wall (thermal shunt). The respective conductive heat flux provided by the gauge, which also represents the convective heat flux if radiation is neglected, can then be formulated as follows:

$$\dot{q}''_{cond} = \frac{k}{d}\left(T_{top} - T_{bottom}\right) = \frac{\left(T_w - T_{bottom}\right)}{R_{th}} \tag{2.8}$$

With k being the thermal conductivity of the insulating polyimide substrate, d

is the thickness of the substrate and T_{top} and T_{bottom} is the gauge temperature information of the top and bottom sensing element, respectively. The inverse of k/d is typically termed as the thermal resistance R_{th} of a material. The top sensor temperature is equivalent to the wall temperature T_w. The direct proportionality between temperature difference and heat flux extends from 0 to a few tenths of Hertz for the used gauge. Above 0.5 kHz, the insulator appears infinitely thick to the top surface such that a quasi 1D assumption can be applied to derive the time-resolved heat flux. Using the top and bottom temperature data and a one-dimensional transient heat conduction model (as originally documented by Weaver et al. [191]) enabled deduction of the unsteady heat flux data. The gauges used were able to provide high-speed data with a measurement frequency bandwidth up to 100 kHz. Temperature data were typically acquired with a sampling rate of 200 kHz.

Heat Flux Gauge Positioning The heat transfer study was conducted in the overlap-type rim seal, which was previously introduced in section 2.2.3. The positioning of the gauges inside the hub cavity and rim seal space is depicted in Figure 2.27.

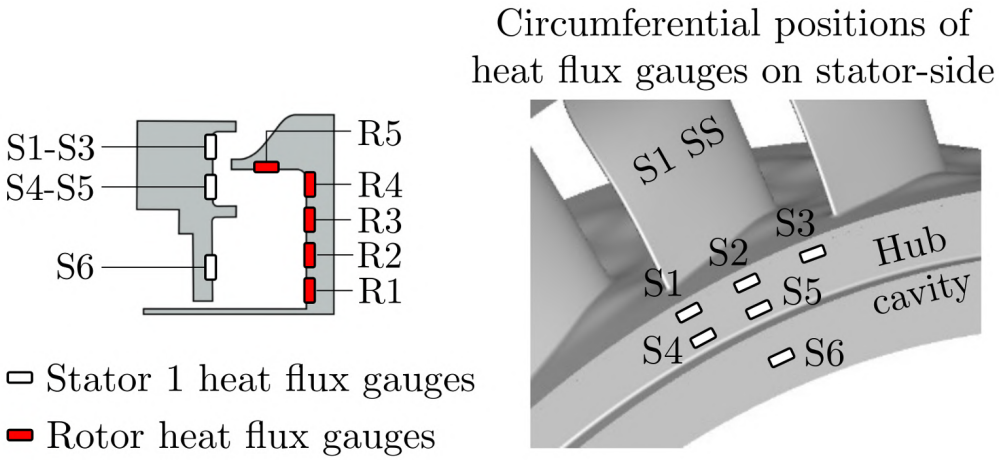

Figure 2.27.: Heat flux gauge positions in the hub cavity and rim seal space on stator 1 and rotor cavity walls

The stator-sided gauges were distributed at three different radial positions separated by the different sealing arms and were pitch-wise distributed in agreement with the unsteady pressure sensors previously described in section 2.4.1. The rotor-sided gauges were radially aligned and covered distinct positions along the radial coordinate as well as the delicate position below the rotor-sided sealing arm.

Calibration of Heat Flux Gauges The calibration of the thin-film heat flux gauges was conducted in-house in a highly stable calibration oven that showed temperature fluctuations well below 0.2 K. The reference temperature

information was provided by highly accurate temperature sensors (PT100) providing an accuracy of ±0.05 K within the targeted temperature calibration range. The sensors were typically thermally cycled in order to assess potential temperature-induced sensor drifts and repeatability. All gauges were calibrated after complete installation and wiring on the respective carrier inserts. To exclude or determine any sensor damage during the experimental campaign, all sensors were post-calibrated after the testing. The temperature calibration range was set between 15 °C and 75 °C in steps of 5 °C.

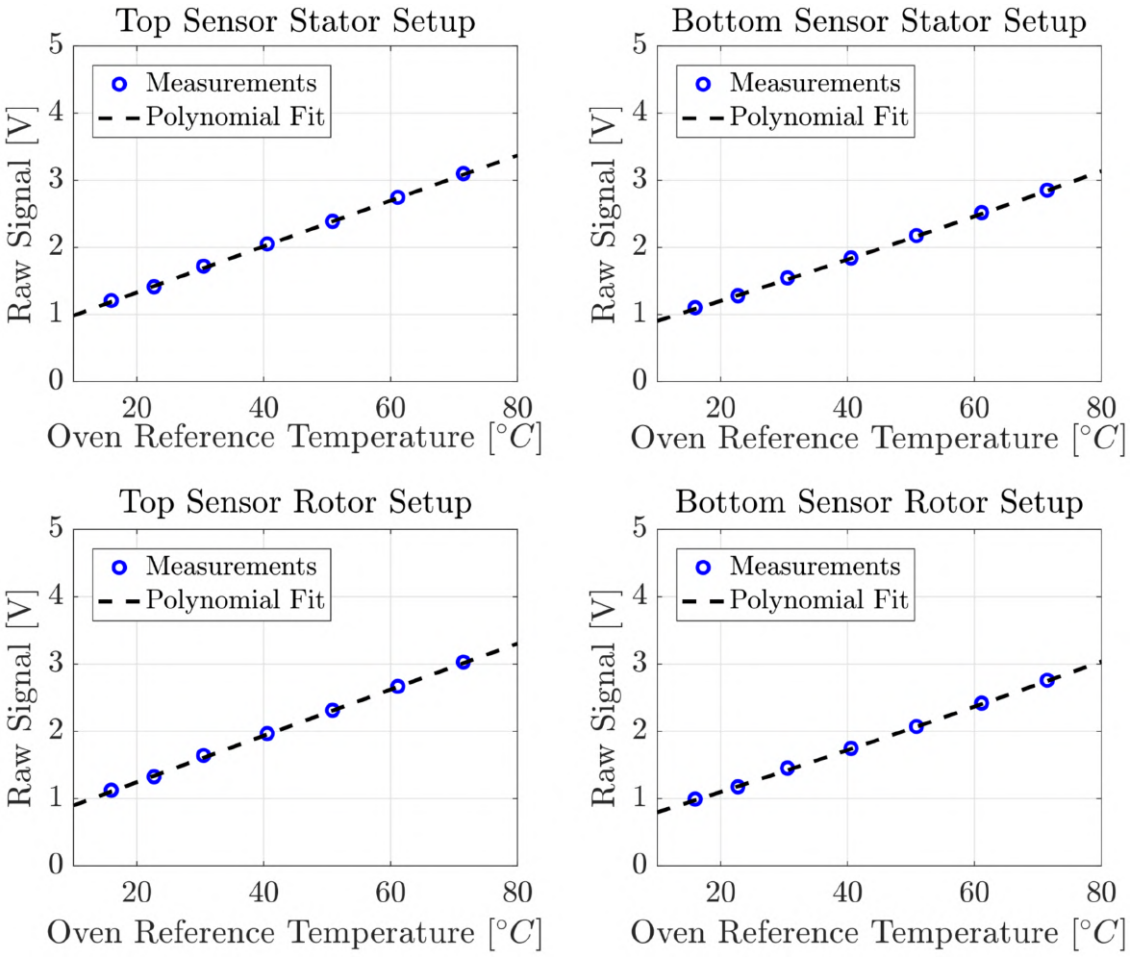

Figure 2.28.: Exemplary heat flux gauge temperature calibrations for top and bottom sensors for stator- and rotor-sided setup

The stability of the calibration oven and accuracy of the reference temperature allowed for the provision of high-quality calibration curves, using a linear regression scheme between temperature T and voltage output V, as illustrated in Equation 2.9.

$$T(V) = a_T\, V + T_0 \tag{2.9}$$

In Figure 2.28, typical calibration curves are provided for the top and bottom sensors of the stator- and rotor-sided setup. The rest of the used gauges provide a similar quality of the calibration curves. The typical R^2 values

clearly exceed 0.9999 for all temperature-sensing elements of the gauges.

2.4.3.2. Chemical Deposition of Thin-Film Heaters on Carrier Insert

To apply different thermal boundary conditions during the test runs of the turbine, a thin-film heater was integrated on a high strength, electrically and thermally insulating carrier insert that was manufactured out of PEEK. The heating element was based on a thin layer of nickel (1.5 μm thickness), which was applied by a direct chemical deposition technique that offered a low weight per unit area heating element and therefore provided appropriate robustness for the rotating frame of reference measurements, as previously demonstrated by Hänni et al. [57].

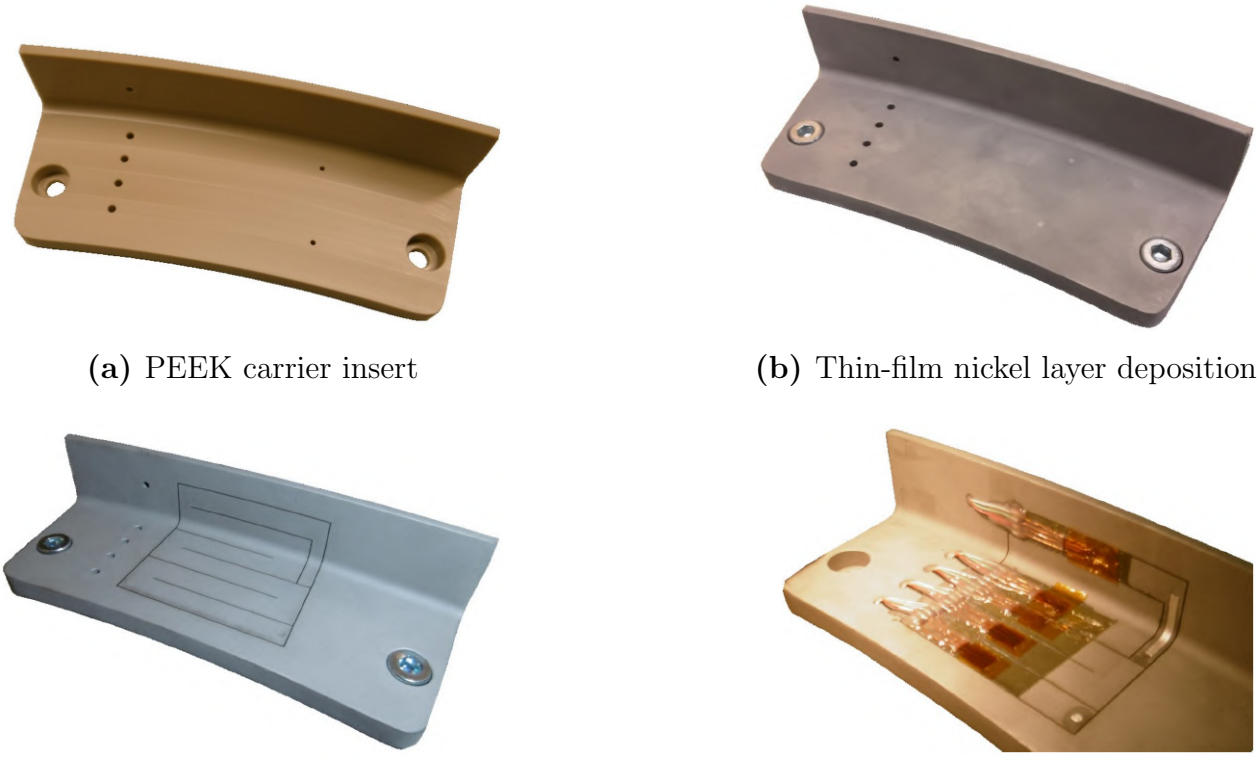

(a) PEEK carrier insert

(b) Thin-film nickel layer deposition

(c) Heating track manufactured

(d) Instrumented carrier insert

Figure 2.29.: Hub cavity heat transfer setup, rotor-sided carrier insert: exemplary manufacturing and instrumentation steps

The heating tracks were subsequently created by pulsed laser ablation, with a uniform track width of 5.4 mm. The lower limit of the track width was constrained by the width of the double-sided heat flux gauge substrate as it is favorable to fit one gauge within the track width to allow proper bonding. The different manufacturing and instrumentation steps are illustrated in Figure 2.29. The electrical connection to the thin-film heater was established using copper pins that were fixed with high-strength adhesive and subsequently coated with the nickel layer during the same processing step as the rest of

the insert surface. To guarantee the electrical connection, conductive epoxy was applied to reinforce the transition from the copper pin to the thin-film heater, which is of specific importance for the rotating frame of reference measurements. To achieve different thermal boundary conditions, the heater was powered with different voltage levels: typically between 0 to a maximum of 100 V.

2.4.3.3. Data Acquisition of Heat Transfer Measurement Setup

The stator- and rotor-sided temperature information were both acquired using a purpose-made WiFi telemetry system as described in section 2.4.4. The data were recorded with a sampling rate of 200 kHz for typically 2 seconds. The amplification factor of recording was set to 64 to ensure that the wider temperature range was covered and that the data were not out of calibration range. The synchronization of the rotor data was offered using an infrared laser installed in the turbine drum, which triggered the microcontroller of the telemetry module through a phototransistor.

2.4.3.4. Measurement Principle and Approach

The measurement principle and sequence to determine the time-averaged convective heat transfer coefficient and adiabatic wall temperature included the systematic change of the thermal boundary conditions of the carrier insert by applying different heating levels. Typically, five to seven heating steps were set to deduce the heat transfer quantities. Between each step, a temperature stabilization time of 10 minutes was chosen (although the dynamics were usually much faster as the gauges were thin). The correlation between the measured wall temperatures T_w and the calculated convective heat fluxes $\dot{q}''_{conv}$ was represented by a linear fit. The slope of the linear fit characterized the convective heat transfer coefficient wherein the adiabatic wall temperature T_{ad} corresponded to the null heat flux and the intercept with the x-axis, respectively. The time-averaged dependency of the wall temperature with respect to the measured heat flux for one rotor-sided gauge is depicted in Figure 2.30, highlighting the appropriate linear behavior of the measurements. Furthermore, prior to the measurements (in turbine standstill mode), when a steady-state temperature was reached inside the rig, a check measurement of all heat flux gauges was done to assess potential sensor drifts. Reference temperature sensors that were installed close to the carrier insert were used to eliminate any potential resistance drift in the post-processing of the data.

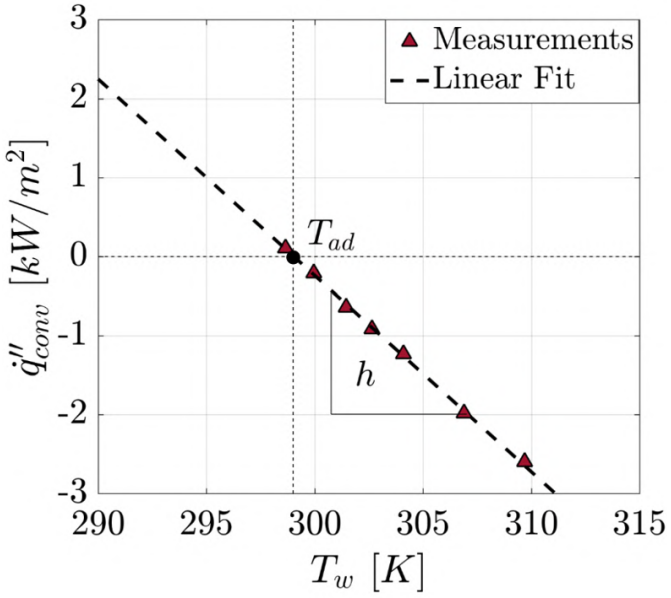

Figure 2.30.: Exemplary variation of wall heat flux with the wall substrate temperature for a rotor-sided heat flux gauge

2.4.4. Rotor Onboard Data Acquisition System

2.4.4.1. Telemetry Module Details

The different sensor voltages of the rotor instrumentation were acquired using wireless purpose-made data acquisition boards developed by ILPRA SA. The data acquisition (DAQ) system consisted of a fast analog-to-digital recorder and logger with a 16 bit resolution. The boards were designed to be operated on spinning components, such as the rotor disk assembly of the test rig, and were able to cope with accelerations of 15'000 g.

Each data acquisition board had four analog input channels connected to the same analog-to-digital converter, which provided synchronicity of the measurements. Per board, either two fast-response (piezo-resistive) pressure transducers or four single-resistance temperature sensors, such as the temperature-sensing elements of the double-sided heat flux gauges, could be operated in a constant current mode. The eight installed connectors permitted stacking the boards, as depicted in Figure 2.31. A maximum of eight boards could be stacked, however. Due to mechanical integrity reasons, stacks of two or three boards were typically considered for installation in the test turbine. The microcontroller could be triggered by an infrared laser through a photo-transistor, allowing startup of all the installed boards simultaneously.

In LISA, the stack of boards was distributed around the circumference and accordingly supported. A 5 mm clamping lip around the circuitry enabled clamping and reduced the stress concentration. An axial distance of 9 mm was covered by each board. The piezo-resistive pressure sensors and thin-film heat flux gauges were operated with a constant current of 1 mA through individual programmable current sources on the module. The maximum

sampling frequency of the modules was designed to be 200 kHz, and could be programmed differently for specific applications. The measured data were stored temporarily on a flash storage and permanently on an onboard SD card. The flash storage space enabled acquisitions over 8 s for the maximum sampling rate. The data transfer of the acquired measurement data to an exterior processing computer was provided by an embedded WiFi-module.
In order to optimize the instrumentation signal sensitivity and signal-to-noise ratio, each channel of the data acquisition boards was equipped with two programmable amplifiers, ranging from 1 to 128, and a voltage offset. The flexibility provided allowed fitting the sensing element signal range to within 0–5 V of the analog-to-digital converter. The unsteady pressure transducers typically were operated with an overall gain of 128, whereas the temperature-sensing elements of the thin-film heat flux gauges were usually recorded with a gain of 64 due to the wider operating temperature range. Typical peak-to-peak white noise values for the pressure measurements were 160–170 μV, which resulted in a minimum pressure resolution of 5–10 Pa. The white noise for the temperature measurements of the thin-film heat flux gauges was found to vary for the used gauges within 155–180 μV. This corresponded to a temperature resolution well below 0.01 K and was typically one order of magnitude higher than the effective measurement uncertainty of the sensor.
Further information on the data acquisition modules and a demonstration of their capabilities are provided in the work of Rebholz [151], Mansour et al. [101], and Bosdas et al. [16].

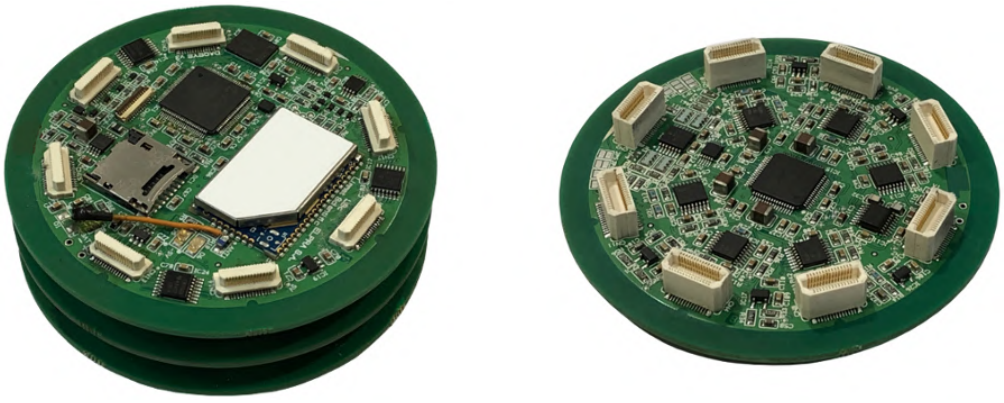

Figure 2.31.: Top (left) and bottom (right) view of the rotor onboard telemetry system. Stack of three DAQ boards is shown in the left representation.

2.4.4.2. Integration into the Test Rig

For the integration of the onboard telemetry modules on the rotor disk, the mechanical integrity and the stable power supply from an exterior power source to the rotating frame of reference had to be enabled. Additionally, the setup needed to supply power to other consumers, such as the thin-film heaters

of the heat transfer measurement setup. The complete assembly of such a system is provided in Figure 2.32. The rotor blades in the representation are black-painted, which was required for the additional optical heat transfer measurements on the rotor hub platform (details can be found in Hänni et al. [57] and Lazzi Gazzini et al. [93, 94]).

Mechanical Fixation and Wiring on DAQ Carrier Disk The safe operation of the turbine test rig was of the highest importance. Therefore, the mechanical integration of the telemetry modules had to provide a high safety factor coupled with the least invasive installation approach, such that the rotor dynamics of the turbine shaft train were not substantially affected.
The chosen integration approach was as follows: the telemetry modules were installed in six stacks on a high-strength aluminum disk, termed as the "DAQ carrier disk," on the backside of the rotor disk. Stackable clamping rings supported and aligned the modules and were form-fitted into a groove, which carries part of the centrifugal forces. An array of axial screws through the whole stack, which are additionally secured from the back of the DAQ carrier disk with screw nuts and locking rings, carry the load that is provoked by the axial shift of the center of gravity due to the stacking. Circumferentially displaced openings in the clamping ring assembly provided ventilation to the individual telemetry boards under rotation. As the WiFi connectivity was weakened due to the aluminum clamping rings, two high-gain receiving antennas were installed inside the plenum of the test rig in the stationary frame of reference.
The DAQ carrier disk was fixed and aligned by an array of 24 axial screws to the rotor disk on the outer perimeter and extended radially inwards toward the fixation of the rotor disk. The thickness of the carrier disk was limited by the rotor disk itself on the inner perimeter and was carefully designed by Rebholz [151] using FEM analyses to carry the load of stacks of three boards and avoid potential eigenmodes that provoke an unfavorable interaction with the turbine characteristic modes.
The wiring for the power supply, the signal transmission, and synchronization of DAQ boards was routed in the specifically designed grooves of the carrier disk. The radially inwards starting power lines were guided to each of the six stacks and connected in parallel to two capacitors that offer low-pass filtering on oscillations provoked by the power transfer slip ring. The signal transmission lines were connected to a specifically designed terminal printed circuit board (PCB), which sits below each of the six stacks. The sensing elements were directly connected to this additional PCB to reduce soldering spots. The combination of good quality soldering and shielded wires provided appropriate signal-to-noise ratios ranging from 10 to 20 for both pressure and temperature measurements. The wiring was kept in place using a combination

of high-strength epoxy resin and adhesive silicone. The whole DAQ carrier disk assembly added approximately 4 kg to the overall rotor assembly, which was about one-eighth of the rotor disk mass. Prior to each measurement campaign, the rotor assembly was dynamically balanced using compensating balancing masses and fixation screws at defined circumferential positions in order to comply with the ISO 1940-1 norm for gas turbines. The integration of additional components at the rotor backside also was assessed regarding their impact on the torque measurements of the turbine. As the board stacks can potentially provoke additional windage losses that could affect the aerodynamic performance measurements, performance repeatability tests were performed with and without the DAQ carrier disk installed. The result of the study showed that the differential performance levels were within the measurement uncertainty band (±0.32 % points) and were found to be 0.05 % points. Consequently, further performance measurements were conducted without removing the fully equipped onboard system.

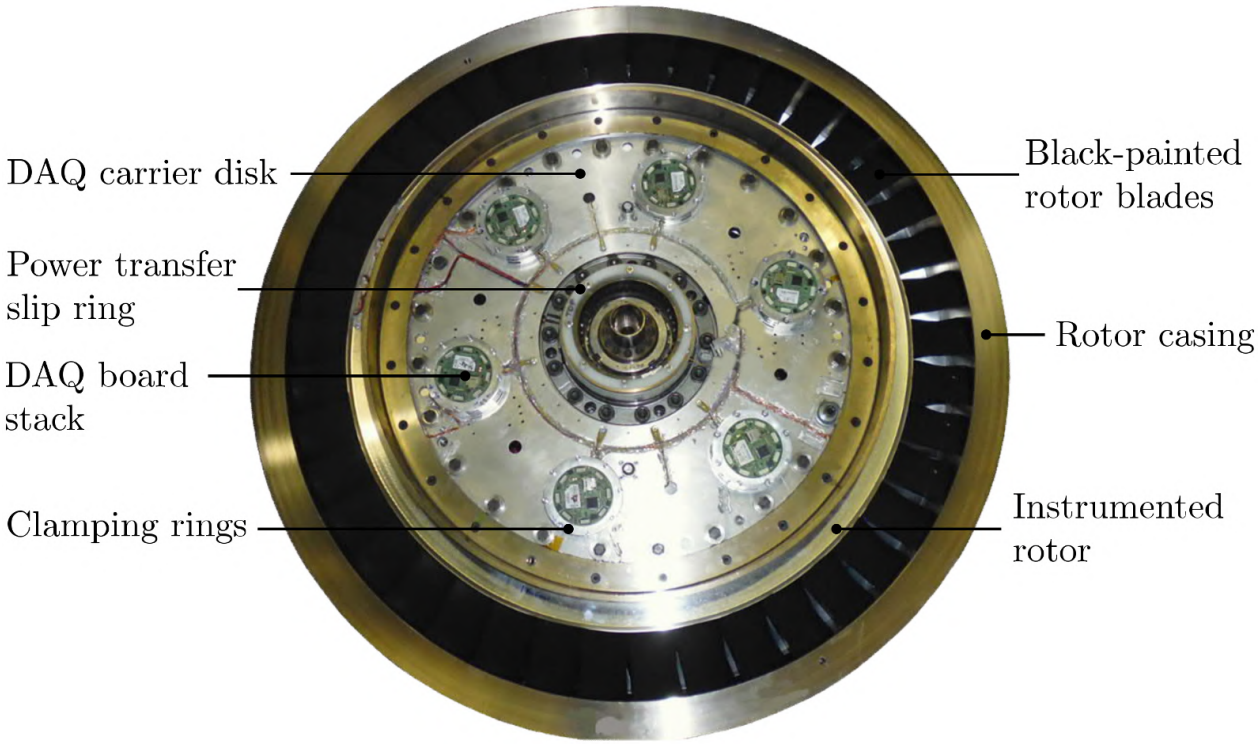

Figure 2.32.: Illustration of the rotor disk backside with installed DAQ carrier disk, telemetry system, and power transfer slip ring

Two-Channel Power Transfer Slip Ring Each of the telemetry modules consumed about 2 W of electrical power. Due to the additional power that is needed to supply current to the thin-film heaters for the hub cavity heat transfer measurement setup and the instability of Lithium-Ion batteries under rotation, an in-house developed slip-ring setup was chosen for the power transfer. The slip ring was installed at the innermost diameter that allowed

for proper installation and provided a reduced relative speed between the electrodes and the contact surface. For the current densities and rotational speeds required for this work, a combination of electro-graphite brushes and brass contact rings were chosen [158]. The slip ring was operated in a two-channel mode where one of the channels was supplying the telemetry modules with electrical power, and the second one was specifically dedicated to powering the thin-film heaters used for the rotor heat transfer setups. The two-channel brass terminals were properly separated by a Teflon-type insulation material, which can be identified in Figure 2.32 (whitish rings toward the center of the assembly).
The two brass rings were contacted using spring-loaded graphite electrodes. The usage of two electrodes per brass terminal permitted reduction of unfavorable fluctuations in the power supply due to manufacturing and assembly tolerances. A combination of a slidable arm and pneumatic cylinders provided the appropriate contact between the brushes and the terminals. The three-dimensional adjustment of the brush holder assembly led to a proper alignment between the brushes and the slip ring. After the installation, the brushes were run-in, first at low-speed operation, and afterward at design speed. Typical resulting resistance values of less than $0.5\,\Omega$ were achieved following this procedure.

2.5. Data Reduction

2.5.1. Pneumatic Probes 4HP and 5HP

The determined sensitivity coefficients K_i for the different flow quantities introduced in section 2.3.3.1 were used to determine the aerodynamic calibration coefficients $k_{\varphi,ij}$ (flow yaw angle), $k_{\gamma,ij}$ (flow pitch angle), $k_{\mathrm{t},ij}$ (total pressure), and $k_{\mathrm{s},ij}$ (static pressure). The bivariable combination of the sensitivity coefficients and the aerodynamic calibration coefficients allowed for calculation of the flow yaw angle, pitch angle, total pressure, and static pressure. The flow field evaluation started with the calculation of the flow angles as provided in Equation 2.10 and 2.11. The calculated flow angles were in the probe relative frame of reference such that the set angles of the probe traversing had to be added. The flow angle convention was set as follows: positive yaw angles pointed in the direction of the rotor rotation, and positive pitch angles pointed radially outwards.

$$\varphi_{probe} = \sum_{i=0}^{m} \sum_{j=0}^{n} k_{\varphi,ij} {K_\varphi}^i {K_\gamma}^j \tag{2.10}$$

$$\gamma_{probe} = \sum_{i=0}^{m} \sum_{j=0}^{n} k_{\gamma,ij} K_{\varphi}{}^{i} K_{\gamma}{}^{j} \tag{2.11}$$

In the definition of the total and static sensitivity coefficients (Equation 2.2 and 2.3), the measured values in the freejet facility were used to determine the coefficients. However, these quantities were unknown in the turbine test rig; hence their calibration coefficients were based on the flow angles as suggested by Equation 2.12 and 2.13. To obtain the total and static pressure, the values for K_{t} and K_{s} needed to be rearranged according to the definition given in Equation 2.2 and 2.3.

$$K_{\mathrm{t}} = \sum_{i=0}^{m} \sum_{j=0}^{n} k_{\mathrm{t},ij} \varphi^{i} \gamma^{j} \tag{2.12}$$

$$K_{\mathrm{s}} = \sum_{i=0}^{m} \sum_{j=0}^{n} k_{\mathrm{s},ij} \varphi^{i} \gamma^{j} \tag{2.13}$$

The polynomial orders m and n were chosen to gain accurate and robust results. For the probe calibration range of $\pm 24°$ for the flow yaw angle and $\pm 20°$ for the pitch angle range, the best results were obtained by a fifth-order polynomial $m = n = 5$ for both 4HP and 5HP. Higher polynomial orders can result in better accuracy locally in the grid but are typically more prone to unstable behavior, including higher oscillations of the sensitivity coefficients on the calibration map that result in larger global errors of the calibration scheme.

Based on the isentropic relations for an ideal gas, the Mach number M was calculated using the total- and static-pressure data. The corresponding expression is given in Equation 2.14. The absolute flow velocity was derived from the Mach number calculation using the speed of sound, which was determined by the average static temperature T_s provided by FRAP measurements at the same measurement plane. The axial velocity V_x, radial V_r, and circumferential flow velocity V_θ were obtained using the local flow angles as suggested in Equations 2.16 – 2.18. The convention for the circumferential and radial flow velocities follows the conventions of the flow angles: positive circumferential velocities point in the direction of the rotor rotation and positive radial velocities point radially outwards.

$$M = \sqrt{\frac{2}{\kappa - 1} \left(\left(\frac{p_{\mathrm{t}}}{p_{\mathrm{s}}} \right)^{\frac{\kappa-1}{\kappa}} - 1 \right)} \tag{2.14}$$

$$V = M \sqrt{\kappa R T_{\mathrm{s}}} \tag{2.15}$$

$$V_x = V \cos(\varphi) \cos(\gamma) \tag{2.16}$$

$$V_r = V_x \tan(\gamma) \tag{2.17}$$

$$V_\theta = V_x \tan(\varphi) \tag{2.18}$$

2.5.2. Fast-Response Probes: FRAP and FENT

The data post-processing routine for the fast-response probes was an in-house developed software package. Detailed information can be found in the work of Schlienger [170]. First, the acquired sensor data needed to be converted into pressure and temperature before the actual aerodynamic calibration scheme could be applied. Second, the virtual 4 (3)-sensor mode for FRAP (FENT) was applied to determine the relevant flow quantities. This required the synchronization of three individual measurements per measurement point by using the shaft trigger signal of the facility. The input file structure to the post-processing routine required three files: (1). the probe sensor raw data, (2). the probe operating files (which included the applied back pressure to the MEMS sensors and the probe set angles), and (3). the turbine rig operating file for potential normalization of the flow quantities. The data reduction was divided into four steps.

Step 1: Rig Operating Conditions and Turbine Geometry Initialization In this first step, the turbine geometry details and the measurement grid for the associated traversing plane were defined. In addition, the reading and synchronization of the turbine operating parameters (e.g., turbine inlet total pressure and turbine torque) with the corresponding probe measurement data was performed. Furthermore, the probe operating pressure information was read.

Step 2: Pre-processing of Probe Raw Data: Phase-Locking In the second step, the binary raw data files were read, containing the pressure and temperature voltages U and U_e as well as the shaft optical trigger voltage. With the help of the shaft trigger signal, which was triggered once per rotor revolution, the raw data were reduced and phase-locked to typically three rotor blade passing periods (e.g., 247 samples) after each trigger signal. Out of 90 available rotor revolutions (2 s data acquisition at 200 kHz), 85 revolutions were stored for the later executed phase-lock averaging. At this stage of the post-processing, the data were not averaged.

Step 3: Offset Gain Calibration and Flow Quantities Calculation The phase-locked voltage data from the previous step were, in a third step, converted to pressure and temperature with a bivariable polynomial combination of the pressure and temperature voltage signal and the corresponding calibration

coefficients $k_{p,ij}$, $k_{T,ij}$ (Equation 2.19 and 2.20). For the FRAP, the polynomial order $m = n = 6$ was chosen.

$$\Delta p = \sum_{i=0}^{m} \sum_{j=0}^{n} k_{p,ij} U^i U_e^j \tag{2.19}$$

$$T = \sum_{i=0}^{m} \sum_{j=0}^{n} k_{T,ij} U^i U_e^j \tag{2.20}$$

This calibration scheme was valid for the FRAP yaw and pitch sensor as well as for the FENT pressure transducer. The calculation of the unsteady temperature for the FENT probe was explained in detail by Mansour [98]. An offset-gain calibration was executed before and after each radial traverse to remove the sensor drift effects as described by Kupferschmied [88]. In this process, the probe was retracted to the tower position where the static pressure was measured and two different back-pressure levels were applied to the probe so that a linear offset and gain calculation for all sensors could be performed in the post-processing. More information is provided by Schlienger [170]. The offset and gain values were then applied to the measured pressure difference and temperature at each radial traverse.

The absolute pressure was calculated for each sensor by subtracting the differential pressure Δp from the sum of the atmospheric pressure p_{atm} and the applied reference back pressure p_{ref} (Equation 2.21).

$$p = p_{\text{atm}} + p_{\text{ref}} - \Delta p \tag{2.21}$$

Based on the absolute pressures, the aerodynamic calibration scheme could be applied in the same way as presented for the pneumatic probes (Equations 2.10 - 2.13). In that the FENT probe does not have a pitch pressure sensor, the calibration post-processing scheme was modified as described by Equations 2.22 – 2.24.

$$\varphi = \sum_{i=0}^{m} k_{\varphi,i} {K_\varphi}^i \tag{2.22}$$

$$K_{\text{t}} = \sum_{i=0}^{m} k_{\text{t},i} \varphi^i \tag{2.23}$$

$$K_{\text{s}} = \sum_{i=0}^{m} k_{\text{s},i} \varphi^i \tag{2.24}$$

A polynomial order of $m = n = 6$ for both probes was used. The subsequent steps in the post-processing routine were the phase-lock averaging over the 85

rotor revolutions. At last, the unsteady flow field quantities could be derived applying, for example, Equations 2.14 - 2.18.

Step 4: Additional Flow Quantities and Flow Visualization Other flow quantities such as streamwise vorticity, stochastic flow unsteadiness (turbulence quantities), and entropy change also could be derived, which are presented in the subsequent sections 2.5.2.1 - 2.5.2.3 . Multiple visualization options are available in this step which were initiated in the work of Schlienger [170] and Behr [8].

2.5.2.1. Non-Deterministic and Non-Synchronous Pressure Unsteadiness

The drawback in the phase-lock averaging of time-resolved pressure data is the damping of fluctuating pressure content, which is not associated with the turbine rotational speed nor multiples of it. Non-deterministic fluctuations provoked by turbulence and non-synchronous flow excitation are therefore averaged out. However, since especially non-synchronous pressure oscillations are one characteristic of cavity flows, this flow information needs to be extracted out of the vast amount of data. To gain this flow field content, Porreca et al. [145, 146] suggested a decomposition of the measured raw pressure signal into a mean pressure $\overline{p}$ component, a periodic pressure part $\tilde{p}(t)$, and a stochastic content $p'(t)$ in order to derive the turbulent quantities (Equation 2.25).

$$p(t) = \overline{p} + \tilde{p}(t) + p'(t) \tag{2.25}$$

Consequently, this expression could be used for the assessment of asynchronous content in the pressure field of the turbine flow. Recalling the different probe positions from the virtual 4-sensor measurement concept, the p_1 position of the probe (Figure 2.22) was aligned with the mean flow direction that was provided by the pneumatic probe measurements. The measurements in this position therefore resembled the unsteady total pressure measurements. To be precise, flow incidence variations relative to the probe pressure access hole could also be detected as pressure fluctuations by the yaw pressure sensor. Rebholz [151] estimated that deviations from the total pressure due to flow angle variations are at most 1.5 % but typically less than 0.2 % of the turbine inlet total pressure based on an assessment in a very comparable turbine flow field regime.
Equation 2.26 provides a relation for the root-mean-square $p'_{1,rms}(t)$ of the difference between the raw pressure signal and the sum of the mean and periodic component [151]. This quantity provides increased values if there are fluctuating components in the flow field other than multiples of the rotational speed of the rotor.

$$p'_{1,rms}(0 \leq t \leq 3\,T_{RBP}) = \sqrt{\frac{1}{N}\sum_{i=0}^{N-1}[p(t+i\cdot T_{rot}) - \overline{p} - \tilde{p}(t+i\cdot T_{rot})]^2} \quad (2.26)$$

The expression is typically evaluated for three rotor blade passing periods T_{RBP} and the root-mean-square $p'_{1,rms}$ was calculated using $N = 85$ instants in time when the rotor was at the same relative position to the stator, which is implied in Equation 2.26 by a once per rotor revolution (T_{rot}).

2.5.2.2. Streamwise Vorticity and Circulation

The scalar product of the vorticity vector $\overrightarrow{\Omega}$ and the primary flow velocity vector $\overrightarrow{V}$, as expressed in Equation 2.27, provided the magnitude of the streamwise vorticity Ω_S.

$$\Omega_S = \overrightarrow{\Omega} \cdot \overrightarrow{V} \quad (2.27)$$

The primary flow velocity was given by the circumferentially and mass-averaged velocity profile. The vorticity vector in cylindrical coordinates could be decomposed into an axial vorticity component Ω_x, a radial one Ω_r, and a circumferential component Ω_θ. The corresponding expressions can be found in Equation 2.28 to 2.30. The axial velocity gradients were calculated using a frozen flow assumption as described by Schuepbach et al. [174].

$$\Omega_x = \frac{1}{r}\left(\frac{\partial}{\partial r}(rV_\theta) - \frac{\partial V_r}{\partial \theta}\right) \quad (2.28)$$

$$\Omega_r = \frac{1}{r}\frac{\partial V_x}{\partial \theta} - \frac{\partial V_\theta}{\partial x} \quad (2.29)$$

$$\Omega_\theta = \frac{\partial V_r}{\partial x} - \frac{\partial V_x}{\partial r} \quad (2.30)$$

Great care must be taken when interpreting the contribution of each of the three components to the overall streamwise vorticity levels. Vortical flow structures that are aligned to the primary flow direction, such as the secondary flows, can be associated with an increased level of streamwise vorticity. As a qualitative measure of the vortex strength, the circulation can be calculated as described in Equation 2.31. Based on the approach by Jenny [75], the integration of the streamwise vorticity over a certain area yields to the flow circulation, following Stoke's theorem. Typically, iso-levels of streamwise vorticity were used as integration boundaries to determine the integral.

$$\Psi = \int_{\Omega_S \geq 0} \Omega_S dA \tag{2.31}$$

2.5.2.3. Entropy Rise

The FENT probe provided simultaneous measurements of the total pressure and total temperature, which enabled calculation of the local entropy change in the flow relative to the turbine inlet conditions (inlet total pressure $p_{\mathrm{t,in}}$ and inlet total temperature $T_{\mathrm{t,in}}$). The corresponding relation, based on the second law of thermodynamics for the entropy change Δs, is provided in Equation 2.32.

$$\Delta s = c_p \ln\left(\frac{T_\mathrm{t}}{T_{\mathrm{t,in}}}\right) - R \ln\left(\frac{p_\mathrm{t}}{p_{\mathrm{t,in}}}\right) \tag{2.32}$$

2.5.3. Data Averaging: Mass- and Area-Averaging

The proper averaging of non-uniform flow is of importance for the analysis of measurements in turbomachines. Cumpsty and Horlock [34] provided an extensive overview of different averaging approaches for different flow regimes. In this work, therefore, convective flow quantities such as total pressure and total temperature are mass averaged. Non-convective quantities, such as static pressure and static temperature, are area averaged. The averaging can be applied in a radial or circumferential direction or in combination. Since the measurement grid is discrete, the integration is a numerical process. A cell center average was calculated, given by four points of the measurement grid.

Area-Averaging The area-averaged quantity $\overline{\chi}$ was determined by cell centering the local flow quantity χ and weighting by the corresponding local area dA. The area-weighted integral, given in Equation 2.33, is expressed for a structured grid in cylindrical coordinates.

$$\overline{\chi} = \frac{\sum \chi \, dA}{\sum dA} \tag{2.33}$$

with:

$$dA = r dr d\theta$$

Mass-Averaging The local flow quantity is χ was cell centered and weighted by the corresponding mass flow $d\dot{m}$ through the cell to determine the mass-averaged flow quantity $\overline{\chi}$. The expression for the mass-averaged quantity is presented in Equation 2.34.

$$\overline{\chi} = \frac{\sum \chi \, d\dot{m}}{\sum d\dot{m}} \tag{2.34}$$

with:

$$d\dot{m} = \rho V_x dA = \rho V_x r dr d\theta$$

2.5.4. Pressure and Temperature Normalization

In that the turbine test rig was quasi-closed and opened to atmosphere at the exit, the operating point was characterized by a constant total-to-static pressure ratio. The change in atmospheric pressure affected the local pressure information throughout the turbine, starting from the turbine inlet total pressure down to the exit static pressure. To compare measurements of different test days, the pressure and temperature data were normalized by the corresponding inlet total pressure and total temperature as provided in Equation 2.35.

$$C_p = \frac{p}{p_{\mathrm{t,in}}} \qquad\qquad C_T = \frac{T}{T_{\mathrm{t,in}}} \tag{2.35}$$

2.5.5. Torque-Based Turbine Efficiency

For most of the aerodynamic performance evaluations in this work, a torque-based, total-to-total turbine efficiency definition was used. The expression related the actual turbine work output to the isentropic work (Equation 2.36). Additionally, the formula included piping losses of the rim seal purge flow before injection into the flow by the total pressure information $p_{\mathrm{t,cavity}}$ inside the rim seal hub cavity and the corresponding purge flow injection rate IR (as defined in Equation 2.1).

$$\eta_{tt} = \frac{\frac{\omega \cdot M}{\dot{m} \cdot c_p \cdot T_{\mathrm{t,in}}}}{1 - (1 - IR)\left(\frac{p_{\mathrm{t}}}{p_{\mathrm{t,in}}}\right)^{\frac{\kappa-1}{\kappa}} - IR\left(\frac{p_{\mathrm{t}}}{p_{\mathrm{t,cavity}}}\right)^{\frac{\kappa-1}{\kappa}}} \tag{2.36}$$

The actual work output of the turbine was given by the turbine rotational speed ω and torque M. The isentropic work was defined by the local total pressure p_{t} (e.g., at rotor exit or stator 2 exit) measured with the 5HP.

2.5.6. Temperature-Based Turbine Efficiency

The torque-based turbine efficiency presented in the previous section cannot be applied to turbine configurations that feature different geometries on the rotor for the same run. In the present work, a rainbow rotor was installed to test

different blade tip geometries during the same measurement day. Due to the different designs, the torque measurements, and consequently the associated total-to-total efficiency, cannot be linked to the respective design. Therefore, a temperature-based isentropic efficiency η_{is} definition was used as given in Equation 2.37. The expression related the actual work to the ideal work for each fluid particle. Using the FENT probe, the efficiency definition also included the local unsteady temperature contribution.

$$\eta_{is} = \frac{1 - \frac{T_{\mathrm{t}}}{T_{\mathrm{t,in}}}}{1 - \left(\frac{p_{\mathrm{t}}}{p_{\mathrm{t,in}}}\right)^{\frac{\kappa-1}{\kappa}}} \tag{2.37}$$

When using this definition, two assumptions need to be made and properly stated [75]: (1). The fluid is adiabatic, and (2). The entire fluid has the same initial conditions. Assuming certain heat losses through the stage could artificially increase the actual work output of the machine, which would result in higher isentropic efficiency. Although the heat loss throughout the test rig cannot be accurately determined, it can be assumed to be similar for the same run, which enables at least a relative comparison of the quantity. The turbine cooling flows were not included in the definition as it is a local definition.

2.6. Measurement Uncertainty

Significant and trustworthy experimental studies can only be appreciated by properly stating and analyzing the involved uncertainties. It is commonly known that all experimentally determined results have inherent errors that are provoked by a vast number of sources (e.g., instrumentation, data acquisition, the test rig). Especially in turbomachinery research, the role of uncertainty analysis is of highest importance in order to be able to judge the significance of a change in a specific quantity or to compare the absolute values to numerical results out of complex simulations. Also, the determination of measurement accuracy can contribute to locating the source of trouble in a misbehaving experiment. For the aerodynamic probes, the commercially available software package "Guide of Uncertainty in Measurements" (GUM) [72] was used. The hub cavity heat transfer and rotor pressure uncertainties were determined using a direct numerical approach introduced by Moffat [117].
The following sections focus on the individual expected measurement uncertainties associated with the different measurement techniques that were used throughout this work. All the uncertainty bandwidths cover two standard deviations ($\pm 2\,\sigma$), which means that the likelihood that a measurement result lies outside of the specified measurement uncertainty range is 1:20.

2.6.1. Aerodynamic Probes

Detailed uncertainty analysis for the aerodynamic probes (4HP, 5HP, and FRAP) was conducted by Lenherr [95] using the commercially available software package "Guide of Uncertainty in Measurements" (GUM) [72]. Following the same approach, Mansour [98] determined the measurement uncertainty for the FENT probe. The GUM tool is a standardized method that converts all the available uncertainties into probability distributions. If correlated parameters are considered, so-called cross-correlation coefficients need to be evaluated in order to determine their combined uncertainty. The underlying methods for the uncertainty evaluation are defined in DIN 1319-3.
The propagation of the independent measurement uncertainties and the correlated parameters are typically evaluated for a coverage factor of $k = 2$ (informal $\pm 2\,\sigma$). In case the result is normally distributed, this value corresponds to a confidence level of 95 %, which is judged to be rather conservative. The expanded uncertainties for the respective aerodynamic probes are presented in Table 2.9, including references. The uncertainties provided for the flow angles are presented as a percentage of their respective calibration ranges (yaw angle: $\pm 24°$, pitch angle: $\pm 20°$). The typical flow angles within all considered turbine configurations cover approximately 85 % of the angle calibration ranges and the presented Mach numbers are representative of the measurement planes. The total- and static-pressure uncertainty is given as a percentage of the local dynamic head.

2.6.2. Torque-Based Turbine Efficiency

The uncertainty level for the torque-based total-to-total aerodynamic efficiency (Equation 2.36) was calculated using the previously introduced "GUM" [72] approach and was documented in detail by Schuepbach [173] for the same rig devices and turbine operating point. The calculation of the measurement uncertainty included the respective standard uncertainty of all input quantities such as torque, rotational speed, turbine mass flow, and purge flow injection. In Table 2.10, the standard uncertainties for each input quantity and the corresponding uncertainty contribution are presented.
Out of the given standard uncertainties, the calculated absolute expanded uncertainty of the total-to-total aerodynamic efficiency was determined to be ± 0.37 % points with a coverage factor of $k = 2$ (confidence interval of 95 %). Importantly, the exit total pressure measured with the aerodynamic probes had the largest contribution (45.8 %) to the overall efficiency uncertainty. Consequently, the 5HP was used to determine aerodynamic performance, which provided the lowest measurement uncertainty as specified in Table 2.9. The main turbine mass flow and the torque contributed to 29.6 % and 17.0 %, respectively. The uncertainty contribution of the bypass and drum leakage

Table 2.9.: Range of expanded uncertainty ($k = 2$) for all considered aerodynamic probes

	Parameter	$M = 0.25$	$M = 0.3$	$M = 0.5$
5HP [95]	φ	$\pm 0.7\,\%$	-	$\pm 0.5\,\%$
	γ	$\pm 1.0\,\%$	-	$\pm 0.8\,\%$
	p_t	$\pm 1.9\,\%$	-	$\pm 0.7\,\%$
	p_s	$\pm 2.2\,\%$	-	$\pm 0.9\,\%$
4HP [95]	φ	-	$\pm 0.5\,\%$	$\pm 0.3\,\%$
	γ	-	$\pm 0.7\,\%$	$\pm 0.5\,\%$
	p_t	-	$\pm 1.5\,\%$	$\pm 0.8\,\%$
	p_s	-	$\pm 1.6\,\%$	$\pm 1.1\,\%$
FRAP [95]	φ	$\pm 1.3\,\%$	-	$\pm 0.5\,\%$
	γ	$\pm 1.6\,\%$	-	$\pm 0.8\,\%$
	p_t	$\pm 2.8\,\%$	-	$\pm 1.0\,\%$
	p_s	$\pm 3.7\,\%$	-	$\pm 1.2\,\%$
FENT [98]	p_t	-	$\pm 1.9\,\%$	-
	T_t	-	$\pm 2.5\,\%$	-
	Δs	-	$\pm 2.8\,\%$	-

mass flow, as well as the cavity pressure, was found to be negligible. The expanded uncertainty level ($k = 2$) for the comparative total-to-total efficiency ($\Delta\eta_{tt}$) of two measurements was evaluated to be $\pm 0.32\,\%$ points. This value held under the circumstance when the same probe with the same calibration file was used. Furthermore, the contribution of the discharge coefficient on the turbine main mass flow uncertainty calculation could be excluded.
Repeatability measurements were conducted to gain additional confidence in the measured performance levels. Throughout the tested turbine configurations, the integral values of the total-to-total stage efficiency remained within a range of $\pm 0.07\,\%$ points. The repeated measurements were typically carried out 10 to 20 measurement days after the original one.

2.6.3. Temperature-Based Turbine Efficiency

The temperature-based turbine efficiency was used to determine performance levels for the rotor blade tip study. Due to the rainbow rotor design, the differential efficiency levels could be determined during the same test run. Nevertheless, since the total temperature drop across the turbine section was relatively small (about 30 K), the use of a temperature-based efficiency increased the uncertainty in the performance levels compared to a torque-based definition. However, determining the performance during the same test run

Table 2.10.: Standard uncertainties of the torque-based total-to-total stage efficiency related input quantities as detailed by Schuepbach [173]

Input quantity		Standard uncertainty	Contribution
Rotational speed	ω	$\pm 0.06\,\mathrm{rad/s}$	1.1 %
Torque	M	$\pm 0.866\,\mathrm{Nm}$	17.0 %
Main mass flow	$\dot{m}_{main}$	$\pm 0.013\,\mathrm{kg/s}$	29.6 %
Bypass mass flow	$\dot{m}_{bypass}$	± 0.0009 kg/s	0.0 %
Drum leakage mass flow	$\dot{m}_{drum}$	± 0.0003 kg/s	0.0 %
Inlet total temperature	$T_{t,in}$	$\pm 0.1\,\mathrm{K}$	2.4 %
Inlet total pressure	$p_{t,in}$	$\pm 18.4\,\mathrm{Pa}$	4.0 %
Exit total pressure (5HP)	p_t	$\pm 45\,\mathrm{Pa}$	45.8 %
Cavity total pressure	$p_{t,cavity}$	$\pm 25\,\mathrm{Pa}$	0.0 %

facilitated a reduction in the comparative uncertainty levels to a certain degree. The main contributors to the temperature-based efficiency uncertainty were the local total temperature and total pressure measurements provided by the FENT probe. Since the efficiency levels were mainly investigated in a time-averaged manner, the uncertainty of the fluctuating component was not included in the uncertainty analysis. Mansour [98] determined the expanded uncertainty ($k = 2$) of the time-averaged total temperature to be 0.27 % of the local flow temperature for a Mach number condition of M=0.3 and 0.16 % for M=0.5, respectively. These values resulted in a relatively large absolute uncertainty in the efficiency levels. For the rotor blade tip study, the comparative uncertainty was of interest, and because the measurements were conducted during the same run, the differential uncertainties could be reduced. Therefore, the following assumptions and approaches were used to provide uncertainty levels. For the comparative efficiency level measurements, the same probe with the same calibration coefficients was used so that the expectation was that the uncertainty induced by the temperature calibration would cancel out. The relative uncertainty of the time-averaged convective heat flow, which was necessary to derive the FENT total temperature (Mansour [98]), was estimated to be 1.6 %, assuming that the local absolute Mach number was not substantially changing between the tip designs. The resulting standard uncertainty of the FENT total temperature measurements was therefore found to be 0.1 K. The standard uncertainty of the FENT total pressure measurements was estimated to be 0.04 % of the local total pressure, excluding the uncertainties of the aerodynamic and static calibration. Additionally, it was assumed that the uncertainty contribution from the turbine inlet total temperature and pressure could be excluded for the comparative efficiency levels as the measure-

ments were conducted during the same test run. The resulting comparative temperature-based efficiency $\Delta\eta_{is}$ uncertainty ($k = 2$) was calculated to be $\pm 0.80\,\%$ points. The contribution of the total temperature uncertainty was evaluated to be 82 % and the total pressure share was accordingly 18 %.

2.6.4. Stator-Sided Hub Cavity Wall Pressure

The unsteady pressure in the hub cavity was captured using a similar chip technology and static calibration methodology as for the FRAP. The calibration covered a pressure range of 600 mbar divided into 13 steps. The expected calibration range for the temperature was set between 40–60°C subdivided into five calibration steps. The resulting calibration polynomials were fifth order in pressure and fourth order in temperature. The quality of the model was characterized by standard deviations for the pressure in the order of 10 Pa and 0.02 K for the temperature. The overall uncertainty for the unsteady pressure was therefore calculated to be $\pm 0.1\,\%$ of the turbine inlet total pressure (typically even around $\pm 0.03\,\%$).

2.6.5. Rotor-Sided Hub Cavity Wall Pressure

The usage of an advanced rotor onboard telemetry system and the associated determination of the pressure levels required a separate measurement uncertainty analysis compared to the stationary measurements. The expected uncertainty of the rotor-sided pressure measurements was provided following the approach suggested by Moffat [117]. Rebholz [151] provided an extensive analysis of the derivation of uncertainty levels for the mean pressure and pressure amplitudes for which the resulting values were applicable to the measurements provided in this work due to similar operation of the measurement setup and comparable turbine operating conditions. As the variables for the current application were not all independent, the approach offered by Moffat [117] was modified to perturb independent and coupled variables iteratively. The overall calculation was therefore perturbed with a $2\,\sigma$ uncertainty of all relevant input quantities. The resulting uncertainties were then calculated as root sum square of all computed values for the mean pressure and the pressure amplitude. The largest contributors to overall measurement uncertainty were identified as the electronics temperature, the centrifugal acceleration under rotation, and the sensor temperature during the offset calibration at turbine standstill conditions [151]. The calculated expected uncertainty levels for mean pressure and pressure amplitude are provided in Table 2.11.

Table 2.11.: Normalized measurement uncertainty ($2\,\sigma$) for the rotor-sided pressure measurements as detailed by Rebholz [151]

	Mean pressure [% $p_{t,in}$]	Pressure amplitude [% $p_{t,in}$]
Absolute	4.5	0.053
Comparative	0.25	0.04

2.6.6. Hub Cavity Heat Transfer Quantities

Considering the calculation procedure of the convective heat transfer quantities (h, T_{ad}) in the Equations 2.6 and 2.8, one can identify analytically the dominating terms for the uncertainty analysis of the time-averaged quantities which are expressed in Equations 2.38 - 2.40.

$$\frac{\partial T_{ad}}{\partial T_w} = 1 + \frac{1}{h\,R_{th}} \tag{2.38}$$

$$\frac{\partial T_{ad}}{\partial T_{bottom}} = -\frac{1}{h\,R_{th}} \tag{2.39}$$

$$\frac{\partial h}{\partial R_{th}} = -\frac{h}{R_{th}} \tag{2.40}$$

These terms underscore the importance of the thermal resistance R_{th} of the insulating substrate of the double-sided Kapton heat flux gauges as a measurement uncertainty contribution. The thermal resistance is the inverse of the k/d. Diverging information can be found in open literature for the thermal conductivity k of the Kapton polyimide. Kapton is a powerful material that offers reliable and robust thermal and mechanical properties to temperatures as high as 360 °C. The specified thermal conductivity for the used Kapton type can be found in the datasheet provided by the manufacturer (DuPont) and amounts to 0.12 W/(m K) [44]. The dimensional tolerance information of the Kapton thickness d is even more difficult to find. Therefore, the most reliable source to get detailed information of the k/d values is from the published work that used Kapton-based heat flux gauges. Epstein et al. [45] used a specifically developed calibration setup and found that the k/d value for 1 mil (25 μm) Kapton is 8'086 W/(m^2 K), which represents a 40 % deviation from the published thermal properties by DuPont. Finally, a systematic work is available (which was provided by the Ohio State Gas Turbine Laboratory [65]) that employed different calibration procedures to elaborate the thermal resistance of different Kapton thicknesses. The resulting values for the k/d value for 2 mil (51 μm) Kapton was found to be 4'333 W/(m^2 K), providing an accuracy of ±5 %.

After having introduced the uncertainty contribution of the insulating substrate material, the measurement accuracy of the gauge temperatures had to be quantified. The uncertainty related to the gauge temperature measurements was mainly provided by the calibration accuracy and the stochastic uncertainty induced by the white noise of the output voltage. As described in the experimental setup section, the double-sided heat flux gauges were calibrated in a temperature-controlled oven with typical temperature stability values below 0.2 °C and a set of highly accurate (±0.05 °C) reference temperature sensors (PT100). The accuracy of a temperature-voltage calibration using a linear regression scheme is given by the uncertainty of the calibration coefficients. Throughout the eleven installed heat flux gauges (corresponding to 22 temperature calibrations), the uncertainty related to the calibration slope a_T varied within 0.05–0.13 %, and for the calibration offset parameter T_0 between 0.02–0.06 %, for a temperature calibration range of 15–75 °C. These values were determined following the procedure documented by Pinilla et al. [141]. The stochastic contribution to the uncertainty induced by white noise was quantified using the relationships for the shot noise and thermal noise presented in the work of Johnson [78], which are specified as follows:

$$\sigma_{shot} = R\sqrt{2\,q\,i\,\Delta f} \tag{2.41}$$

$$\sigma_{thermal} = \sqrt{4\,\kappa_b\,T\,R\,\Delta f} \tag{2.42}$$

In these equations, R represents the gauge resistance, q the electron charge, i the current supplied to the gauge, Δf the maximum frequency bandwidth of the measurement setup, κ_b the Boltzmann's constant, and T the sensor temperature. Applying the correlations to the effective measurements for a typical amplification factor of 64, the calculated white noise levels resulted in a range of 160–185 μV, for a typical sensor output voltage of around 2 V. Having elaborated the input standard uncertainty contributions, the typical expanded uncertainty of the gauge temperature measurements was found to be $\delta T_w = 0.15\,\mathrm{K}$ $(2\,\sigma)$.

As the final determination of the convective heat transfer quantities is computer-based and requires a linear regression, the uncertainty calculation scheme described by Moffat [117] (with successive perturbation of the input uncertainty quantities) was used, which is illustrated in Equations 2.43 and 2.44.

$$\delta h = \sqrt{\left(\frac{\partial h}{\partial T_w}\right)^2 \delta T_w^2 + \left(\frac{\partial h}{\partial T_{bottom}}\right)^2 \delta T_{bottom}^2 + \left(\frac{\partial h}{\partial R_{th}}\right)^2 \delta R_{th}^2 + \ldots} \tag{2.43}$$

$$\delta T_{ad} = \sqrt{\left(\frac{\partial T_{ad}}{\partial T_w}\right)^2 \delta T_w^2 + \left(\frac{\partial T_{ad}}{\partial T_{bottom}}\right)^2 \delta T_{bottom}^2 + \left(\frac{\partial T_{ad}}{\partial R_{th}}\right)^2 \delta R_{th}^2 + \ldots} \quad (2.44)$$

The procedure was performed for all measurements and operating conditions, and the resulting uncertainty levels are depicted with error bars in Chapter 5, for a confidence interval of 95 % ($\pm 2\,\sigma$). For convenience and orientation, the respective relative uncertainty levels for each sensor position and the nominal turbine operating condition are provided in Table 2.12 for the rotor-sided setup. The typical uncertainty ($\pm 2\,\sigma$) for the adiabatic wall temperature was calculated to ± 1.5 K for the nominal operating condition, and typical relative uncertainty levels for the convective heat transfer coefficient were in the order of 10–15 %. The calculated uncertainty levels were subsequently translated into the uncertainty quantification for the adiabatic effectiveness and the Nusselt number, which are presented in Chapter 5.

Table 2.12.: Relative uncertainty levels ($2\,\sigma$) of the rotor-sided hub cavity heat transfer quantities for the nominal turbine operating condition (IR=0.8 %) and each sensor position

Sensor position	$\delta h/h$ [%]	$\delta T_{ad}/T_{ad}$ [%]
R1	11.8	0.39
R2	11.5	0.44
R3	14.4	0.54
R4	10.5	0.49
R5	10.6	0.52

2.7. Unsteady Numerical Modeling

The turbine configurations used to study the unsteady cavity dynamics (Chapter 3) and the novel rim seal design (Chapter 4) were also modeled computationally to provide insights on the flow field regime, which is difficult to access with aerodynamic probes or any other invasive instrumentation type. With the help of numerical tools, the complex interactions and mechanisms in the rim seal and hub cavity space can be qualitatively investigated. The computations were conducted using an in-house developed, explicit unsteady Reynolds-averaged Navier–Stokes (RANS) solver, called MULTI3. The numerical setup of the two considered turbine configurations, as well as the simulations, was generated and performed in the course of two master's theses at the laboratory. Hänni [56] provides detailed information on the unsteady

hub cavity numerical setup, whereas Bagnara [5] details the setup for the purge control feature configuration.

2.7.1. Computational Domain and Boundary Conditions

As the two considered turbine configurations were different in their respective scope, the numerical setups also were generated differently. Therefore, the description of the numerical work within this section is addressed for each setup separately.

Unsteady Hub Cavity Setup A full-annular mesh for the unsteady hub cavity turbine configuration was generated consisting of the first stator and rotor as well as the rotor upstream hub cavity and blade fillets (Figure 2.33 (right)). The main annulus flow path and the hub cavity were meshed via the commercial mesh generator "NUMECA Autogrid 5" and the clustering was locally adapted using the sub-tool "IGG 5". To build up the 360° computational model, a 20° section model was meshed, copied, and rotated 17 times for the remaining 340° of the full annulus. One of these sectors is illustrated in Figure 2.33 (left). The total mesh size of the full-annular model was 36 million nodes, which is judged to be coarse. With a fixed first cell height of 5 μm, the resulting non-dimensional wall distance y^+ presents a general range between 1.1 and 2.3. The main flow path was resolved with 57 radial nodes, whereas 13 were used for the rotor tip gap. Pitch-wise, 85 nodes for two stator or three rotor pitches were chosen. To inject rim seal purge flow, a cavity inlet duct was integrated, which is representative of the measured turbine configuration. The hub cavity was modeled in the stationary frame of reference and was attached to the stator domain.
The turbine inlet boundary conditions were taken from FRAP measurements upstream of the first stator, which were performed with the same turbine configuration. The inlet total pressure and turbulent intensity level profiles were imposed at the turbine inlet. The turbulence level was set to 1 % turbulence intensity. The inlet total temperature was taken constant across the span and was equal to the value shown in Table 2.1. The turbulent length scale at the inlet was assumed to be 5 mm. At the exit of the turbine stage, a radial equilibrium condition was used. For all solid surfaces, no-slip and adiabatic wall boundary conditions were set. The stationary and rotating components were coupled using a sliding interface for the transient rotor-stator interaction. Two simulations for the rim seal purge flow rates IR=0.0 % and IR=0.8 % were performed to better understand the cavity dynamics and the associated flow field.

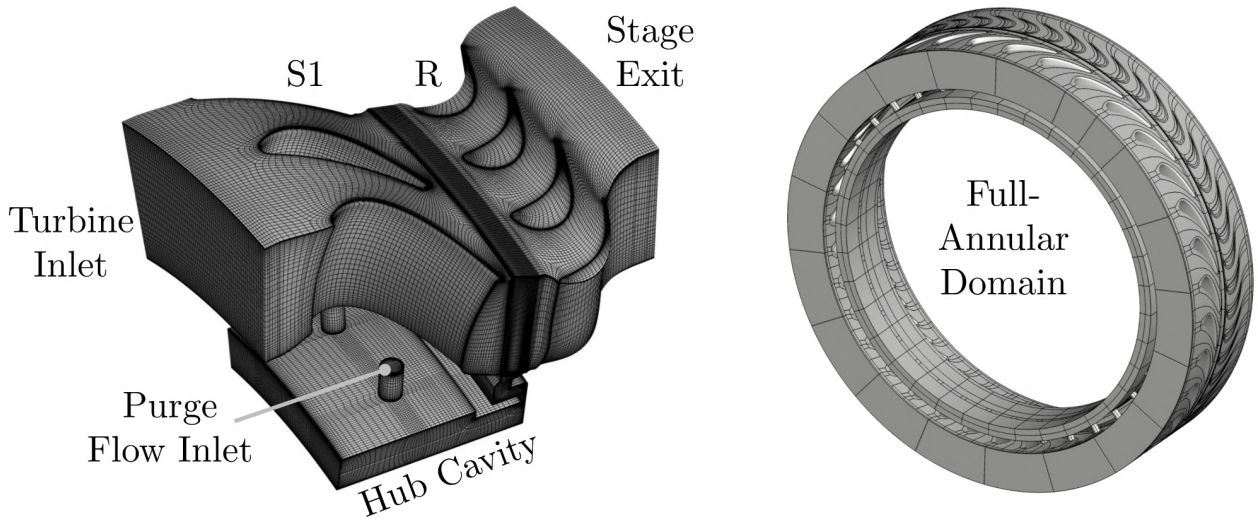

Figure 2.33.: Illustration of the computational domain for the unsteady hub cavity turbine configuration. Representation of the 20° sector model mesh of the full-annular domain (left) and of the 360° domain (right).

Purge Control Features Setup For the purge control feature numerical study, two meshes were generated in order to model the baseline configuration as well as the turbine setup with novel geometrical features integrated. To provide a higher mesh density, a 20° 1.5-stage sector model domain was chosen, which provided a 1:1 pitch ratio and a 2/3/2 blade count ratio. The computational domains (Figure 2.34) included all the geometrical details, such as the rotor up- and downstream hub cavity, the non-axisymmetric end wall contouring of all three blade rows, the purge flow inlet tubes, the baseline rim seal design, and the complex purge control features on the rotor- and stator-side.

The main annulus flow path and the hub cavity again were meshed via the commercial mesh generator "NUMECA Autogrid 5," and the clustering was locally adapted using the sub-tool "IGG 5." The delicate purge control features were meshed using the surface models of the features, which defined their shape in the "IGG 5" mesh generator. The basis of the mesh was given by the baseline rim seal design. Subsequently, the internal grid lines of the baseline mesh were manually moved onto the edges of the imported surface to give constraints to the automatic projection of the original surfaces onto the newly imported ones. Some iterations and adaptation of the local node numbers were required to provide an appropriate mesh quality.

The resulting mesh size of both 1.5-stage 20° sector models was about 17 million nodes. The first wall cell height was fixed to 5 μm which resulted in a general y^+ value range between unity and 2.5. The span-wise direction of the main annulus flow path was mapped with 89 nodes having a hyperbolic distribution toward the end walls. The rotor tip gap was meshed with 21 nodes. The automatic smoothing process of the mesh generator was used to improve the mesh quality. During that process, the first cell height at

the wall was monitored to avoid an unwanted increase due to the smoothing algorithm. The maximum expansion ratio of the generated flow path was 1.2. The turbine inlet boundary conditions were identically set as described for the unsteady hub cavity setup, using FRAP measurement data upstream of the first stator and setting the turbulence length scale to 5 mm. At the exit of the turbine section, a radial equilibrium condition was set such that a total-to-static pressure ratio of $\Pi_{1.5} = 1.65$ was reached. Again, for all solid surfaces, no-slip and adiabatic wall boundary conditions were set. The stationary and rotating components were coupled using a sliding interface for the unsteady rotor-stator interactions. Both numerical setups (baseline and purge control features) were simulated with a rim seal purge flow injection rate of IR=0.8 %.

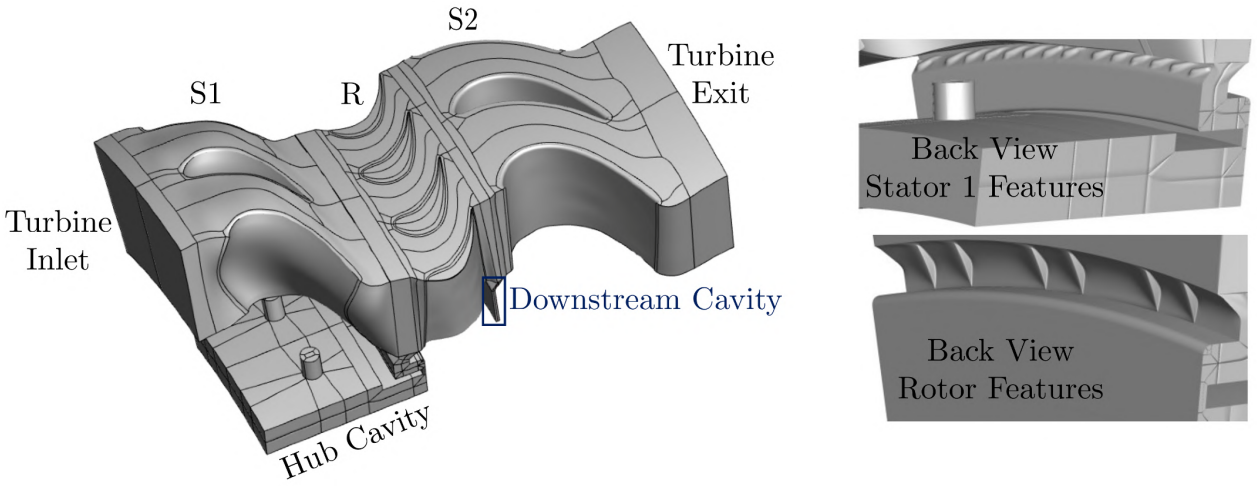

Figure 2.34.: Computational domain for the purge control features turbine configuration. Representation of the 20° sector model domain (left) and back view of the integrated purge control features for the stator- and rotor-sided cavity wall (right).

2.7.2. Numerical Solver – MULTI3

For all presented computational results, the in-house developed solver "MULTI3" was used to solve the unsteady compressible RANS equations. The algorithm used a Ni-Lax-Wendroff [122] approach in the context of the finite-volume method, which was second-order accurate in both time and space. To prevent high-frequency oscillations and capture shock waves (not needed in this study), a JST [74]-type scalar, anisotropic artificial dissipation algorithm was integrated, which is based on a blending of the second- and fourth-order dissipation. The adaptive scaling of the smoothing coefficients accounts for the discrepancy in the local Courant–Friedrichs–Lewy (CFL) numbers in different cell dimensions in the high aspect ratio cells, typically found at the walls. The modeled eddy viscosity was considered in the scaling of the smoothing coefficients. (Basol [6] developed that scheme to reduce the artificial dissipation

in high aspect ratio cells.) For modeling the turbulence, the two-equation Wilcox [192] k–ω turbulence model in its low Reynolds number form was used. To speed up the convergence, a local time-stepping approach was used for steady simulations and dual time-stepping for unsteady simulations. The latest version of the code (running on GPUs) was used for this study. Further information is provided by Basol [6] and Papagiannis [131]. The parallelization approach of the computations was described by Raheem [148].

The computations for the unsteady hub cavity configuration were conducted on the central high-performance cluster "Brutus" of ETH Zurich. Besides the traditional nodes with CPUs, the cluster also featured 18 special nodes with two NVIDIA Fermi C2050 GPUs, which were used for the simulations. As the "Brutus" cluster went out of service, the calculations for the purge control feature numerical setup were performed on the LEC's in-house, high-performance GPU cluster. The cluster contains 12 GPUs, 4 NVIDIA Tesla K40 and 8 NVIDIA Tesla P100. The K40 GPUs have 12 GB memory each, allowing an upper limit close to 11 million nodes per computation in single-GPU simulations. The P100 GPUs have 16 GB memory each, offering an upper limit close to 15.5 million mesh nodes per computation in single-GPU simulations.

The mesh quality and solver stability for the unsteady hub cavity configuration was first conducted by performing unsteady runs for one 20° sector. To achieve a physical hub cavity flow field, a variety of different time step and sub-iterations combinations were tested. More details can be found in the flow field validation, presented in section 3.2. Based on the extensive analysis, 84 time steps and 150 sub-iterations were chosen, which resulted in 1'512 time steps per rotor revolution for the full-annular simulation. Due to the coarse full-annular mesh, a relatively low CFL number of 0.4 was used for the explicit solver. The root-mean-square residuals were found to be in the order of $10^{-4.5}$, whereas the mass flow imbalance was found to be in the order of 10^{-4}. The main flow path was judged to be converged within 0.6 rotor revolutions based on the periodicity of the static-pressure field probed by different monitoring points in the main annulus. The convergence of the hub cavity flow field was found to be much slower than the main flow path such that 4 to 5 rotor revolutions were required to reach a state of convergence. More details are provided in section 3.2.

For the purge control feature setups, the same time-step settings were used as for the unsteady hub cavity, which provided appropriate results in the hub cavity. The sub-iterations were increased to 250 mainly due to the increased mesh density of the numerical setup. The CFL number could be increased to 0.6. The mass flow imbalance between inlet and outlet (excluding the injection of rim seal purge flow in the budgeting) was as low as 10^{-4}; the root-mean-square residuals were comparable to the unsteady hub cavity setup, and therefore in the order of $10^{-4.5}$. Based on the periodicity of the static

pressure in the main annulus, the main flow path was judged to be converged after half a rotor revolution.

2.7.3. Validation of the First Stator and Rotor Exit Flow Field

In this section, the computational data were validated using highly accurate, traversing aerodynamic probe measurements at the inter-stage planes. The quality of the predictions complements the experimental data in this thesis, especially in regions that are difficult to access with intrusive measurement techniques.

Unsteady Hub Cavity Setup The complexity of the unsteady hub cavity flow required a higher level of detail for the validation of the computations and is therefore provided in a separate section in Chapter 3. Unsteady wall-mounted pressure transducers, as well as traversing probe measurements, were used to validate the hub cavity and the main annulus flow field. A detailed assessment of the unsteady parameter settings for the applied explicit solver was addressed, highlighting the importance of appropriate time-step and sub-iteration settings for a physical hub cavity flow field.

Purge Control Features Setup The availability of accurate experimental data on the inter-stage traversing planes offers to provide a valuable judgment of the accuracy of the numerical predictions. A baseline and purge control feature numerical representation is available for the experimentally tested turbine configuration. This section discusses the agreement between the computations and measurements of the first stator exit flow field as well as the rotor exit flow field. The comparison is provided for the purge control feature setup since it is more demanding in terms of meshing due to the integration of the complex features at the rim seal exit.
In Figure 2.35, the time- and circumferentially mass-averaged profiles of the absolute flow yaw angle and normalized total pressure at the exit of the first stator are provided for both experiments and computations. The experimental data were provided by traversing 4HP measurements for one stator pitch and extended into the hub cavity, down to $-20\,\%$ span. The total pressure data were normalized by the turbine inlet total pressure. In general, the absolute flow yaw angle and the normalized absolute total pressure distributions agreed well between simulation and experiment. The dominant flow features were mostly well represented by the computations. The largest deviation within the main annulus was found between the mid-span and $80\,\%$ span, where the span-wise yaw angle and total pressure gradients were not fully captured by the simulation, which provokes a maximum difference in flow yaw angle of

0.6°. Additionally, at this span-wise coordinate range, the simulation tended to overpredict the total pressure deficit by up to 0.7 %. The described flow field region was typically dominated by the tip passage vortices. The radial distribution of both flow quantities inside and at the interface of the hub cavity was well captured by the computations. The most pronounced differences were observed between −10 % down to −20 % span, where the yaw angle was overpredicted in the simulations by 0.7°. The total pressure was overpredicted by as much as 1 %. Nevertheless, the agreement between computations and experiments was judged to be appropriate for the first stator exit flow field, especially considering the complexity of the setup.

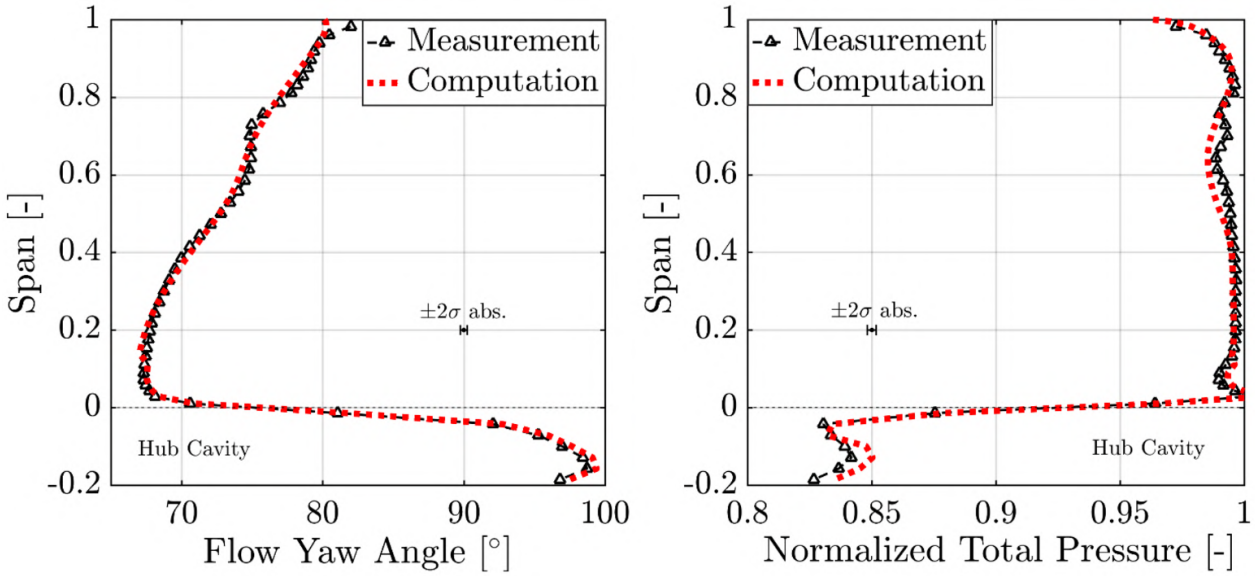

Figure 2.35.: Comparison of the mass- and time-averaged profiles for the absolute flow yaw angle (left) and the normalized total pressure C_{pt} (right) at the exit of the first stator between experiments and computations (purge control feature case, IR=0.8 %)

The validation is supported by the contour diagrams of the time-averaged absolute total pressure at the first stator exit. In Figure 2.36, the spatially resolved total pressure coefficient is presented for both measurements and computations. The data were normalized by the respective turbine inlet total pressure. The deviation within 60 % and 80 % span that was described in the radial profiles becomes more evident if the contour diagrams are considered. Within this span-wise coordinate range, the experimental data showed a loss region formed by two separate flow structures (0.75 stator pitch and 63 % and 77 % span), whereas for the simulation one loss core was observed. The bowed wake was well captured by the computations; however, the wake thickness was moderately overpredicted. The hub secondary flow structure zone at 0.6 stator pitch and 5–10 % span was spatially more compact for the computations. The peak total pressure deficit was, however, at a comparable level.
In addition to the first stator exit flow field, the agreement between computations and experiments was assessed at the exit of the rotor. The measurements

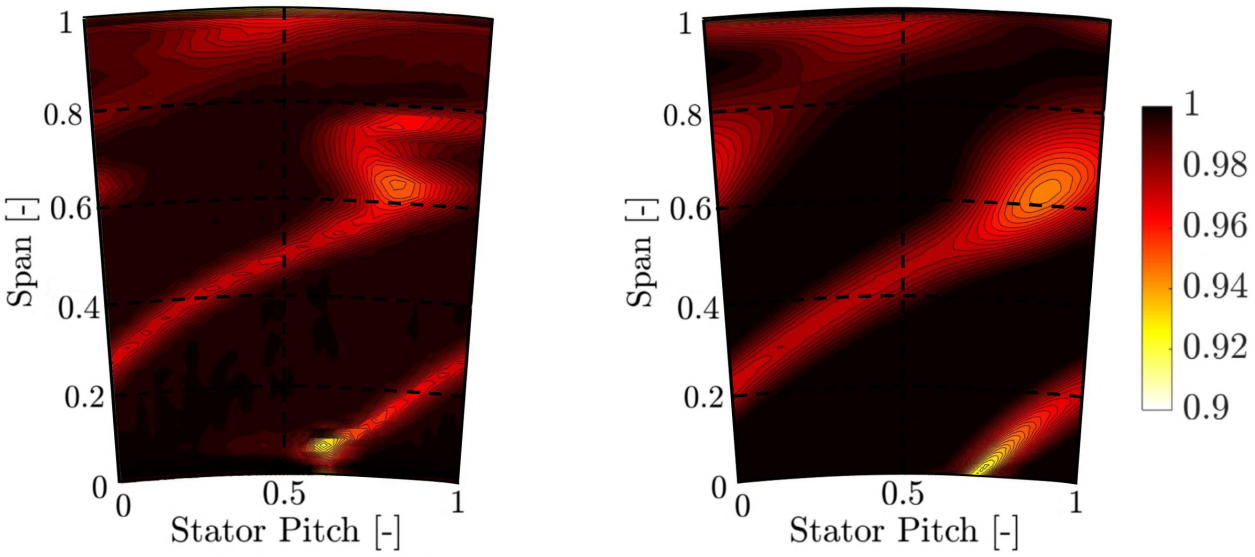

(a) Measurement (4HP) **(b)** Computation

Figure 2.36.: Time-averaged normalized absolute total pressure C_{pt} [-] contours at the exit of the first stator including measurements and computations (IR=0.8 %)

were conducted using the miniature 5HP at the inter-row measurement plane downstream of the rotor. In Figure 2.37, the time- and circumferentially mass-averaged profiles of the flow yaw angle and normalized total pressure are depicted.

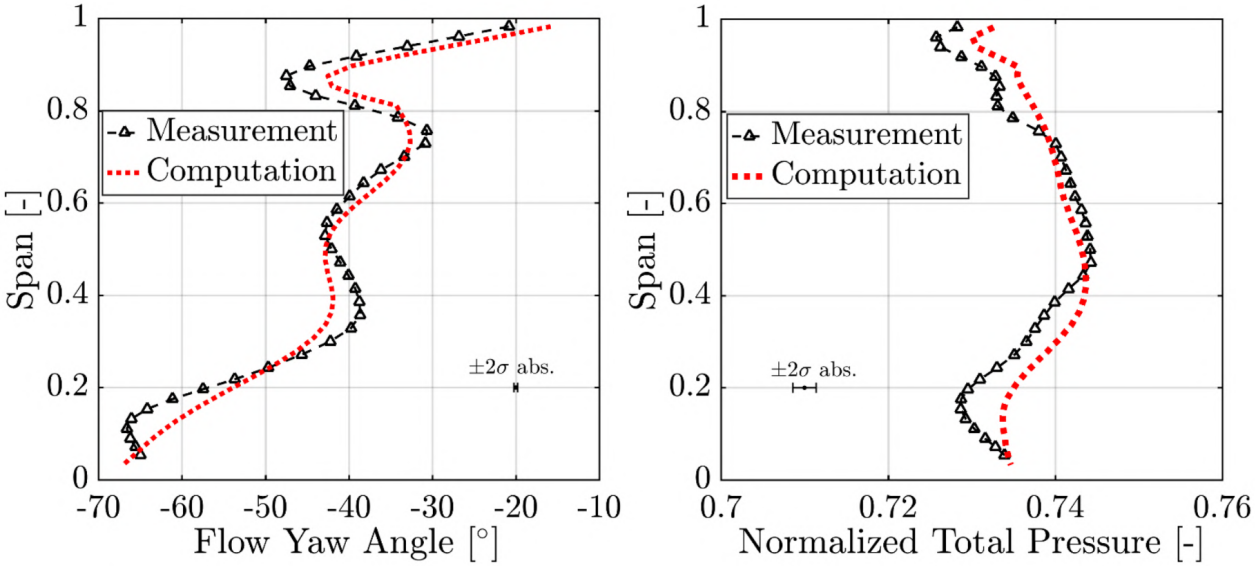

Figure 2.37.: Comparison of the mass- and time-averaged profiles for the absolute flow yaw angle (left) and the normalized total pressure C_{pt} (right) at the exit of the rotor between experiments and computations (purge control feature case, IR=0.8 %)

The yaw angle distribution generally followed the trend of the experiments. Nevertheless, in regions where the rotor secondary flow structures dominated, such as at 10 %, 40 % and 90 % span, the computations cannot follow the strong spatial gradients that were captured by the experiments. The peak deviations

were found close to the hub at 11 % span with 5.5°, at 35 % span with 3.5° and in close vicinity to the tip at 88 % span with 5°. Specifically, in the top 30 % span, the change from under- to over-turning of the flow was not precisely predicted by the computations. At mid-span, acceptable agreement was found with a deviation of 0.3°. The deviation in the flow yaw angle was also reflected in the normalized total pressure distribution. The pressure data were again normalized by the respective turbine inlet total pressure. The discrepancy between computation and experiments was largest at the tip region, where a maximum deviation of 0.5 % was presented. A similar deviation was found at about 13 % span with 0.6 %. The mid-span region again agreed well with the experiments.

In summary, the comparison between experimental data and the computations for the purge control feature configuration show good agreement at the exit of the first stator. The rotor exit computations reveal difficulties in accurately capturing the strong spatial gradients in the flow quantities. The purpose of the provided simulations is primarily to resolve the hub cavity flow field to show the effect of the purge control features and get a qualitative comparison of the ingestion behavior of the configuration. The resulting predicted flow field is therefore taken as a complementary set of data to support the analysis of the experimental results. In Chapter 4, the outcomes of the computations are detailed.

3. Non-Synchronous Flow Excitation in the Rim Seal Space

Rim seals and cavities were shown to bear the potential to establish flow structures that are not driven by the dominant dynamics of the main annulus. The resulting non-synchronous flow perturbations, which are termed as cavity modes, and their impact on the characteristics of a turbine stage are only moderately addressed in open literature and rarely underlined by experimental data. However, in the context of improving the aerothermal performance of rim seals and turbine stages, the understanding of the driving mechanisms is key to advance in the respective fields. In the presented chapter, the non-synchronous flow excitation in the rim seal space is studied by the extensive probing of an angel-wing-type rim seal design using fast-response aerodynamic probes (FRAP), wall-mounted pressure transducers and employing full-annular unsteady Reynolds-averaged Navier–Stokes (RANS) calculations.
In an initial step, the characteristics and implications of the non-synchronous hub cavity modes are investigated for a turbine configuration equipped with an angel-wing-type rim seal, as introduced in section 2.2.1. Time-resolved measurements reveal the existence of low-frequency (below blade passing frequency) excitation; their dependency on the amount of injected rim seal purge flow also is assessed. The impact of the induced pressure oscillations on the acoustic field of the rim seal space is experimentally quantified, and their downstream convection through the turbine is investigated using traversing fast-response probe measurements. An extensive numerical analysis is provided in the last section of the chapter. Full-annular unsteady RANS calculations for the considered rim seal design were employed to complement the experimental work and provide more evidence on the essence of the hub cavity modes, also under consideration of varying rim seal purge flow rates. In that context, the limitations and accuracy of full-annular computations in resolving hub cavity structures are elaborated and compared to sector model calculations. The unsteady calculations are furthermore used to give a first quantification of potential additional hot gas ingestion into the rim seal cavity induced by the presence of non-synchronous, large-scale cavity modes.
This chapter aims to enlarge the knowledge of the non-synchronous flow excitation in hub cavities and tries to elaborate on the potential detrimental effects of such modes on the characteristic aerothermal design quantities.

3.1. Characteristics of Low-Frequency Hub Cavity Modes

Several studies in open literature report on the presence of complex large-scale flow structures that form in cavities. Especially in rotor-stator cavities for turbines, these modes are characterized by a low-frequency content in the pressure spectral analysis, which is typically below the rotor blade passing frequency (f_{RBPF}) and not coupled to the rotational speed of the rotor. Very little evidence can be found that relate the impact of injecting rim seal purge flow to the strength of the non-synchronous flow perturbations. Therefore, part of this section addresses the effect of purge flow on the cavity modes for an angel-wing-type rim seal design. Additionally, the implications of such non-synchronous pressure oscillations on the acoustic field in the rim seal space is experimentally quantified.

3.1.1. Purge Flow Effects and Migration of Cavity Modes

For the given angel-wing-type rim seal design, the dynamics within the hub cavity is studied by means of unsteady pressure transducers installed on the stator-sided cavity wall in close vicinity to the interface between the cavity and main annulus flow as well as by employing FRAP measurements. The sensitivity of the cavity flow dynamics to different injection rates of rim seal purge flow is investigated. Note that the temperature ratio between the rim seal purge flow and the main annulus flow is close to unity.

By means of wall-mounted, fast-response pressure transducers installed at $-12\,\%$ span, a pressure spectral analysis inside the hub cavity was performed for four different purge flow injection rates, ranging from IR=0.0 % up to IR=1.2 %. The wall-mounted sensors were used in order to minimize the potential intrusive effects on the cavity dynamics by the presence of instrumentation. Figure 3.1 gives the normalized pressure amplitude for the frequency content up to three times the rotor blade passing frequency f_{RBPF}. The measurement location is schematically introduced by an inset in Figure 3.1 (a). The pressure amplitude is normalized by the respective turbine inlet total pressure. The reader should not be misled by the small numbers of the quantity, even levels around 1 % of the turbine inlet total pressure represent strong oscillations in the pressure field in the order of 1'500 Pa. For all four considered rim seal purge flow injection rate cases, the presence of the rotor blade passing event (f/f_{RBPF}=1) is sensed and shows an increase from the lowest considered rim seal purge mass flow IR=0.0 % to the highest one, IR=1.2 %, by a factor of 2.5. The presence of low-frequency pressure fluctuations below the rotor blade passing frequency can clearly be identified for the injection rates IR=0.0 %

up to the nominal injection rate case IR=0.8 %. This low-frequency content is further on termed as "hub cavity mode." The dominating cavity mode frequency f_{cav} is added to the respective figures. The fact that these modes are not defined by one single peak in the pressure frequency spectrum but by a band of frequencies with elevated amplitudes implies that they are not linked to a geometrically triggered acoustic mode. Furthermore, there is no coupling found between the vane and blade counts that triggers exactly the dominating modes. Two characteristic trends are observed for these three cases.

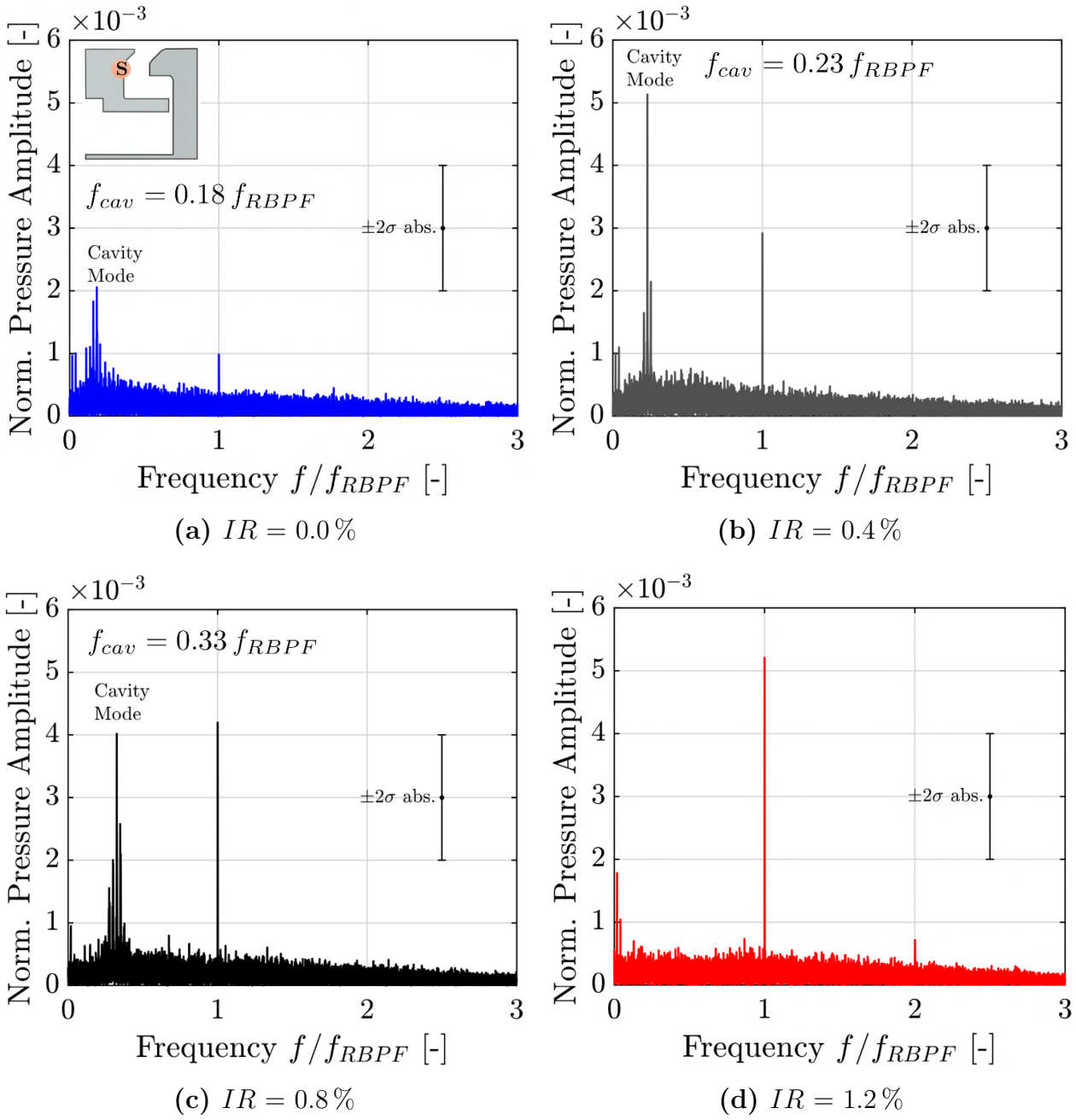

Figure 3.1.: Experimentally determined pressure frequency spectra for different rim seal purge flow injection rates IR inside the hub cavity. Dominating cavity mode frequency f_{cav} is included for three purge flow rates.

First, the band of frequencies with elevated amplitudes is shifted toward higher

frequencies by increasing the purge mass flow. By characterizing these bands by the half-power bandwidth method, the IR=0.0 % case reveals a frequency content between 13–20 % of the rotor blade passing frequency, whereas the IR=0.4 % case shows a shift of the spectrum to 21–26 % of the f_{RBPF}. Furthermore, the IR=0.8 % case is defined by a band of frequencies with elevated amplitudes in the range of 25–38 % of the rotor blade passing frequency. On the other hand, for the high rim seal purge flow case IR=1.2 %, no contribution to the pressure spectrum in the low-frequency range is observed other than the general turbulence levels. The lack of the cavity mode for IR=1.2 % indicates a stabilization effect of pressure fluctuations inside the hub cavity by providing a sufficiently high purge mass flow. In addition, the measurements performed in the range of 0.0 % to 0.8 % injection rate suggest that these modes are driven by a mass flow exchange between hub cavity and main annulus flow, meaning that both local purging and ingestion need to take place in order to trigger theses modes.

A second trend is observed in terms of pressure amplitude which shows that the hub cavity associated fluctuations are dominant with respect to the rotor blade passing amplitude for the two injection rate cases IR=0.0 % and IR=0.4 %. Specifically, the IR=0.4 % case shows a pronounced resonance, which is almost double as high as the measured rotor blade passing-induced pressure fluctuations. By further increasing the rim seal purge flow to IR=0.8 %, the dominance of the cavity mode is weakened and disappears completely when the cavity pressure fluctuation stabilization occurs (IR=1.2 %). This suggests that there is a critical purge mass flow rate at which the cavity mode response is maximized.

Since the performed measurements were limited to distinct locations within the hub cavity, the analysis is complemented by the traversing FRAP measurements in close vicinity to the rim seal exit. This allows for tracking the signature of the non-synchronous modes at various span-wise positions and helps assess the interaction mechanisms with the first stator exit flow field. Of specific interest is the tracing of the flow unsteadiness generated by the purge flow entrainment and mass flow exchange process between the cavity and main annulus flow. Schuepbach et al. [175] have shown that purge flow mixing and migration have a pronounced impact on the local unsteadiness of the flow field. The non-deterministic pressure unsteadiness $p'_{1,rms}$ acquired by FRAP provides an indication of the unsteadiness present in the flow field which is not associated with the blade passing. The extraction of this quantity from the measured pressure signal is detailed in section 2.5.2.1 and formulated in Equation 2.26. To identify regions of high flow unsteadiness, the time-averaged non-deterministic flow unsteadiness is shown in Figure 3.2 for IR=0.8 % and IR=1.2 % up to 30 % span. By comparing the two purge flow injection cases, a clear increase of the unsteadiness level is observed. Especially around 0.5

stator pitch and toward 1 % blade span, the region of purge flow intrusion into the main annulus flow is identified. Furthermore, the injection of additional purge mass flow IR=1.2 % is not only intensifying the local flow unsteadiness but also showing more spreading around the circumference in close vicinity to the hub. Comparing both purge flow rates, the high injection rate case IR=1.2 % shows an up to 40 % higher non-deterministic pressure unsteadiness in close vicinity to the hub compared to the nominal injection rate IR=0.8 %.

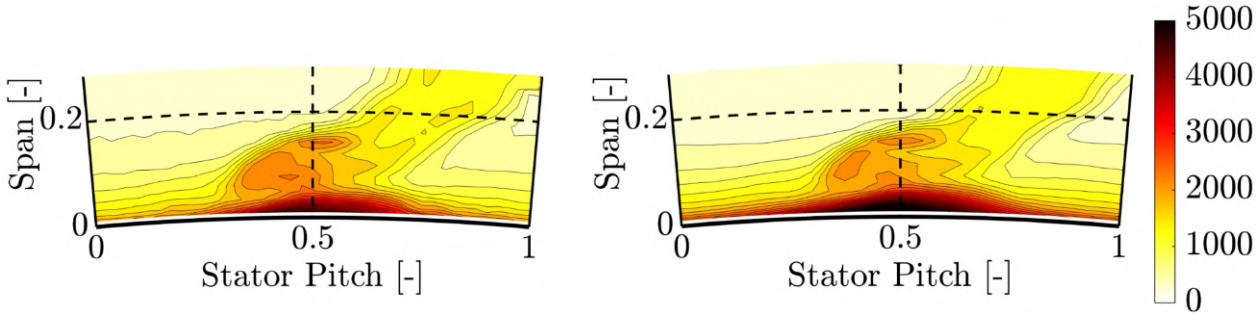

(a) $IR = 0.8\,\%$ **(b)** $IR = 1.2\,\%$

Figure 3.2.: Time-averaged pressure unsteadiness $p'_{1,rms}$ [Pa] in the absolute frame of reference at first stator exit for two purge flow injection rates (FRAP)

Based on the flow unsteadiness levels, the assessment of the migrating signature of the hub cavity modes should be focused on the region around 0.5 stator pitch, where the highest transport of cavity fluid into the main annulus flow takes place. This location is insensitive to the amount of injected rim seal purge flow, which has also been described by Jenny [75]. The author reports that the upstream located stator defines where the purge flow leaves the rim seal hub cavity. In addition to that, both injection rate cases show an increased unsteadiness in the region at 10 % span and 0.4 stator pitch, which is induced by the first stator hub passage vortex and trailing edge shed vortex. The traces of these secondary flow structures are depicted in Figure 3.3 by means of the measured time-averaged axial vorticity for two purge flow rates.

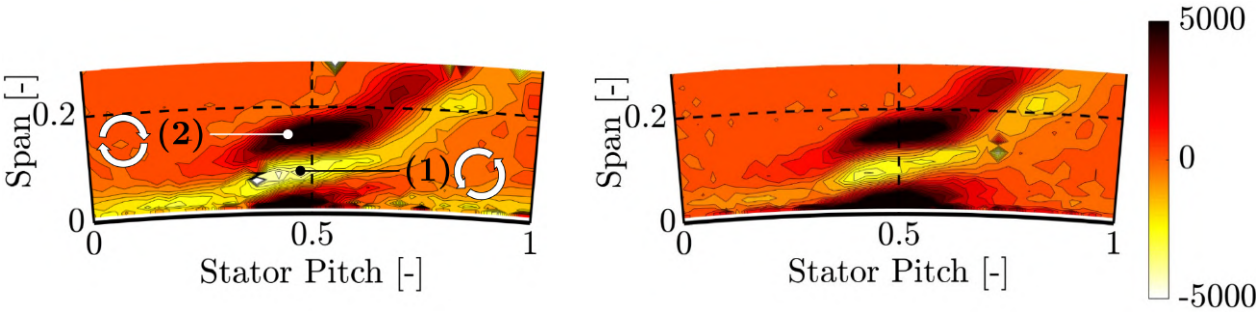

(a) $IR = 0.8\,\%$ **(b)** $IR = 1.2\,\%$

Figure 3.3.: Time-averaged axial vorticity Ω_x [Hz] in the absolute frame of reference at first stator exit for two purge flow injection rates (FRAP)

The stator hub passage vortex is characterized by regions of pronounced negative axial vorticity at around 0.4 stator pitch and 6 % span and is indicated with region **(1)** in Figure 3.3 (a). The trailing edge shed vortex, on the other hand, shows pronounced positive axial vorticity at 0.5 stator pitch and 15 % span (region **(2)**). Remarkably, the region of the purge flow injection from the hub cavity into the main annulus and the circumferential position of the secondary flow structures is aligned radially. This implies that the presence of the first stator hub passage vortex and trailing edge shed vortex benefits the intrusion of the purge flow, most likely due to the static pressure drop provoked by the presence of the secondary flow structures.

Based on the presented measurements, a radial spectral analysis of the flow field was performed starting from −3 % span up to +30 % span using the measured absolute pressure of the FRAP pitch pressure sensor. The circumferential position is kept constant at 0.5 stator pitch where most of the injected rim seal purge flow leaves the hub cavity and penetrates into the main annulus flow. In Figure 3.4, three spectral analysis plots are shown for IR=0.8 % and IR=1.2 %, respectively. The frequency is presented in terms of the rotor blade passing frequency f_{RBPF}, and the pressure amplitude was normalized by the respective turbine inlet total pressure. The Fast Fourier Transformation (FFT) of the measured absolute pressure clearly shows three frequencies with elevated amplitudes for the IR=0.8 % case, wherein two of them are related to the rotor blade passing defined by the first and second harmonic. For all three span-wise positions, the rotor blade passing event (f/f_{RBPF}=1) shows the highest amplitude across the spectrum. However, the band of frequencies with elevated amplitudes in the range of 25–35 % of the rotor blade passing frequency reach up in pressure amplitude to 84 % of the dominant frequency at −3 % span and even 91 % at 10 % span. This frequency content is in the same range as the wall-mounted pressure transducers have shown.
Furthermore, the dominance of rotor blade passing effects is broken up by the presence of the cavity resonances. In other words, the interaction mechanisms for the flow field at the rim seal exit take place at two different characteristic time scales, which are defined by the rotor blade passing period (fast) and the cavity mode induced period (slow). The measurements indicate that the presence of the first stator hub passage vortex and trailing edge shed vortex (region around 10 % span) does not lead to a change of the cavity-induced frequency content but intensifies the strength of the pressure fluctuations.

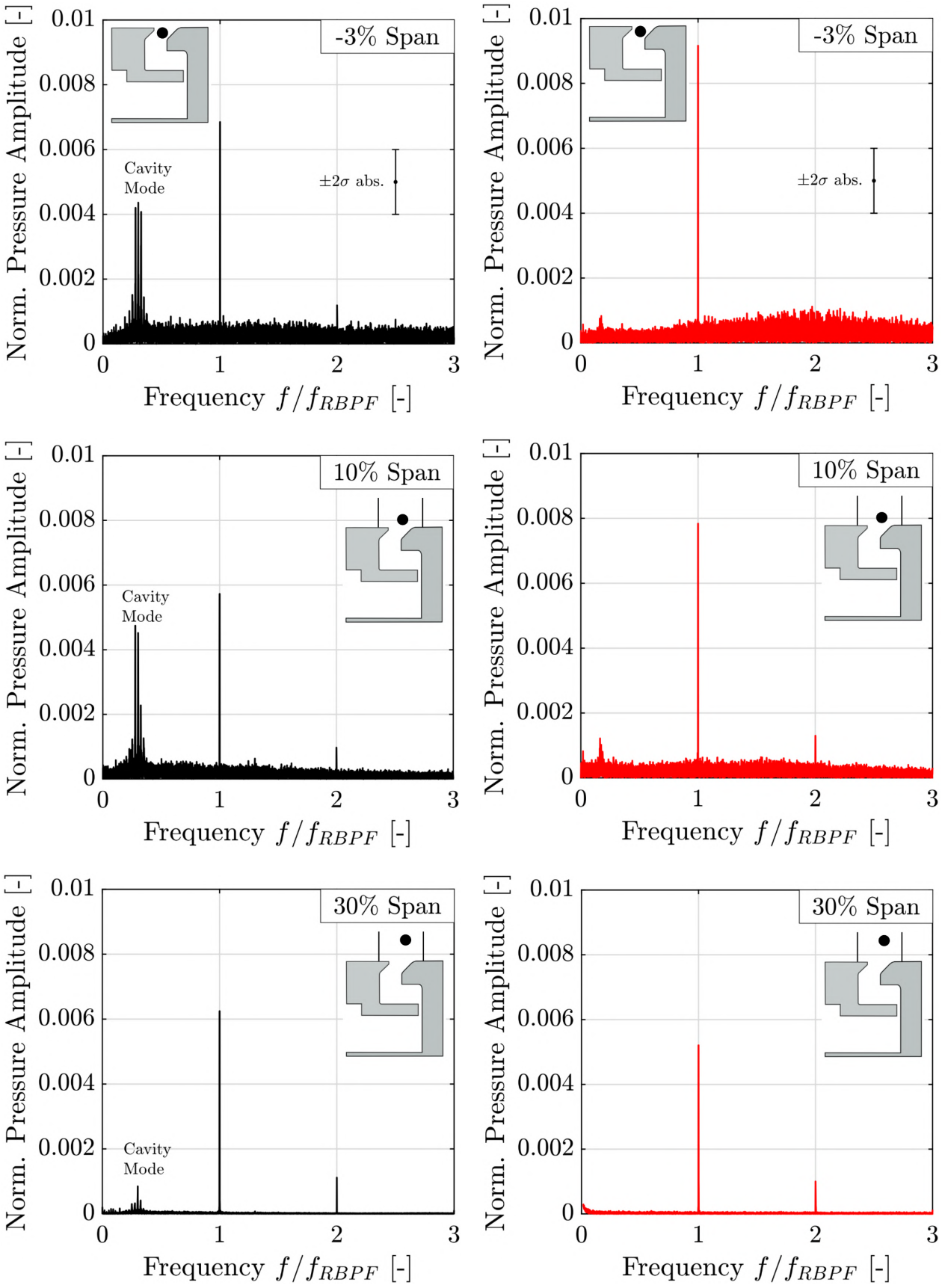

Figure 3.4.: Pressure spectral analysis measured with FRAP at three span-wise positions at 0.5 stator pitch for purge flow injection rate IR=0.8 % (left column) and IR=1.2 % (right column)

After crossing the unsteadiness of the secondary flow structures toward 30 % span, a clear reduction of the pressure amplitude by a factor of 5 peak-to-peak is observed. Still at 30 % blade span, the signature of the hub cavity originated resonances are present and in the same order of magnitude as the second harmonic of the rotor blade passing (f/f_{RBPF}=2). The IR=1.2 % case in Figure 3.4 reveals that the cavity induced pressure fluctuations are significantly reduced compared to the previous case. Considering the low frequency range at −3 % span, a moderate signature of a cavity mode is suspected in the range of 14–20 % of the rotor blade passing frequency.
In this frequency band, the presence of the secondary flow structures is again enhancing the strength of the pressure fluctuations and not shifting the frequencies. However, the level of the pressure fluctuations defined by the cavity modes is by a factor of 4 lower than for the IR=0.8 % case. The signature of the cavity mode has completely vanished at 30 % blade span. Together with the results provided by the wall-mounted pressure transducers at −12 % span, the presented data underline the phenomena of stabilization of the pressure fluctuations inside the hub cavity by increasing the purge mass flow to IR=1.2 %.
To complement the investigation of the migration of the cavity mode signature, a high spatial resolution pressure spectral analysis based on the FRAP measurements is performed. A Fast Fourier Transformation of the measured pressure signal at each point of the measurement grid is performed when the FRAP yaw pressure tap is aligned with the mean flow direction. Out of the processed data, the peak pressure amplitude of the frequency band, limited to 25–35 % of the rotor blade passing frequency, is extracted for the IR=0.8 % case. Unfortunately, fast-response measurements at the first stator exit are only available for the nominal and high purge flow rate operating point. In Figure 3.5, the resulting contour diagram is presented. The figure depicts the normalized peak pressure amplitude of the hub cavity mode around the hub portion at the first stator exit. The pressure data were normalized by the respective turbine inlet total pressure. The most pronounced levels of the cavity mode induced pressure amplitude are found around 0.5 stator pitch within 0 % to about 20 % span. Considering the findings of the non-deterministic pressure unsteadiness in Figure 3.2 and the axial vorticity in Figure 3.3, the highest values of the peak pressure amplitude are sensed in the region where the first stator secondary flows are present. This implies that the cavity mode response is enhanced by the presence of the first stator secondary flows.
This section shows the existence of non-synchronous, low-frequency flow excitation within the rim seal space. These hub cavity modes are characterized by a dependency on the amount of injected rim seal purge flow, both in pressure amplitude and frequency content. The strength of the non-synchronous modes can exceed the typical dominance of the blade passing. High purge flow

rates (IR=1.2 %) are found to be beneficial to eliminate these modes. The signature of the modes is found to radially migrate in the main annulus flow and show a detectable interaction with the upstream stator hub secondary flows. This potential to interact with the main flow underscores that if such cavity dynamics are modeled numerically, the computational domain should include the blade rows to accurately predict the hub cavity response. More information on the computational aspects can be found in section 3.2.

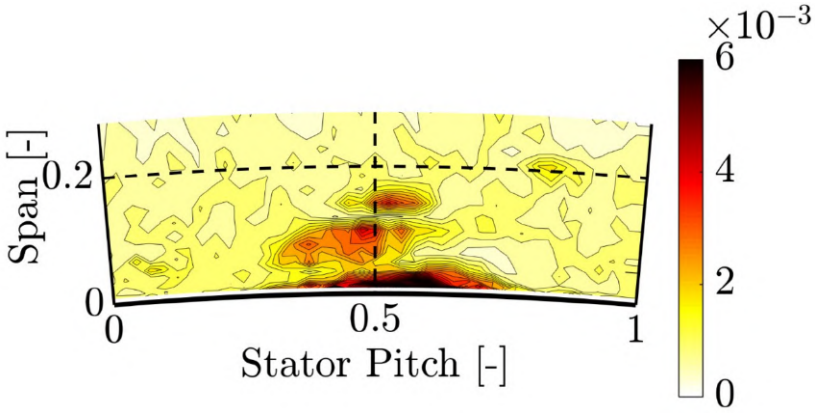

Figure 3.5.: Experimentally determined normalized peak pressure amplitude [-] of the hub cavity mode at first stator exit for the purge flow injection rate IR=0.8 % (FRAP)

3.1.2. Downstream Propagation and Aeroacoustic Implications of Hub Cavity Modes

A strong dependency of the hub cavity induced modes on the injected purge mass flow was identified relative to frequency content and pressure amplitude. Regarding the acoustic characteristics, these cavity modes are within the human perception of sound (frequency range 13–35 % of rotor blade passing frequency). The modulation of the amplitude of the cavity mode pressure fluctuations provoked by the different purge flow rates is transferred into a change in the acoustic field. To translate this change in pressure amplitude into an aeroacoustic consideration, the peak pressure intensity change of the different cavity modes in relation to the high purge flow injection rate case (IR=1.2 %) is determined. The incremental increase of the peak pressure intensity is presented in Figure 3.6. The reader should be aware that these levels are related to the measurements inside the hub cavity (at source).
The presence of the cavity modes has a significant impact on the noise level with an increase up to 18 dB for IR=0.4 % compared to the operating point IR=1.2 %. Even in the absence of purge flow, an increase of the noise level of 11 dB was found. Given the presented measurements, the order of magnitude in the local noise reduction that is achieved by suppressing the cavity modes is substantial. Nevertheless, an acoustic investigation typically

asks for an assessment of the propagation of such modes throughout the turbine. Accordingly, the measurements inside the hub cavity should be complemented by downstream measurements (e.g., at rotor exit).

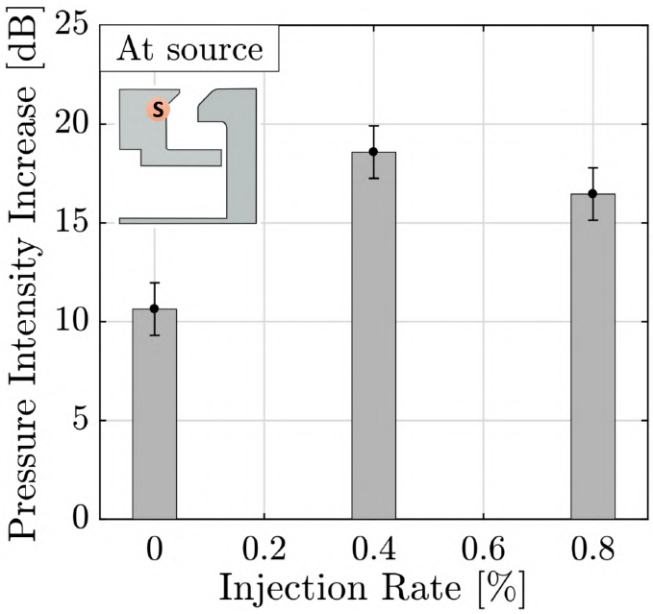

Figure 3.6.: Measured pressure intensity increase inside the hub cavity (at source) induced by the hub cavity modes relative to the high rim seal purge flow case (IR=1.2 %)

In Figure 3.7, a highly spatially resolved pressure spectral analysis is presented at the rotor exit measurement plane for different rim seal purge flow injection rates. The pressure amplitudes are determined similarly to the first stator exit flow field. Within the respective frequency band that was detected at the rim seal exit region (Figure 3.1), the peak pressure amplitudes are extracted for each measurement point and normalized by the respective turbine inlet total pressure. The contour diagrams for different purge flow rates reveal the presence of the cavity mode signature within the bottom 40 % blade span. Specifically, for the IR=0.4 % and IR=0.8 % case, regions of elevated pressure amplitudes can be detected, which are pitch-wise spread. The highest levels of the pressure amplitude are found for all three cases at around 0.5 stator pitch where distinct zones are formed within 20 % to 40 % span. Comparing the overall levels with the magnitude of the pressure amplitudes in the rim seal space suggests that the signature of the cavity modes is weakened for the considered frequency range by at least a factor of 2 peak-to-peak. The trend of circumferential spreading of the high-pressure amplitude zones in Figure 3.7 might be associated with the passing of the rotor. To relate the presence of the elevated pressure amplitudes at the specific locations, the rotor exit flow field needs to be visualized in more detail.

In Figure 3.8, the normalized relative total pressure at the rotor exit in the rotor relative frame of reference for two purge flow rates is depicted. As the signature of the hub cavity modes is most pronounced for the IR=0.4 % and

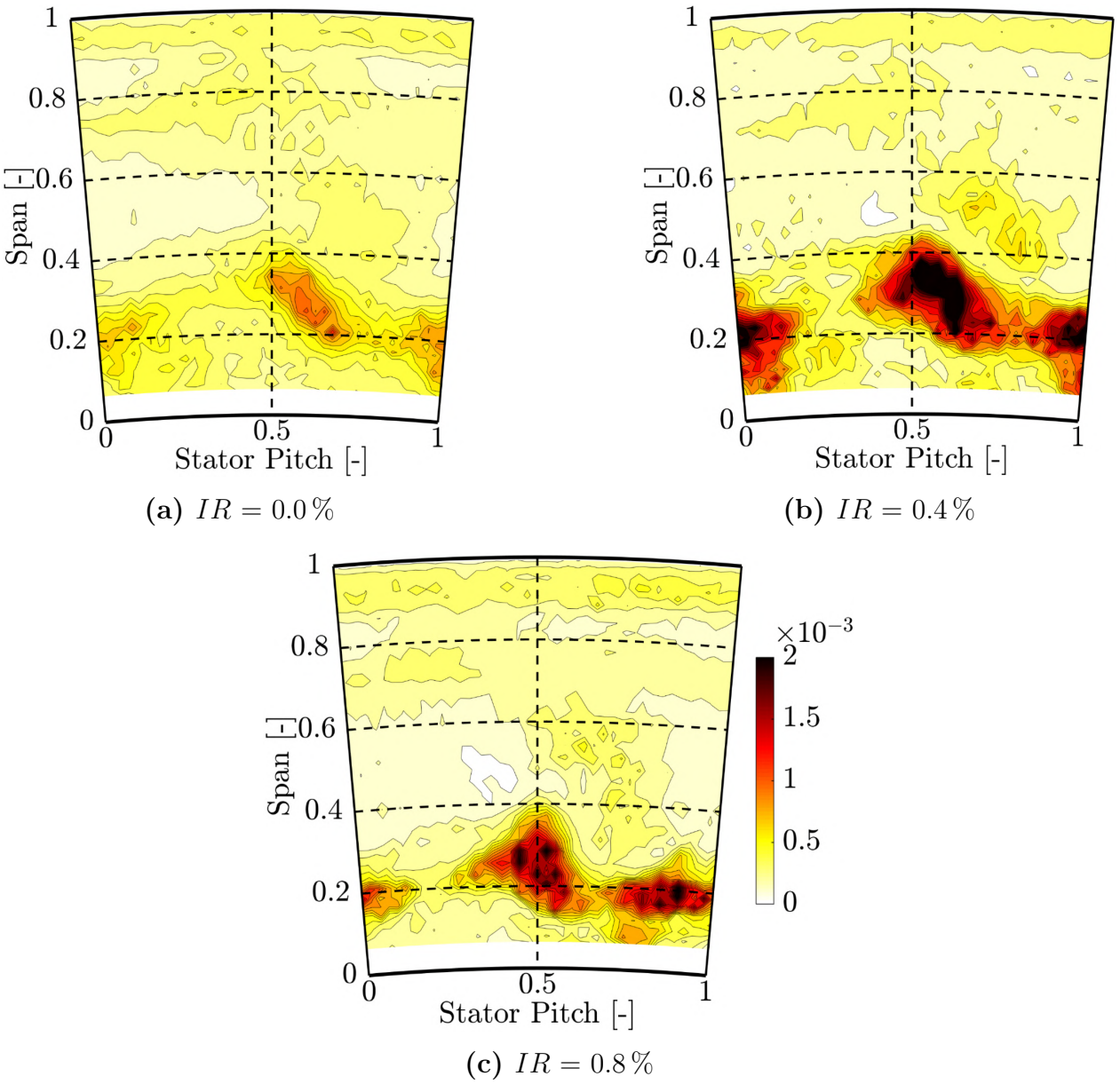

(a) $IR = 0.0\,\%$ **(b)** $IR = 0.4\,\%$

(c) $IR = 0.8\,\%$

Figure 3.7.: Experimentally determined normalized peak pressure amplitude [-] of the hub cavity modes at rotor exit for different purge flow rates (FRAP)

IR=0.8 % case downstream of the rotor, the two injection rates were chosen for the flow field illustration. The pressure data were normalized by the turbine inlet total pressure. The contour diagrams show three pronounced regions with lower relative total pressure, which indicate potential losses associated with the rotor flow structures. The low relative total pressure zone labeled with **(1)** is attributed to the rotor hub secondary flow structures (hub passage and hub trailing edge shed vortex). The region indicated by **(2)** shows the signature of the tip passage and tip trailing edge shed vortex whereas the relative total pressure loss in zone **(3)** is associated with the tip leakage vortex. The pronounced footprint of the hub secondary flows between 20 % to 40 % span encourages the analysis of the time-resolved behavior of these flow structures, especially in the context of the elevated pressure amplitudes of the

cavity modes at this span-wise coordinates (Figure 3.7).

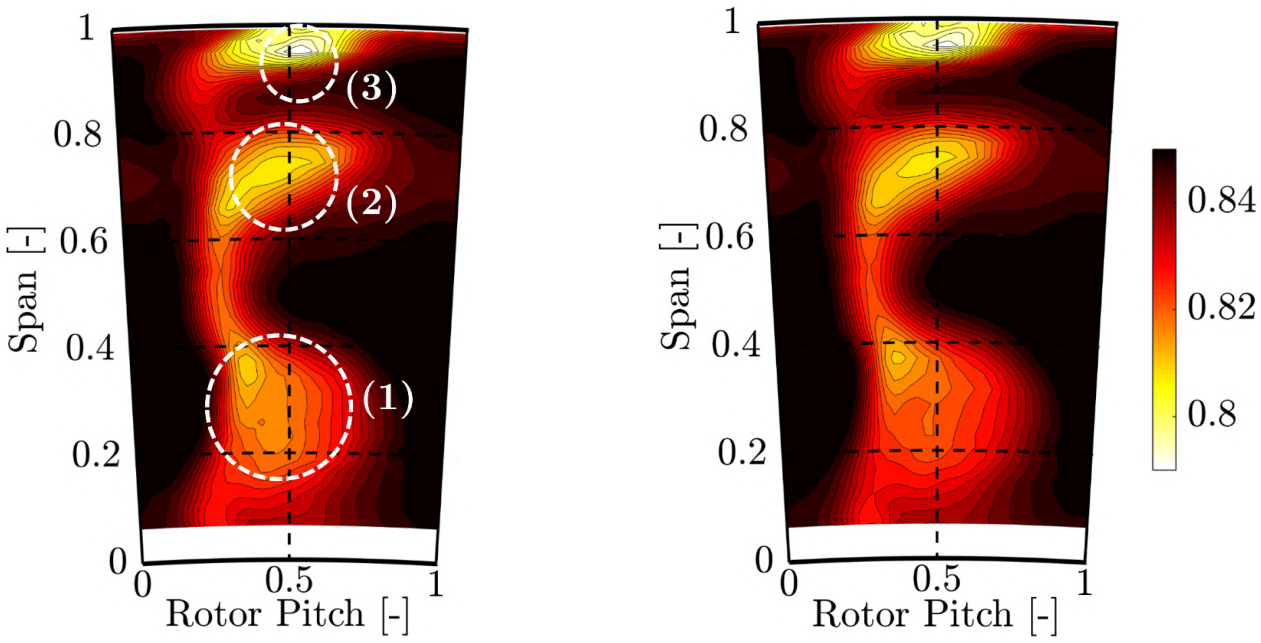

(a) $IR = 0.4\,\%$ **(b)** $IR = 0.8\,\%$

Figure 3.8.: Time-averaged normalized relative total pressure $C_{pt,rel}$ [-] at rotor exit in the rotor relative frame of reference for two purge flow injection rates (FRAP)

To track the dynamics of the rotor hub secondary flow structures, the time-resolved measurements of the non-deterministic unsteadiness at the rotor exit for the rim seal purge flow injection rate IR=0.4 % is considered. Figures 3.9 (a) - (f) present the time series of the pressure unsteadiness within one blade passing event. The time scale is expressed as a fraction of the rotor blade passing period T. The secondary flow system, introduced in Figure 3.8, is found in the time-resolved measurements and represented by high-pressure unsteadiness (black dashed line in Figure 3.9 (a)). Pronounced non-deterministic pressure unsteadiness can be found within the first 40 % blade span for all time instants, which is attributed to the passing of the rotor hub secondary flows. As the rotor passes, the signature of the rotor flow structures is modulated. The hub vortex system migrates radially in- and outward, meaning that a pitch-wise variation of the radial position is observed. The augmented passage area also varies with time, which goes along with an intensification of the vortex strength. This behavior is detected when comparing Figure 3.9 (c) with the contour diagram presented in Figure 3.9 (e). Clearly, a strong modulation of the vortex system in time is detected. Reconsidering the pressure amplitude of the hub cavity modes at rotor exit (Figure 3.7), the most pronounced levels are found around 0.5 stator pitch and within 20–40 % span.

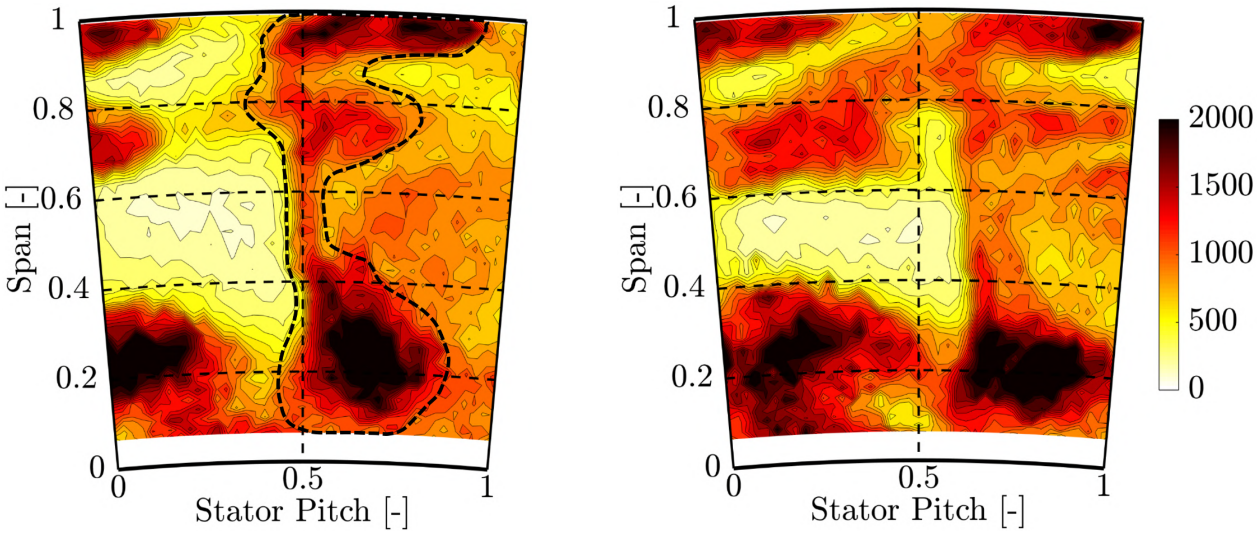

(a) $t/T = 0$ **(b)** $t/T = 0.20$

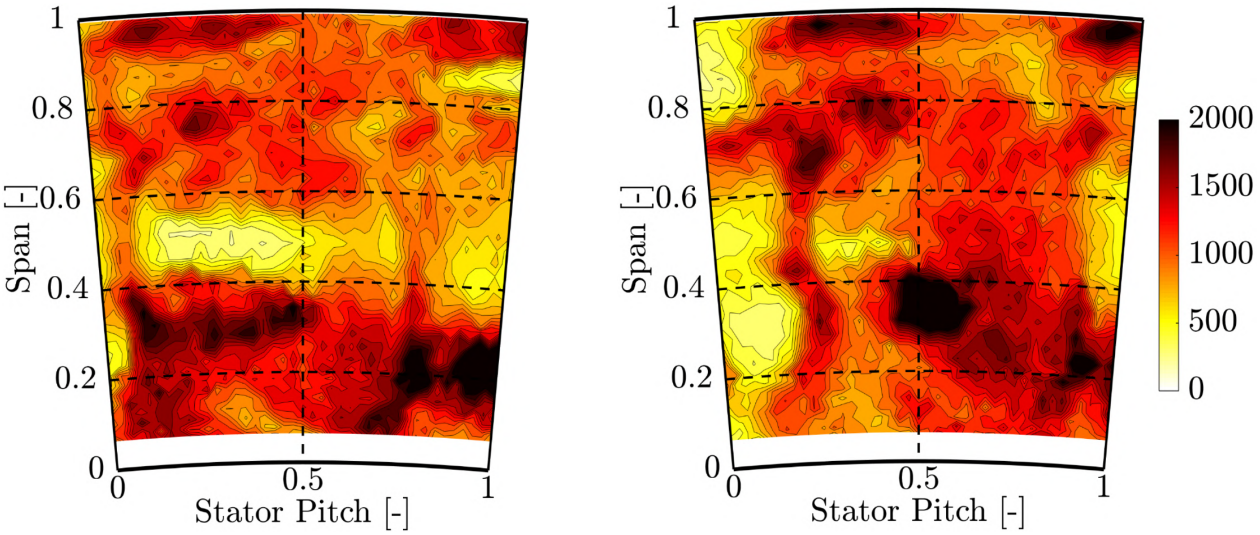

(c) $t/T = 0.40$ **(d)** $t/T = 0.60$

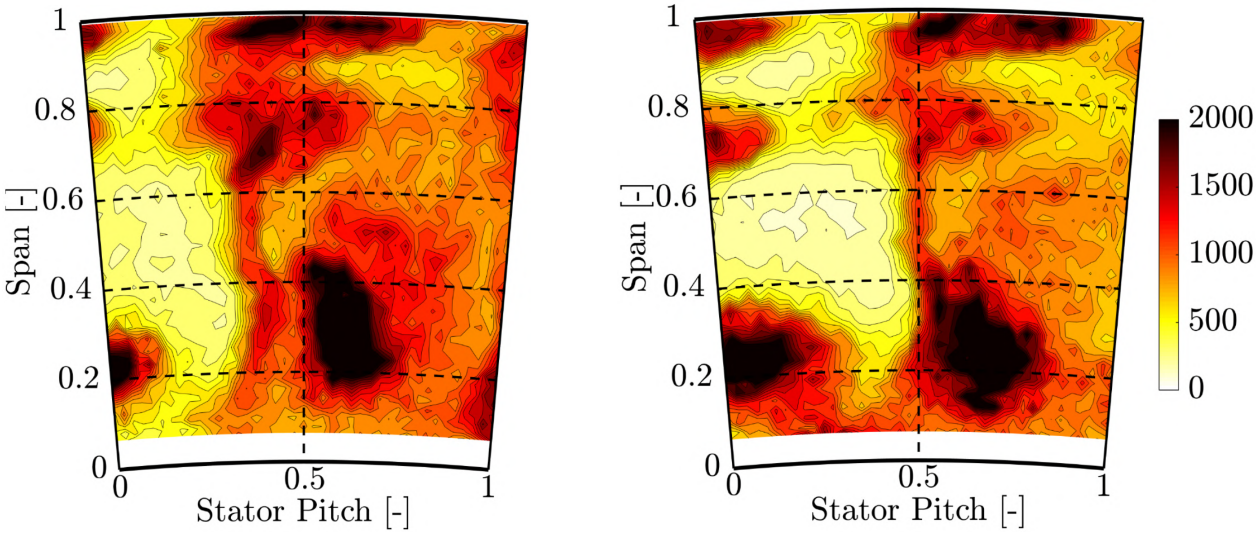

(e) $t/T = 0.80$ **(f)** $t/T = 1.00$

Figure 3.9.: Time series of the non-deterministic pressure unsteadiness $p'_{1,rms}$ [Pa] at rotor exit in the absolute frame of reference for IR=0.4 % (FRAP)

The dynamics of the non-deterministic pressure unsteadiness suggests that the increase in cavity mode pressure amplitude at that location is correlated to the intensification of the rotor hub secondary flows in time. This, in turn, would mean that the time-resolved behavior of the rotor hub secondary flow is affected by the presence of the hub cavity modes. One potential explanation might be associated with the interaction of the hub cavity response with the first stator hub secondary flows as indicated in Figure 3.5. As the first stator hub secondary flows are bent (or chopped) around the rotor leading edge, a pressure and suction side limb of the vortex is formed [8, 24]. Chaluvadi et al. [25] found that the pressure-side limb merges with the forming rotor hub passage vortex within the rotor passage. Therefore, the cavity mode interaction with the first stator hub secondary flows and the consecutive merging of that vortex system with the rotor hub passage vortex could be interpreted as the downstream propagation mechanism that leads to the detectable pressure oscillation at the exit of the rotor.
To complement the propagation analysis of the hub cavity modes, the investigation needs to be supported by the pressure spectral analysis at the second stator exit. The flow field at the exit of the second stator is visualized in Figure 3.10 using the time-averaged normalized absolute total pressure for the nominal purge flow injection rate IR=0.8 %. The contour diagram reveals that the total pressure is reduced, specifically around 0.6 stator pitch and around 60 % span. This total pressure loss zone is typically associated with the tip passage vortex of the second stator.

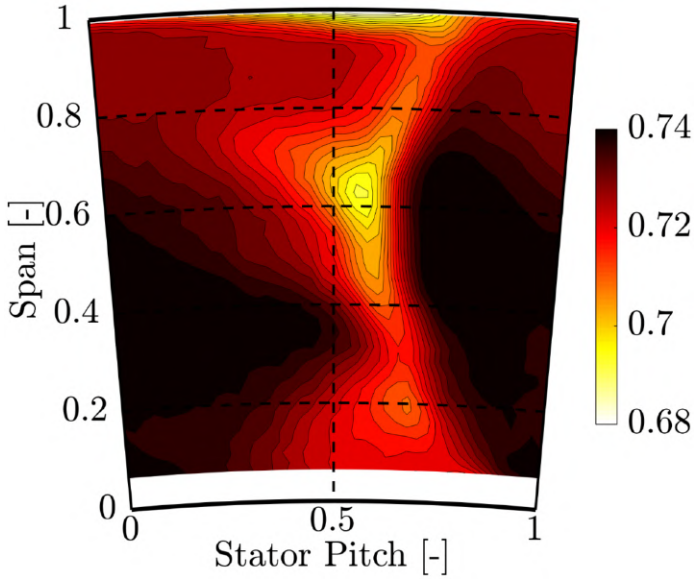

Figure 3.10.: Time-averaged normalized absolute total pressure C_{pt} [-] at second stator exit for IR=0.8 % (FRAP)

However, Rebholz et al. [152] and Jenny [75] suggested that the rotor tip secondary flows (tip leakage and tip passage vortices) are able to migrate radially downward throughout the stator passage and affect the total pressure

levels around mid-span of the second stator exit. The second stator hub passage vortex provokes the region of lower total pressure at 0.7 stator pitch and 20 % span. Similar to the tip passage region, the hub loss region also is affected by the rotor hub secondary flows, which merge within the second stator passage with the forming hub passage vortex [75]. In summary, the exit of the second stator is characterized by the presence of its own secondary flows but is additionally affected by the upstream rotor flow structures.
To check for the presence of the cavity mode signature, again, a spatially resolved pressure spectral analysis is performed at the second stator exit. In Figure 3.11 (a), the normalized pressure amplitude of the cavity mode for the nominal purge flow injection rate IR=0.8 % is depicted. Considering the overall levels of the pressure amplitude, one can observe that the magnitude clearly dropped, by a factor of 3.4 peak-to-peak, compared to the amplitudes found inside the hub cavity. Throughout the rotor and the second stator, the signature of the cavity modes is attenuated. Nevertheless, the presence of the cavity mode at the second stator exit is still detectable and most pronounced at 0.6 stator pitch and 40 % span (dashed circle in Figure 3.11 (a)). As mentioned before, this region can be associated with the migrating hub passage vortices (including the one from the rotor). Figure 3.11 (b) provides the pressure spectral analysis in one single measurement point at 0.6 stator pitch and 40 % where the highest amplitude of the cavity mode signature is measured. The frequency spectrum confirms the existence of the cavity mode at the second stator exit within the frequency range previously found inside the hub cavity (25–35 % of the rotor blade passing frequency).

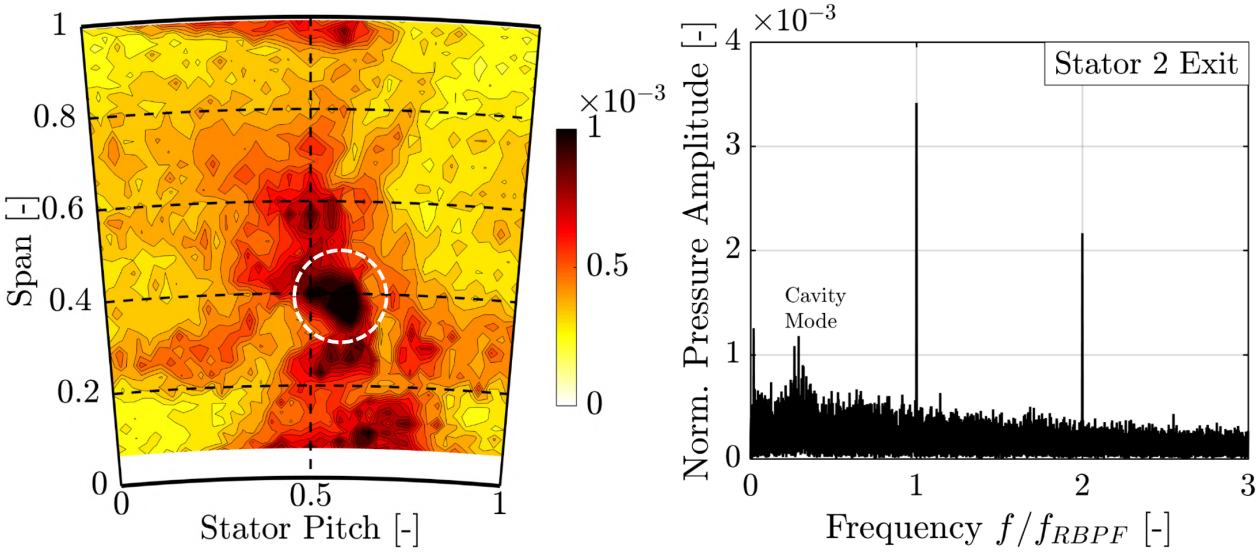

(a) Pressure Amplitude Cavity Mode **(b)** Amplitude Spectrum

Figure 3.11.: Measured normalized pressure amplitude [-] of the cavity mode and pressure amplitude spectrum at second stator exit (0.6 stator pitch, 60 % span) for IR=0.8 % (FRAP)

Since the pressure fluctuations induced by the cavity modes are still detectable at the exit of the turbine, it is worth to quantify the fluctuation intensity change within the cavity mode frequency band with respect to the high purge flow case (IR=1.2 %) where the cavity modes are eliminated. In Figure 3.12, the span-wise evolution of the peak pressure intensity changes within the frequency band of 25–35 % of the rotor blade passing frequency is presented.

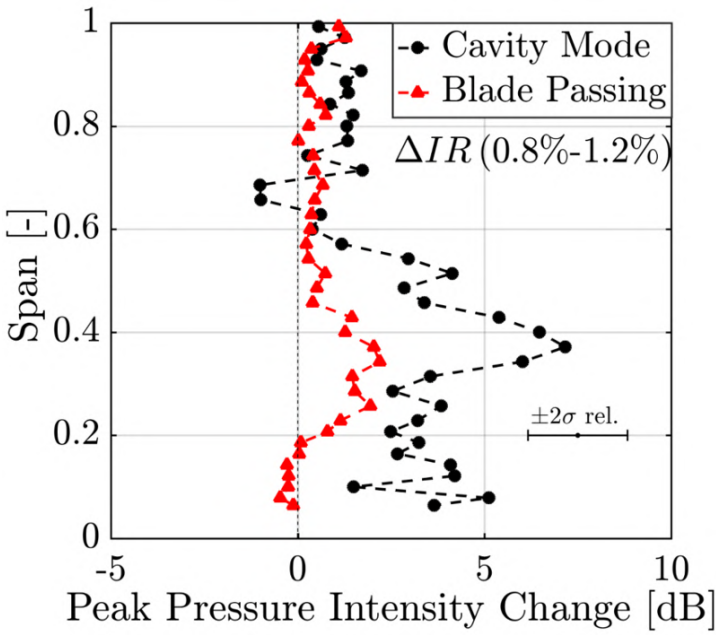

Figure 3.12.: Span-wise peak pressure intensity change of the IR=0.8 % case (cavity modes) relative to the IR=1.2 % case (no cavity modes) at second stator exit (FRAP)

The peak pressure intensity change distribution for the cavity mode reveals that the most pronounced changes are measured at around 40 % span which coincides with the presented contour diagram in Figure 3.11 (a). An increase of up to 7 dB is detected for the IR=0.8 % case which shows cavity modes contribution. Even close to the hub, a higher fluctuation intensity in the order of 5 dB is present. The tip region only shows a moderate change in the specified frequency range. In order to compare these detected changes induced by the cavity modes, Figure 3.12 includes the span-wise evolution of the tonal peak pressure intensity change due to the rotor blade passing. The distribution shows a relatively moderate change in the blade passing pressure amplitude (maximum +2 dB) for the IR=0.8 % case relative to the IR=1.2 % case. Nevertheless, the blade passing-induced pressure oscillations are overall the dominating contribution to the noise level at the turbine exit. The low-frequency pressure fluctuations show some contribution to the acoustic field, especially on a relative basis.

In this section, an extensive investigation of the propagation of the non-synchronous pressure fluctuations induced by the hub cavity modes is presented. The aeroacoustic consideration has shown that the cavity modes provide a significant contribution to the acoustic field around the rim seal space by up

to 18 dB. The signature of the cavity modes is found to propagate throughout the rotor and second stator passage and anticipated to be driven by the hub secondary flow convection. The propagation of these modes is found to go along with a substantial attenuation throughout the blade row passages. Nevertheless, the pressure intensity changes induced by the cavity modes at the turbine exit suggest that they should be budgeted in the acoustic design of the turbine.

3.2. Prediction of Hub Cavity Non-Synchronous Modes

In the design process of state-of-the-art gas turbines, the integration of computational fluid dynamics (CFD) brings in great potential for the performance optimization of turbine components. Compared to an experimental assessment, the cost associated with computational work is significantly less, and the accessibility to different flow field regions that are hard to reach is enabled. On the other hand, the complexity of the Navier–Stokes equations typically requires a simplification of the computational problem for the simulation domain, turbulence modeling, and many more aspects. The need for experimental validation is still enormous, specifically for delicate flow regimes, as the designer still has to face the trade-off between prediction accuracy and computational cost.
The substantial increase in computational power in recent years enabled the design process of turbomachinery components by using three- and four-dimensional RANS solvers. Such solvers facilitate the integration of complex three-dimensional geometrical features, such as advanced blade geometries, non-axisymmetric end wall profiling as well as tip geometries and rim seals. Experimentally confirmed examples were recently given by Jenny et al. [76] and Regina et al. [155]. The findings in computational research of recent years suggest that it is ever-more important to include unsteady numerical modeling in the design phase, even for integral quantities such as efficiency. The presence of different flow field regimes in a turbine and the associated flow dynamics, require time-resolved computations. In the previous sections, the presence of specific low-frequency, non-synchronous flow perturbations was discussed, which ask for unsteady modeling of hub cavities. This section elaborates the capabilities and limitations of unsteady RANS simulations to predict such specific flow perturbations in hub cavities. The major part of the presented results was derived from extensive numerical work in collaboration with Hänni [56] within the framework of a master's thesis at the laboratory. The numerical work was conducted using the in-house developed, unsteady RANS solver MULTI3 for a one-stage full-annular computational domain to increase the chances to resolve the low-frequency, non-synchronous excitation

in the hub cavity. Two injection rates (IR=0.0 % and IR=0.8 %) were chosen as purge flow operating conditions, which both have shown the existence of cavity modes in the experimental data.

3.2.1. Validation of the Inter-Stage Flow Field and Unsteady Solver Parameter Assessment

The comparison of the experimental data and the computational results are provided for the unsteady cavity flow configuration for the nominal turbine operating point and a rim seal purge flow injection rate of IR=0.8 %. Similar agreement between measurements and computations was found for the IR=0.0 % case. As the main purpose of this study is to capture the non-synchronous modes within the rim seal space, the focus of the validation is kept at the first stator exit flow field. In section 2.7, the reader is informed that the number of grid points of the mesh is relatively low (about 36 million mesh nodes for the full-annulus including hub cavity) so some discrepancies between simulations and experiments are expected to occur, especially in flow field regions characterized by high spatial gradients (e.g., secondary flows). The general agreements between the computations and the experiments for the nominal turbine operating conditions are summarized in the time- and circumferentially mass-averaged flow quantities depicted in Figure 3.13. The data were extracted out of the pneumatic four-hole probe (4HP) measurements. The time-averaged flow field data of the computations were extracted after five revolutions and averaged over three blade passing events. The chosen flow quantities are the normalized absolute total pressure and the absolute flow yaw angle at the exit of the first stator. The pressure information is normalized by the respective turbine inlet total pressure. The results show an appropriate match between computations and experiments in most parts of the main annulus flow. The span-wise averaged deviation in the absolute total pressure is 0.2 % of the turbine inlet total pressure. The yaw angle deviation between 20 % and 70 % span is within ±0.5°. The deviation in the absolute total pressure between 20–70 % span is attributed to an overprediction of the total pressure deficit within the first stator wake of around 1.3 % of the inlet total pressure. The peak deviation in the absolute total pressure is found at 20 % span where the total pressure loss is overpredicted on average by about 0.5 % of the inlet total pressure and locally by up to 2 %, respectively. The shape and radial extent of the first stator hub secondary flows are anticipated to cause that difference. Similarly, the larger discrepancies of the absolute flow yaw angle at around 20 % and 80 % span are most likely associated with hub passage and tip passage secondary flow modeling. Especially, the radial gradient in the absolute flow yaw angle from 70–90 % span is underpredicted by the computations.

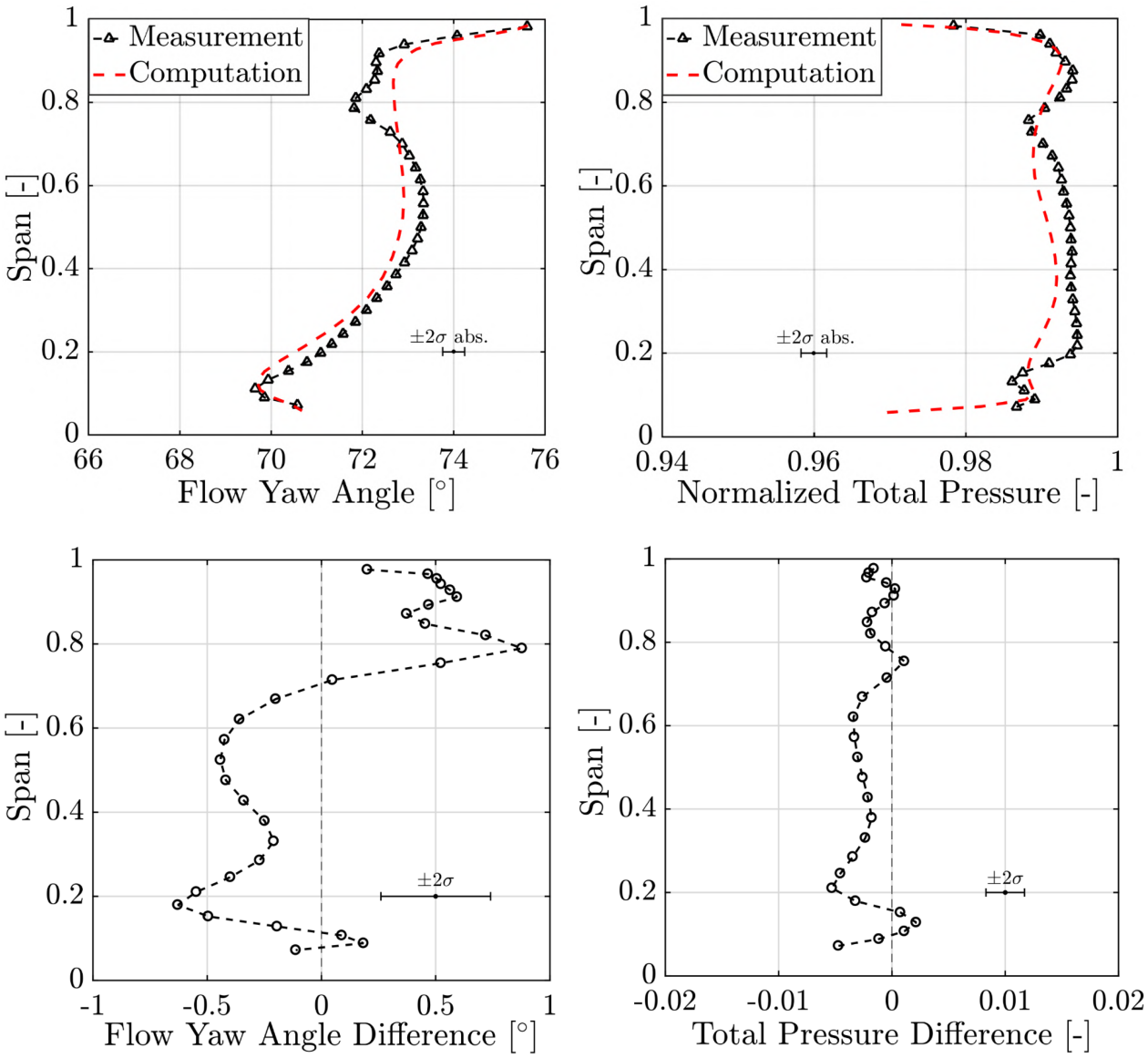

Figure 3.13.: Time- and circumferentially mass-averaged profiles comparison of the flow yaw angle and the normalized absolute total pressure C_{pt} at the exit of the first stator between computation and 4HP measurements (IR=0.8 %); second row includes the absolute differences

The signature of the three-dimensional flow structures, such as the stator passage vortices, is detected by the computations and the probe measurements between 7–20 % span and around 80 % span and is characterized by a pronounced total pressure deficit region as well as by an over- and under-turning behavior of the flow. This is also reflected in Figure 3.14, where the time-averaged contour diagrams of the normalized absolute total pressure at the exit of the first stator are depicted. When comparing both diagrams, it can be noticed that the radial position of the hub secondary flow loss region (1.1 stator pitch and 10 % span for computations) is at a comparable span position for the computations and the experiments, however, the shape is clearly altered compared to the probe data. The experiment presents a more

pitch-wise stretched hub loss region, whereas the simulation reveals a radially extended region. The losses within the hub secondary flow region are locally overpredicted by the computations by up to 3 % of the inlet total pressure. Furthermore, the first stator wake portion around mid-span is enlarged in width by roughly 12 %, contributing to the increased total pressure deficit that has already been registered in Figure 3.13.

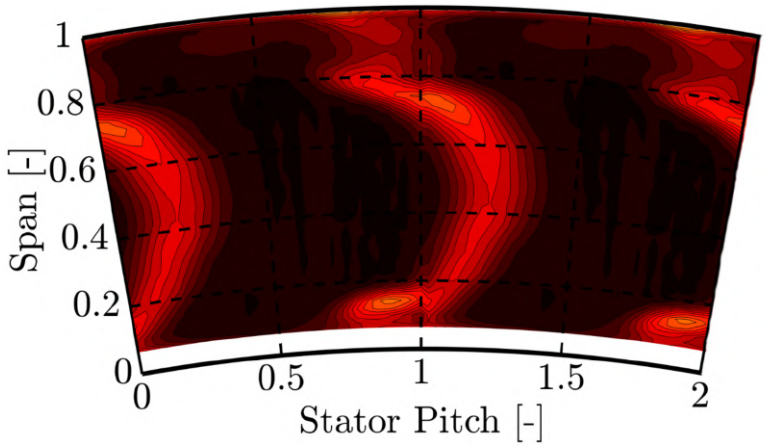

(a) Measurement (4HP)

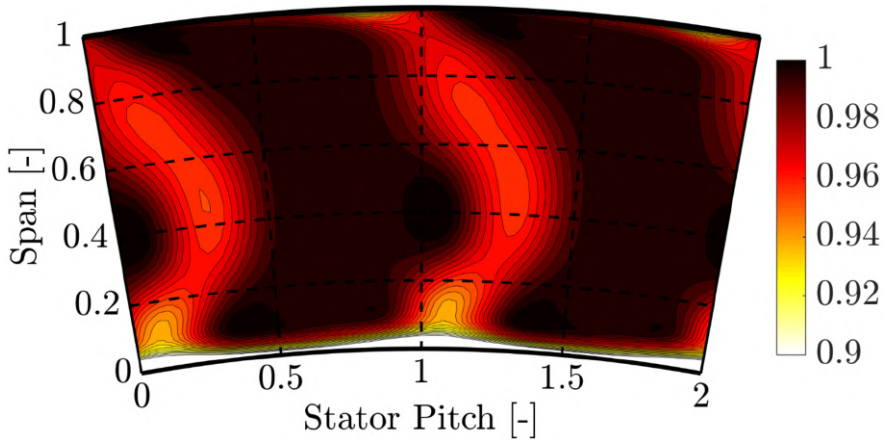

(b) Computation

Figure 3.14.: Time-averaged normalized absolute total pressure C_{pt} [-] contours at the exit of the first stator including measurements and computations (IR=0.8 %)

The strength of the tip passage vortices is underpredicted by the computations: the measurements show a clear loss zone at 1.0 stator pitch and 80 % span, whereas in the prediction, the tip passage region tends to be smoothed out. It is anticipated that the relatively coarse mesh is responsible for more diffusive flow structures. Additionally, Rebholz [151] found that the turbulence parameters at the inlet of the turbine have a significant impact on the evolution of first stator secondary flows and profile losses. In order to improve the agreement between experiments and simulation in this flow region, a parametric study of the turbulence intensity and turbulent length scale would be beneficial. Nevertheless, the agreement is judged to be sufficient to perform a first attempt

at resolving the non-synchronous flow perturbations within the hub cavity. In the course of setting up the full-annular simulations, the flow field was preliminary assessed performing computations for a 20° sector with periodic boundary conditions. The stability of the computations and the physical accuracy was checked in doing so. The analysis of the sector model has revealed that the unsteady solver parameter settings, such as the chosen time steps and sub-iterations, has a strong impact on the results and simulation stability. Specifically, the hub cavity is found to be prone to high static-pressure oscillations induced by certain parameter settings. A first run with 100 time steps and 80 sub-iterations for the sector model ran without crashes but revealed high-frequency pressure fluctuations inside the rim seal hub cavity. The amplitude of these oscillations increased over time, reaching values of up to 60 % of the turbine inlet total pressure, which, in turn, indicates a non-physical behavior of the flow field. In the work of Krebietke [87], a similar dynamic of the static pressure inside the tip shroud cavity of a model low-pressure turbine was reported. The author suspected that the high-frequency static-pressure oscillations have their origin in the numerical setup and consequently increased the sub-iterations and decreased the time steps to damp the unsteadiness. Based on the previous findings, a proper simulation setup required a sensitivity study on the unsteady parameter settings. The computations were set up with time steps varying between 30 and 84 per period (for a 20° sector model). The sub-iterations were varied between 150 and 500. Out of twenty test simulations, eight runs without numerical instabilities and negative pressure incidences occurred. However, some simulations revealed the presence of high-frequency oscillations inside the hub cavity. In Figure 3.15, the normalized static-pressure fluctuations inside the cavity are depicted for two cases, one revealing high-frequency pressure perturbations with substantial amplitudes and another one with a physical stable time series of the static pressure. The stable simulation shows pressure amplitudes in the order of 0.5 % of the turbine inlet total pressure, whereas the unstable one shows amplitudes up to 60 % of the turbine inlet total pressure. The complete analysis revealed that the high-frequency pressure oscillations inside the hub cavity is not limited to one parameter setting but found for various combinations of the chosen time steps and sub-iterations.

The detailed investigation of the flow field in the rim seal space resolved by the computations reveals that the high-frequency perturbations are not provoked by distinct small instabilities coincidentally captured by one of the monitoring points. The whole rim seal flow field is affected by the unstable behavior which is underlined with the contour diagrams provided in Figure 3.16. The figure depicts the normalized total temperature on a radial plane at −18 % span for different unsteady parameter settings. The temperature data are normalized by the respective turbine inlet total temperature. The

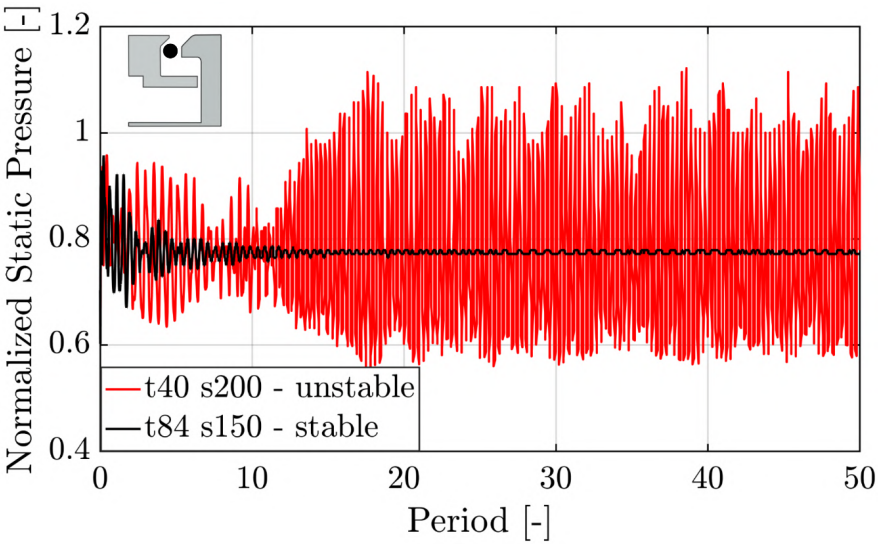

Figure 3.15.: Time series of normalized static pressure inside the hub cavity for two unsteady parameter settings (CFD, modified from [56])

physical unstable computations with 100 time steps and 80 sub-iterations as well as the one with 40 time steps and 200 sub-iterations show strong pitch-wise alterations and gradients of the total temperature inside the hub cavity (Figure 3.16 (a) and (b)). Local total temperature drops up to 40 K are detected, which is judged to be non-physical as there is no work extraction happening in the rim seal and the temperature ratio between the turbine inlet total temperature and the purge flow temperature is close to unity. Contrary to that, the physical and numerical stable simulation with 84 time steps and 150 sub-iterations presents moderate pitch-wise total temperature changes (peak-to-peak 1.3 K) which is illustrated in Figure 3.16 (c).

Based on this study, the physical stability and accuracy of the cavity flow field depend on the time step and sub-iteration settings. Furthermore, the complete set of conducted simulations suggests that for the given hub cavity geometry and associated mesh, a minimum computational effort for reaching numerical and physical stable results requires at least 10'000 iterations per period (20° sector model) or 500 iterations per domain degree. In Figure 3.17 this threshold is indicated. The unsteady parameter setting combination which led to a computational effort above 500 iterations per domain degree provided a physical stable cavity flow field, whereas the settings below the threshold are characterized by non-physical behavior. Finally, 84 time steps and 150 sub-iterations were chosen for the presented computational problem which results in 1'512 time steps per rotor revolution for the full-annular simulation. The advantage of using 84 time steps per 20° domain is that with 85 circumferential mesh nodes, the sliding mesh of the rotor domain is matching with the one of the stators at each time step, which is anticipated to reduce potential interpolation inaccuracies at the rotor-stator interface. With

the chosen time-step settings a sampling frequency of about 68 kHz is achieved, which, in turn, results in a frequency bandwidth of 34 kHz which is sufficient to resolve the expected main annulus and cavity flow dynamics.

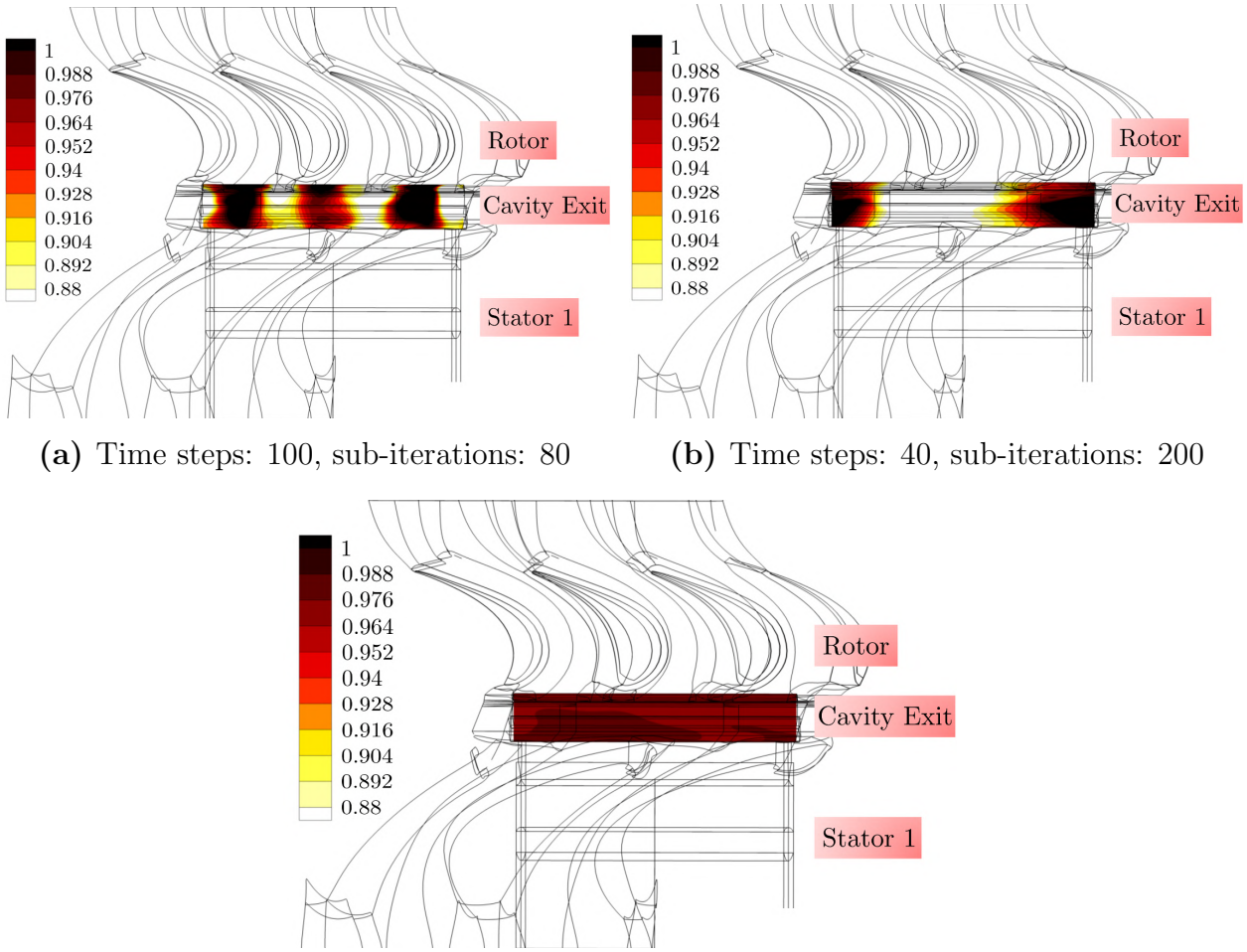

(a) Time steps: 100, sub-iterations: 80

(b) Time steps: 40, sub-iterations: 200

(c) Time steps: 84, sub-iterations: 150

Figure 3.16.: Instantaneous normalized total temperature [-] contours inside the hub cavity on a radial plane at −18 % span for three different unsteady parameter settings (CFD, modified from [56])

In summary, the computational flow field data of the main annulus were validated against the available experimental data extracted from traversing probe measurements. The agreement is judged to be appropriate to continue the analysis within the hub cavity. The unsteady solver parameter settings were systematically elaborated with respect to physical and numerical stability of the results. In the subsequent section, the cavity dynamics resolved by the computations are carefully investigated with a specific focus on the low-frequency flow excitation.

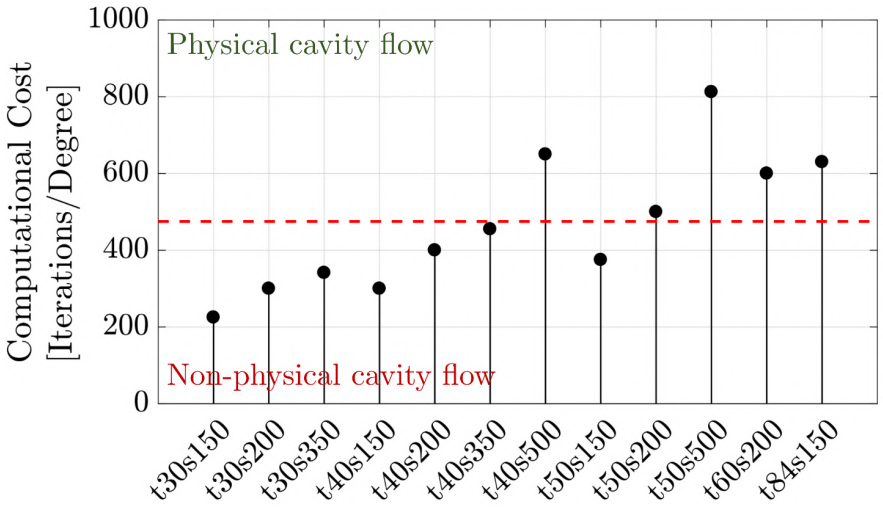

Figure 3.17.: Computational effort requirements for physical stable hub cavity flow field (t: time steps, s: sub-iterations), red line indicates the threshold to prevent high-frequency pressure oscillations inside the cavity (modified from [56])

3.2.2. Prediction of Hub Cavity Flow Excitation

The main purpose of the computational study is to examine the capabilities of the extensive unsteady RANS calculations to resolve the specific dynamics within the rim seal hub cavity and gain knowledge of the nature of the forming flow structures. Different studies, found in open literature, report on the complexity and computational effort in resolving such structures within turbine cavities with numerical tools [73, 189]. It is expected that the size of the simulation domain and the associated boundary conditions play a major role in resolving the specific structures within the rim seal space. Rebholz et al. [151, 153] suspected that the integration of periodic boundary conditions has a high-pass filter effect on the non-synchronous flow perturbations in tip shroud cavities. Based on that, a full-annular computational domain, including the injection of rim seal purge flow, was chosen for the assessment of the low-frequency hub cavity modes.

At first, the evolution of the non-synchronous cavity modes with computational time is investigated. As the cavity flow dynamics seem to be characterized by a slower dynamic than the blade passing period, which was indicated in the experimental part, it is anticipated that the formation of the low-frequency structures needs more computational time. To check for the formation of the cavity modes, the static-pressure data of monitoring points inside the hub cavity are analyzed. A short-time Fast Fourier Transformation is performed for a signal window length of 1'890 time steps corresponding to 1.25 rotor revolutions. Subsequently, the window is shifted by 189 time steps (0.125 rotor revolution). This post-processing approach provides a sufficient frequency resolution. The resulting temporal evolution of the cavity modes is illustrated in Figure 3.18 for two rim seal purge flow injection rates IR=0.0 % and

IR=0.8 %. The contour levels of the plots present the normalized pressure amplitude of the spectral analysis. In agreement with the experiments, the pressure amplitude is normalized by the respective turbine inlet total pressure. The frequency axis is normalized by the rotor blade passing frequency f_{RBPF} and limited to the frequency bandwidth below it. For both rim seal purge flow rates, low-frequency pressure fluctuations are detected inside the hub cavity. For the IR=0.0 % case the elevated pressure amplitudes are registered at around 13 % of the blade passing frequency. The IR=0.8 % simulation shows a broader range of low frequencies with increased pressure amplitudes, but specifically in between 30–39 % of the blade passing frequency.

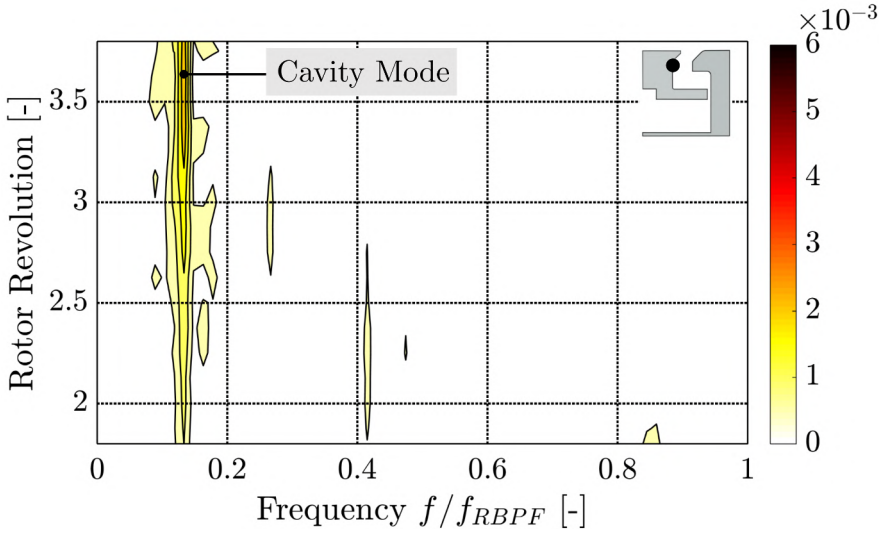

(a) $IR = 0.0\,\%$

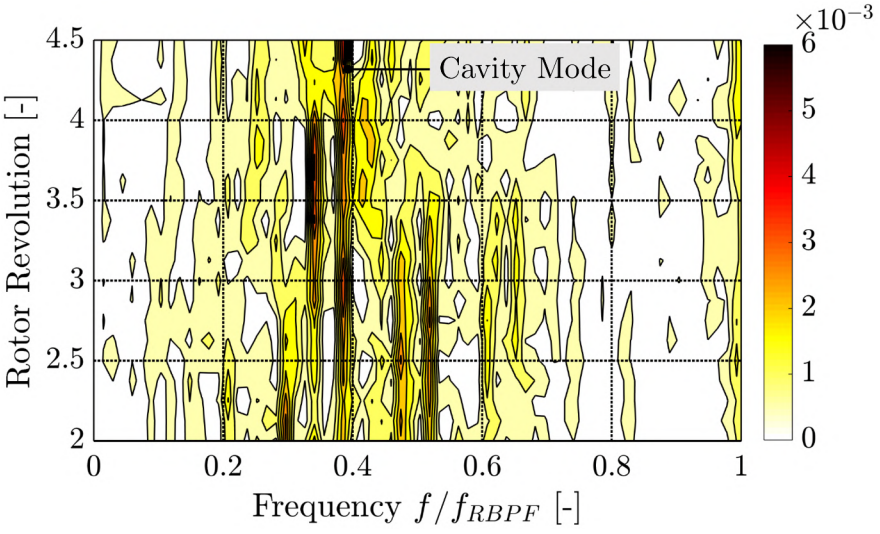

(b) $IR = 0.8\,\%$

Figure 3.18.: Evolution of the normalized pressure amplitude [-] in the frequency domain for two different purge flow rates based on full-annular computations (adapted from [56])

The striking observation, however, of these figures is related to the com-

putational time scale that it takes to establish the non-synchronous flow perturbations. For both injection rates, the typical computational effort is about two rotor revolutions until the frequency content of the modes is clearly visible in the spectral analysis. For comparison, the main annulus flow is found to be typically converged after about half a rotor revolution for the given computational setup. Still, after three rotor revolutions the pressure amplitude of the modes is changing by about 9–13 % (IR=0.8 %). The final convergence state of the low-frequency modes is difficult to assess. Both simulations were run for at least four rotor revolutions. The IR=0.8 % case was even run for five rotor revolutions to assess the convergence behavior. The effective computational time for one rotor revolution of the full-annular is about 80 hours for parallel computing on 18 GPUs. The pressure amplitudes for both cases in the last quarter of a rotor revolution was changing by about 2–3 %. At this state, the computational data within the cavity are further compared to the available experimental data inside the hub cavity.

Figure 3.19 shows the predicted pressure spectral analysis at the representative location of the unsteady pressure transducers (−12 % span) in order to compare the predicted cavity dynamics to the experiments. The presented spectra, as well as all subsequently shown flow quantities, are evaluated after four rotor revolutions for the IR=0.0 % case and after five rotor revolutions for the IR=0.8 %, respectively. The results show that the simulation is able to predict the dominant cavity mode for the IR=0.0 % operating point (Figure 3.19 (a)). The band of frequencies with elevated amplitudes ranging for the IR=0.0 % computations is narrower and ranges between 13–17 % of the blade passing frequency. Also, the simulation provides a band of frequencies with slightly elevated amplitudes between the dominant cavity mode and the rotor blade passing frequency (frequency range around 50 % of the blade passing frequency). The pressure amplitude of the dominant cavity mode is overpredicted by about 13 %, whereas the rotor blade passing related pressure fluctuation is underpredicted by 13 %. The frequency difference between computations and experiments of the dominant frequency is evaluated to be around 55 Hz (note the discrepancy with the second-highest amplitude of the experiments is only 3 Hz).

The predicted pressure frequency spectrum for the IR=0.8 % case (3.19 (b)) also captures the experimentally determined frequency content and the shift toward higher frequencies. The simulation shows that the cavity mode is shifted to a frequency band in the range of 21–46% of the rotor blade passing frequency. Therefore, the simulation predicts a broader range of frequencies in the presence of rim seal purge flow compared to the experiments. The dominant cavity mode pressure amplitude is overpredicted by 15 %, whereas the rotor blade passing related pressure amplitude is underpredicted by 33 %. The frequency discrepancies between the predicted dominant cavity mode fre-

quency and pressure sensor data are about 43 Hz. Considering the complexity of the problem, the agreement is judged to be appropriate, and the results encourage the statement that the full-annular unsteady RANS computations are able to capture the main dynamics of the hub cavity in the presence of the non-synchronous modes and rim seal purge flow.

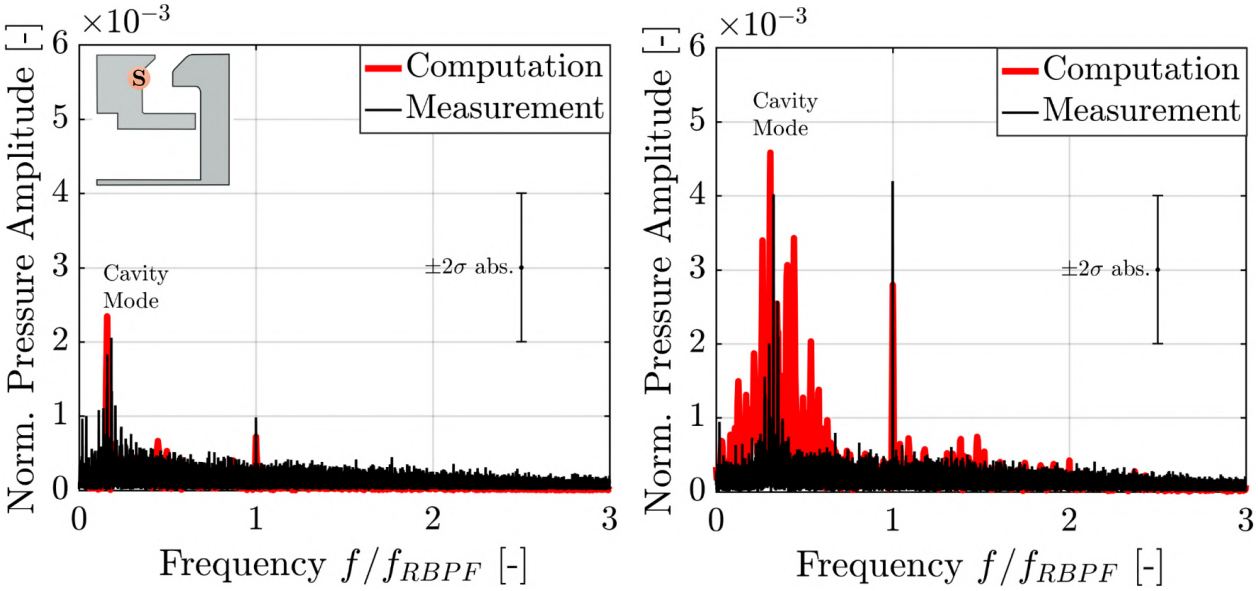

Figure 3.19.: Computationally (full-annular CFD) and experimentally determined pressure frequency spectra for two different rim seal purge flow injection rates inside the hub cavity

The further question that arises is whether the significant computational effort of a multi-revolution full-annular unsteady RANS calculation is justified. Therefore, the spectral analysis of a 20° sector model (1:1 pitch ratio) is performed after the simulation was run for 4 rotor revolutions. As the full-annular simulation mesh is constructed out of 18 sector model each containing 20°, the mesh for the sector model used for this comparison is identical to the 360° domain. The inlet and outlet boundary conditions are the same as for the full-annular simulation as well as the chosen time steps and sub-iterations per domain size. The rim seal purge flow rate is chosen to be IR=0.8 %. The resulting pressure spectral analysis inside the hub cavity is shown in Figure 3.20 for a sample monitoring point. Compared to the experiments, the low-frequency band below blade passing is only moderately excited for the sector model computations. A peak pressure amplitude is found at around 18 % of the rotor blade passing period. No distinct elevated pressure amplitude is found in the range of the experimentally determined pressure excitation. It is suspected that the excited frequency content in the sector model simulation is related to a propagating pressure instability induced by the periodic boundary conditions that force a weak pressure wave to build up within the sector

that has a different wave speed than the rotor speed. Therefore, full-annular simulations are required to capture the hub cavity dynamics.

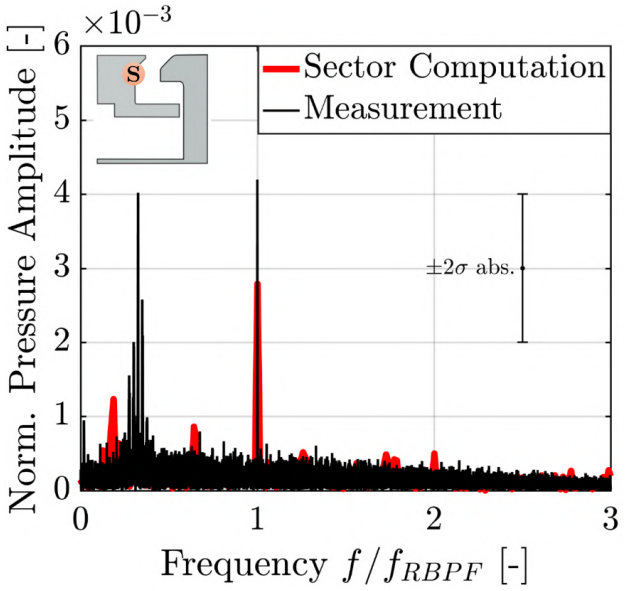

Figure 3.20.: Computationally (sector model CFD) and experimentally determined pressure frequency spectra for the purge flow injection rate IR=0.8 %

Since the dominant effects of the cavity modes are captured with the full-annular computations, a qualitative investigation of the flow field inside the hub cavity is valid to investigate the source of the low-frequency content. In Figure 3.21, the normalized static pressure between the first stator and rotor is shown using an axial slice for the two purge flow injection rates IR=0.0 % and IR=0.8 % for a specific time instant. The presented pressure data are normalized by the respective turbine inlet total pressure. The depicted slice is located 34 % of the rotor axial chord upstream of the rotor leading edge. The results show pronounced regions of lower static pressure distributed over the circumference (Figure 3.21, indices 1 to 8 (IR=0.0 %) and 1 to 22 (IR=0.8 %)). The number of low static-pressure zones shows strong sensitivity to the amount of injected rim seal purge flow. The IR=0.0 % case shows 8 pronounced low static-pressure zones, whereas the IR=0.8 % case reveals 22 zones around the circumference. The core of these regions shows a reduction in static pressure up to 0.7 % compared to the circumferential average in the cavity. A low static pressure suggests that the level of ingestion from the main annulus flow into the hub cavity is increased due to the local pronounced radial pressure gradient.

The low static-pressure zones were found to rotate with the rotor at a rotational speed of 89 % (IR=0.0 %) and 91 % (IR=0.8 %) of the rotational speed of the rotor. Therefore, a stationary pressure monitoring point inside the hub cavity experiences these low-pressure zones with a frequency of 13.2 % (IR=0.0 %) and 37.1 % (IR=0.8 %) of the blade passing frequency which is in agreement with the band of frequencies with elevated amplitude in the predicted and

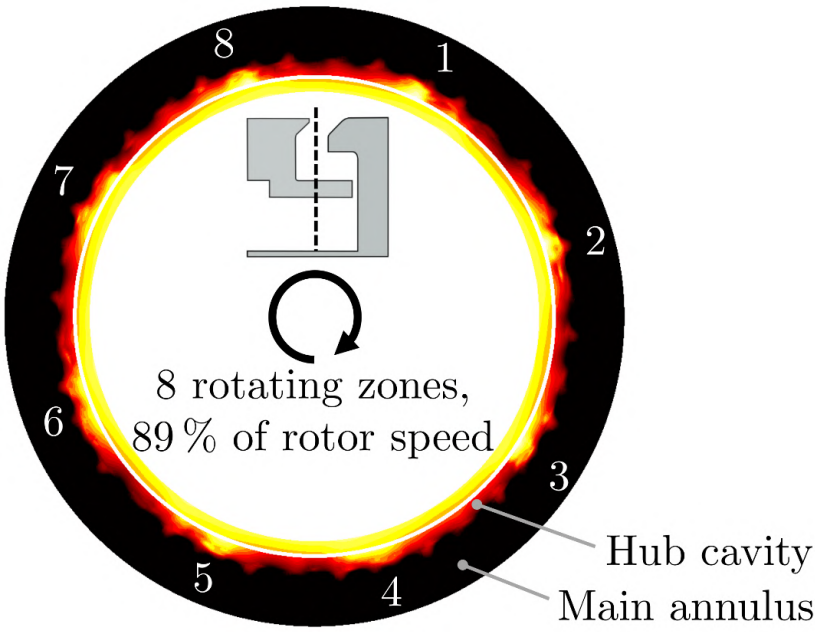

(a) $IR = 0.0\,\%$

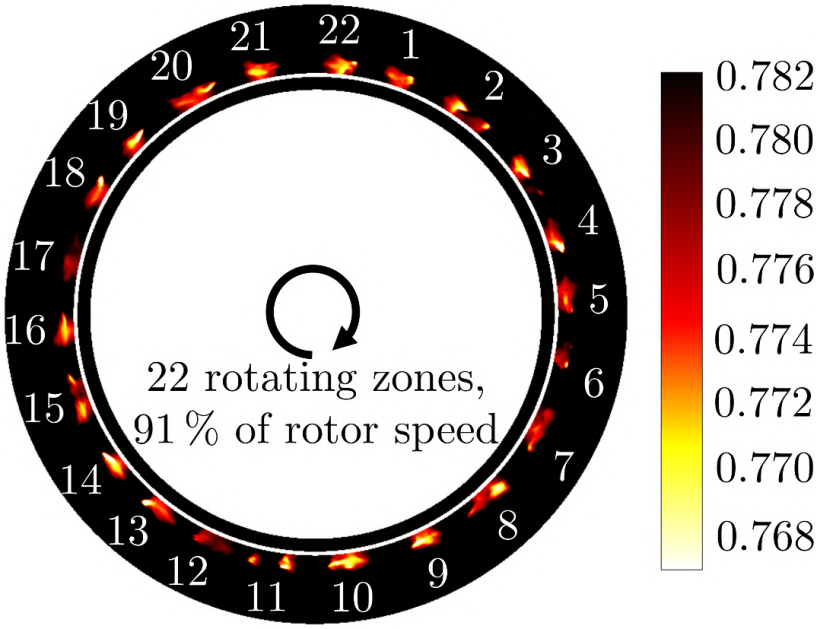

(b) $IR = 0.8\,\%$

Figure 3.21.: Instantaneous map of predicted normalized static pressure C_{ps} [-] over the full-annulus for two purge flow rates. Indication of 8 (IR=0.0 %) and 22 (IR=0.8 %) low static-pressure zones inside the hub cavity (CFD).

measured pressure frequency spectrum. The spectral analysis suggests a characteristic time scale of the peak ingestion of hot gas into the cavity in the absence of purge flow. Furthermore, the presence of the low-frequency pressure fluctuations implies that the ingestion of hot gas into the cavity is still taking place and gives, therefore, an appropriate measure of ingestion behavior to the turbine designer plus a judgment whether the amount of purge mass flow is sufficient in order to suppress ingestion. In the case of the

IR=0.0 %, the presence of the upstream first stator also is captured inside the hub cavity, which is characterized by 36 zones of low static pressure around the circumference.
In order to understand the source of the low static-pressure zones, the flow field inside the hub cavity needs to be further investigated. Figure 3.22 shows the close-up view of four meridional slices that provide the normalized radial velocity inside the hub cavity superimposed with the projected streamlines. The radial velocity was normalized by the rotor speed at the hub. The first slice **(1)** is radially aligned with the core of the low static-pressure zone (index 1, Figure 3.21 (a)) observed for the IR=0.0 % case. The normalized radial velocity contour clearly shows a pronounced zone of negative radial velocity, which describes that flow is going toward the axis of the machine with a velocity up to 60 % of the rotor hub tangential velocity. The high negative radial velocity component is anticipated to be induced by the shape of the rim seal, which locally accelerates the flow. However, the presence of the vortical structure (Figure 3.22 slice **(1)**, vortex (a)), reduces the effective flow cross-section and leads to local acceleration. The center of this vortex is found to be at the same radial position as the most pronounced region of the negative radial velocity.
Consequently, the pronounced negative radial velocity zone and, therefore, the low static-pressure zone is triggered by the vortical structures and the shape of the rim seal. The results imply that the center of the vortex needs to have a certain radial position and spatial extent, meaning that the axial width of the vortex needs to be in the order of magnitude of the gap between stator sided cavity wall and the rotor angel wing (around 20 % of the first stator axial chord). Because the hub cavity flow structures undergo a modulation in time and along the circumference, which also is depicted in Figure 3.22 (a) in slice **(2)**, the cavity mode is associated with a vortex modulation and formation. The contour plot shows that the radial velocity is increased toward positive values and the vortex radially migrates toward the exit of the rim seal (Figure 3.22, slice **(2)**, vortex (b)). Similar findings are identified by considering the IR=0.8 % case. The radial position of the vortex core also for this case affects the radial velocity distribution inside the hub cavity (Figure 3.22 slice **(3)**), whereas in regions in between the low-pressure zones dominantly purging occurs (Figure 3.22, slice **(4)**).
Based on the flow visualization, the hub cavity modes are characterized by rotating low static-pressure zones that rotate with the rotor at a fraction of the rotor speed. The ingestion and egress dynamics, in combination with the rim seal shape, seem to be strongly linked to the evolution of the non-synchronous modes, suggesting that as long as regions of ingestion are present, the modes are triggered. This statement would be in agreement with the observation for the highest considered purge flow rate (IR=1.2 %), which does not show the

signature of the cavity modes in the spectral analysis. Hence, high purge flow rates are beneficial to eliminate non-synchronous modes.

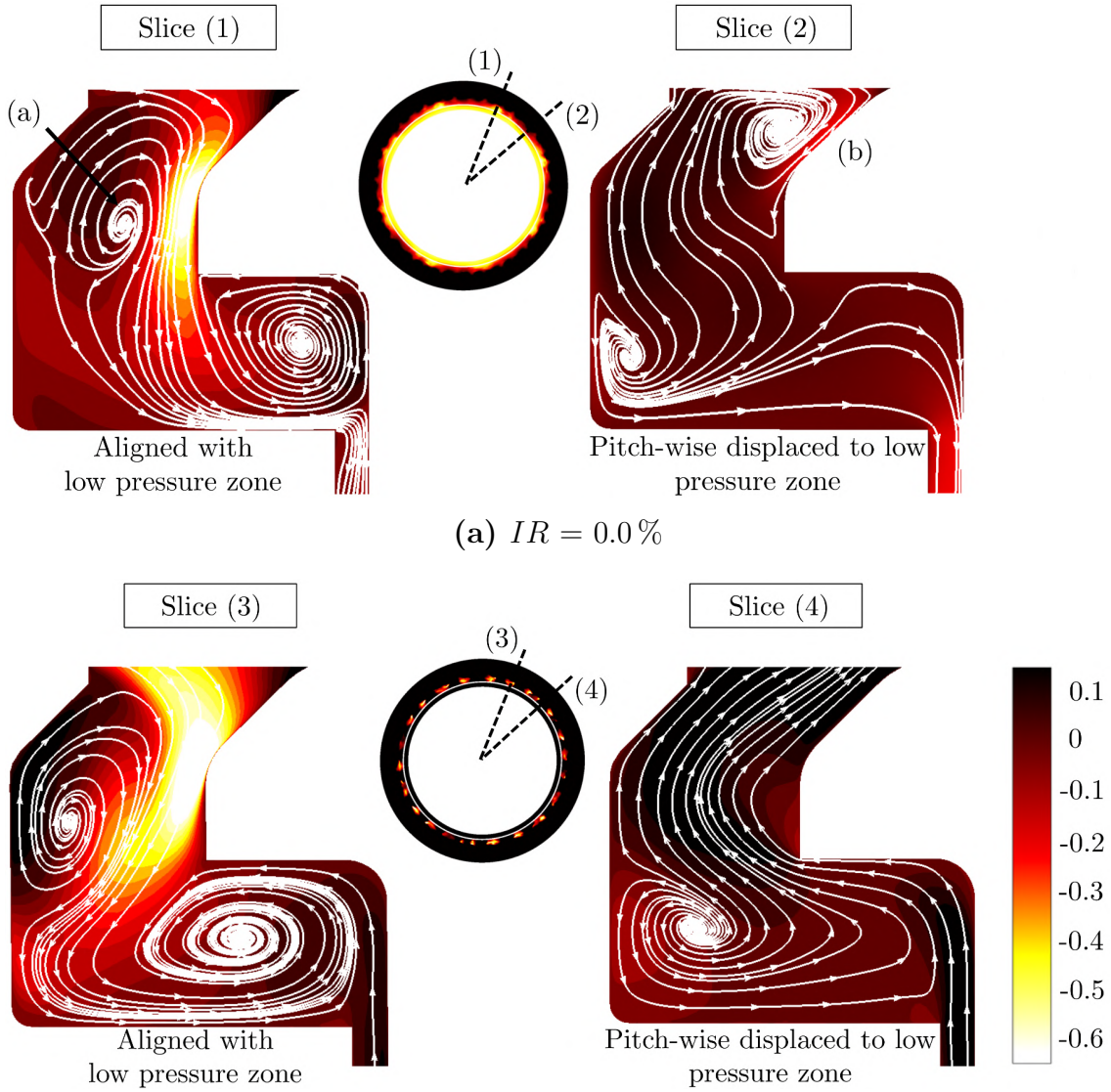

(a) $IR = 0.0\,\%$

(b) $IR = 0.8\,\%$

Figure 3.22.: Close-up view of meridional slice through local low static-pressure zones and between two low-pressure zones for two injection rates superimposed with normalized radial velocity contour [-] and hub cavity stream lines (CFD)

3.2.3. Impact of Hub Cavity Modes on Hot Gas Ingestion

The previously shown results indicate that the hub cavity modes provoke large-scale, rotating low static-pressure zones. As the pressure-driven ingestion mechanism in rim seals depends on the non-uniform, pitch-wise pressure distribution inside the hub cavity and the main annulus, such pressure perturbations point toward additional ingress. The full-annular computations are therefore used to support the ingestion investigation. For two different radial planes, the normalized ingestion mass flow is calculated. To underline the impact

of the non-synchronous modes on the ingestion behavior, the instantaneous distributions of the ingested mass flow are considered. For both considered planes, the mass flow rate is calculated with a pitch-wise resolution of one degree over the full-annular domain and is determined along with the axial extent of the cavity. The mass flow rate is then normalized by the turbine mass flow for the full-annulus and given in percent. The radial plane **(I)** is located right at the exit of the hub cavity (0 % span), whereas plane **(II)** is defined inside the hub cavity at −14 % span. Both planes are schematically shown as insets of Figure 3.23 (a). The resulting, ingress mass flow ratios for the two considered purge flow injection rates are shown in Figure 3.23. For the IR=0.0 % case, presented in Figure 3.23 (a), the oscillating patterns of the ingress mass flow can be observed. Over the full-annular domain, 54 peaks in ingress mass flow are counted for plane **(I)**, corresponding to the 54 rotor blades. The potential field of the rotor leading edge is anticipated to be responsible for the ingestion dynamics by forcing the flow into the cavity due to the excess of the static pressure. However, besides the fluctuations induced by the rotor blades, eight peaks of local higher ingestion are detected, which are attributed to the eight rotating low static-pressure zones previously shown in Figure 3.21 (a). For the plane **(II)** of the IR=0.0 % case, the presence of the rotor potential field effect is clearly diminished, and predominantly eight zones of ingestion are identified. The flow ingested into the hub cavity by the rotor leading edge potential field is not penetrating inward to the buffer arm. Hence, the radial momentum induced by the rotating low-pressure zones is much more pronounced and enables the flow to penetrate much deeper into the upper hub cavity. The instantaneous ingress mass flow peaks induced by the cavity modes are found to be up to twice as high as the one induced by the rotor potential field. The integrated instantaneous ingress mass flow ratio over the full-annular for plane **(I)** is determined to be about 0.9 % and for plane **(II)** around 0.5 % of the turbine mass flow rate, respectively.

A similar assessment is conducted for the nominal purge flow injection rate IR=0.8 %. The most pronounced peaks in the ingress mass flow are triggered by the presence of the 22 low static-pressure zones, which were detected and visualized in Figure 3.21 (b). Contrary to the dynamics found for the IR=0.0 % case, the impact of the rotor leading edge potential field effect is barely visible for both considered radial planes. Interestingly, the ingress mass flow peaks are very comparable for plane **(I)** and **(II)**, which implies that the flow has a higher radial momentum compared to the IR=0.0 % case. Furthermore, even in the presence of a nominal purge flow injection rate, the ingress peaks are found to be stronger than for the low purge flow case. Considering the higher pressure amplitude of the cavity modes for the IR=0.8 % compared to the IR=0.0 %, this ingress behavior is in agreement with the increased strength

of the non-synchronous modes. The integrated instantaneous ingress mass flow ratio for plane **(I)** is found to be about 1.1 %, and for plane **(II)** around 0.8 % of the total turbine mass flow rate. The stronger presence of the non-synchronous cavity modes for the IR=0.8 % case benefits the ingestion into the cavity and clearly exceeds the dynamics of the rotor potential field-driven ingestion.

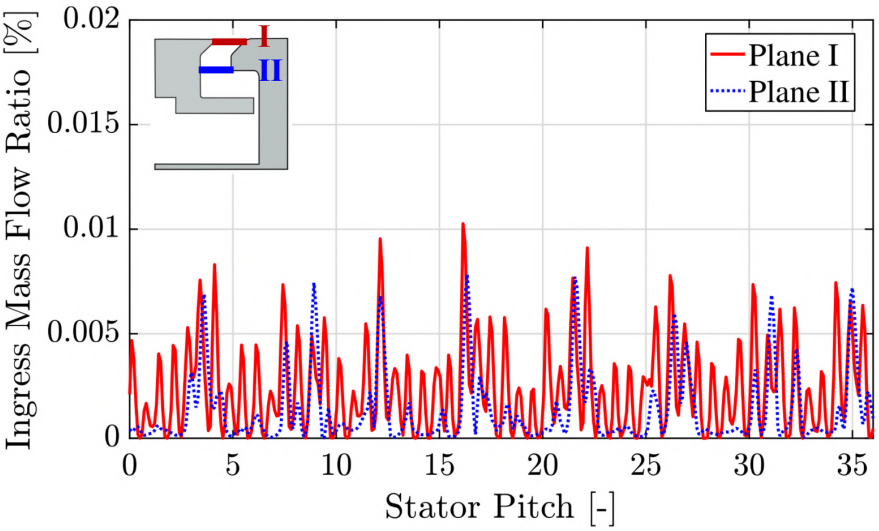

(a) $IR = 0.0\,\%$

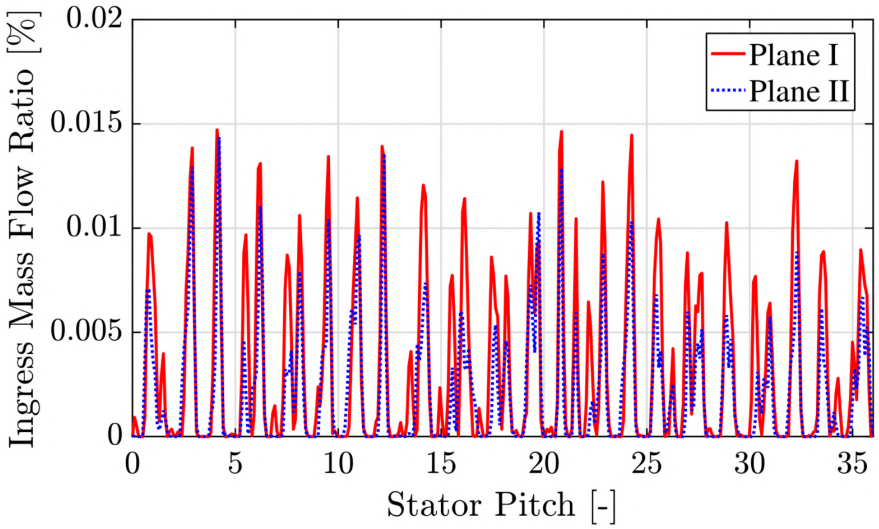

(b) $IR = 0.8\,\%$

Figure 3.23.: Instantaneous ingestion mass flow ratio for two radial planes and rim seal purge flow injection rates (CFD, adapted from [56])

In summary, the non-synchronous hub cavity modes have a non-negligible impact on the hot gas ingestion dynamics. Even at a nominal purge flow injection rate, the ingestion is found to be enhanced due to the increased strength of the cavity mode. Consequently, the presented ingestion mechanism driven by the large-scale rotating pressure zones needs to be accounted for in the aerothermal design of rim seals.

3.3. Conclusions

The current chapter presents a unique dataset of experimental and numerical results, detailing the nature and significance of the hub cavity non-synchronous flow perturbations. Based on the investigations, the following conclusions can be extracted. The characteristic flow structures in the rim seal space could be successfully traced utilizing fast-response probe and wall-mounted pressure measurements, and their essence could be characterized by unsteady numerical modeling. Based on the measurements and computations, the low-frequency, non-synchronous flow structures (termed as "hub cavity modes") formed in the rim seal and hub cavity space are found to have a non-negligible impact on the turbine characteristics and impose challenges on a broad range of turbine design aspects.

The asynchronous flow perturbations found in the hub cavity need to be budgeted in the acoustic design of turbines. The pressure oscillations induced by the low-frequency modes are found to be in the order or even exceed the originally dominating blade passing-induced fluctuations and are sensitive in their strength and frequency content to the rim seal purge flow. Consequently, these modes provoke an excitation of the aeroacoustic field in the low-frequency range which results in a peak pressure intensity increase of up to 18 dB at the source. The signature of the cavity induced flow structures is found to radial migrate up to 30 % span of the main annulus and are convected by the hub secondary flows of the adjacent stator and downstream rotor, resulting in a noise increase in the low-frequency band of up to 7 dB at turbine exit.

The detected cavity modes provoke an additional pressure-induced hot gas ingestion mechanism, which has to be eliminated in order to provide sufficient sealing effectiveness of the rim seal. The low-frequency, asynchronous nature of the cavity modes is induced by rotating large-scale low-pressure zones, which provoke peaks in the ingress mass flow that are twice as high as the ones induced by the rotor blade passing.

Computationally expensive unsteady RANS calculations, including the vanes and blades of the main annulus, are capable of capturing the non-synchronous hub cavity modes. Specifically, full-annular unsteady calculations are required to accurately predict the non-synchronous excitation in the hub cavity. Sector models with a 1:1 pitch ratio fail to predict the hub cavity dynamics correctly when cavity modes are present, most likely due to the high-pass filter effect of the periodic boundary conditions that limit the formation of the pressure waves inside the cavity. Multiple rotor revolutions have to be simulated (typically 4–5, coarse grid) to stabilize the dominating cavity mode pressure oscillations. It is advised to perform a detailed sensitivity study on the unsteady solver parameters (number of time steps and sub-iterations) to provide accurate numerical results. For coarse full-annular meshes (in the order of 35 million nodes), the designer has to expect an overprediction of the cavity mode

pressure amplitude between 10–15 %.
As a measure to attenuate the low-frequency modes, the rim seal purge flow rate was evaluated to be a tuning parameter, since sufficiently high rim seal purge flow rates that seal the cavity against ingress are favorable to completely eliminate the hub cavity induced flow perturbations.

4. Aerodynamic Effects of Rim Seal Purge Control Features

Rim seals throttle flow and have been shown to impact the aerodynamic performance of gas turbines. The results of an experimental investigation of a rim seal exit geometry variation and its impact on the high-pressure turbine flow field are presented in this chapter. A one-and-a-half stage unshrouded and highly loaded axial turbine configuration with 3-dimensionally shaped blades and non-axisymmetric end wall contouring was tested (section 2.2.2). The exit of the rotor upstream rim seal was equipped with novel geometrical features which are termed as "purge control features" (PCF) and a baseline rim seal geometry for comparison (Figure 2.16). The time-averaged and unsteady aerodynamic effects at the rotor inlet and exit were measured with the pneumatic probes and the fast-response aerodynamic probe (FRAP) for three rim seal purge flow injection rates. Measurements at rotor inlet and exit reveal the impact of the geometrical features on the rim seal exit and main annulus flow field, highlighting regions of reduced aerodynamic losses induced by the modified rim seal design. Measurements at the rotor exit with the purge control features installed show a benefit in the total-to-total stage efficiency up to 0.4 % points for nominal and high rim seal purge flow rates. The chapter shows the potential to improve the aerodynamic efficiency for an already optimized turbine stage using a well-designed rim seal exit geometry without losing the potential to block hot gas ingestion from the main annulus.

4.1. Impact on the Aerodynamic Performance

In this section, the sensitivity of the total-to-total stage efficiency for two different injection rates and two rim seal exit geometries are presented. The definition of aerodynamic efficiency used in this study, accounting for the rim seal purge flow injection, is given in Equation 2.36. In the post-processing, the definition is evaluated at each point of the measurement grid. The total pressure at the rotor exit (Figure 2.2) is measured by the pneumatic five-hole probe (5HP), whereas the rest of the quantities are acquired with different instrumentation installed in the rig.
In Figure 4.1 (left), the circumferentially and mass-averaged total-to-total stage efficiency difference ($\Delta\eta_{tt}$) profiles for two rim seal purge flow injection

rates are presented. The efficiency difference (in percentage points: % points) is based on the total-to-total stage efficiency values of the purge control feature case (PCF) compared to the baseline case. The radial distributions of the stage efficiency difference reveal two flow field regions where the purge control features lead to significant improvement of the aerodynamic performance for both purge flow injection rates. Between 6 % and 15 % span, the PCF geometry reduces the losses in close vicinity to the hub. Figure 4.1 indicates an improvement up to 0.75 % points (IR=1.2 %). The radial distribution around mid-span (40–70 % span) shows pronounced improvement in aerodynamic performance up to 0.71 % points for the IR=0.8 % case and 0.77 % points for the IR=1.2 % case, respectively. Insights for the improvements in these regions will be given in the following rotor inlet and exit flow field sections. Overall, the results imply that the modified rim seal exit geometry leads to an improvement across the whole span. Furthermore, the features seem to perform locally even better (+0.20 % points at 8 % span) in the presence of high rim seal purge flow rates (IR=1.2 %) compared to the nominal injection rate.

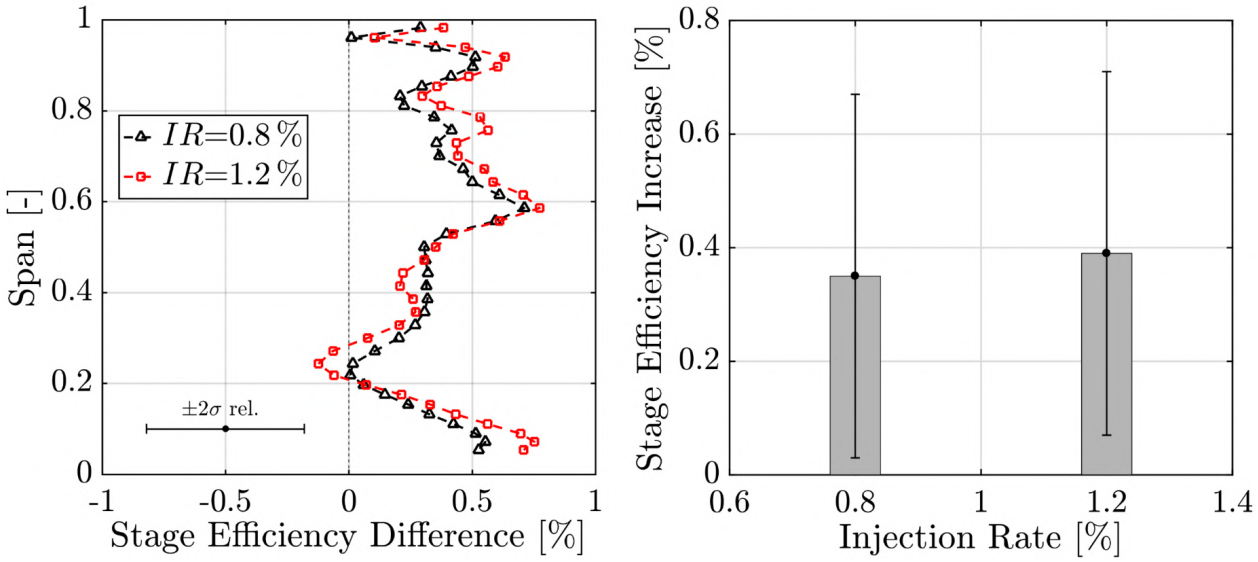

Figure 4.1.: Mass- and circumferentially averaged total-to-total stage efficiency change $\Delta\eta_{tt}$ (5HP) due to purge flow control features (PCF): radial profiles (left) and integral efficiency increase (right). Efficiency changes are given in percentage points.

By averaging over the whole measurement grid, the integral values of the total-to-total stage efficiency are obtained. The absolute increase in stage efficiency integral values by changing from the baseline to the purge control feature geometry is depicted in Figure 4.1 (right). For both rim seal purge flow injection rates, an improvement in the integral values are found, whereas a moderately higher increase is found for the high injection rate case IR=1.2 %. The purge flow features increase the integral efficiency value by 0.35 % points for IR=0.8 % and 0.39 % points for the IR=1.2 % case, respectively.
Furthermore, a purge flow sensitivity study on the integral values shows a 19 %

lower sensitivity of the stage efficiency with respect to the injected amount of rim seal purge flow for the PCF. In the case of the baseline geometry, the stage efficiency sensitivity with respect to purge flow was found to be -0.53 % points per percent of injected purge mass flow, whereas the purge control feature configuration provides a sensitivity of -0.43 % points per percent injected mass flow.

4.2. Aerodynamic Effects at the Rotor Inlet

To relate the performance benefits for the nominal and high rim seal purge flow rates to the aerodynamics, the flow field at the rotor inlet is investigated via probe measurements at the S1ex plane. The FRAP and pneumatic four-hole probe (4HP) are able to penetrate into the rim seal hub cavity, such that it is possible to study the effects right at the interface between the cavity and main annulus flow. Before explaining the effects of the novel rim seal design, the effect of purge flow on the flow field at the rotor inlet is studied. The impact of the purge control features will then be assessed, also under consideration of the aforementioned design intention which is documented in section 2.2.2.

4.2.1. Impact of Rim Seal Purge Flow on the Aerodynamic Flow Field

The assessment of the purge flow effects at the rotor inlet is provided by the basic flow quantities, such as flow yaw angle, static pressure, and Mach number. Note that the purge flow sensitivity provided in this part of the work was investigated for the baseline rim seal design because only for that design three different purge flow rates were measured. Similar effects, as presented in this section, have also been reported by Schuepbach [173] and Jenny [75].
In Figure 4.2, the mass- and circumferentially averaged relative flow yaw angle β distribution at the rotor inlet is presented. The effect of injecting rim seal purge flow into the main annulus flow is presented in Figure 4.2 (left), highlighting that across the whole span, a reduction of relative flow yaw angle is measured by increasing the purge rate from 0.0 % to 1.2 %. The highest rim seal purge flow case shows a reduction of relative flow yaw angle up to 1° at mid-span and 2.3° in close vicinity to the hub, respectively. A reduction of the relative flow yaw angle at rotor inlet induces negative incidence on the rotor leading edge, as indicated in Figure 4.2 (right). A schematic of the velocity triangles at the rotor leading edge, which is included in the figure as an inset, provides a qualitative explanation on the flow field effect. The schematic emphasizes that the purge flow leads to a non-beneficial flow distortion relative to the rotor leading edge, which also provokes that the relative flow velocity W is reduced as the purge rate is increased from 0.0 % to 1.2 %.

The effect of the rim seal purge flow injection into the main annulus flow field is also reflected in the measured static pressure at the rotor inlet. In Figure 4.3 (left), the time- and area-averaged normalized static pressure distribution is presented. The pressure data are normalized by the turbine inlet total pressure. It is interesting to see that the purge flow injection affects the radial distribution of the static pressure over the whole span-wise coordinate. As the purge flow is increased the static pressure also is increased. The most pronounced change is observed in close vicinity to the hub at around 3 % span and amounts to 1.2 % when raising the purge flow rate from 0.0 % to 1.2 %.

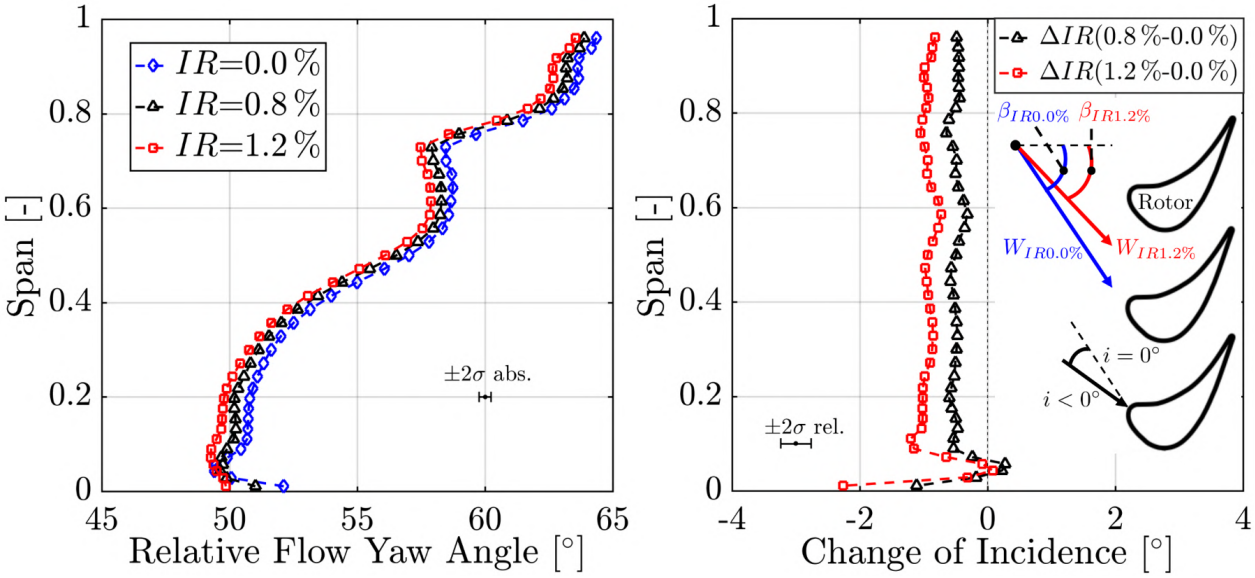

Figure 4.2.: Mass- and time-averaged relative flow yaw angle at rotor inlet (FRAP) for the baseline rim seal design: purge flow sensitivity (left) and change of incidence angle (right), including comprehensive schematic

In conjunction with the static pressure, it is worth investigating the Mach number distribution at the rotor inlet. In Figure 4.3 (right), the mass- and circumferentially averaged absolute Mach number is depicted. As the static pressure is increased when the purge flow is increased, and the total pressure is only moderately affected, the Mach number tends to drop with higher purge flow rates. Close to the interface between the cavity and main annulus flow, the Mach number is decreased up to 3.5 %.

Jenny [75] explained the effect of purge air at the rotor inlet as follows: the mass of air is constant in the volume defined between the first stator throat and rotor throat, but as mass is added by injecting purge flow into the volume, the internal pressure is increased which goes along with an increase of the static pressure at rotor inlet. Since the purge mass flow is added in front of the rotor leading edge, the flow must react to the new conditions. Two possibilities are given to the flow, either increase the mass flow through the rotor throat or decrease it through the first stator. The higher static pressure at the rotor inlet causes the relative total pressure to rise. Assuming a constant rotor

capacity, this would lead to an increased mass flow through the rotor throat. On the other hand, the increased static pressure at the rotor inlet moderately lowers the mass flow through the first stator (the first stator is not choked). Since the turbine configuration is operated under a constant total-to-static pressure ratio over the 1.5-stage configuration, the total pressure at the inlet of the first stator is barely affected by the purge flow injection.

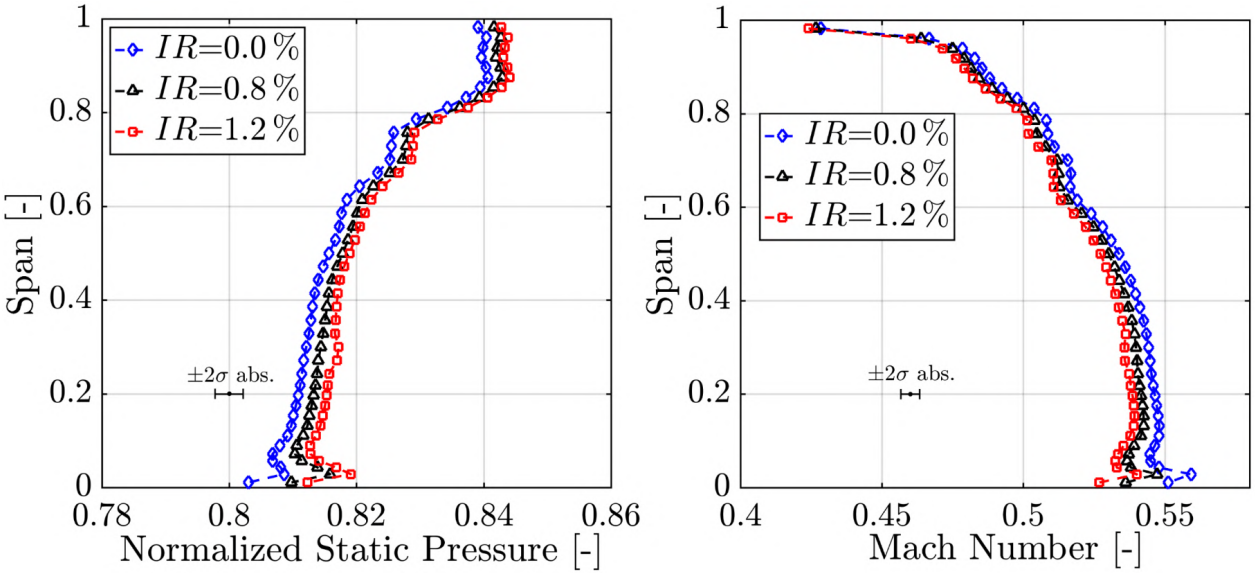

Figure 4.3.: Area- and time-averaged measured normalized static pressure C_{ps} (left) and mass-averaged Mach Number (right) for different injection rates at rotor inlet (FRAP) for baseline rim seal design

It was shown that the injection of rim seal purge flow causes a pronounced negative incidence angle on the rotor leading edge, especially close to the hub. In that context, also the circumferential flow velocity has to be studied. In Figure 4.4, the time- and mass-averaged normalized absolute circumferential velocity at the rotor inlet are presented for the baseline rim seal. The presented values are normalized by the rotational speed of the rotor at the hub. The span-wise consideration was extended, as the probe is immersed into the hub cavity, which reveals the circumferential velocity down to −20 % span. The effect of purge flow is depicted in the figure, showing a gradual decrease of the absolute circumferential velocity over the full span by increasing the purge flow from IR=0.0 % to IR=1.2 %. The most pronounced reduction is found in the upper part of the hub cavity from 0 % down to −20 % span. The radial gradient of the absolute circumferential velocity across the rim seal interface was found to increase up to 48 % by increasing the purge rate from 0.0 % to 1.2 %. Hence, the purge flow not only changes the flow direction but also reduces the magnitude of the absolute circumferential flow velocity. As the radial gradient of the absolute circumferential velocity increases, the so-called tangential shear over the interface between the hub cavity (at 0 % span) and main annulus flow is increased. The associated viscous shear layer generates

entropy due to the dissipation of the velocity gradients which contributes to the aerodynamic loss production at the rotor inlet.

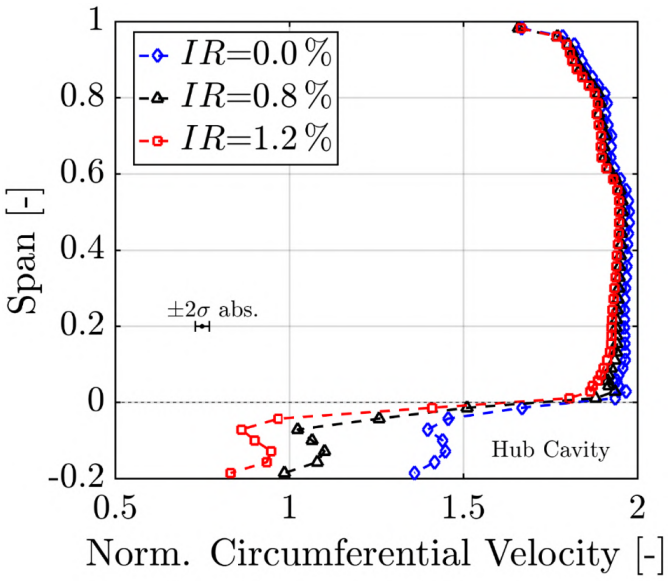

Figure 4.4.: Mass- and time-averaged measured normalized absolute circumferential velocity for different injection rates at rotor inlet (FRAP) for baseline rim seal design, data are provided also for the upper hub cavity down to −20 % span

The explanations given above also are reflected in the absolute total pressure profile. In Figure 4.5 (left), the time- and mass-averaged normalized absolute total pressure is provided. Again, the pressure data are normalized by the respective turbine inlet total pressure. The most pronounced change in the total pressure radial profile is found right at the hub, where a 0.6 % reduction is measured when increasing the purge flow rate from 0.0 % to 1.2 %. The rest of the flow field is not considerably affected by the injection of purge flow with respect to the total pressure. The non-deterministic pressure unsteadiness $p'_{1,rms}$ is evaluated to assess the effect of the purge air on the flow unsteadiness at the rotor inlet. The pressure unsteadiness is derived as introduced in Equation 2.26 and described in section 2.5.2.1. Similar to the total pressure profiles, a change in the pressure unsteadiness is mainly detected in close vicinity to the hub. An up to 72 % increase in the $p'_{1,rms}$ values is found at around 1 % span when the rim seal purge flow mass flow is increased from 0.0 % to 1.2 %. Interestingly, the increase of the non-deterministic pressure unsteadiness from the nominal to the highest injection rate is very moderate (about 2.5 %). The data suggest that by injecting purge flow into the main annulus flow, the flow unsteadiness at the hub is enhanced potentially provoked by the increase in tangential shear across the interface between the cavity and main flow.

The characteristics of the purge flow injection into the main annulus flow field can also be described by investigating the time-resolved non-deterministic pressure unsteadiness close to the hub. In Figure 4.6, the experimentally

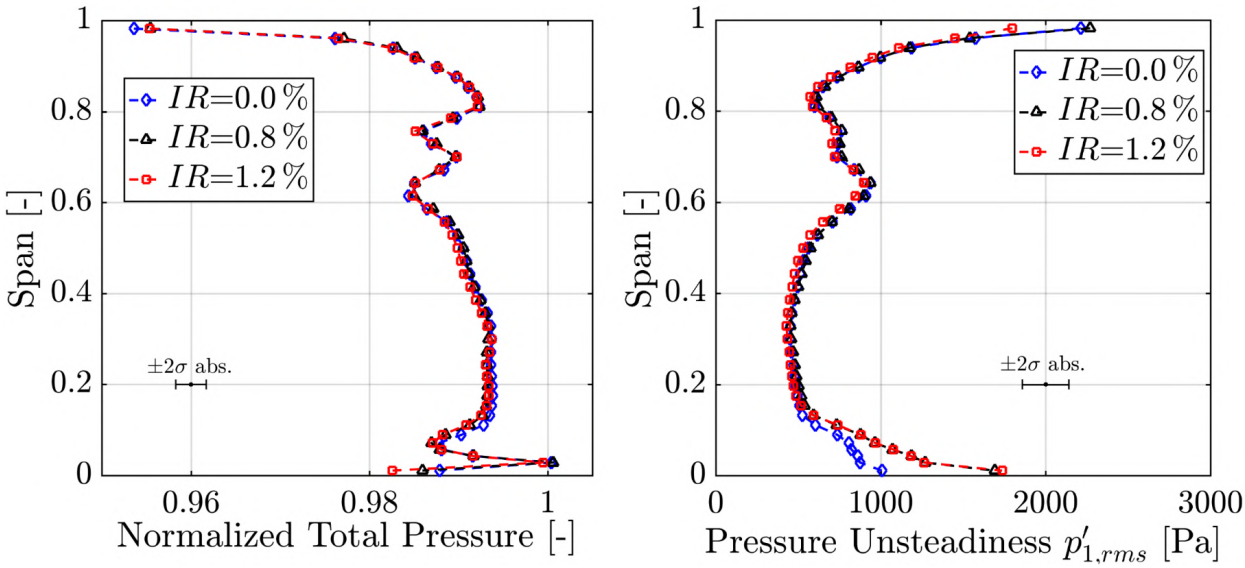

Figure 4.5.: Mass- and time-averaged normalized total pressure C_{pt} (left) and area-averaged pressure unsteadiness $p'_{1,rms}$ (right) for different injection rates at rotor inlet (FRAP) for baseline rim seal design

determined pressure unsteadiness $p'_{1,rms}$ in a space-time plot is depicted for two injection rates at 3.5 % span. The x-coordinate of the plot is the first stator pitch. On the y-coordinate of the figure, the time-axis for the rotor blade passing period is included and covers three rotor blade passing events. For both considered rim seal purge flow injection rates, a vertical band of higher-pressure unsteadiness is measured between 0.45 and 0.6 stator pitch (dashed white rectangle). Since this feature leaves a vertical band, it is stationary in space with respect to time, which suggests that it is a feature associated with the upstream first stator (most likely the signature of the first stator wake and hub secondary flows). When comparing both injection rates to each other in Figure 4.6, the overall pressure unsteadiness is increased for higher purge flow rates. Since the purge flow injection is the only difference between the plots, the higher purge flow is likely responsible for the increase in unsteadiness levels. Additionally, for the IR=1.2 % case, three inclined zones (dashed white ellipse in Figure 4.6 (b)) of higher pressure unsteadiness can be observed between 0 and 0.4 stator pitch. Since these three features are inclined in the space-time plot, it is interpreted that the rotor is responsible for the modulation of the non-deterministic pressure unsteadiness at that location. It is also suggested that these high levels are provoked by the purge flow injection into the main flow, meaning that at each rotor blade passing event a jet of purge flow enters the main annulus and leaves a signature of high pressure unsteadiness. As sharply reported in the work of Jenny [75], in the absolute frame of reference, the upstream stator decides where the purge flow is leaving the cavity, whereas the rotor decides when in time this happens.

In summary, the analysis shows that the injection of rim seal purge flow has a pronounced impact on the incidence angle, the magnitude of the absolute

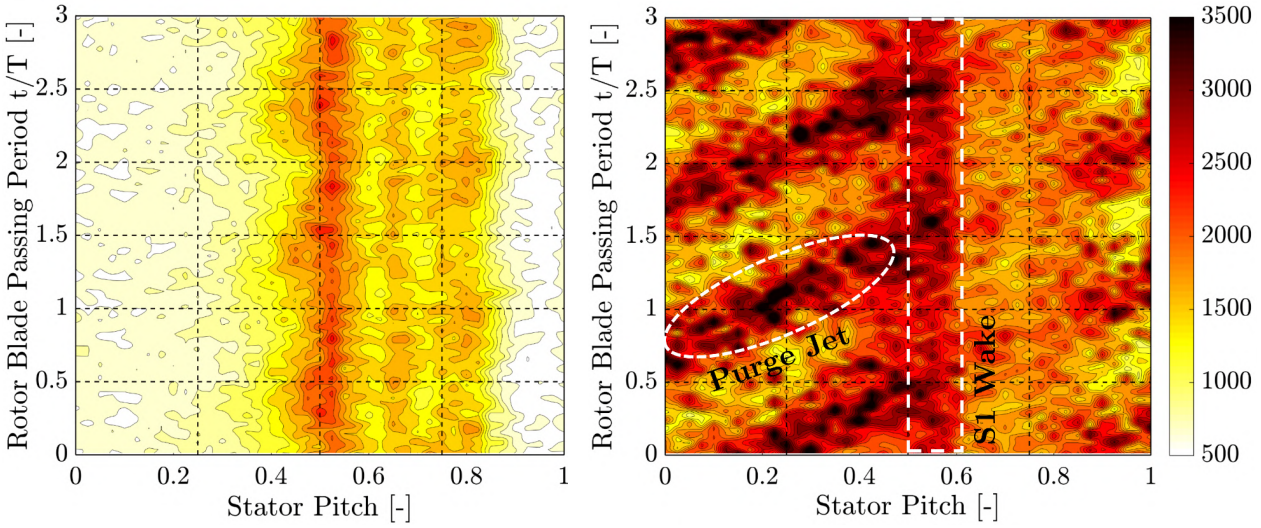

(a) $IR = 0.0\,\%$ **(b)** $IR = 1.2\,\%$

Figure 4.6.: Space-time plot in the absolute frame of reference of the measured $p'_{1,rms}$ [Pa] at 3.5 % span for the zero and the high injection rates at rotor inlet (FRAP)

circumferential velocity as well as on the pressure unsteadiness levels, especially in close vicinity to the hub. The novel rim seal design should, therefore, be assessed in terms of these quantities, and specific attention should be taken regarding the realignment of the flow and reduction of tangential shear as formulated in the rim seal design intentions in section 2.2.2.

4.2.2. Purge Control Feature Effects at the Rotor Inlet

When the turbine is operated under rim seal purge flow injection, it was found that the relative flow yaw angle at rotor inlet is reduced, which induces negative incidence on the rotor. Typically, a non-zero incidence angle provokes that the profile losses of the blade are rising [134, 182]. Therefore, a first assessment of the flow angles at the rotor inlet is performed when the purge control features are installed and subsequently compared to the baseline rim seal design.

In Figure 4.7, the impact of the purge control features is shown by comparing the PCF radial distributions of the relative flow yaw angle to the one of the baseline geometry for the design point at IR=0.8 %. The strongest impact of the PCF is seen close to the hub, where an increase of 1.4° is found (Figure 4.7, right), whereas for the rest of the span, the change of the relative flow yaw angle fluctuates around zero. Overall, the purge control features have a beneficial impact on the negative incidence angle provoked by the injection of purge flow. The relative flow yaw angle distributions of the PCF case imply that the features installed at the rim seal exit counteract the misalignment of the low-momentum cavity fluid with the main annulus flow. When comparing the measurements and the flow angles at the rotor inlet, it is also necessary to

address the potential change in mass flow at both measurement days. First, the turbine capacity has not changed for the purge control feature configuration. Second, the changes of the turbine mass flow due to day-to-day variations of the atmospheric pressure was fortunately only moderate, meaning that the purge control feature configuration on that particular measurement day only had a 0.3 % higher turbine mass flow compared to the day at which the baseline case was measured. This change in turbine mass flow does not alter the relative flow yaw angles close to the hub by 1.4°.

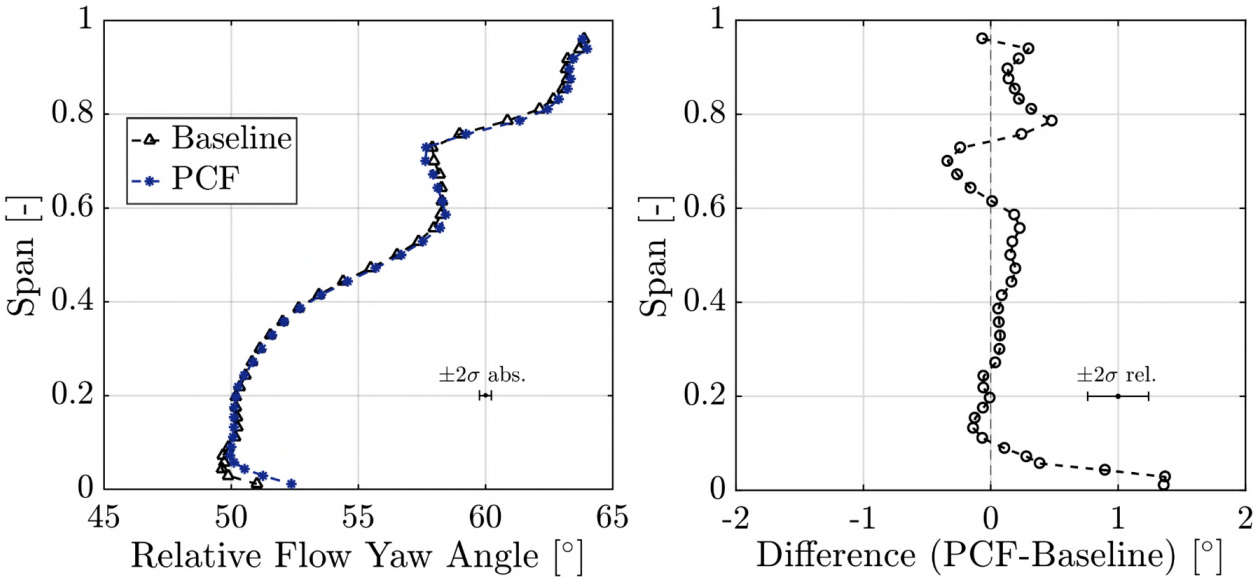

Figure 4.7.: Mass- and time-averaged relative flow yaw angle comparison (FRAP) between baseline and PCF rim seal for nominal injection rate IR=0.8 %, span-wise distribution (left) and change in relative flow yaw angle (right)

Furthermore, the effect of the novel rim seal design on the circumferential velocity distribution and the respective tangential shear is worth considering. The effect of the purge control features on the absolute circumferential velocity is shown in Figure 4.8 for the design point IR=0.8 %. The provided data are again normalized by the rotational speed of the rotor at the hub. The figure also provides a close-up view of the interface between the hub cavity and the main annulus flow (Figure 4.8, right). Of specific interest is the region below the hub from −5 % to 0 % span where at location **(1)**, a deceleration of the flow is found compared to the baseline. This effect is most probably associated with the stator-sided control features, where part of the hub cavity fluid enters the pocket-like feature. On the other hand, at location **(2)**, the flow is accelerated compared to the baseline case which was intended in the design of the features. Comparing the velocity gradients across the hub region reveals that the purge control features reduce the radial gradient of the absolute circumferential velocity by 11 %.

The impact of the reduction in circumferential shear is visible in the vorticity level close to the rim seal interface. Specifically, the circumferential shear has

a first-order impact on the axial vorticity (Equation 2.28). Therefore, the circumferentially and mass-averaged axial vorticity is shown for both rim seal designs in Figure 4.9 (left). The plot indicates that at the rim seal exit (1 % span) strong positive axial vorticity is present, which is the signature of a vortex formed by the interaction between cavity fluid and main annulus fluid. The positive impact of the purge control features is visible in this location where a reduction in axial vorticity of 48 % is observed. This implies that reducing the tangential shear at the rim seal exit results in a reduction of the vorticity levels at the interface between the hub cavity and the main annulus.

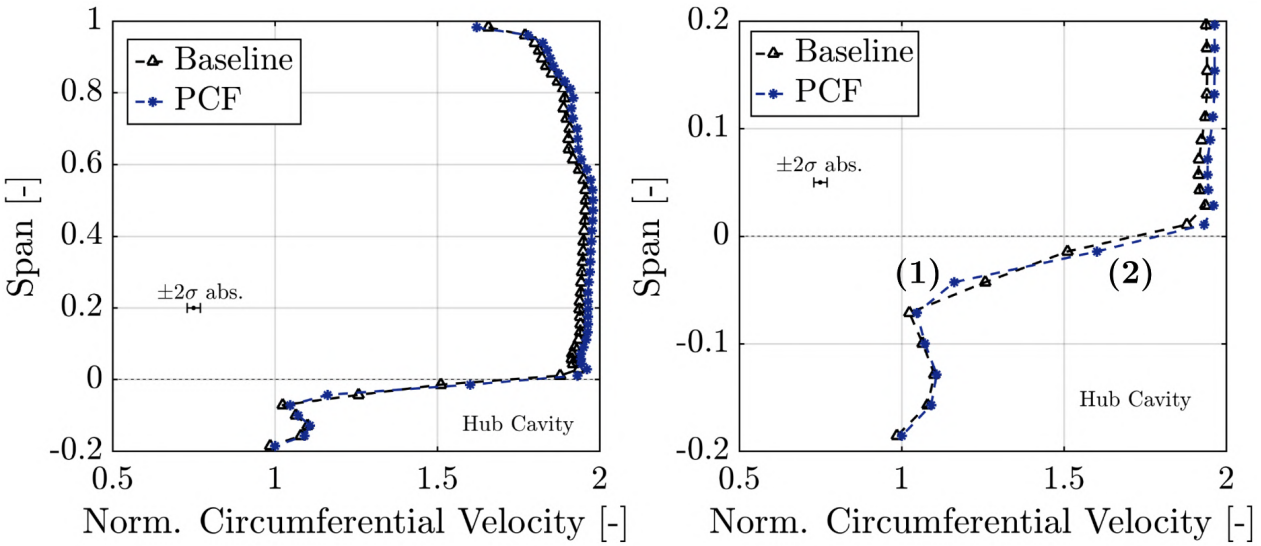

Figure 4.8.: Mass- and time-averaged normalized circumferential velocity comparison (FRAP) between baseline and PCF rim seal for nominal injection rate IR=0.8 %, span-wise distribution (left) and close-up view hub cavity interface (right)

Similar to the purge flow sensitivity study, presented in the previous section, the non-deterministic flow unsteadiness $p'_{1,rms}$ is investigated for the rim seal comparison. In Figure 4.9 (right), the area- and time-averaged pressure unsteadiness is shown for both rim seal designs operated under the design purge flow injection rate IR=0.8 %. The impact of the purge control features is very local and slightly visible at 1 % span where a 4 % reduction in the stochastic pressure unsteadiness can be found. The rest of the span is almost not affected by the presence of the features.
In addition to the axial vorticity and the pressure unsteadiness, the performance of the first stator in conjunction with the new rim seal design is assessed. Therefore, the total pressure levels associated with each rim seal design are analyzed. In Figure 4.10 (a) and (b), the contour diagrams of the time-averaged normalized total pressure is presented for both rim seal designs and IR=0.8 %, indicating the regions where the secondary flow structures of the upstream located stator are present. The data are normalized by the respective turbine inlet total pressure. The hub secondary flow structures of the first stator (S1) are located at around 10 % span (0.6 stator pitch), which include the hub

trailing edge shed vortex **(3)** and the hub passage vortex **(4)**. The tip passage vortex and tip trailing edge shed vortex are found between 60–80 % span (0.75 stator pitch) and are labeled with **(1)** and **(2)** in Figure 4.10 (a), respectively. Additionally, the wake of the first stator is identified by an inclined band of lower total pressure (dashed white line).

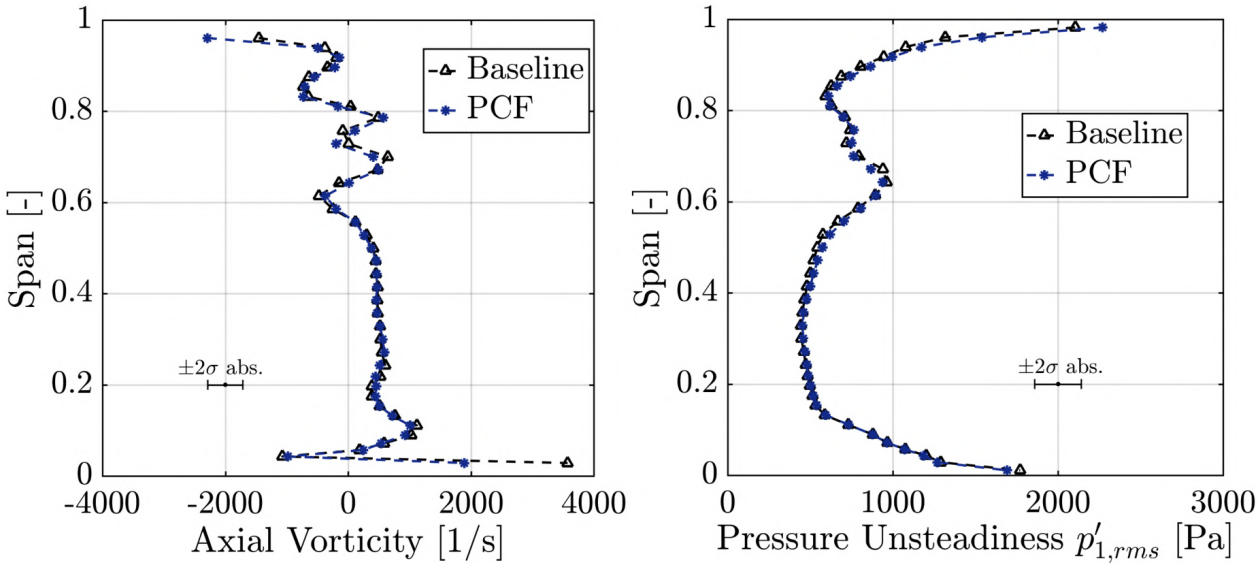

Figure 4.9.: Mass- and time-averaged axial vorticity comparison between baseline and PCF rim seal (left) and area- and time-averaged pressure unsteadiness $p'_{1,rms}$ (right) for design injection rate IR=0.8 % (FRAP)

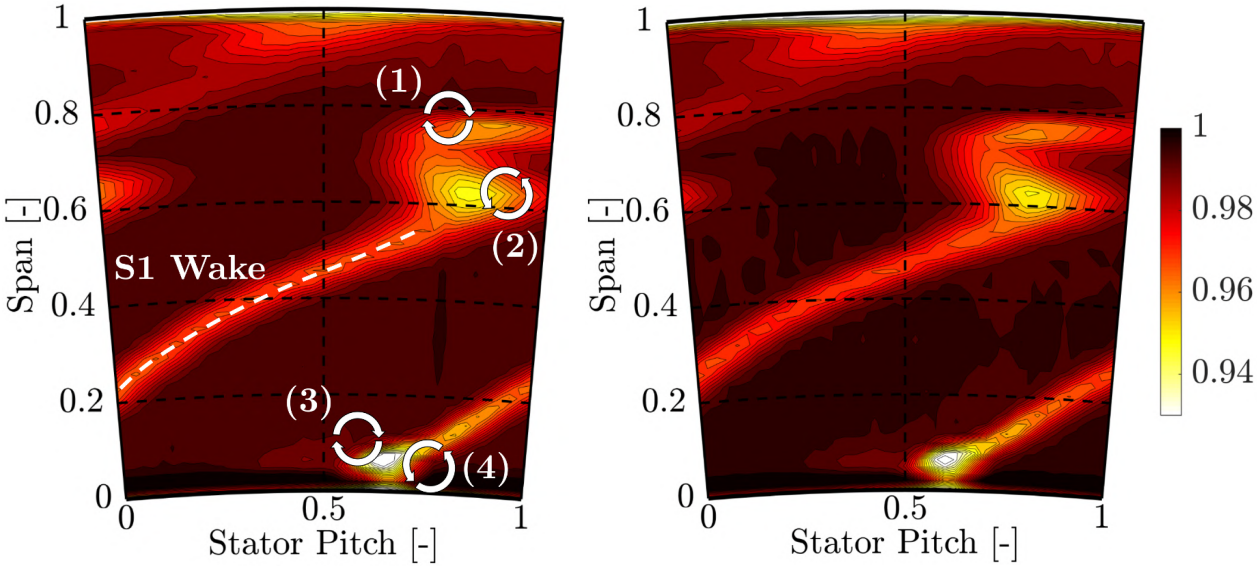

(a) Baseline **(b)** Purge Control Features (PCF)

Figure 4.10.: Time-averaged normalized total pressure C_{pt} [-] at first stator exit for both rim seal designs operated under purge flow injection rate IR=0.8 % (FRAP)

The mass- and circumferentially averaged absolute total pressure profiles for both rim seal designs are presented in Figure 4.11. The values are normalized

by the total pressure at the turbine inlet. Comparing the baseline geometry and the purge control feature case, an increase in absolute total pressure is observed over the full span for the purge control features. The most pronounced increase of 1 % is found at around 1 % span. At around 65 % span, an increase of 0.4 % is found. Overall, the purge control features seem to lower the total pressure losses downstream of the first stator and specifically in close vicinity to the hub.

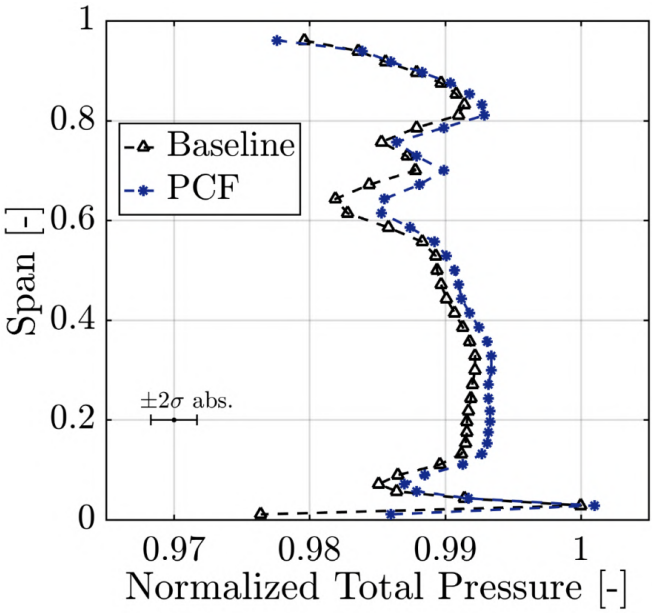

Figure 4.11.: Mass- and time-averaged normalized total pressure C_{pt} comparison between baseline and PCF rim seal for IR=0.8 % (FRAP)

A further explanation for the total pressure increases over most parts of the span is anticipated to be related to increasing circumferential velocity along the span, as presented in Figure 4.8 (left). As the circumferential velocity increases, the static pressure is increasing, following the radial pressure gradient expression in Equation 4.1. This would result in increased total pressure levels over the span. The reduction in tangential shear in close vicinity to the hub would then be the key driver to enhance the whole rotor inlet flow field.

$$\frac{dp}{dr} = \rho \frac{V_\theta^2}{r} \tag{4.1}$$

The previous investigations of the rotor inlet flow field suggest that the purge control features have a beneficial impact on the rotor inlet flow field. However, it was reported that an increase in the purge flow swirl coincides with a reduction in the sealing effectiveness against hot gas ingestion [142, 199], which is driven by the circumferential pressure non-uniformity induced by the presence of the rotor blades. In the absence of hot gas ingestion measurements, a quantitative investigation of the mass flow exchange between the main annulus flow and rim seal is performed by analyzing the time-resolved radial

velocity at the rim seal exit measured with FRAP. Figure 4.12, presents the space-time plots for the normalized radial velocity for both rim seal designs at 1 % span. The values are normalized by the rotational speed of the rotor at the hub. The time axis covers three consecutive rotor blade passing events and the space axis covers one stator pitch. Positive radial velocities indicate that flow is leaving the hub cavity toward the casing of the machine, whereas negative radial velocity indicates that flow is entering the hub cavity (toward the axis of the machine).

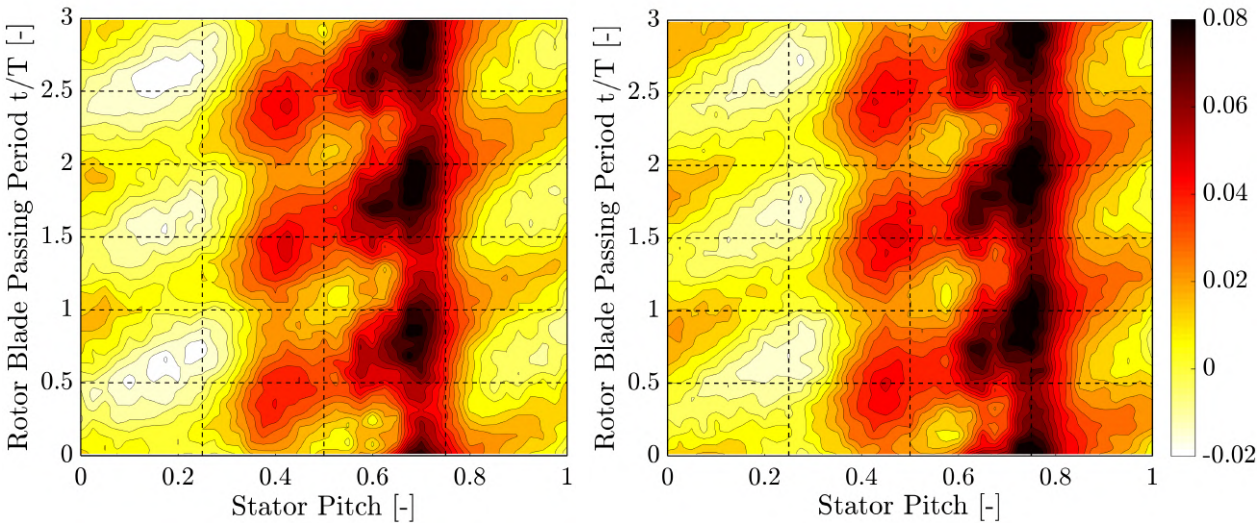

(a) Baseline **(b)** Purge Control Features (PCF)

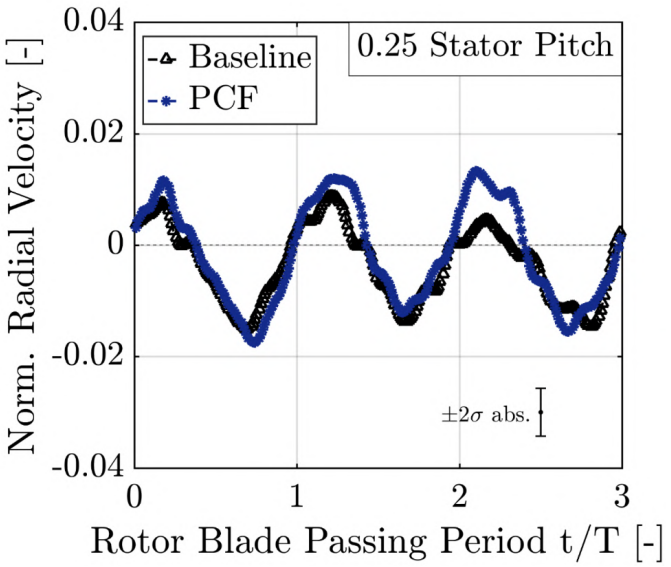

(c) Time-series at 0.25 Stator Pitch for both rim seal designs

Figure 4.12.: Space-time plots in the absolute frame of reference of the normalized radial velocity [-] at 1 % span for both rim seal designs operated under rim seal purge flow IR=0.8 % (FRAP)

Both plots show a vertical band of positive radial velocities at around 0.75

stator pitch. Within these bands, spots of pronounced positive radial velocities are found that are modulated by the rotor blade passing. These zones of high positive radial velocities are the signature of the purge flow leaving the hub cavity. Therefore, most of the purge flow is leaving the hub cavity at around 0.75 stator pitch. At this location, the hub secondary flow structures of the upstream stator 1 are present (Figure 4.10), which benefit the intrusion of purge flow into the main annulus by locally reducing the static pressure at the rim seal exit. The stator 1 secondary flow structures seem to decide where the purge flow is leaving the hub cavity, whereas the rotor decides when the purge flow is leaving the hub cavity.
Around 0.25 stator pitch, zones of moderate negative radial velocities are found for both the baseline as well as the purge control features. This indicates for the given purge flow rate of IR=0.8 % zones of ingress. Again, this effect is modulated by the rotor blade passing, suggesting that the potential field of the rotor leading edge is interacting with the upstream stator. By comparing the space-time plots of the baseline and purge control feature case, the peak positive radial velocity at around 0.75 stator pitch is increased for the PCF case by about 2 %. The negative radial velocity zones at around 0.25 stator pitch show a similar level of negative velocity which is pointed out in Figure 4.12 (c). Based on the available data, the modified rim seal design shows the potential of keeping a similar level of ingestion blockage by increasing the aerodynamic performance of the turbine.

4.2.3. Comprehensive Flow Model at the Rotor Inlet

The presented results in the previous section allow translating the main effects of the purge control features into a comprehensible flow model, which is shown schematically in Figure 4.13. The main aspects of the novel rim seal design focus on the realignment of the cavity fluid with the main annulus flow and the reduction of tangential shear across the rim seal interface, which was shown to have a beneficial impact on the rotor inlet flow field. The drivers identified to improve the flow effects at the rotor inlet can be formulated as follows:

- Counteract reduction in relative flow yaw angle (especially increase of relative flow yaw angle at rim seal interface β_{rim}) provoked by rim seal purge flow and hub secondary flow structures by aligning cavity flow closer to main annulus flow. Therefore, the negative incidence is reduced at the rotor inlet.

- Accelerate flow in circumferential direction (increase of $V_{\theta,rim}$) and reduction of tangential shear (reduced ΔV_θ). This leads to lower axial vorticity levels and lower total pressure losses close to the hub.

Both aspects are depicted in the flow model, which highlights the main drivers listed above employing rim seal and main annulus velocity triangles for both

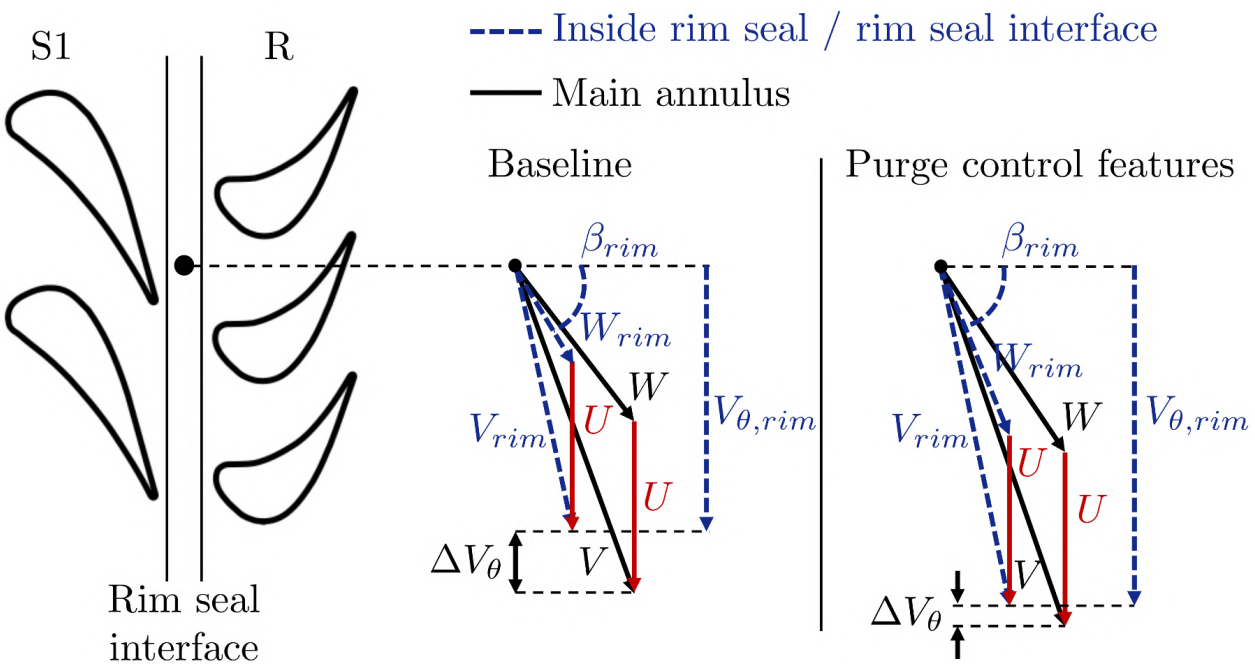

Figure 4.13.: Comprehensive flow model of purge control feature effects at rotor inlet by means of annulus and rim seal velocity triangles (not to scale). Velocity triangles consist of absolute flow velocity V, relative flow velocity W, blade speed U and circumferential velocity V_θ.

rim seal designs. One should consider the difference of the relative flow yaw angle at the rim seal interface β_{rim} and the different levels of the tangential shear indicated by the difference in tangential velocity ΔV_θ from the baseline and purge control feature geometry.

4.3. Impact of Purge Control Features on the Rotor Exit Flow Field

The flow field study at the rotor inlet needs to be complemented with an investigation of the aerodynamic effects at the exit of the rotor. The main effects of the novel rim seal design are provided in a follow-up section, specifically highlighting the impact of the purge control features on the performance parameters of the turbine stage. The analysis focuses on the two rim seal purge flow injection rates IR=0.8 % and 1.2 % as the purge control features are originally designed for moderate to high injection rates. To increase the measurement accuracy of the provided data, 5HP data are chosen for the comparison at the rotor exit. The time-resolved probe (FRAP) data were used to underline the effects seen in the pneumatically averaged data.
The flow field analysis is carried out for the basic quantities such as the relative flow yaw angle and the relative total pressure. In Figure 4.14 (left), the circumferentially mass- and time-averaged relative flow yaw angle distribution is depicted for both rim seal designs under purge flow injection IR=0.8 %. For

both configurations, a strong variation of the quantity is seen between 10 % and 40 % span, which is caused by the hub secondary flows. Typically, strong radial gradients of relative flow yaw (and relative circumferential velocity) provoke pronounced levels of axial and streamwise vorticity (Equation 2.27 and 2.28). The significant changes of the relative flow yaw angle above mid-span are indicative for the presence of the tip passage vortices and tip leakage vortex, which are addressed in more detail later in this section. The impact of the novel rim seal design can be better appreciated in Figure 4.14 (right), where the difference in the relative flow yaw angle for two purge flow injection rates is presented. The most pronounced change is detected at around 20 % span where the purge control features increase the relative flow yaw angle by 1° with respect to the baseline for the highest injection rate. Considering the relative flow yaw angle distribution at rotor inlet (Figure 4.7), the increase of the relative flow yaw angle at this span-wise coordinate suggests a very moderate increase of flow turning. In the rest of the span, moderate changes can be seen. At 70 % span, an increase up to 0.5° is measured, whereas at 80 % span the relative flow yaw angle is reduced by about 0.5° for both injection rates in case the features are installed.

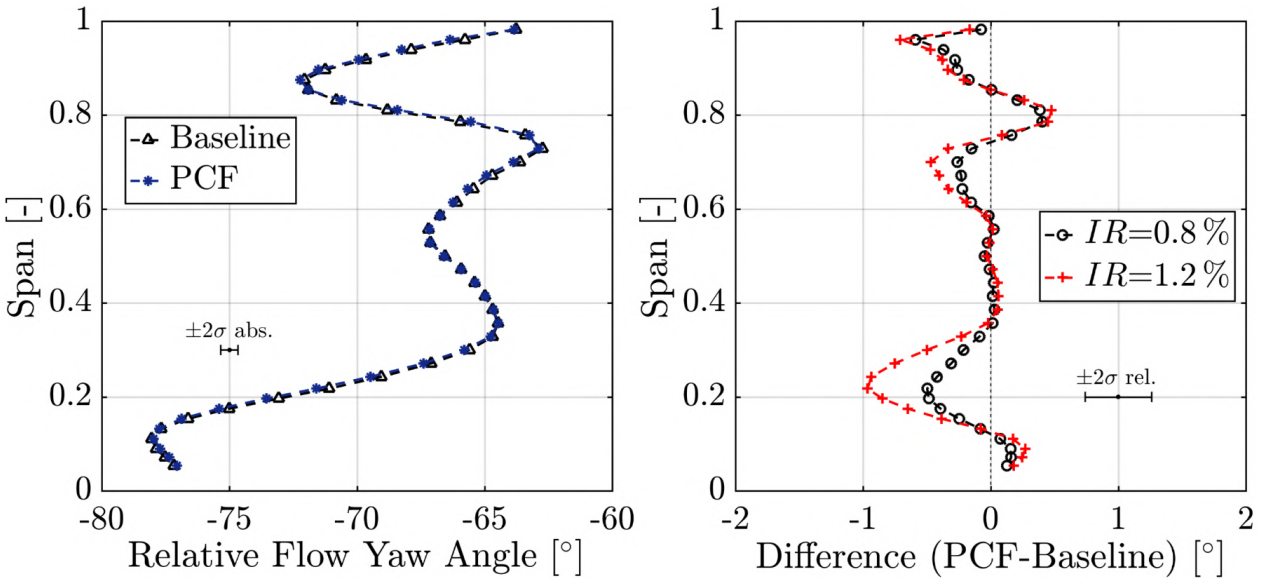

Figure 4.14.: Mass- and time-averaged relative flow yaw angle comparison (5HP) between baseline and PCF rim seal for nominal injection rate IR=0.8 % (left), change in relative flow yaw angle for two injection rates (right)

In order to assess the impact of the purge control features on the aerodynamic losses at the rotor exit, the relative total pressure is an appropriate starting point. In Figure 4.15, the circumferentially mass- and time-averaged normalized relative total pressure is depicted for the purge flow cases IR=0.8 % and IR=1.2 % measured with the 5HP. Again, the pressure data are normalized by the respective turbine inlet total pressure. The relative total pressure profiles reveal the performance increase by means of reduced losses in the relative

frame of reference. Specifically, the region between 50–80 % span, shows an increase in relative total pressure up to 0.5 % for the purge control feature case (IR=0.8 %). This trend is in agreement with the increase in total-to-total stage efficiency presented in Figure 4.1 (left). A relative total pressure increase up to 0.3 % (IR=0.8 %) in close vicinity to the hub is shown when the purge control features are installed. Not only the close mid-span and hub regions are affected by the change of the rim seal exit geometry, but also the tip region.

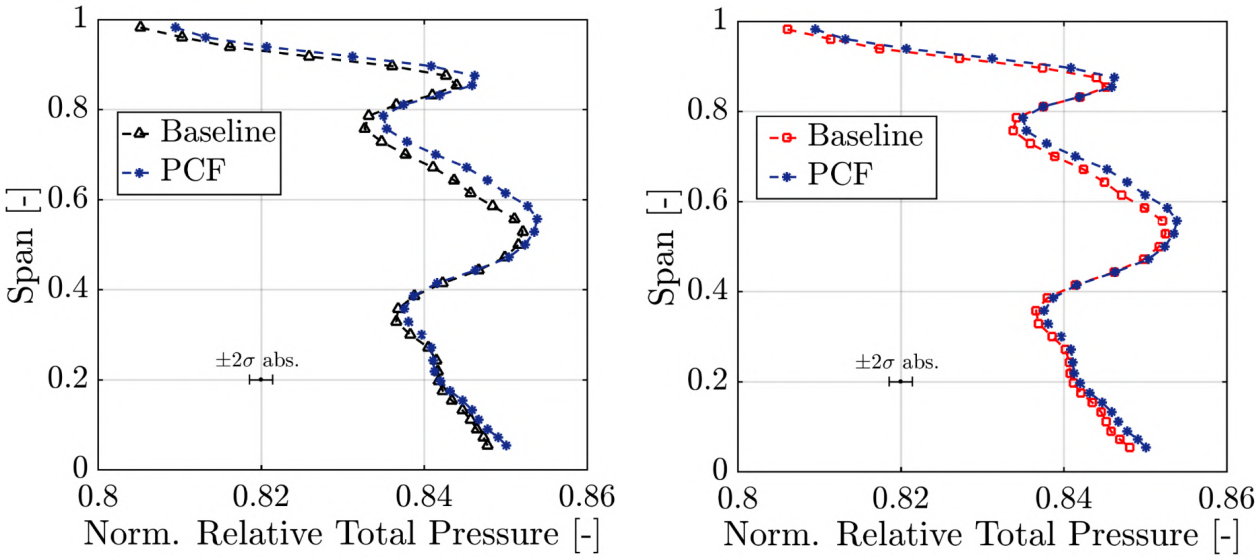

(a) $IR = 0.8\,\%$ **(b)** $IR = 1.2\,\%$

Figure 4.15.: Mass-averaged normalized relative total pressure $C_{pt,rel}$ for both rim seal geometries at rotor exit for two rim seal purge flow injection rates (5HP)

The mass-averaged flow investigation needs to be supported by the pitch-wise resolved flow field in order to reveal zones of improvement. In Figure 4.16, the contour diagrams of the normalized relative total pressure in the rotating frame of reference are shown for both rim seal exit geometries and nominal purge flow injection IR=0.8 % measured with FRAP.
The traces of the tip leakage vortex (zone **(3)**) and the tip passage vortex (zone **(2)**) are seen at 95 % span and 70 % span, respectively. The rotor hub secondary flow structures are observed around 40 % span (zone **(1)**). By comparing Figure 4.16 (a) and (b), the purge control features do not lead to a radial displacement of the secondary flow structure loss cores. The beneficial impact of the PCF is found in Figure 4.16 (c) where the time-averaged increase of relative total pressure in percentage is presented. Regions of increase in relative total pressure up to 3 % are located along the span where the rotor wake and the trailing edge shed vortices dominate (40 % and 70 % span). It is anticipated that the reduction of the negative incidence on the rotor leading edge leads to a reduction of the rotor profile losses, which is demonstrated in Figure 4.16 (c) by highlighting the regions of highest improvements induced by the purge control features.

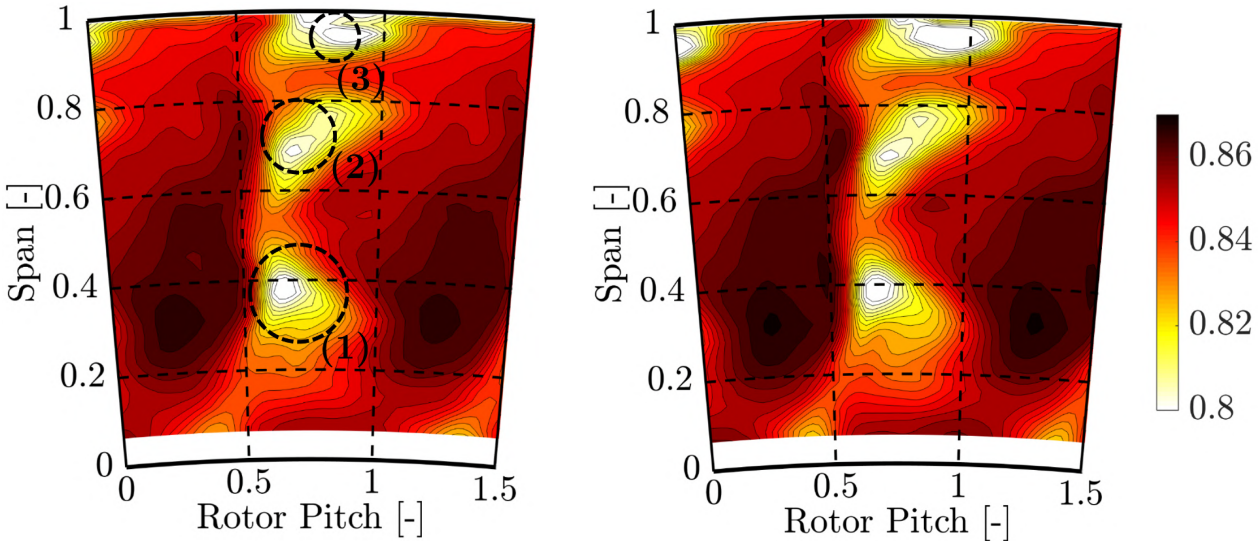

(a) Baseline

(b) Purge Control Features (PCF)

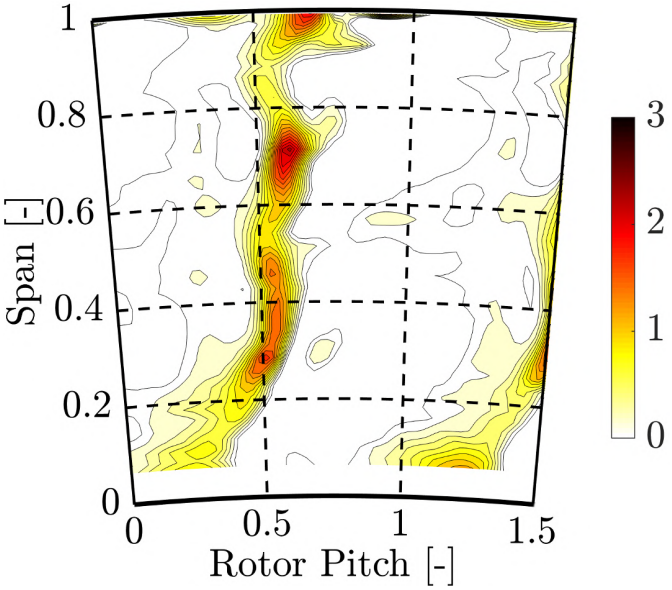

(c) Difference (PCF-Baseline)

Figure 4.16.: Time-averaged normalized relative total pressure $C_{pt,rel}$ [-] and difference $\Delta C_{pt,rel}$ [%] in rotating frame of reference for both rim seal designs operated under IR=0.8 % (FRAP)

Furthermore, the time-resolved effects are investigated where pronounced improvement is present at 70 % span. In Figure 4.17, the space-time plots of the normalized relative total pressure in the rotor relative frame of reference for two consecutive vane passing events are presented. For both rim seal designs a vertical band (0.65 stator pitch) of low relative total pressure is found, which is the signature of the rotor hub secondary loss core. The loss core is a stationary flow feature in the rotating frame of reference and therefore appearing as a vertical band. Moreover, the total pressure losses induced by the secondary flow structures are found to be modulated by the upstream stator row, which is reflected in the inclined bands of low relative total pressure.

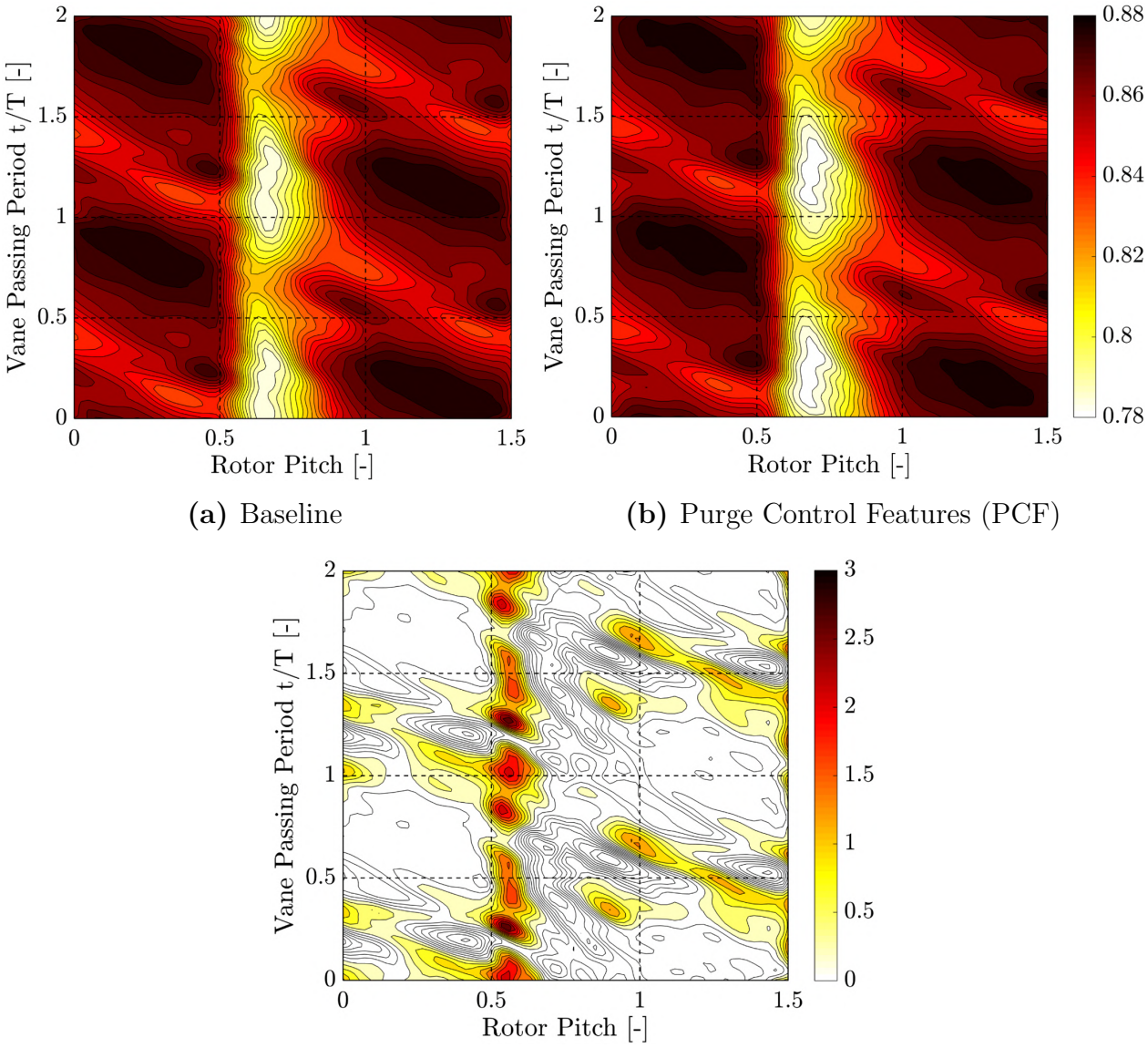

(a) Baseline

(b) Purge Control Features (PCF)

(c) Difference (PCF-Baseline)

Figure 4.17.: Space-time plots in the relative frame of reference of the normalized relative total pressure $C_{pt,rel}$ [-] difference $\Delta C_{pt,rel}$ [%] at 70 % span for both rim seal designs operated under rim seal purge flow IR=0.8 % (FRAP)

In Figure 4.17 (c), the time-resolved increase of the relative total pressure is depicted, highlighting that the purge control feature case performs better in the region which is dominated by the rotor secondary flow structures and wake. An increase of up to 3 % was found for the purge control features. Additionally, the PCF case seems to perform better in the region, which is induced by the upstream first stator flow (inclined bands, Figure 4.17 (c)). This might be the result of the improved flow field that was detected at rotor inlet which is convected through the rotor passage.

A similar assessment as for the relative total pressure can be conducted for the non-deterministic pressure unsteadiness $p'_{1,rms}$. In Figure 4.18 (a) and (b), the contour diagrams and circumferentially area-averaged pressure unsteadiness

is depicted. The contour diagrams reveal the signature of the secondary flow structures in the rotating frame of reference by means of high-pressure unsteadiness levels.

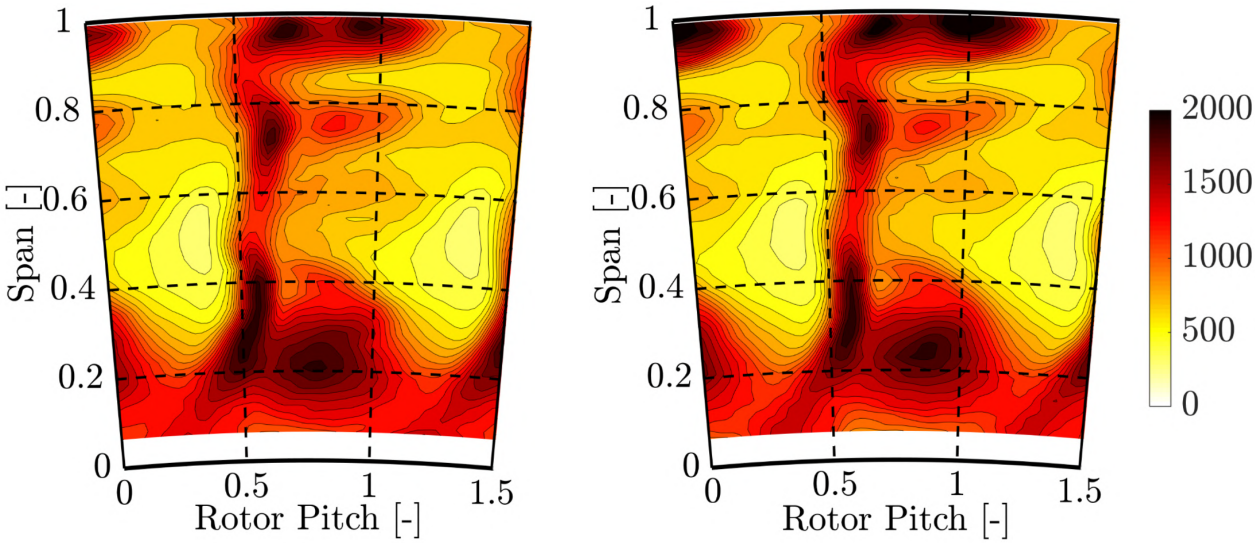

(a) Baseline **(b)** Purge Control Features (PCF)

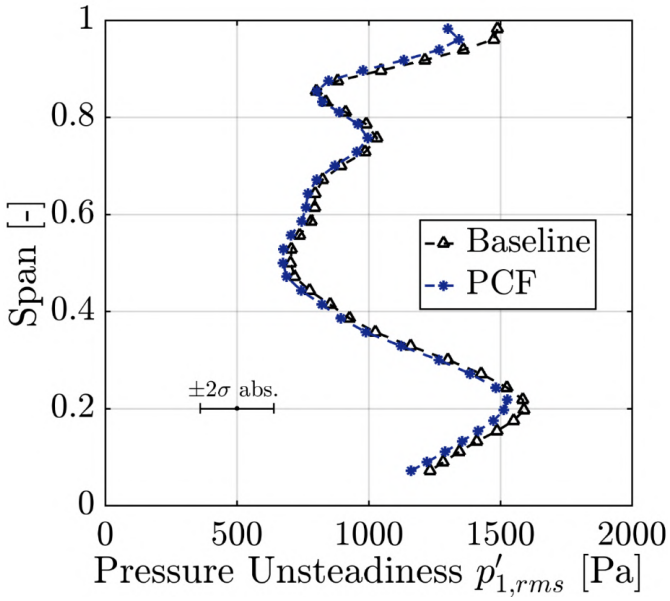

(c) Circumferentially area-averaged distribution

Figure 4.18.: Time-averaged pressure unsteadiness $p'_{1,rms}$ [Pa] in rotating frame of reference and area-averaged distribution for both rim seal designs operated under IR=0.8 % (FRAP)

The flow structures have already been identified and introduced in Figure 4.16. Based on the pitch-wise resolved pressure unsteadiness, it is hard to identify the difference between the two configurations. In Figure 4.18 (c), the circumferentially area-averaged pressure unsteadiness is shown. Generally, the purge control feature case shows a very moderate reduction in the stochastic pressure unsteadiness across the whole span, but specifically in close vicinity to

the hub. Especially the hub region agrees with the trend shown in the relative total pressure profiles (Figure 4.15). Nevertheless, it must be considered that the changes are small and within the measurement uncertainty band. Furthermore, a change in the unsteadiness levels cannot be directly translated into a change of aerodynamic losses.

In the total-to-total stage efficiency distribution, provided in Figure 4.1 (left), it was shown that the aerodynamic performance is improved over most of the span. This also asks for an investigation of the basic turbine quantities, such as stage loading ψ and flow coefficient ϕ. The stage loading coefficient would indicate a change in the flow turning in the absolute frame of reference, whereas the flow coefficient detects the change in the mass flow distribution. The two quantities are defined as follows:

$$\psi = \frac{\Delta V_\theta}{U} \tag{4.2}$$

$$\phi = \frac{V_x}{U} \tag{4.3}$$

Where ΔV_θ is the change in the absolute circumferential velocity across the rotor, U the blade speed, V_x the axial flow velocity. In Figure 4.19, the circumferentially mass- and time-averaged stage loading and flow coefficient are presented for the design purge flow injection rate IR=0.8 %. The stage loading distribution indicates that the flow is turned most close to the rotor hub, whereas less turning is present at the tip in order to unload the tip region. Comparing both rim seal designs, Figure 4.19 (left) illustrates that there is no significant change in the stage loading coefficient across the whole span. The flow coefficient radial distribution shows that most of the mass flow is within 30–80 % span. The hub and tip regions only cover a moderate share of the total mass flow. Again, no significant change in the flow coefficient is observed (changes are well within measurement uncertainty). Both quantities do not present a considerable change, which suggests that the work extracted out of the fluid is comparable, and the turbine capacity has not changed substantially. Therefore, the purge control features do not change the torque or work output of the turbine but provide the same work output more efficiently. This is also reflected in the mass flow specific torque $M/\dot{m}_{main}$, which shows that the difference between the purge control feature case and the baseline rim seal is only 0.07 % (IR=0.8 %).

Based on the provided analysis, the purge control features are classified as aerodynamic loss reduction features. As the work extraction is not substantially changed, the only way of increasing the stage efficiency levels is by increasing the total pressure levels (Equation 2.36). Figure 4.20 shows the

circumferentially mass- and time-averaged absolute total pressure profiles for the two purge flow injection rates IR=0.8 % and IR=1.2 %.

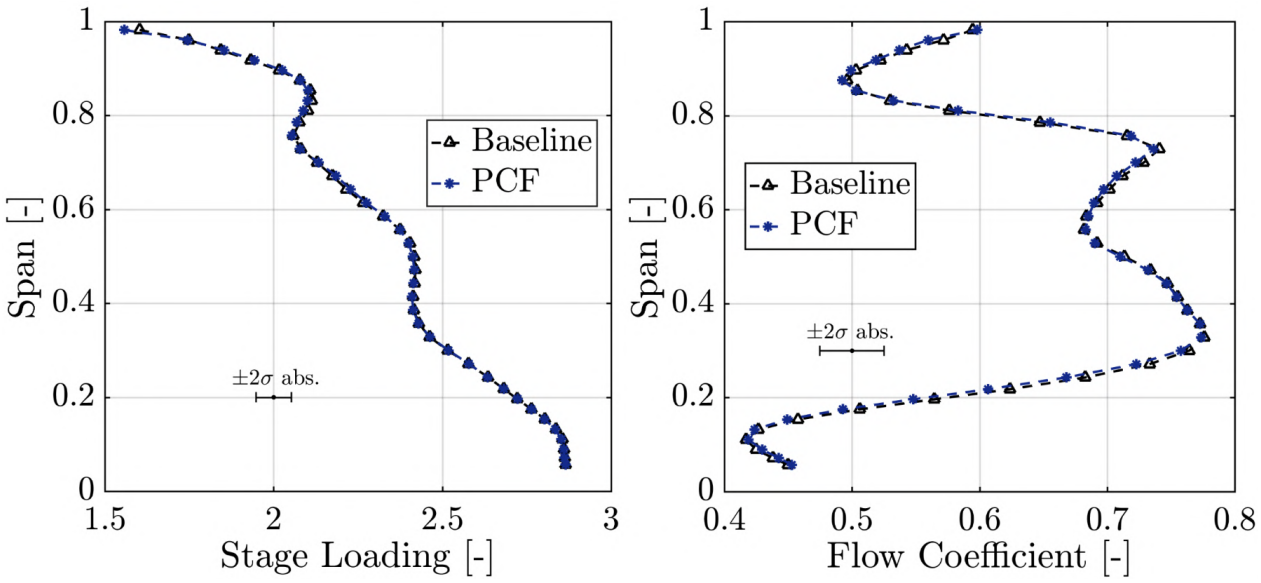

Figure 4.19.: Mass- and time-averaged stage loading (left) and flow coefficient (right) of the baseline and PCF rim seal for nominal injection rate IR=0.8 % (4HP and 5HP)

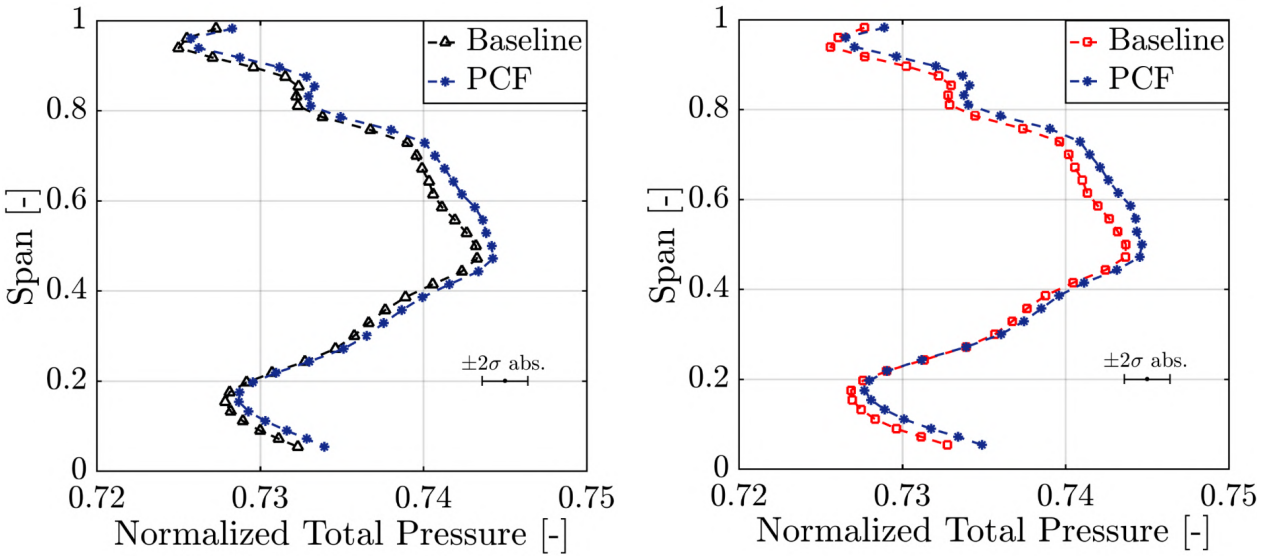

(a) $IR = 0.8\,\%$ **(b)** $IR = 1.2\,\%$

Figure 4.20.: Mass-averaged normalized absolute total pressure C_{pt} for both rim seal geometries at rotor exit for two rim seal purge flow injection rates (5HP)

The novel rim seal design provides higher total pressure above 50 % span for both injection rates. Additionally, also the lower span-wise regions between 6–18 % are improved for the purge control feature case. It is interesting to see that the features that are installed at the rim seal exit have a positive impact on the rotor exit flow field even above mid-span. Part of this improvement is anticipated to be linked to the reduced profile losses, which are detected by

the relative total pressure distribution (Figure 4.16). Another effect might be linked to the rotor inlet flow field, where across the whole span a higher total pressure level is detected (Figure 4.11). As the work extraction between the two cases is very comparable, the improved rotor inlet flow field contributes to an overall improvement of the stage performance.

4.4. Purge Control Features against Hub Cavity Modes

In the previous chapter, an extensive analysis of the low-frequency, non-synchronous flow excitation in the hub cavity was performed. The rotating flow structures are found to interact with the main annulus flow. Since the purge control feature turbine configuration has the same rim seal design (at least for the baseline case), it is worth to investigate the impact of the novel rim seal design on the characteristics of the low-frequency modes. As described in Chapter 3, the presence and strength of the hub cavity modes depends on the injected rim seal purge flow. For the current analysis, a purge flow injection rate of IR=0.8 % is chosen due to the strong presence of the modes, and since measurements at IR=0.4 % have not been performed. It is important to remember that the airfoils and end walls were changed compared to the unsteady cavity flow configuration introduced in section 2.2.1.
A starting point to track the non-synchronous flow excitation, which is not linked to the blade passing and its harmonics, is to investigate the non-deterministic pressure unsteadiness. This quantity shows increased levels when flow features are present that are not only modulated by the blade passing. Figure 4.21 depicts the measured time-averaged pressure unsteadiness $p'_{1,rms}$ for both rim seal designs for the purge flow injection rate IR=0.8 %. Of specific interest are the lower span-wise positions as it is expected that the cavity modes are well detectable at the rim seal exit. Therefore, a close-up view at the interface between the hub cavity and main annulus (−20 % to +20 % span) is provided. Elevated levels of the stochastic pressure unsteadiness are found for both rim seal designs where the first stator wake (dashed black line) and hub secondary flow structures **(1)** are appearing.
When the FRAP is immersed into the hub cavity (0 to −20 %), it detects pronounced pressure unsteadiness over the whole stator pitch. Therefore, it is anticipated that the non-synchronous modes are specifically strong in their presence within this span-wise coordinate range. When comparing both rim seal designs in relation to pressure unsteadiness, it appears that the occurrence of potential modes is of similar strength. However, this statement needs to be supported by a pressure frequency analysis within the hub cavity, especially since the non-deterministic pressure unsteadiness contains not only

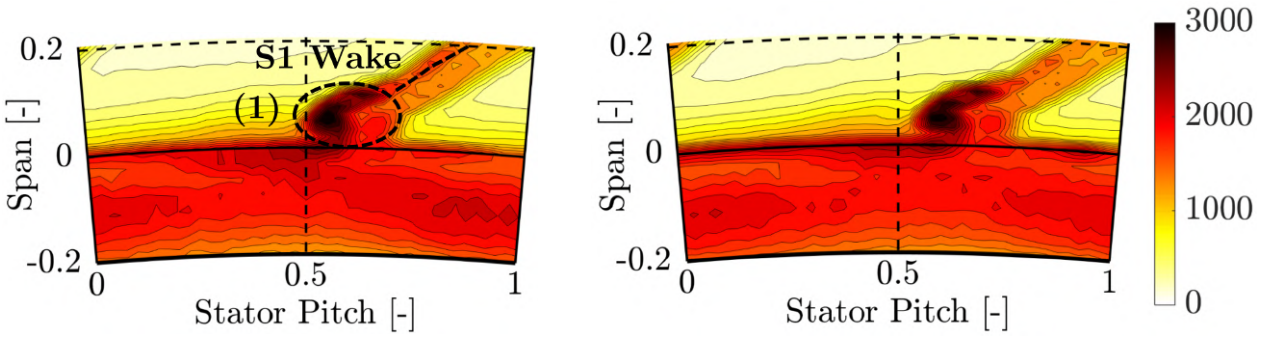

(a) Baseline **(b)** Purge Control Features (PCF)

Figure 4.21.: Time-averaged pressure unsteadiness $p'_{1,rms}$ [Pa] in absolute frame of reference at S1 exit for both rim seal designs operated under IR=0.8 % (FRAP)

one frequency but also frequency content that is linked to turbulence occurrence. To study the low frequency content in the pressure field, this content needs to be extracted out of the pressure frequency spectrum of each measurement point. Before doing so, the presence and frequency content of potential low-frequency cavity modes has to be checked for this turbine configuration.
In Figure 4.22, the pressure frequency spectra at -1 % span and 0.6 stator pitch is depicted for both rim seal designs and a purge flow injection rate of IR=0.8 %. The specific circumferential position was chosen because of the strong interaction between the cavity fluid and the main annulus flow due to the presence of the first stator hub secondary flow structures. The pressure amplitude is normalized by the respective turbine inlet total pressure. The frequency is given as a fraction of the rotor blade passing frequency f_{RBPF}. The dominant frequency for both rim seal designs at this specific location is the blade passing frequency $f/f_{RBPF} = 1$. The harmonic of the rotor blade passing frequency is clearly visible at $f/f_{RBPF} = 2$.
Nevertheless, some non-synchronous low-frequency content is detected by the FRAP within a frequency range of 29–39 % of the rotor blade passing frequency, where the dominant peak is around 34 % of the f_{RBPF}. In comparison to the investigations provided in Chapter 3, the frequency content is comparable for the same purge flow injection rate (25–35 % of f_{RBPF}). Both rim seal designs contain the specified frequency content which is termed with “Cavity Modes” in the figure. For the baseline rim seal, the maximum pressure amplitude, which is associated with the cavity mode, is about 70 % of pressure amplitude induced by the blade passing. The purge control features show a significant reduction (factor 1.8) of the pressure amplitude for the same frequency which suggests that the features can reduce the strength of these modes. The peak in the pressure amplitude which is even at a lower frequency (18.5 % of f_{RBPF}) than the cavity mode is found to be a multiple of the rotational speed of the rotor (10-times) which is anticipated to be a duct mode provoked by the 10 injection tunnels of the bypass flow in the lower hub cavity.

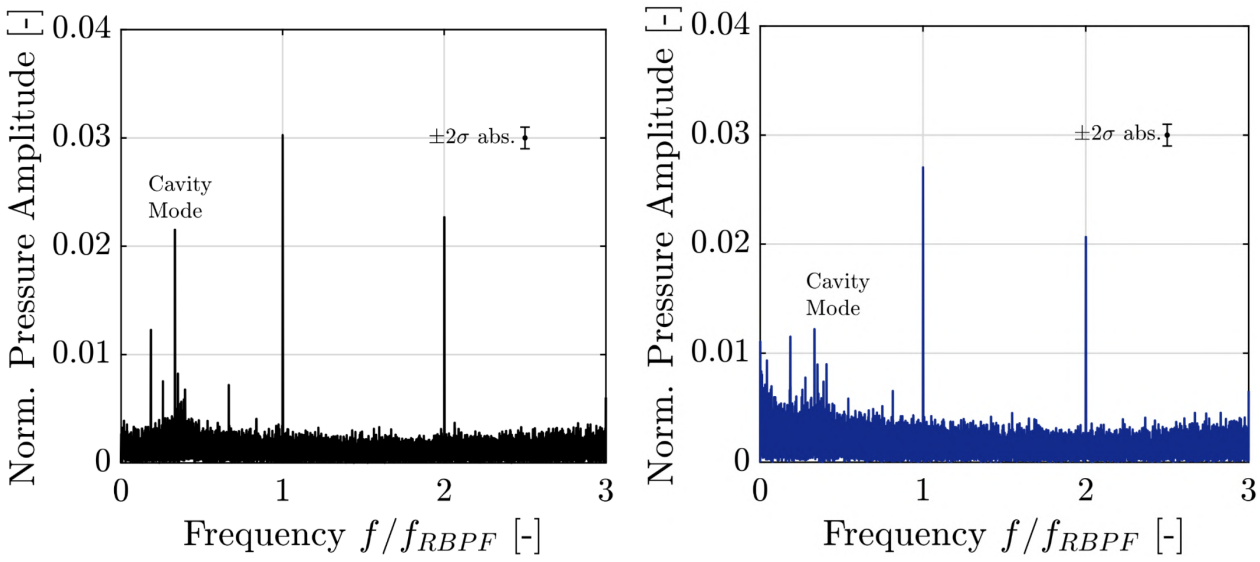

(a) Baseline **(b)** Purge Control Features (PCF)

Figure 4.22.: Experimentally determined pressure frequency spectra for both rim seal designs at -1 % span and 0.6 stator pitch for IR=0.8 % (FRAP)

The pressure frequency spectra, provided in Figure 4.22, suggest that the purge control features have a beneficial impact on the strength of the hub cavity mode at IR=0.8 %. To underline this statement, the pressure amplitude of the mode must be spatially resolved which would provide more confidence. Therefore, the pressure frequency spectrum of each measurement point was calculated when the FRAP yaw pressure tap is aligned with the mean flow direction. The maximum pressure amplitude of the frequency spectra has then been extracted within the frequency bandwidth in which the cavity mode is expected (29–39 % of f_{RBPF}). The result of this procedure is depicted in Figure 4.23 for both rim seal designs. The amplitude is normalized with the respective turbine inlet total pressure. For both rim seal designs, the most pronounced pressure amplitude is found right at the hub, where the presence of the first stator hub secondary flows seems to benefit the excitation (0.6 stator pitch). The measured peak pressure amplitude at 0.6 stator pitch and 1 % span is reduced by a factor of up to 2 for the purge control feature configuration. In general, the measurements show that the novel rim seal design reduces the pressure amplitude of the mode in the upper hub cavity (−20 % to 0 % span) by factors up to 2.5.

The measurements reveal a tendency of the purge control features to attenuate the strength of the non-synchronous low-frequency modes. Based on the flow field effects that were described in section 4.2.2, it is anticipated that the reduction in tangential shear across the interface between hub cavity and main annulus flow has a beneficial impact on reducing the pressure amplitude of these modes. Furthermore, one should recall that the ingress in the upper hub cavity is not substantially changed—most likely due to the imparting of

radial momentum to the cavity fluid. The combination of reducing the radial gradient of the circumferential velocity and sustaining the radial momentum of the purged cavity fluid is therefore interpreted as a driver diminishing the presence of the low-frequency hub cavity mode.

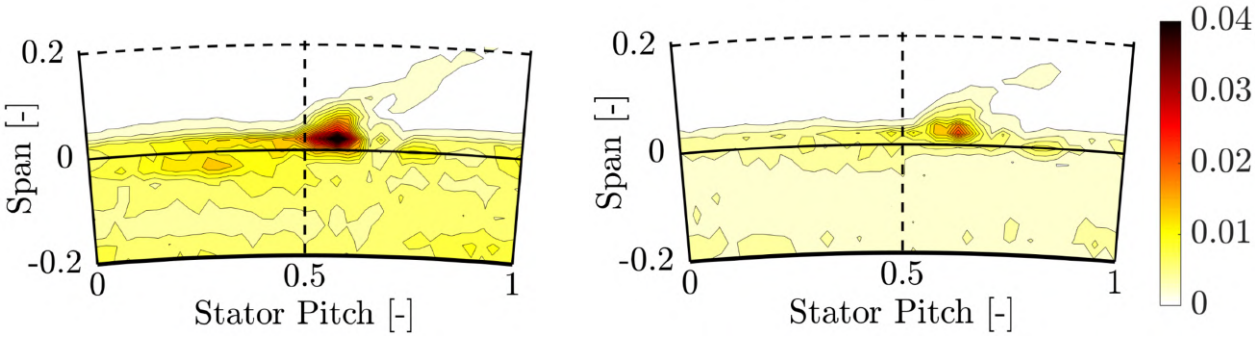

(a) Baseline **(b)** Purge Control Features (PCF)

Figure 4.23.: Experimentally determined normalized peak pressure amplitude [-] of the hub cavity mode at $f/f_{RBPF} = 34\,\%$ for both rim seal designs and IR=0.8 % (FRAP)

4.5. Complementary Unsteady Computations for Hot Gas Ingestion

To this point, the presented chapter described the flow field behavior in the presence of the purge control features by means of aerodynamic probe measurements at two axial planes. Since the probes can spatially and temporarily resolve the aerodynamics at discrete axial planes, complementing unsteady computations would contribute to a deeper understanding of the features. Furthermore, the computations could help to assess the difference in the ingestion behavior of the two rim seal designs. In this section, results of unsteady Reynolds-averaged Navier–Stokes (RANS) calculations of the 1.5-stage domain are presented for both rim seal designs and a purge flow injection rate of IR=0.8 % with special focus on the hot gas ingress. Note that the mesh generation, as well as the conduction of the simulations, was carried out in the framework of a master's thesis at the laboratory in collaboration with Bagnara [5].

The hot gas ingestion into the hub cavities is typically associated with the pumping effect of the centrifugal forces acting in the boundary layer at the rotor-sided surface of the cavity as well as to the circumferential non-uniformity of the pressure field at the cavity interface provoked by the vane-to-blade interaction [77]. The altering circumferential pressure field induces radial velocities at the cavity exit that vary between positive (toward casing) and negative (toward the axis of the machine), which implies egress (purge) and ingress,

respectively. This behavior is reflected in Figure 4.24 where the normalized radial velocity at a specific time instant is displayed for the baseline rim seal. The data is normalized by the blade speed at the hub. The interaction of the first stator flow field with the rotor leading edges generates local high static pressure regions which are exceeding the static pressure levels inside the upper hub cavity, which forces part of the main annulus flow to penetrate into the cavity (downward pointing arrows). These regions are characterized by negative radial velocity and are termed as locations of ingestion.

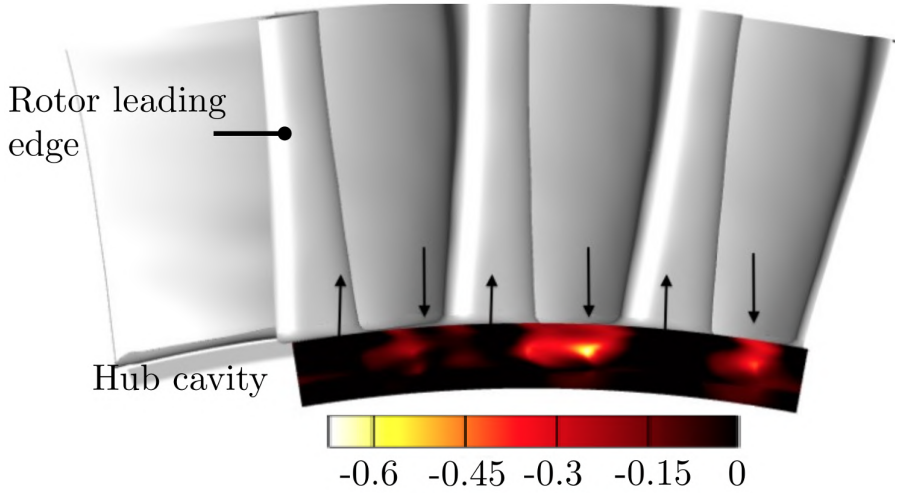

Figure 4.24.: Axial slice of instantaneous normalized radial velocity [-] at the interface between hub cavity and main annulus flow for the baseline rim seal and IR=0.8 % (CFD, adapted from [5])

On the other hand, the presence of the rotor blade suction side lowers the static pressure in time such that the cavity static pressure exceeds the one in the main annulus. Cavity fluid is therefore purged into the main annulus flow (egress, outwards pointing arrows). In conclusion, the blade passing modulates the time-dependent mass flow exchange between the hub cavity and the main annulus. To investigate the effect of the purge control features on the radial velocity distribution in close vicinity to the hub, Figure 4.25 (a) displays the normalized radial velocity contour at 3 % span for the baseline rim seal which covers the rim seal exit and part of the rotor passage. The pitch-wise alternating patterns between ingress and egress are visible, again where positive radial velocity implies egress and negative radial velocity, ingress. The constant radius plane reveals that indeed, the presence of the rotor blade suction side benefits the purging of the cavity fluid. When considering Figure 4.25 (b), it is seen that locally a pronounced increase by up to 20 % in the radial velocity is predicted when the purge control features are installed (specifically, six zones of significant increase in radial velocity, which are aligned with the rotor-sided purge control features). The imparting of additional radial momentum by the purge control features is in agreement with the stated design intentions in section 2.2.2. The blanked regions of the negative radial velocity delta

correspond to the ingestion zones characterized by increased negative radial velocity. As the circumferential alteration of the radial velocity is pronounced, the effective ingress mass flow should be calculated at the rim seal interface such that a final assessment can be provided.

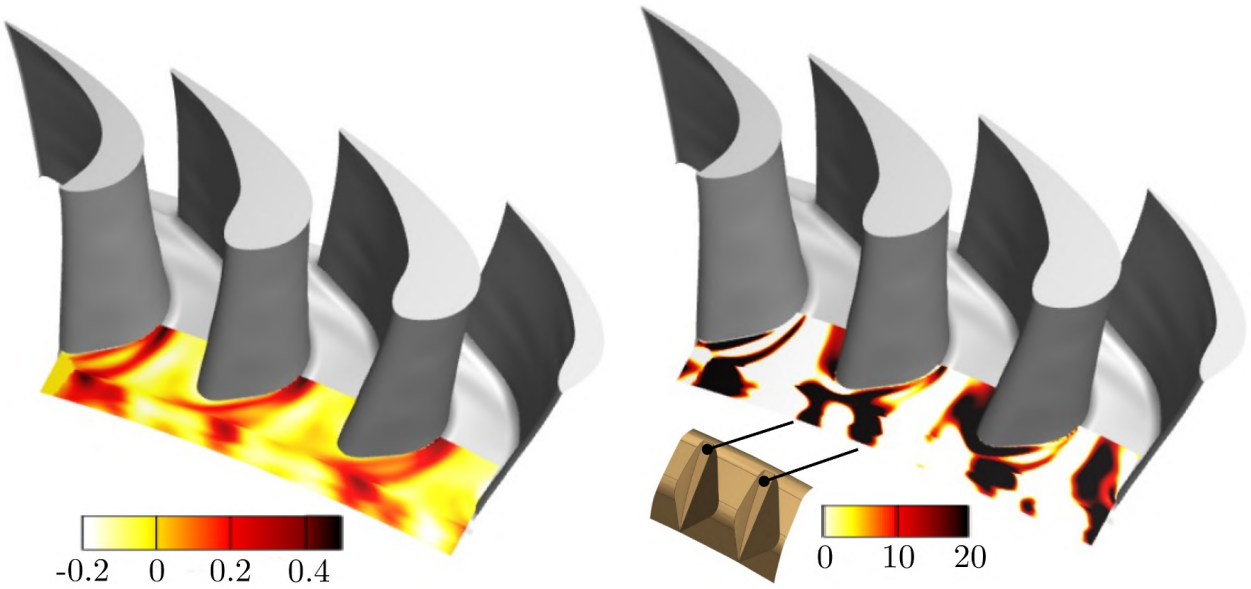

(a) Baseline **(b)** Percentage difference (PCF-Baseline)

Figure 4.25.: Normalized radial velocity contours [-] of the baseline rim seal and difference of radial velocity [%] at 3 % span for IR=0.8 % (CFD, adapted from [5])

At two radial planes, the instantaneous ingress mass flow is calculated along the axial extent of the cavity for each circumferential position. The radial plane **(I)** is located right at the exit of the hub cavity (0 % span), whereas plane **(II)** is defined inside the hub cavity at −14 % span. Both planes are schematically shown as insets of Figure 4.26. The figure presents a distribution of the ingress mass flow as a percentage of the turbine mass flow through the sector model for two stator pitches. At the exit of the cavity, three peaks are predicted along the stator pitch, which are associated with the presence of the three rotor blades that locally increase the static pressure at the rim seal interface and provoke ingress. The purge control feature configuration presents a higher peak ingress mass flow (+0.07 %) at 1 stator pitch compared to the baseline case. However, the integral ingress mass flow ratio which is integrated over the whole radial plane is for the baseline case about 0.62 %, and for the PCF case 0.6 %. Despite the larger peak ingress mass flow, the ingestion zone for the PCF case is pitch-wise more concentrated. The smaller circumferential extent implies that the penetration depth of the ingress might be increased. Hence, a similar assessment is provided for the radial plane **(II)** (Figure 4.26 (right)).
In contrast to the distribution provided in Figure 4.26, the mass flow profiles at plane **(II)** only reveals two pronounced bands of higher ingress for both

rim seal designs. It is anticipated that rotor-stator interaction strength is, pitch-wise, not uniform due to the vane-to-blade count ratio such that the strength of the ingestion zones is also non-uniform along the circumference. Therefore, some fraction of the ingress mass flow does not reach the lower span-wise position and only recirculates close to the cavity exit. Nevertheless, the PCF case shows at 1 stator pitch a higher ingress mass flow, which is expected to be linked to the larger peak at Figure 4.26 (left). The integrated ingress mass flow over the plane is again very comparable for both rim seal designs; the baseline rim seal is calculated to have 0.4 % of the turbine mass flow as ingress, whereas 0.38 % is calculated for the purge control feature configuration.

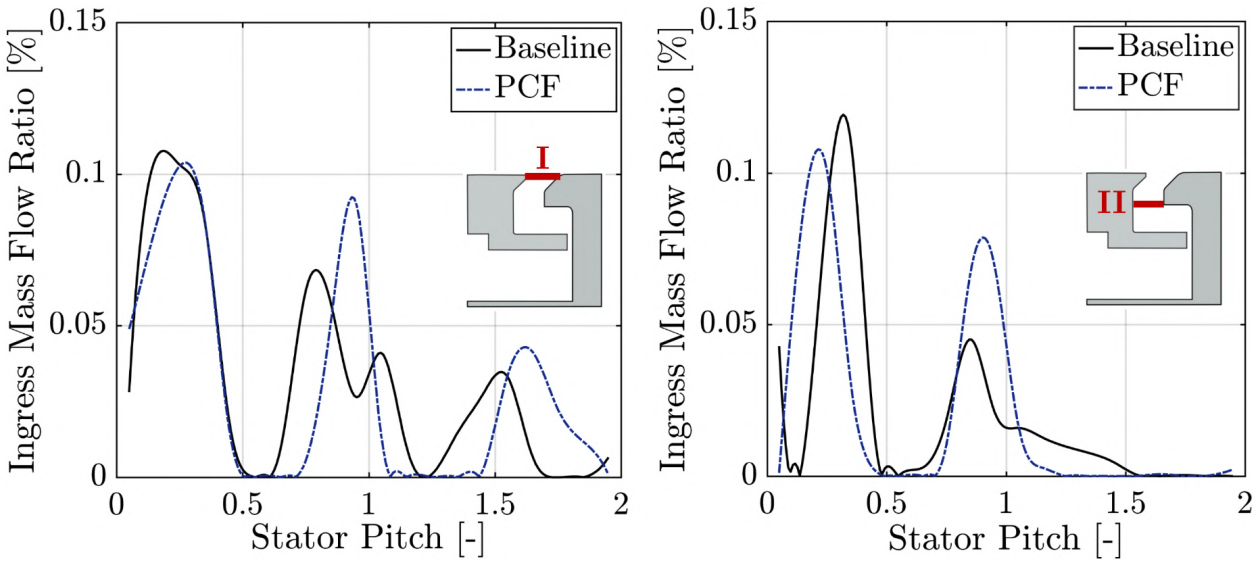

Figure 4.26.: Instantaneous distribution of ingress mass flow ratio for radial plane **(I)** and **(II)** and both rim seal designs at IR=0.8 % (CFD, adapted from [5])

To complement the hot gas ingestion assessment, it is convenient to translate the extracted mass flows from the computational fluid dynamics calculations into a sealing effectiveness. The University of Bath defined an orifice model [128, 129] that can cope with different types of ingestion mechanisms, for instance, externally induced ingress, rotationally induced ingress, and combined ingress. Within the derivation of this model, the authors suggest defining sealing effectiveness as a mass flow ratio between the sealing mass flow and the sum of ingress mass flow and sealing mass flow through a specified orifice ring (Equation 4.4).

$$\varepsilon = \frac{\dot{m}_{sealing}}{\dot{m}_{ingress} + \dot{m}_{sealing}} \tag{4.4}$$

The time-averaged flow field is used to derive the integral mass flows for this definition, not the instantaneous flow field. In Table 4.1, the resulting mass flow-based sealing effectiveness ε is provided for both rim seal designs with

respect to the two radial planes **(I)** and **(II)**. For both radial planes, the purge control feature case shows moderately higher sealing effectiveness by up to 4 %. Note that the major part of the sealing (with lower purge flows) is provided by the buffer arm, which is located well below the two radial planes. Nevertheless, it is encouraging to see that the novel rim seal design does contribute to additional sealing against the hot gas ingestion at a larger radius than the buffer sealing arm.

Table 4.1.: Sealing effectiveness ε [-] based on sealing and ingress mass flows for IR=0.8 % for both rim seal designs (CFD)

Rim Seal Design	Plane **(I)**	Plane **(II)**
Baseline	0.825	0.954
PCF	0.853	0.998

From a combined judgment, including the experimentally determined radial velocity distribution and the CFD calculations, the purge control feature does not provoke additional hot gas ingestion into the upper hub cavity. The predictions even suggest that the features contribute to additional sealing at a larger radius than the sealing arm for a nominal purge flow rate of 0.8 % of the turbine mass flow. When reconsidering the design features regarding the potential to block hot gas, it is implied that it is beneficial to impart additional radial momentum to the cavity fluid in close vicinity to the rim seal exit. Part of the ingestion blockage can also be attributed to the reduction in tangential velocity difference over the interface between the hub cavity and the main annulus. As the circumferential velocity deficit at the exit of the cavity is reduced, so is the static pressure difference between main annulus and cavity according to the radial pressure gradient expression (Equation 4.1).

4.6. Conclusions

The presented chapter underlines the potential to reduce the aerodynamic efficiency deterioration due to the injection of rim seal purge flow by integrating novel geometrical features, termed as “purge control features,” right at the interface between the hub cavity and the main annulus. The absolute stage efficiency increase due to the features was determined to be 0.4 % points with respect to an already optimized turbine configuration operated under the same purge flow rates. The sensitivity of the stage efficiency to purge flow has been reduced by about 18 % when the purge control features are installed which improves the flexibility of the purge flow design range. The study proposes two effective measures—induced by the geometrical features—to enhance the

turbine stage performance in the presence of purge flow: realignment of the vented cavity fluid with the main annulus and tangential shear reduction over the interface between hub cavity and main annulus.
The qualitative assessment of the ingestion characteristic of the novel features found a higher potential to block hot gas from the main annulus. Imparting radial momentum by rotor-sided geometrical features, installed right at the exit of the rim seal, is therefore favorable to discourage ingress mass flow. The combination of tangential and radial acceleration of the vented cavity fluid, promoted by the features, is expected to outperform conventional pre-swirl approaches.
The implementation of geometrical features at the exit of the rim seal attenuated substantially (factor 2.5) the low-frequency, asynchronous flow perturbations inside the hub cavity. It is consequently anticipated that increasing the radial momentum and reducing the tangential shear at the interface between cavity and main annulus should be targeted by the designer in order to eliminate hub cavity modes.
Overall, the presented chapter proposes a geometrical solution at the rim seal exit to overcome the trade-off between aerodynamic performance increase and penalties in hot gas ingestion blockage. Besides the aerothermal implications of the novel rim seal design, the attenuation of low-frequency flow excitation within the hub cavities is anticipated to beneficially contribute to the aeroacoustics and rotor dynamics of the turbine.

5. Ingestion and Hub Cavity Heat Transfer

The first stage of the high-pressure turbine section in gas turbines is subjected to substantial thermal loads. Along with the vanes and blades in the main annulus, the disk cavities need to be supplied with cooling air in order to prevent overheating of sensitive components such as bearings and shaft and control the thermal stresses in the rotor disk. In that context, purge flow is used as active cooling air to reduce the temperature on the rotating components and discourage the ingestion of hot gas into the hub cavity. In order to make the most efficient use of the supplied cooling flow, the detailed knowledge of the convective heat transfer characteristics and ingestion dynamics is required. Additionally, the wall-temperature distributions within the hub cavities are necessary to know in order to predict stress levels and durability which in turn have a direct effect upon the rotor disk dimensions, the radial positioning and blade tip gaps. In open literature, most studies dedicate their research focus on the hot gas ingestion quantification, whereas the convective heat transfer characteristics are rarely addressed, especially for rotating rigs equipped with vanes and blades.

In the presented chapter, the hot gas ingestion dynamics and the convective heat transfer in an engine-representative high-pressure turbine rim seal (section 2.2.3) for varying purge flow rates are investigated. A purpose-made heat transfer measurement setup was designed and installed into the rotor- and stator-sided hub cavity wall such that temperature and heat transfer data can be provided. The integration of a cold purge flow secondary air system enables reaching a greater temperature difference between cavity fluid and main annulus flow to detail the sealing effectiveness and unsteady variation in wall temperature. First, the main flow dynamics within the rim seal space were investigated, also with respect to non-synchronous, low-frequency perturbations which were previously discussed in Chapter 3 for an angel-wing-type rim seal. Second, the temperature distributions at the hub cavity wall and adiabatic effectiveness of the rim seal were assessed for different purge flow rates. The chapter concludes with the quantification of the heat transfer levels, including adiabatic wall temperature and convective heat transfer coefficient, on the rotor- and stator-sided walls inside the hub cavity.

5.1. Hub Cavity Dynamics in an Overlap-Type Rim Seal

As the hot gas ingestion behavior and convective heat transfer characteristics are anticipated to be coupled with the dynamics present in the rim seal space and lower main annulus flow region, a first investigation is conducted assessing the driving pressure oscillations inside the hub cavity. The results presented in Chapter 3 emphasize that hub cavities are prone to establish low-frequency, non-synchronous pressure oscillations which can be in the order of magnitude of the typically dominating blade passing amplitude. The nature of the low frequency content was found to be linked to large scale rotating low-pressure zones that have shown to affect the ingestion behavior of a turbine stage. Since the rim seal geometry for this study was considerably changed from an angel-wing-type seal to an overlap-type seal where the sealing effect is taking place at a higher radial position, the pressure dynamics needs to be investigated also with respect to different purge flow rates.
In Figure 5.1, the pressure spectral analysis inside the hub cavity is presented for various rim seal purge flow rates. The data are provided by the stator-sided wall-mounted unsteady pressure sensor located above the rotor sealing arm at $-11\,\%$ span. The position of the sensor is additionally indicated by an inset in the center of Figure 5.1. The pressure amplitude of the spectra is normalized by the respective turbine inlet total pressure and the frequency range is expressed as a fraction of the rotor blade passing frequency f_{RBPF}. The purge flow rate was varied in small steps by $0.2\,\%$ in order to capture potential low frequency oscillations. Comparing the different frequency spectra, one can observe that the rotor blade passing amplitude (f_{RBPF}=1) is captured for all injection rates, whereas the strength of the fluctuations is coupled to the amount of purge flow. The pressure amplitude is increased by a factor of 7.5 when increasing the purge flow from IR=0.0 % to IR=1.2 %. Considering the low frequency range, below the rotor blade passing frequency, most of the injection rates do not exhibit pronounced contribution of non-synchronous perturbations. The distinct peaks below 20 % of the blade passing frequency are typically related to the rotational speed of the rotor (engine orders). The only purge flow rate that shows non-synchronous flow excitation is the IR=0.0 % case which presents a band of elevated pressure amplitudes between 53–64 % of the blade passing frequency. As the frequency content is asynchronous to the rotor speed, the term “cavity mode” is used for the identified band. The dominating frequency presents a pressure amplitude that is by a factor of 4 higher than the blade passing-induced amplitude. Comparing the pressure amplitude to the IR=0.0 % case of the angel-wing-type seal, depicted in Figure 3.1 (a), the level is found to be in the same order of magnitude. However, the frequency range is shifted toward the blade passing frequency. When the purge flow rate

is moderately increased to IR=0.2 %, the signature of the described mode can be anticipated. Nevertheless, the respective pressure amplitudes are clearly attenuated. For the IR=0.4 %, the cavity mode contribution to the spectrum is not distinguishable from the turbulence contribution. The results imply that a change of the rim seal geometry has a beneficial impact on the cavity mode characteristics, meaning that the low-frequency flow excitation seems to vanish at a much lower purge flow rate than for the angel-wing-type seal investigated in Chapter 3.

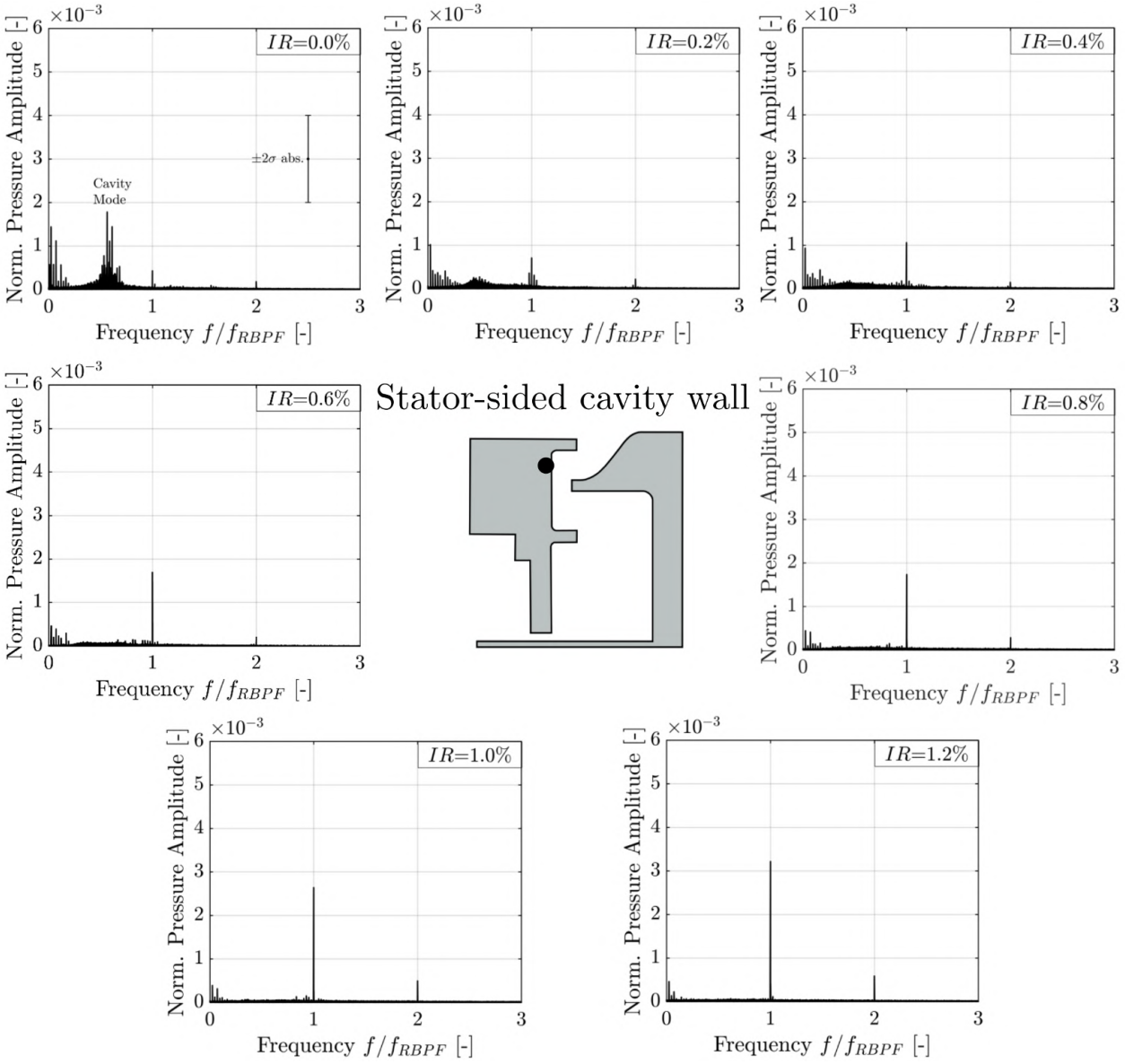

Figure 5.1.: Experimentally determined pressure frequency spectra for different rim seal purge flow injection rates IR on the first stator-sided hub cavity wall

The main differences between the two studies that show different characteristics for the hub cavity modes and could be stated as potential improvements for rim seals that try to eliminate the non-synchronous structures are as follows:

- The rotor sealing arm provides a sealing at a larger radius compared to the

buffer arm for the angel-wing-type seal. Consequently, a trench cavity is built for the overlap-type seal which has a lower volume than the large upper hub cavity space for the angel-wing-type seal. Partitioning the cavity volume into smaller compartments toward the main annulus could be beneficial to eliminate the structures with less purge flow.

- The S-type shape of the rotor sealing arm which smoothly transitions from the rotor hub platform into the hub cavity is contrary to the angel-wing-type seal less prone to provoke additional acceleration of the ingested fluid as for example shown in Figure 3.22 for the angel-wing-type seal.

- The rotor blade count was reduced from 54 to 42. Although the hub cavity modes are asynchronous, the study cannot exclude the effect of different blade-to-vane count ratios on the hub cavity modes.

The array of unsteady pressure sensors installed on the same radial positions but different circumferential coordinates (introduced in section 2.4.1) permits definition of the characteristics of the cavity mode detected for the IR=0.0 % case. In order to do so, the pressure signals, that are simultaneously recorded for all installed sensors, need to be first phase-locked to the dominating cavity mode frequency f_{cav} (56 % of the blade passing frequency) and consecutively phase-lock averaged. The resulting time-series of the measured pressure data is depicted in Figure 5.2 (left). The plot shows the phase-lock averaged normalized pressure fluctuation induced by the cavity mode against time expressed as a fraction of the hub cavity mode period $T_{cav} = 1/f_{cav}$. To be consistent, the pressure data are normalized by the turbine inlet total pressure. The time-series of the three different sensor positions reveals a slight change in the peak amplitude, but more importantly a phase shift between the signals. This phase shift enables to calculate the speed of potential rotating low-pressure zones, which were previously identified for the angel-wing-type seal (Figure 3.21). The explanatory schematic illustrated in Figure 5.2 (right) helps to understand the derivation of the rotational speed of the zones (the distance of the sensors is exaggerated for clarity). The assumptions that were made for the calculation are: the rotating structure consists of a high-pressure region and a low-pressure part (dark blue and light green lobes), the zone travels at constant speed, and the passing of the zone is captured by the different sensor positions ($\Delta t_{lag} < T_{cav}$). The time lag Δt_{lag} is the time it takes for a rotating zone to travel from one sensor to the next one. By calculating the cross-correlation between two signals (beneficially the two signals which have the smallest circumferential sensor distance), the time lag Δt_{lag} can be determined. By design, the angle γ between the two sensors is known, which in the end allows for determination of the circumferential distance, and therefore the speed of the rotating zones $n_{CavityMode}$. A similar approach was used by

Beard et al. [7]. The calculated time lag between two peaks is found to be 20.2 % of the cavity mode period which results with the given geometrical information in a mode rotational speed $n_{CavityMode}$ of about 93 % of the rotor speed N. Knowing the rotational speed of the low-pressure zones permits determination of the expected number of zones that are rotating inside the hub cavity. The calculated number of zones is given by $f_{cav}/n_{CavityMode}$ and results to 26 expected low-pressure zones for the overlap-type seal operated at IR=0.0 %.

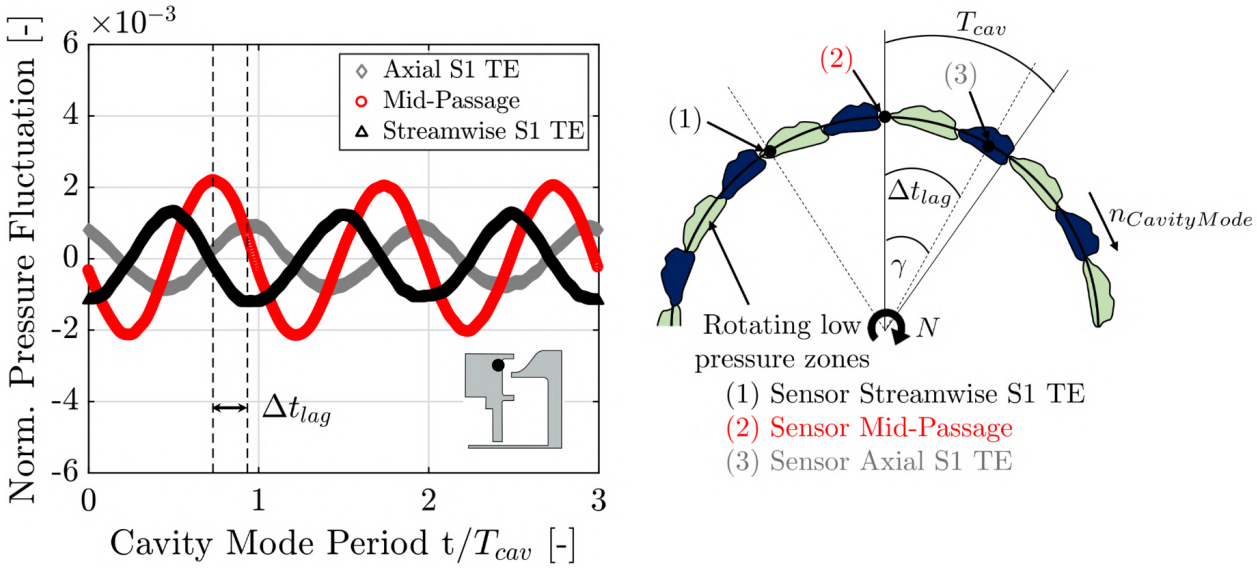

Figure 5.2.: Time-resolved (phase-lock averaged) normalized pressure for different circumferential positions and IR=0.0 % (left) and explanatory schematic of rotating pressure zone speed derivation (right, not to scale, based on [7])

The asynchronous dynamics of the overlap-type rim seal was elaborated for the IR=0.0 % operating point, however, the other purge flow rates are mainly dominated by synchronous pressure oscillations, such as the blade passing-induced ones. In order to assess the impact of the rotor on the inflow and outflow behavior in the rim seal space, the time-resolved pressure difference across the rotor sealing arm can be investigated. The determination of the pressure difference is expected to provide a preliminary indication of potential ingestion and purging. In Figure 5.3, the time-resolved normalized pressure difference across the rotor sealing arm is shown. Three different circumferential positions on the stator-sided cavity wall are considered. The pressure difference is calculated by subtracting the radial inboard pressure signal from the outer one and is normalized by the turbine inlet total pressure. Hence, a positive difference indicates that the flow tends to ingress into the lower hub cavity, whereas a negative one points toward purging. The pressure data are phase-lock averaged with respect to the blade passing frequency and consequently plotted against time expressed as fraction of the rotor blade passing period T. Four different rim seal purge flow rates are considered for the investigation ranging from IR=0.0 % up to IR=1.2 %. Comparing the time-series for the different

injection rates reveals that two out of the three circumferential positions show a negative pressure difference (positions: mid-passage and streamwise S1 TE) which suggests that these locations show less tendency for ingestion. The one location that is more prone to ingestion is the axial projection of the first stator trailing edge into the stator-sided cavity wall. Especially, the zero-injection rate case (IR=0.0 %) reveals a positive pressure difference at this location. Interestingly, the pressure oscillations induced by the rotor blade passing does not lead to a change of sign of the pressure difference for the mid-passage and streamwise projection of the S1 trailing edge position. This implies that not a substantial change between inflow and outflow in the region of the rotor sealing arm is provoked by the passing of the rotor blades.

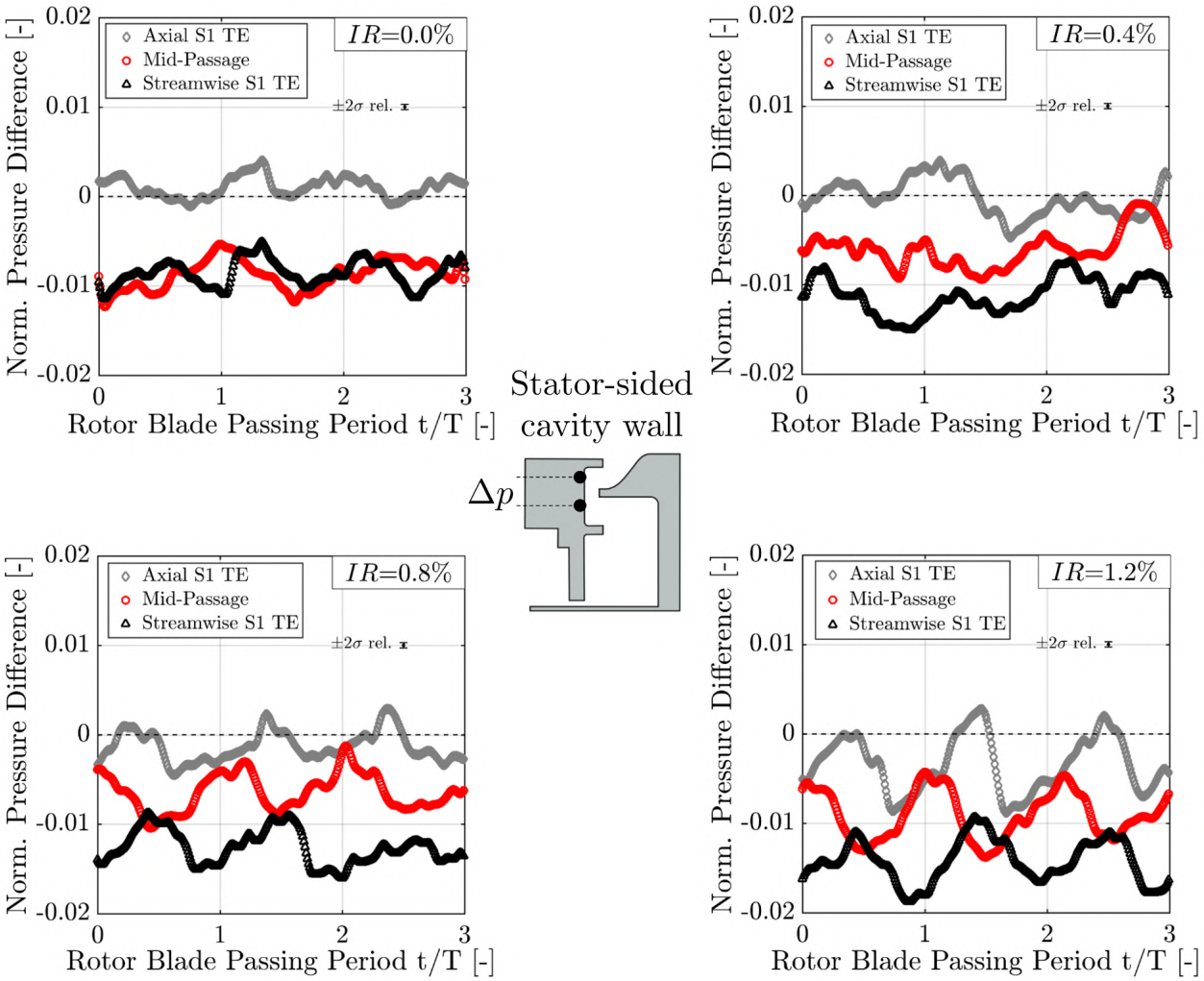

Figure 5.3.: Time-resolved normalized pressure difference (outer minus inner pressure) across rotor-sided sealing arm for different circumferential position and purge flow rates

Only for the axial projection of the S1 trailing edge a time-resolved in- and outflow is detected. As indicated in the pressure spectral analysis plots given in Figure 5.1, the blade passing-induced pressure fluctuations are increased with increasing purge mass flow which is observable when comparing the time-series of the IR=0.0 % and IR=1.2 % case. The pressure data for the

highest considered purge flow injection rate suggest that only minor ingestion is occurring, as the pressure difference becomes rarely positive. Clearly, this is only a qualitative assessment of the inflow and outflow behavior across the rotor sealing arm based on pressure measurements. A more quantitative assessment is provided in the follow-up section.

Up to now, only the dynamics in the stator frame of reference are investigated. As the hot gas ingestion and heat transfer levels are also investigated in the rotor relative frame of reference, the hub cavity dynamic is complemented by time-resolved pressure measurements on the rotor-sided wall. In Figure 5.4, the pressure spectral analysis in the rotating frame of reference for four different rim seal purge flow injection rates are illustrated. The pressure amplitude is normalized by the turbine inlet total pressure and the frequency axis is expressed with respect to the first stator vane passing frequency f_{VPF}. The radial position of the measurement location is schematically detailed by the inset in Figure 5.4. For all injection rates, the pressure frequency spectra reveal the dominance of the vane passing, resulting in pressure amplitudes up to 0.6 % (IR=1.2 %) of the turbine inlet total pressure. The pressure amplitude rise for an increase in purge flow rate from IR=0.0 % to IR=1.2 % is in the order of 45 %. Overall, the measured pressure amplitudes for the driving frequency is up to a factor of two higher on the rotating wall than on the first stator-sided cavity wall. In summary, the wall pressure on the rotating cavity wall is dominated by the first stator vane passing.

Nevertheless, the unsteady pressure sensors capture low-frequency content, which is well below the vane passing frequency, and typically in a range between the rotational frequency of the rotor and 10 % of the vane passing. Part of the low-frequency pressure oscillations can be related to the engine orders; however, some contribution is found from non-synchronous perturbations. As the purge flow rate is increased, the frequency content is mostly unaltered. The pressure amplitudes for specific frequencies on the other hand are changed by the purge flow. The largest peak in the low frequency band for the highest purge flow case is found to be the rotational frequency of the rotor and is about 90 % of the vane passing induced amplitude. Hence, the rotation of the rotor itself reveals the potential to excite the flow field in the lower hub cavity. The cause for the strong presence of this oscillations can be manifold, for example, the axial run out of the rotor can cause a fluctuating pressure field due to the local slight deviations of the rotor axial position. Furthermore, the rotor pumping effect can cause pressure oscillations.

Overall, the considered overlap-type seal and hub cavity is dominated mainly by deterministic effects such as the blade and vane passing, depending on the frame of reference. The beneficial impact of the rim seal design on the formation of non-synchronous rotating flow structures was shown, highlighting that the sealing arrangement can eliminate such structures at a much lower

purge flow rate compared to the previously discussed angel-wing-type seal. In the rotating frame of reference, the presence of the vane passing is dominating, and some contribution from the rotor speed is also measured.

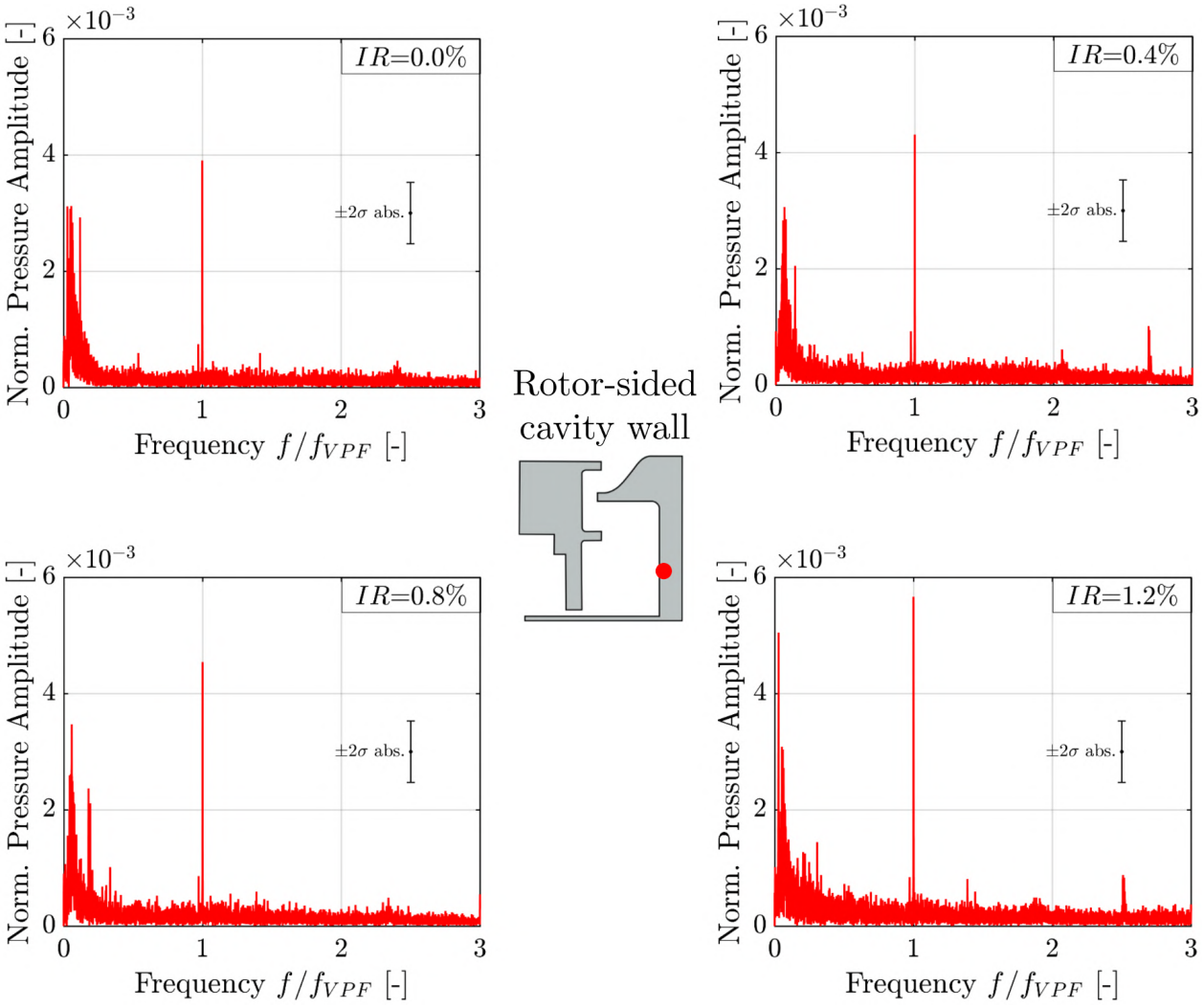

Figure 5.4.: Experimentally determined pressure frequency spectra for different rim seal purge flow injection rates IR on the rotor-sided hub cavity wall

5.2. Ingestion Considerations of a Turbine Rim Seal

Due to the substantial thermal loads that are present in a high-pressure turbine, the quantification of the hot gas ingestion from the main annulus into the stator-rotor cavities is pivotal to improve the aerothermal performance of rim seals. Especially the rotor disk needs to be protected from overheating which in real engine environment is likely to happen if the wrong sealing flow rates are chosen. In particular the designer wants to elucidate the following questions: what is the most efficient rim seal arrangement? How much cooling flow is required to minimize the hot gas ingestion to an acceptable level? How far does

the hot gas fluid penetrate into the hub cavity and more importantly what is the effect on the temperature of the rotor disk? Most of these questions are addressed in open literature, except, the last one. Therefore, this section aims to provide a unique dataset which incorporates the adiabatic wall temperature and effectiveness in the rim seal cavity for different purge flow rates.
After having elaborated the main dynamics in the rim seal and hub cavity space, the ingestion characteristics of the presented rim seal shall be discussed in more detail. When quantifying the ingress of main annulus fluid into the hub cavity, typically one can find concentration measurements where the purge or sealing air is seeded with a known concentration of a non-reacting and non-buoyant gas (e.g., ethylene and CO_2). Based on the concentration measurements, a concentration-based sealing effectiveness is derived. Such studies are, among others, provided by Popović and Hodson [144] and Sangan et al. [169]. On the other side, the effectiveness of a specific rim seal design can be determined based on the adiabatic wall temperature in the hub cavity. The adiabatic wall temperature is the surface temperature acquired by a wall if (perfect) thermal insulation is achieved. The convective heat flux between fluid and wall is therefore assumed to be zero. Hence, an adiabatic temperature-based effectiveness enables to judge on temperature effects given by the supplied purge flow and excludes, in a first order consideration, the impact of the fluid dynamics in the hub cavity. The purpose-made hub cavity heat transfer setup used in this work enables determination of the adiabatic wall temperature by means of thin-film heat flux gauges, which are subjected to different thermal boundary conditions. The approach of finding the adiabatic wall temperature is detailed in section 2.4.3. Based on that, an adiabatic effectiveness ε_{ad} can be determined as given in Equation 5.1.

$$\varepsilon_{ad} = \frac{T_{t,in} - T_{ad}}{T_{t,in} - T_{t,cav}} \tag{5.1}$$

In the expression, T_{ad} is the measured adiabatic wall temperature and $T_{t,in}$ is the turbine inlet total temperature. In this definition the turbine inlet total temperature is chosen as the reference temperature in the main annulus, as it is controlled to be constant (within $\pm 0.3\,\mathrm{K}$) for all purge flow operating conditions. The cavity temperature $T_{t,cav}$ is chosen as the reference coolant temperature and is measured in the lower hub cavity as illustrated in Figure 2.3 and described in section 2.1.4. The introduced adiabatic effectiveness thereby relates the maximum temperature difference between the main annulus and cavity fluid to the local achieved temperature difference at the cavity walls. Since the cavity temperature changes with different purge flow rates, the measured trend of the temperature in the lower cavity is depicted in Figure 5.5 to provide all information for the adiabatic effectiveness analysis. The figure shows that the most pronounced cavity temperature reduction takes

place between the zero net purge flow rate and IR=0.6 %.

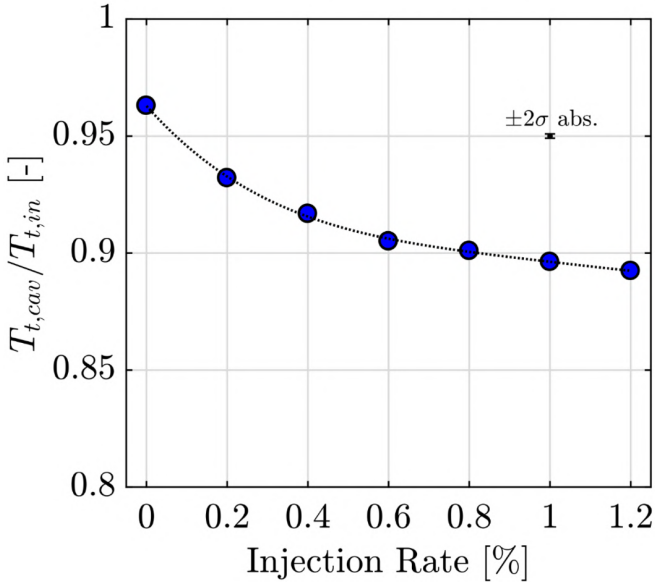

Figure 5.5.: Normalized cavity temperature for different rim seal purge flow injection rates IR

The distributions of the adiabatic effectiveness inside the rim seal and hub cavity space are presented in Figure 5.6 for a systematic change in the rim seal purge flow injection rate and eleven different positions. For the first stator-sided cavity wall, the trend in the adiabatic effectiveness shows that with increasing purge flow rate the effectiveness increases. The injection of purge flow increases the static pressure in the hub cavity and thereby reduces the amount of ingested mass flow from the main annulus. Concentrating the analysis on the stator-side distributions, one can observe that the sensitivity of the adiabatic effectiveness changes depending on the purge flow range and the radial position. The lowest sensor position "S6" for example, shows an already high adiabatic effectiveness for the lower purge flow rates in the order of 80–90 %. For the design purge flow rate IR=0.8 %, the adiabatic effectiveness reaches the upper limit. The sensitivity to the purge flow rate is comparably moderate due to the low radial position, even though, it is anticipated that most of the injected purge flow is vented along the rotor-sided cavity wall due to the radial pressure gradient that is built up by the rotor. Hence, this implies that the purge flow is efficiently guided to the stator-sided radial sealing arm. The radial position right below the rotor-sided sealing arm (sensor positions "S4" and "S5") show similar characteristics. When comparing the distribution with the lowest sensor position "S6", the sensitivity of the adiabatic effectiveness in the lower purge flow range seems to be enhanced. Nevertheless, at the nominal purge flow injection rate IR=0.8 % a high adiabatic effectiveness above 90 % is achieved. The higher sensitivity, in turn, outlines that the stator-sided cavity wall requires more purge flow to achieve appropriate adiabatic effectiveness as the exit of the cavity is approached. At the highest considered purge flow rate, an adiabatic effectiveness of unity is achieved, implying that

the purge flow reaches the stator cavity wall and discourages the ingress of the main annulus fluid. Since the results of the circumferentially displaced sensors "S4" and "S5" fall on top of each other, it is concluded that the pitch-wise wall temperature gradient is moderate.

The most outer radial positions "S1" to "S3" provide similar levels of the adiabatic effectiveness for the purge flow rates above IR=0.8 % compared to the positions below the rotor sealing arm. For the lower purge flow range ($<$ IR=0.8 %) the sensitivity to the injection rate seems to be enhanced, resulting in adiabatic effectiveness values below 60 %. The sensitivity to the circumferential position is still moderate (typically within the uncertainty band of the measurement) even at the most outer position which contrasts with the implications of the time-resolved pressure difference measurements (Figure 5.3). Given the higher sensitivity of the adiabatic effectiveness to the purge flow rate suggests that this part of the stator cavity wall is more demanding to cool. Due to the overlap between the first stator hub platform and the rotor sealing arm, a small-volume trench cavity is formed. Within this trench cavity compartment, typically large scale vortical structures establish which are termed as "slot vortices". These vortices do not necessarily guide the main annulus fluid to the stator cavity wall but recirculate the fluid and re-inject it into the main flow path. Such vortical structures in the trench cavity were previously traced by Popović and Hodson [144]. It is hypothesized that by injecting rim seal purge flow the slot vortex is pushed further away from the stator-sided cavity wall which benefits the adiabatic effectiveness to increase as the hotter recirculating fluid is not reaching the cavity wall. Generally speaking, the results suggest that the overlap-type seal is appropriately sealing the hub cavity, when the cavity is supplied with the nominal purge flow injection rate of IR=0.8 %.

The rotor-sided data reveal, similar to the first-stator one, a gradual increase in the adiabatic effectiveness levels as the rim seal purge flow rate is increased. The zero net purge flow rate IR=0.0 % (gray rectangular) exhibits an outlier behavior with respect to the rest of data. As it cannot fully exclude that it is a physical behavior, the dataset is not removed and displayed for completeness. The two lowest radial positions "R1" and "R2" show moderate sensitivity over the whole rim seal purge flow range. At IR=0.4 %, an effectiveness of 90 % is already reached. It is suspected that most of the injected purge flow is impinging on the lower rotor-sided cavity wall, leading to lower adiabatic wall temperatures and thereby higher adiabatic effectiveness. Due the rotational speed of the rotor, the cavity fluid is accelerated to the speed of the rotor disk and pumped along the radial coordinate, such that a radial pressure gradient is established. Consequently, the injected purge flow is vented following the rotor-sided cavity wall, most likely leading to comparable adiabatic effectiveness, specifically for higher purge rates. This is reflected in the presented

measurements where the adiabatic effectiveness is not substantially changed by the radial position on the rotor-side for higher purge rates. Even at the delicate radial position labeled with "R5" (below rotor sealing arm) appropriate levels of adiabatic effectiveness at the purge flow design conditions are measured. However, it becomes apparent that this position is more challenging to cool since the sensitivity to the purge flow rate is substantially higher than at the radial inboard positions "R1" and "R2".

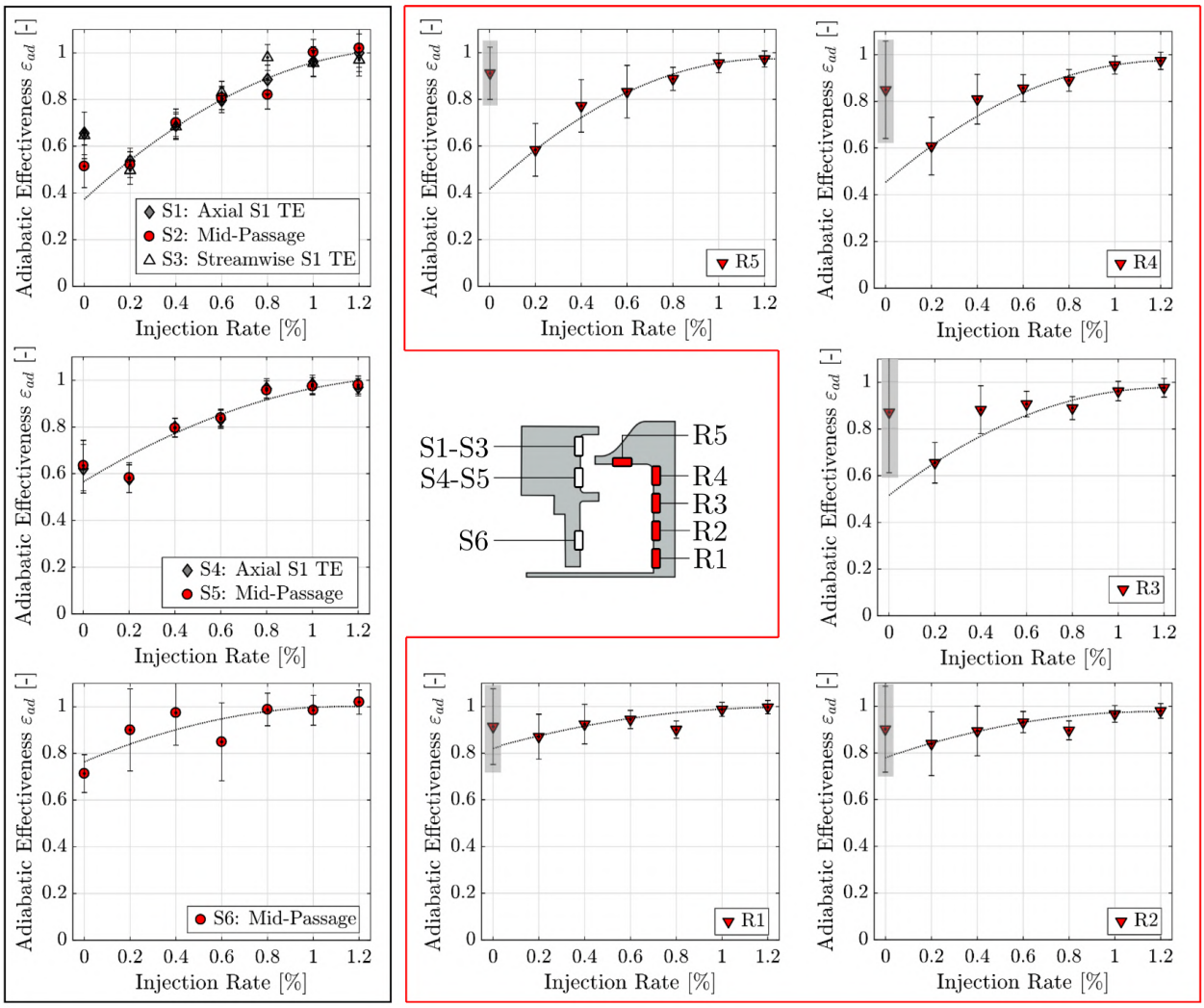

Figure 5.6.: Adiabatic effectiveness ε_{ad} on the first stator- and rotor-sided hub cavity wall for different rim seal purge flow injection rates IR

When further cross-checking these observations with the pure levels of the adiabatic wall temperature, it is found that the adiabatic wall temperature is not altered substantially by the radial and circumferential positions for the same rim seal purge flow rate. The statement is confirmed when the adiabatic wall temperature is plotted for different radial positions inside the hub cavity. In Figure 5.7, the radial distribution of the normalized adiabatic wall temperature is provided. The temperature data are normalized by the respective turbine inlet total temperature. The radial coordinate, termed as cavity radius, is defined using the inner radius of the rotor disk and the nominal

hub radius of the first stator and rotor. For clarity, only four different rim seal purge flow injection rates are considered. Both, the stator- and rotor-sided, distributions highlight the sensitivity of the adiabatic wall temperature to the injected purge flow. On the other hand, the radial alteration of the time-averaged temperatures is moderate, specifically for the higher purge flow rates IR=0.8 % and IR=1.2 %. The moderate rate IR=0.4 % shows the highest sensitivity to the radial coordinate with about a 2.5 % reduction in temperature between the most outer and inner sensor position on the stator-sided wall and a 1.4 % reduction for the rotor-sided wall, respectively. This implies that on a time-averaged basis the spatial gradients of the wall temperatures are at least a second order effect which are outweighed by a change in purge flow.

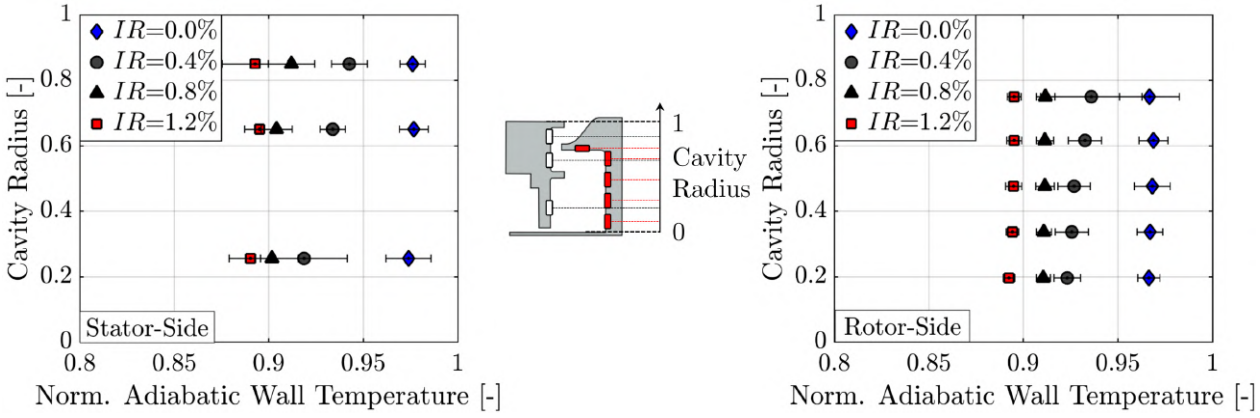

Figure 5.7.: Radial distribution of the normalized adiabatic wall temperature on the first stator- and rotor-sided hub cavity wall for different rim seal purge flow injection rates IR

After having introduced the capabilities of the proposed rim seal design to cope with ingestion from the main annulus into the hub cavity, the time-averaged adiabatic effectiveness and temperature results imply that an efficient use of the supplied purge air is provided with the proposed sealing arrangement, specifically for the design purge flow rate IR=0.8 %. The encouraging sensitivity of the adiabatic effectiveness, even at delicate cavity wall positions, combined with a spatial temperature distribution that provides low gradients point toward a favorable rim seal characteristic.
In addition to the presented analysis, the results need to be put in a broader context. Typically, designers aim to discourage the ingestion of hot gas into the rim seal space, but do not want to compromise the achievements with substantial additional aerodynamic losses. It is therefore interesting to show sensitivities of the adiabatic effectiveness against the injection of rim seal purge flow in conjunction with a stage efficiency consideration. As highlighted before, the injection of purge flow from the stator-rotor cavities into the main annulus provokes a strengthening effect of the hub secondary flows [130, 175] and is found to increase the mixing losses [13]. For the current turbine configuration, accurate aerodynamic performance measurements were performed to deduce

the sensitivity of the turbine stage efficiency with respect to the injection of purge flow. In Figure 5.8, the trade-off between adiabatic effectiveness and the aerodynamic performance is illustrated. On the left ordinate, the measured normalized total-to-total stage efficiency is depicted. The efficiency levels were derived from the pneumatic five-hole probe (5HP) measurements at rotor exit and follows the definition given in Equation 2.36. The data are normalized by the stage efficiency measured for the zero-purge flow rate case IR=0.0 %. On the right y-axis, the adiabatic effectiveness for the radial position right below the rotor sealing arm ("S4") is shown.

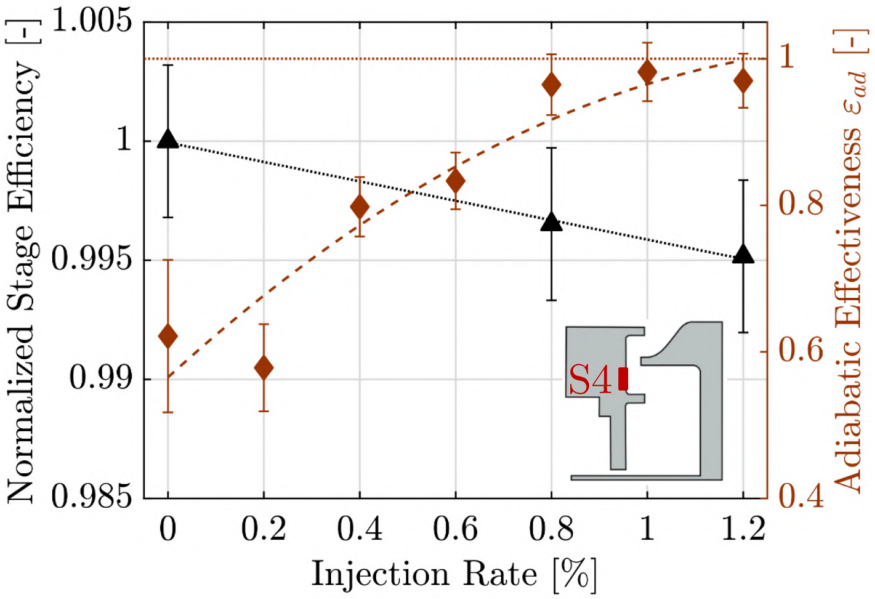

Figure 5.8.: Normalized total-to-total stage efficiency η_{tt} against adiabatic effectiveness ε_{ad} (sensor position "S4") for different purge flow injection rates

The stage efficiency measurements for three different purge flow rates reveals the linear relationship of the quantity to the injection rate and indicate a 0.36 % points reduction in efficiency per percent of rim seal purge flow injection. This is judged to be a relatively low sensitivity to the purge flow compared to published data from other researchers. Jenny [75, 76] reported an up to 1.3 % points efficiency drop per percent of injected purge flow for a low-pressure configuration; Schuepbach et al. [175] found a sensitivity of 0.7 % points per percent injection rate for a high-pressure turbine representative configuration in the same rig. The integration of non-axisymmetric end wall profiling on the rotor hub platform which is axially extended into sealing arrangement (introduced in section 2.2.3), is anticipated to have a beneficial impact on the sensitivity as it diminishes the circumferential pressure gradient and provides a more uniform entrainment of the purge flow into the main annulus which, in turn, helps to reduce the sensitivity of the rotor hub secondary flow strength to the purge flow injection.

The impact of the additional injection of purge flow with the reference being the design injection rate IR=0.8 % is demonstrated in Figure 5.9 (left) where

the circumferentially mass- and time-averaged radial distribution of the total-to-total stage efficiency is depicted for the IR=0.8 % and IR=1.2 % case. The plot reveals that the stage efficiency is barely affected by the purge flow above mid-span. Between 18 % to 40 % span, most of the losses associated with the additional purge flow injection are identified which can reach locally up to 0.5 % points (Figure 5.9, right). This span-wise coordinate range is typically dominated by the rotor hub secondary flows. The data imply that the hub passage vortices are migrating radially outwards up to 40 % span for both injection rates.

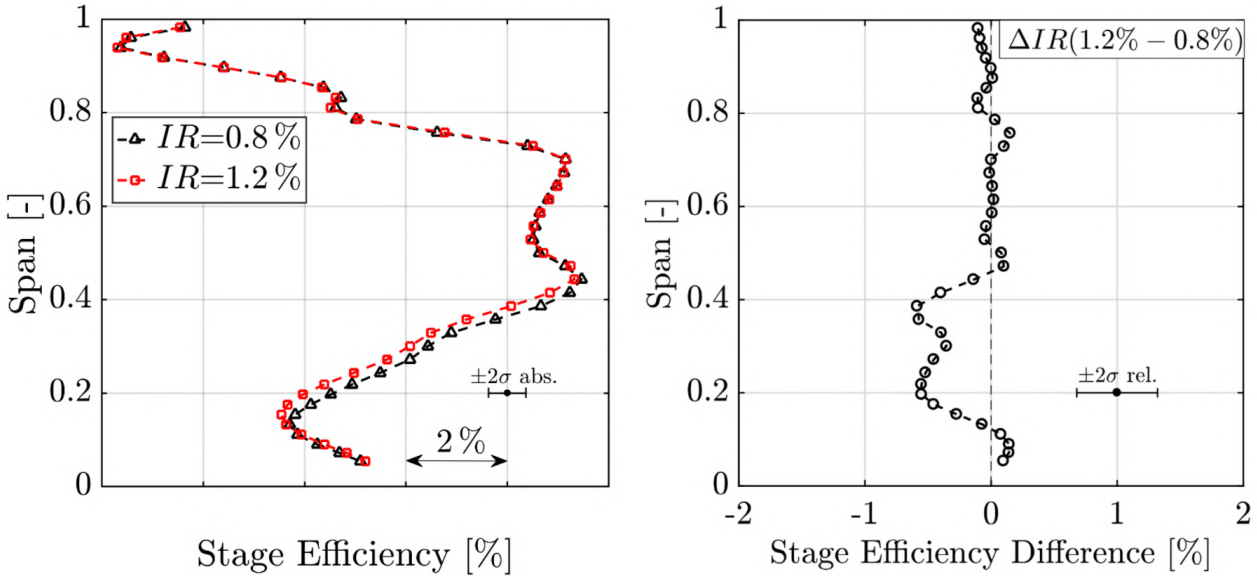

Figure 5.9.: Circumferentially mass- and time-averaged total-to-total stage efficiency distribution (left) and difference $\Delta\eta_{tt}$ in percentage pionts (IR=1.2 % - IR=0.8 %, right) measured with 5HP. Stage efficiency difference is given in percentage points.

As reported by other researchers [130, 175], the purge flow associated losses are attributed to the intensification of the rotor hub passage vortex. The FRAP measurements at the rotor exit confirm these observations and enable tracking of the rotor hub passage vortex in the absolute frame of reference. Figure 5.10 displays the signature of the vortex with respect to its span-wise and circumferential position with superimposed stochastic pressure unsteadiness levels $p'_{1,rms}$ for two purge flow injection rates. The unsteadiness levels are a qualitative measure of the associated aerodynamic losses which was highlighted in the work of Jenny [75]. The position of the hub passage vortex is calculated based on the iso-surface of the positive streamwise vorticity which was defined at 3'000 Hz. The figure highlights that the vortex migrates radially outwards by about 16 % span, starting from 19 % span (IR=0.8 %) and 21 % span (IR=1.2 %), respectively. The intensification and the radial migration of the vortex is judged to be initiated by the presence of the second stator leading edge (LE S2) which is indicated by dashed lines in the figures. The potential field effect of the second stator forces the vortex to accelerate,

meaning that the vortex is quickly swinging around the leading edge. As it is streamwise accelerated, the vortex is stretched which increases the vorticity and unsteadiness levels.

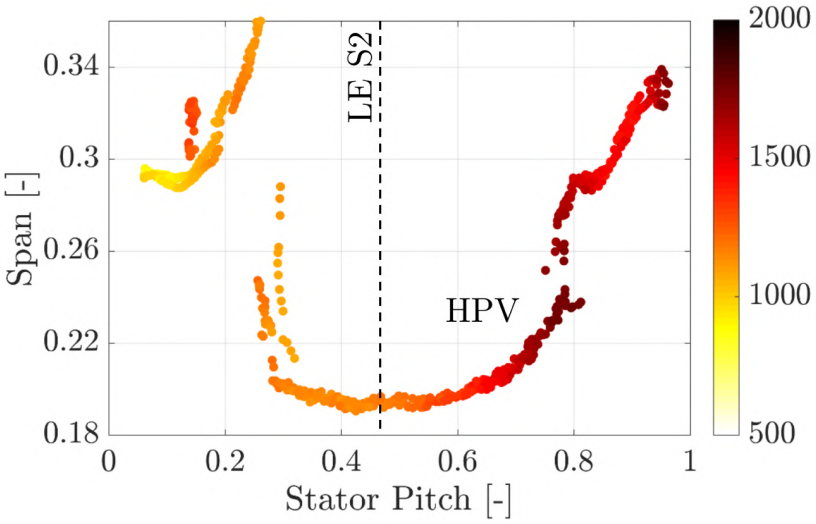

(a) $IR = 0.8\,\%$

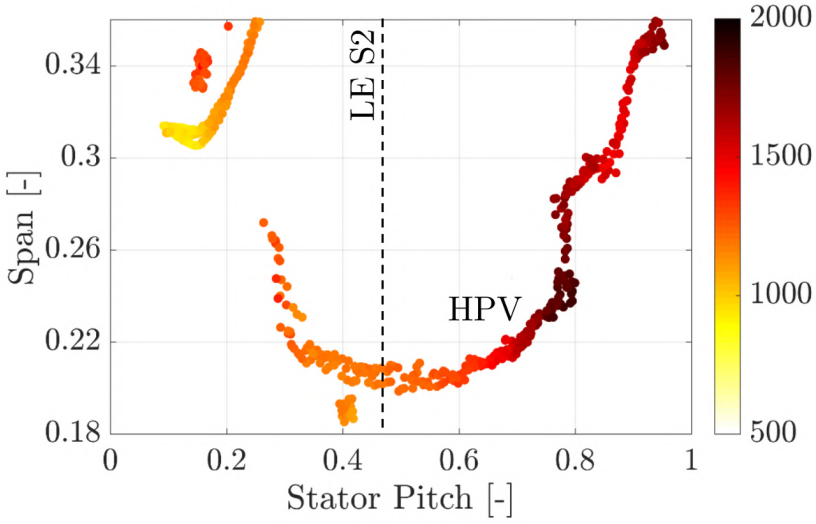

(b) $IR = 1.2\,\%$

Figure 5.10.: Rotor hub passage vortex (HPV) position at rotor exit based on center of iso-surface of the streamwise vorticity (3'000 Hz) for two purge flow injection rates. Dot color indicates the stochastic pressure unsteadiness levels $p'_{1,rms}$ [Pa] (FRAP).

The increase in purge flow rate from IR=0.8 % to IR=1.2 % leads to an increased radial migration by about 2 % span. The peak stochastic unsteadiness levels at around 0.8 stator pitch are increased by about 12 %. In summary, the additional purge flow injection rate is affecting the rotor hub passage vortex losses and should therefore be one of the primary flow features that need to be controlled for an optimization of the aerothermal performance of the stage in combination with the rim seal.

Coming back to the previous investigation of the adiabatic effectiveness and stage performance in Figure 5.8, the following observations can be made: if the analysis is concentrated on the design purge flow injection rate IR=0.8 %, one can observe that an increase to the high purge flow rate IR=1.2 % is associated with a drop in efficiency by about 0.12 % points while achieving a 0.5–3 % points higher adiabatic effectiveness. On the other hand, reducing the purge flow down to IR=0.4 %, the efficiency gain would be around 0.12 % points, however, this efficiency gain would be paid with a 17 % points reduction in the adiabatic efficiency. It is clearly seen that there is a sweet spot within the range of injected purge flow where the sensitivity in the adiabatic effectiveness is reduced. Knowing that point would substantially contribute to an optimized operation of the rim seal. The linear correlation of the stage efficiency with respect to purge flow helps in the lower purge flow band, as the gain in adiabatic effectiveness is relatively cheap. For the purge flow range above the design injection rate, the addition of a few percentage points in the seal effectiveness is expensive with respect to aerodynamic performance. To achieve an improved aerothermal performance of the turbine stage, the specific purge flow range has to be found where the adiabatic effectiveness sensitivity transitions from being higher than the stage efficiency sensitivity toward being lower than that of the stage efficiency. For the proposed rim seal design, this range is around IR=0.8 % for most of the wall positions. Furthermore, the analysis encourages to further lower the sensitivity of the aerodynamic performance with respect to the purge flow injection rate.

5.3. Convective Heat Transfer in the Hub Cavity

In order to accomplish an appropriate level of cooling on the rotor disk with a minimum of cooling air, not only the adiabatic effectiveness and wall temperature are required but also the convective heat transfer characteristics in the rim seal and hub cavity space need to be addressed. As the cooling requirements are cut, the designer also reduces the associated windage losses in the hub cavity, minimizes the penalties on the overall engine efficiency due to bypassing air from the compressor stages, and lowers the aerodynamic performance deterioration due to mixing of the coolant with the main flow. Therefore, experimental evidence of the hub cavity convective heat transfer is of specific importance to the designer to optimize the rim seals and cooling requirements as well as to validate numerical tools.
The investigation of the convective heat transfer levels in the rim seal space is provided for various rim seal purge flow injection rates. In order to provide a non-dimensional level of the convective heat transfer, the convective heat transfer coefficients h are converted into Nusselt number Nu levels. The Nusselt number indicates the ratio between the convective and conductive

heat transfer across a boundary. The characteristic length scale is chosen to be the radial coordinate. The formulation, as it is used in this study, is given in Equation 5.2.

$$Nu = \frac{h\, r_{seal}}{k_{air}} \tag{5.2}$$

Where r_{seal} is the mid-radius of the rotor-sided sealing arm and k_{air} is the thermal conductivity of air. The convective heat transfer coefficient is obtained by using the purpose-made hub cavity heat transfer setup, consisting of double-sided heat flux gauges and a thin-film heater, that enables changing the thermal boundary condition during turbine operation. By systematically changing the thermal boundary conditions, the slope of the linear relationship between the convective heat flux and the measured wall temperature can be calculated, resulting in the convective heat transfer coefficient.
Based on that procedure, the trends in the local Nusselt number can be provided for different rim seal purge flow rates. In Figure 5.11, the experimentally determined time-averaged Nusselt number on the first stator- and rotor-sided cavity wall is displayed. First, the analysis of the provided data shall be focused on the first stator-sided cavity wall. The most outer radial position, containing the sensor positions "S1" to "S3", is characterized by a drop in local Nusselt number when the rim seal purge flow is increased. A 53 % reduction in the Nusselt number per percent of rim seal purge flow injection rate is detected. Considering the distribution for the most outer radial position, one can anticipate a close to linear decay of the heat transfer coefficient. A circumferential change in position seems not to drastically effect the levels (within measurement uncertainty band) which agrees with the results for the adiabatic effectiveness (Figure 5.6). In the absence of detailed flow field measurements, only a hypothetical explanation can be given for the observed trend. As the rim seal purge flow is increased the tangential velocity component of the cavity fluid is typically reduced. This was demonstrated in the purge control feature study in Chapter 4, where velocity measurements within the hub cavity were shown (Figure 4.4). Therefore, it is anticipated that the substantial reduction in the dominating flow velocity goes along with a reduction in the convective heat transfer coefficient which is reflected in the drop in Nusselt number.
The radial position right below the rotor sealing arm ("S4" and "S5") shows contrary to the outer position only a moderate change in Nusselt number with increasing purge flow. This is behavior is not altered by the circumferential position. The Nusselt number levels are comparable to the outer radial position when low purge flow is present (e.g., IR=0.2 %). This might imply, that the blockage effect imposed on the circumferential velocity induced by the purge flow is substantially lower at this radial position which, in turn, would indicate a very specific trajectory of the purge air in the rim seal cavity. Similar to

that, the convective heat transfer at the most inner radial position ("S6") is found to be moderately affected by the purge flow. Additionally, the Nusselt number and hence the convective heat transfer coefficient is found to be very moderate (about 25 % of the peak Nusselt number at the most outer position). It is expected that the trajectory in radial direction of most of the purge air is concentrated toward the rotor-sided cavity wall due to the pumping effect of the disk. Due to the rotor-sided sealing arm, the radial trajectory of the purge flow is anticipated to be converged and might be redistributed toward the stator-side inducing the aforementioned blockage effect on the most outer radial position. Nevertheless, it has to mentioned that this is a purely qualitative explanation. The support of flow visualization would certainly contribute to the understanding of the complex flow regime.
The rotor-sided probing reveals an interesting characteristic of the local Nusselt number distribution. All the radial positions reveal a general increase in the convective heat transfer coefficient as the rim seal purge flow is increased. Nevertheless, some outliers are detected, specifically in the moderate rim seal purge flow rate range between IR=0.2 % and IR=0.4 %. These operating conditions show a drop in the Nusselt number, even with respect to the zero-purge case IR=0.0 %. The fact that multiple sensors present the behavior points more toward a physical phenomenon than a measurement inaccuracy. The largest sensitivity to purge flow is detected for the most outer radial position "R5" right below the rotor sealing arm. A factor of three increase in local Nusselt number is found, highlighting the strong dependency of the convective heat transfer coefficient to the purge flow. The sensors on the front face of the rotor disk are similarly sensitive to purge flow as the "R5" position; an increase of the local Nusselt number between a factor of 1.4 and 2 is measured. The tendency of increasing convective heat transfer rates with increasing rim seal purge flow is most likely attributed to the following flow effect: for low purge flow rate it is expected that main annulus fluid is ingested into the lower hub cavity, the fluid has a high swirl and therefore a certain absolute and relative tangential velocity, especially in the core region of the lower hub cavity (away from the walls). Therefore, the axial gradient of the relative tangential velocity is expected to be reduced with respect to the rotor disk which would reduce the tangential shear and therefore the convective heat transfer. As the purge flow is increased, the blockage effect in the lower hub cavity becomes more pronounced and the core region in the hub cavity is slowed down and as such the axial gradient of the relative tangential velocity with respect to the rotor wall is increased, leading to higher Nusselt numbers.

It is typical, to assess the radial variation of the convective heat transfer properties on the rotor disk front face. Therefore, the current Nusselt number definition was adapted by including the change in radius in the definition. In Figure 5.12, the radial distribution of the Nusselt number $Nu(r/r_{seal})$ for three

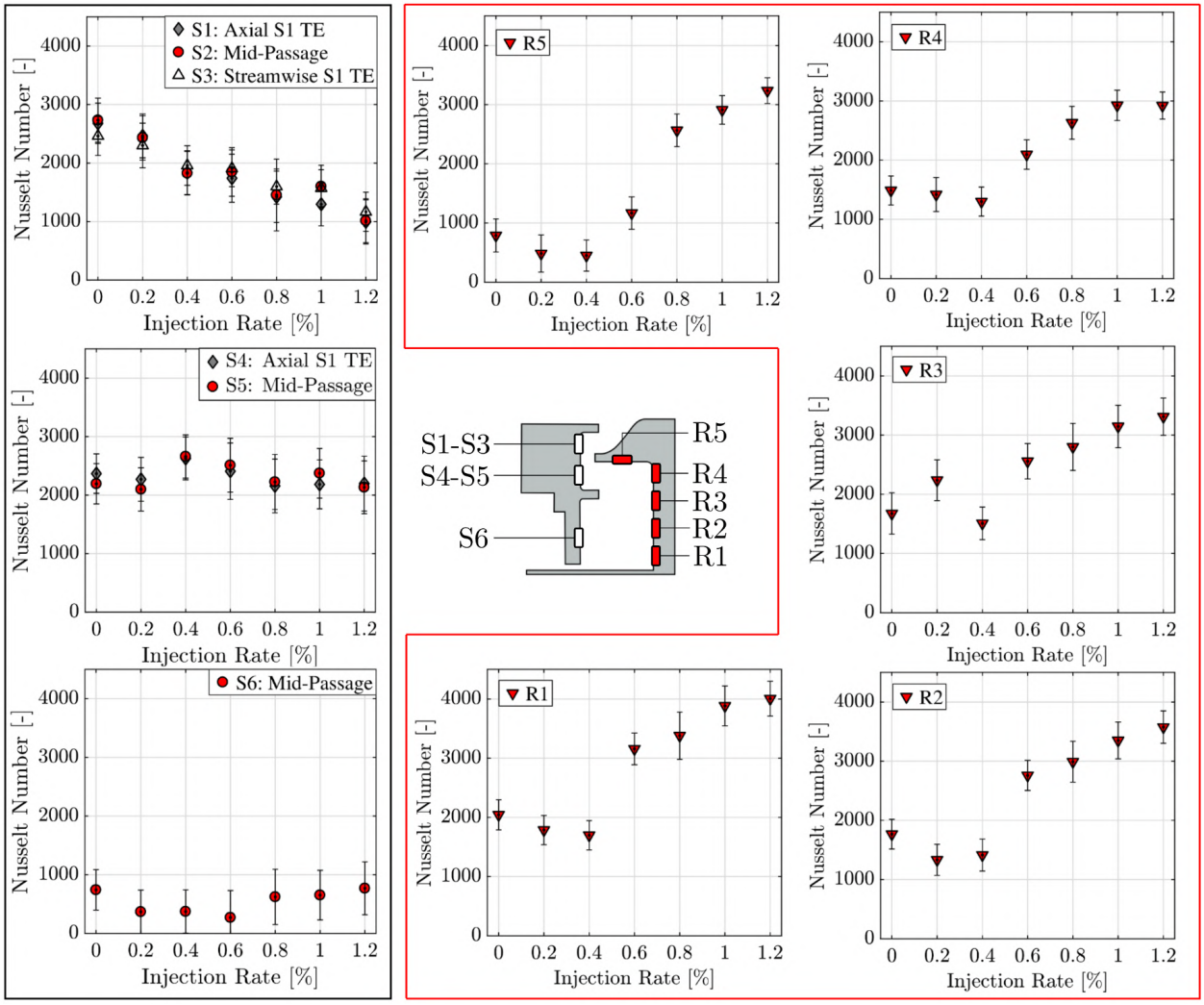

Figure 5.11.: Time-averaged Nusselt number Nu on the first stator- and rotor-sided hub cavity wall for different rim seal purge flow injection rates IR

different rim seal purge flow injection rates is illustrated. The non-dimensional radial coordinate is related to the mid-radius of the rotor-sided sealing arm r_{seal}. One can observe, that the convective heat transfer on the rotor disk wall tends to be reduced as the radial coordinate is increased for most of the points. Only the position below the rotor-sided sealing arm, previously labeled with "R5", shows a slight recovery effect for the higher purge flow rates. It is expected that the growing thermal boundary layer along the rotor-sided hub cavity wall is responsible for the reduction in Nusselt number, as it can be shown that the non-dimensional number is inverse proportional to the thermal boundary layer thickness δ_t (Equation 5.3).

$$Nu \propto \frac{1}{\delta_t} \tag{5.3}$$

It is furthermore of interest to the designers, if empirical correlations can predict the convective heat transfer levels and trends in the rim seal space. One of the few correlations which can be found in open literature is provided by

Owen and Rogers [97] and is termed as "free disk" correlation. The correlation assumes that the temperature variation along the radial coordinate is not substantial and the rotational Reynolds number Re_ϕ is in the turbulent range (typically $Re_\phi > 3 \cdot 10^5$). Furthermore, it is assumed that the thermal boundary layer is not starting at the very center of the rotating disk. The suggested correlation for the rotor-sided Nusselt number distribution is expressed in Equation 5.4. Different values for the tuning coefficient A are available for the presented "free disk" correlation.

$$Nu = A \cdot [(r_{seal}/r)^2 \cdot Re_\phi]^{0.8} \tag{5.4}$$

The rotational Reynolds number for the current turbine operating conditions varies in the range of $Re_\phi = [1.66 - 1.92] \cdot 10^6$, depending on the rim seal purge flow rate. The rotor-sided sealing arm mid-radius r_{seal} was chosen to emulate the outer diameter of the free disk. In addition, the tuning parameter is reported to vary within a range of A = [0.0138–0.0194] [97] which would vary the Nusselt number values by up to 40 %. The range of varying Nusselt numbers based on the correlation including the maximum and minimum distribution is added to Figure 5.12 by means of solid blue lines for the IR=0.0 % case. Comparing the results with the experimental data reveals, that the empirical correlation agrees reasonably well for most of the radial coordinates (±20 %) when the net purge flow rate is set to zero and the rotational Reynolds number is calculated using the fluid temperature (adiabatic wall temperature) of the IR=0.0 % as reference. For the highest purge flow rate (IR=1.2 %), the correlation underpredicts the heat transfer coefficients by at least 31 % of the measured value, however, by unfavorably choosing the tuning parameter deviations up to 60 % can be expected.
In general, these correlations are too sensitive to specific tuning parameters in order to provide a reliable dataset, as the correlation can underpredict the local Nusselt number by up to 60 % for high purge flow rates if an unfavorable tuning parameter is applied. Obviously, the correlation does not directly account for the injection of coolant. The effect of varying the purge flow rate can only by indirectly considered by changing the reference temperature (fluid temperature) for the calculation of the rotational Reynolds number (kinematic viscosity). The most right dotted red line in Figure 5.12 already includes the reduced flow temperature of the high purge flow rate. It is therefore advised to take great care when applying such empirical relationship in the starting design phase, especially in the presence of purge flow.

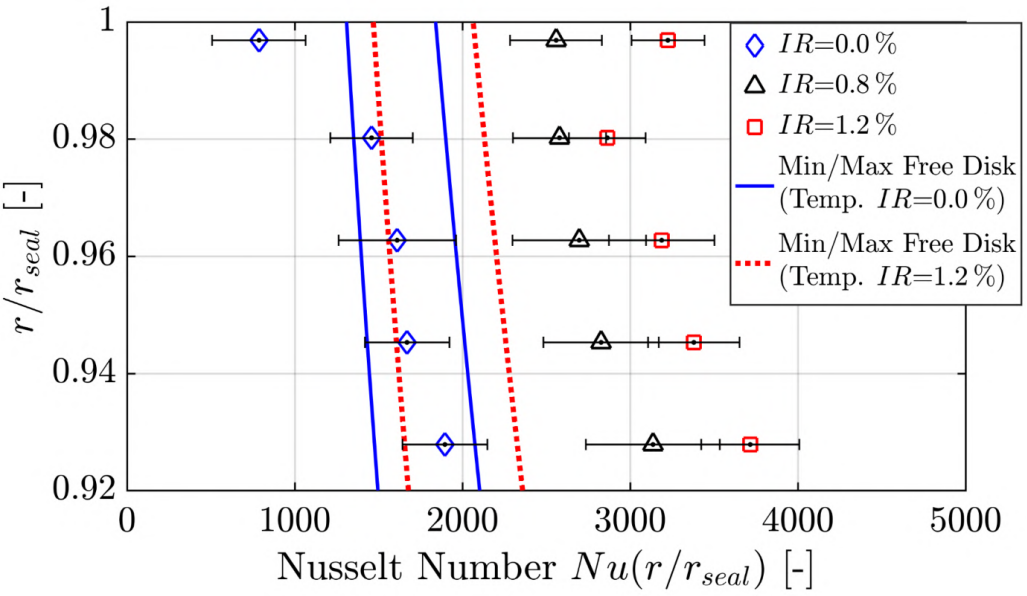

Figure 5.12.: Time-averaged Nusselt number Nu distribution on the rotor disk front face for three different purge flow rates, including free disk correlation as provided in the work by Owen and Rogers [97]

5.4. Conclusions

A unique dataset is provided, quantifying the convective heat transfer and hot gas ingestion quantities for an engine-representative overlap-type rim seal for small integral changes in the rim seal purge flow rates using a purpose-made hub cavity heat transfer measurement setup. The presented overlap-type rim seal is found to appropriately block the ingestion of main annulus fluid at high purge flow rates. Nevertheless, in order to gain the last percentage points for highest sealing effectiveness, the designer must expect that the minor improvements are compromised by a relatively strong decrease in stage efficiency due to the linear decrease with purge flow. Therefore, the study encourages to decrease the sensitivity of the stage performance to purge flow to maximize the overall aerothermal performance of the turbine. Specifically for the hub cavity heat transfer quantities, it was found that: increasing the rim seal purge flow injection rate by 1 %, increases the local heat transfer coefficient on the rotor hub cavity wall by a factor of 2–3, which highlights the importance of the appropriate purge rate as design parameter. Furthermore, "Free disk" empirical correlations are not advised to be used to predict the local heat transfer coefficients for high cooling flow rates on the rotating cavity wall, as they are particularly sensitive to tuning parameters and were found to underpredict the convective heat transfer coefficient for high purge flow rates by up to 60 %. The correlation is more appropriate to use when the net purge flow rates are closer to zero (discrepancies within ±20 % for zero purge flow).

6. Rotor Blade Tip Designs for a Reduced Blade Count Rotor

Engine manufacturers continuously strive to reduce the number of turbine components. Especially with a blade or vane count reduction, the designers aim to reduce the overall operational costs which include production and maintenance costs. In addition, a weight reduction of the engine and lower cooling mass flow requirements can be achieved due to a reduction of the wetted surface which in turn would result in higher overall engine efficiencies. However, reducing the number of blades provokes inherently an increase in blade loading, which drives the secondary flow strength [47] and benefits tip leakage flows as the pressure difference between pressure and suction side of the blade is enhanced [13]. All these effects typically promote the aerodynamic losses in the turbine stage and specifically in close vicinity to the blade tip. Consequently, potential measures to diminish the detrimental effects of high blade loading and pronounced tip leakage flows lie within the geometrical design of the blade tips. Well-designed coolant ejection at the tip of the blade is also found to have a beneficial impact on the aerodynamic performance [149, 150] and protects the highly thermally loaded tip region. As the secondary flow strength is typically enhanced when the number of rotor blades is reduced, the flow field is prone to increased flow unsteadiness induced by the rotor-stator interaction. Consequently, the pronounced flow unsteadiness can drive the noise emissions of the turbine configuration. As the turbine sections become more relevant to the acoustic design of aero-engines, mainly due to the enhanced bypass ratios and advances in the geared turbofan concept, great care has to be taken on that aspect as well. In the open literature only a limited amount of research can be found that combines all the aforementioned aspects in one holistic experimental study.

Therefore, an extensive experimental investigation of different rotor blade tip designs in a highly loaded 1.5-stage turbine with a reduced blade count rotor is presented. The chapter starts with a detailed aerodynamic investigation on the impact of a rotor blade count reduction and describe the associated detrimental effects on the aeroacoustics of the turbine. By means of four different blade tip designs in combination with accurate fast-response probe measurements, the impact of different tip concepts on the near tip aerodynamic losses is studied. The investigation is complemented with a sensitivity analysis

of the various blade tip designs with respect to the coolant ejection at the tip.

6.1. Performance and Aeroacoustics of a Reduced Blade Count Rotor

In the presented section, inter-stage probe measurements in two 1.5-stage turbine configurations assess the potential to improve the stage efficiency for a reduced blade count rotor with 42 blades compare to the baseline configuration with 54 blades. The two turbine configurations that were used for this study are the baseline configuration of the purge control configuration (section 2.2.2), termed as "Baseline", and the reference squealer design of the reduced blade count rotor setup (section 2.2.3), termed as "Reduced". It is important to consider that only the rotors have changed for this investigation. The stator rows, as well as the axial gaps, remained the same. Furthermore, the reduced blade count rotor blisk only contains the reference squealer tip design (no rainbow design). The rim seal purge flow is kept for both designs at IR=0.8 %.

The conducted time-resolved probe measurements reveal the detrimental effects on the turbine tonal noise level. It is found that the periodic vorticity fluctuations induced by the interaction of the rotor passage secondary flow structures with the potential field of the downstream stator, lead at specific span positions to a strong increase in the blade passing-induced pressure fluctuations at rotor exit compared to the baseline. Both the downstream effect of the convected rotor flow structures as well as the periodic interaction of the second stator originated flow structures are found to drive the acoustic field of the turbine. Overall, the stage efficiency benefit achievement of 0.4 % points for a 22 % reduction in rotor blade count is derogated by an increase in tonal noise by up to 13 dB at the second stator exit.

6.1.1. Aerodynamic Performance and Flow Field Analysis

The section provides the aerodynamic performance of the two rotors by means of the measured total-to-total stage efficiency (η_{tt}). The definition of the aerodynamic efficiency which is used in this study is given in Equation 2.36. Again, the total pressure data at the rotor exit are provided by the high accuracy five-hole probe (5HP).
In Figure 6.1, the circumferentially mass- and time-averaged total-to-total stage efficiency profiles (absolute and differential) for both rotor geometries are depicted. The profiles provide a first indication of the main regions of improvement and penalties. Nevertheless, the analysis is further on supported with contour levels of other flow quantities that reveal the three-dimensional

character of the flow. Overall, the reduced blade count rotor presents an aerodynamic performance improvement on a large fraction of the span (hub to about 80 % span). Specifically, at around 40 % and 70 % span, an increase in stage efficiency of up to 1.3 % points and 1.5 % points is measured. A pronounced performance reduction of up to 1.9 % points for the reduced blade count rotor is registered above 80 % span. The absolute integral total-to-total stage efficiency increase ($\Delta\eta_{tt}$) for the reduced blade count configuration compared to the baseline is determined to be 0.37 % points.

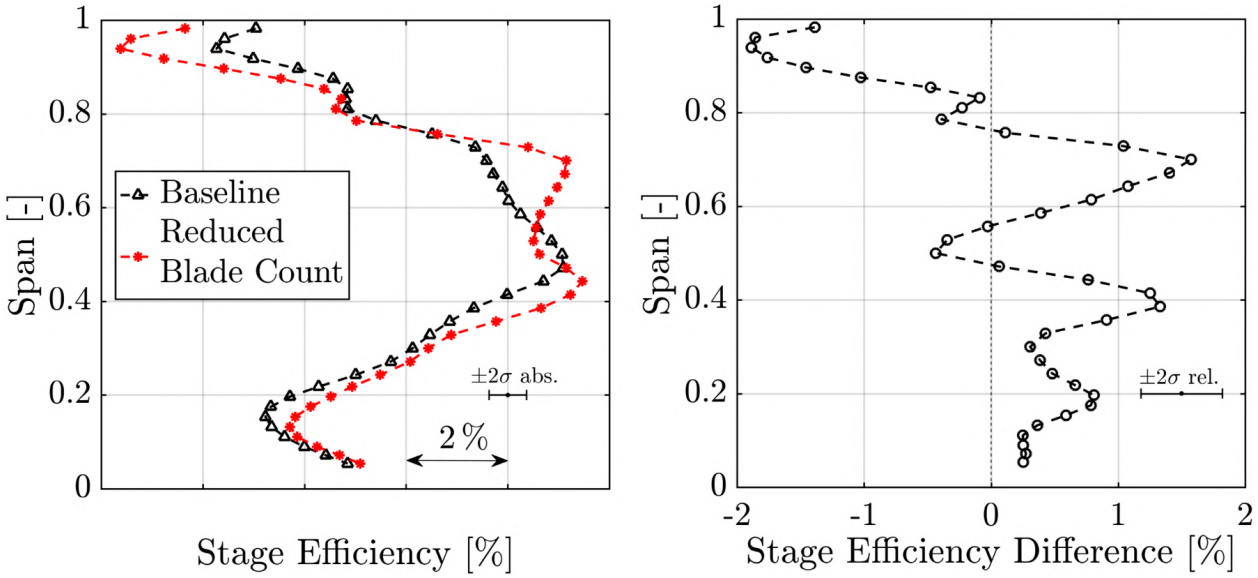

Figure 6.1.: Circumferentially mass- and time-averaged total-to-total stage efficiency distribution (left) and difference $\Delta\eta_{tt}$ (Reduced-Baseline, right) measured with 5HP. Stage efficiency difference is given in percentage points.

The source of the performance increase of the reduced blade count rotor needs to be linked to the flow physics of the stage. Turbine efficiencies are typically linked to stage loading and flow coefficient. In Figure 6.2, the circumferentially mass- and time-averaged profiles of the stage loading and flow coefficient are illustrated. The two coefficients were derived from the definitions given in Equation 4.2 and 4.3. In order to explain the stage efficiency increase around 70 % span, the stage loading and flow coefficient profiles reveal some evidence. At 60–80 % span, the flow turning is moderately reduced by 3 % for the reduced blade count rotor. The reduction in stage loading in this range of the span is induced by the reduction of the absolute flow yaw angle by up to 5°. This under-turning effect of the flow is typically provoked by the rotor tip passage vortex. The characteristics of the secondary flow structures at the rotor exit are further detailed in the subsequent flow analysis. The flow coefficient, on the other hand, is locally enhanced by up to 10 %.
The predominance of the local flow coefficient increase (with a moderate reduction in stage loading) indicates that a larger amount of mass flow is turned at that specific span-wise position. Since the turbine capacity for

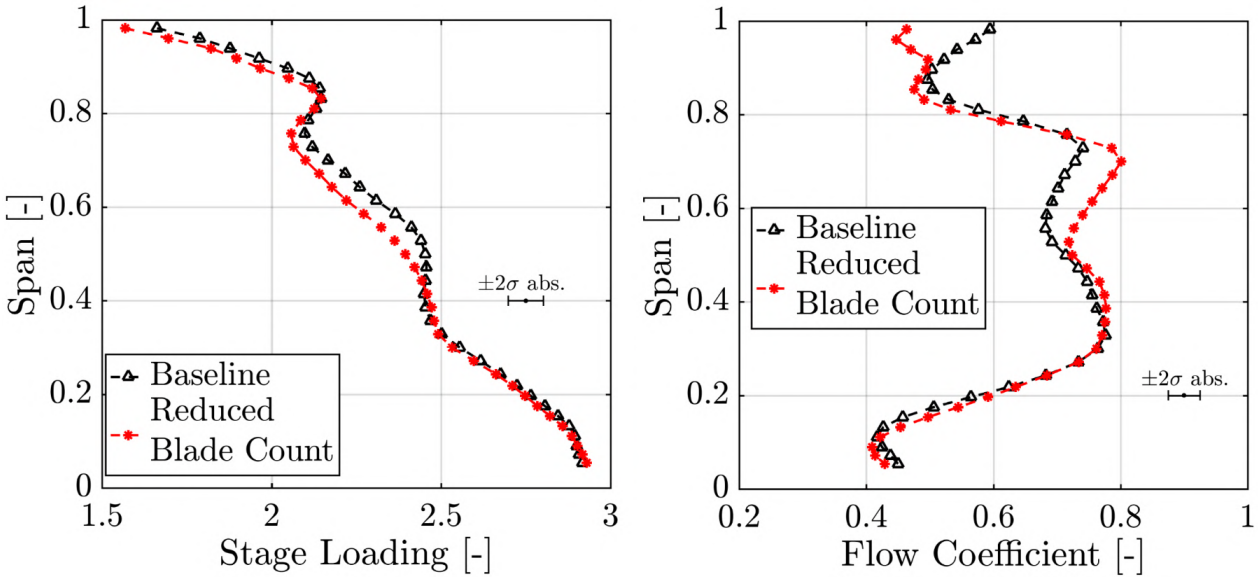

Figure 6.2.: Mass- and time-averaged stage loading (left) and flow coefficient (right) for the baseline and reduced blade count rotor (4HP and 5HP)

both configurations is not significantly changed (changes are well within the measurement uncertainty), the increase in mass flow at 60–80 % span is partly explained by a span-wise redistribution of mass flow. Figure 6.2 (right) shows a local flow coefficient reduction of up to 22 % in the near blade tip region (96 % span) which suggests that part of the mass flow is redistributed from the tip toward 60–80 % blade span. In conclusion, due to the redistribution of mass flow from the tip, a larger amount of flow can be turned more than in close vicinity to the blade tip. This circumstance helps to sustain the rotor torque for the reduced blade count rotor. Considering the stage efficiency distribution in close vicinity to the tip, a reduction in performance for the reduced blade count rotor is measured. The lower mass flow at the tip, in combination with lower turning, reduces the work extraction in this region.
To complement the analysis, the impact of secondary flow structures on the rotor exit flow field is studied. Specifically, at around 40 % span where the stage loading and flow coefficient is moderately changed for the two configurations, an aerodynamic loss quantification is required. In Figure 6.3 (a), the circumferentially mass-and time-averaged normalized relative total pressure is presented for both turbine configurations. The pressure information is normalized by the respective turbine inlet total pressure. The profiles indicate that the relative total pressure is increased by 1 % around 40 % span for the reduced blade count rotor. The flow field in this region is characterized by the presence of the hub secondary flow structures which is demonstrated in the time-averaged contour diagrams in Figure 6.3 (b) and (c). The figures illustrate the presence of low relative total pressure regions in the rotor relative frame of reference around 40 % span and 25 % rotor pitch (zone **(1)**). In detail, the minimum relative total pressure in the loss

core is marginally altered for the reduced blade count rotor (0.2 % reduction). However, the pitch-wise fraction of low loss fluid (60–100 % rotor pitch and 40 % span) is increased by about 17 %. The pitch-wise fraction of the hub secondary flow structure loss core is accordingly reduced at this span position.

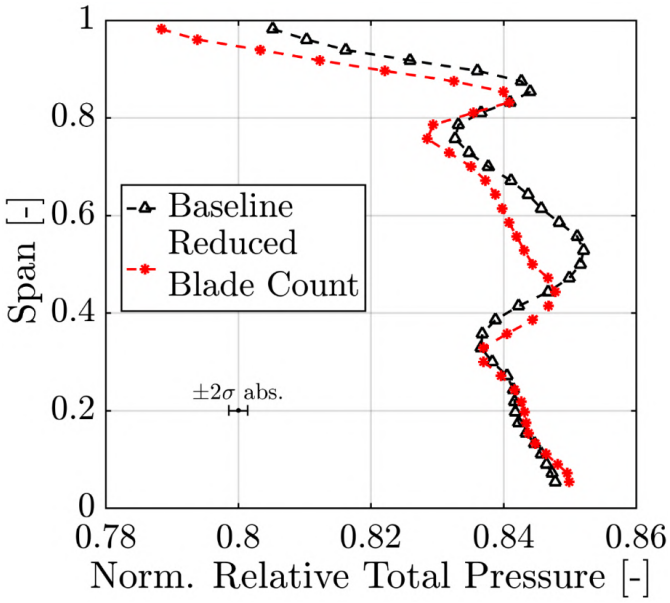

(a) Mass-and time-averaged profiles

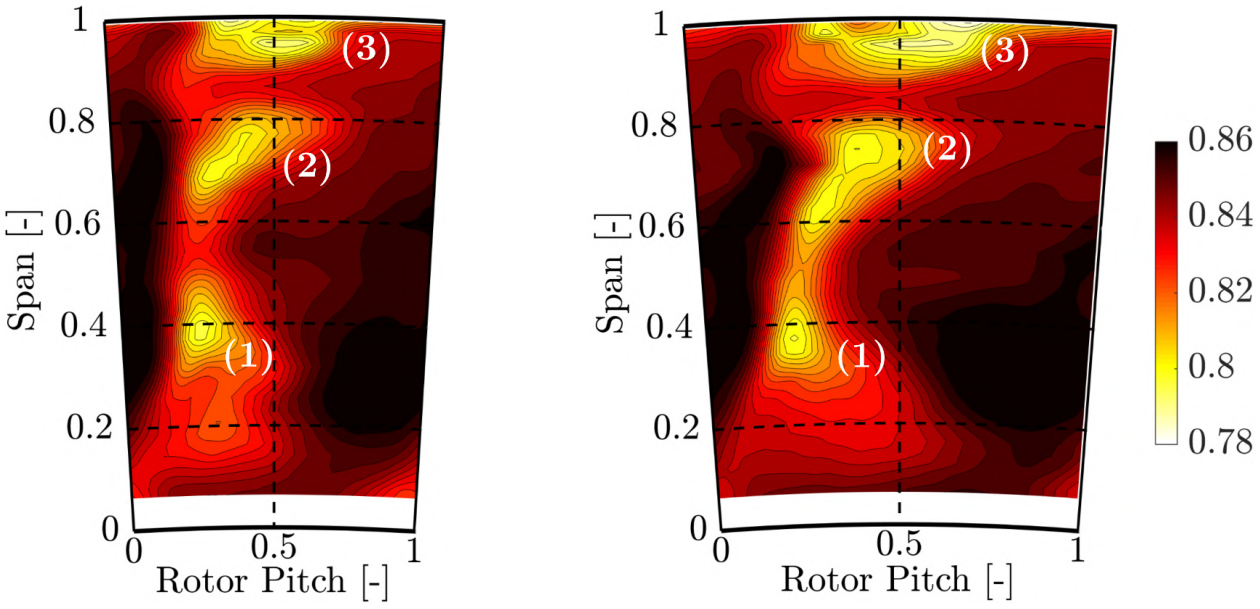

(b) Baseline **(c)** Reduced Blade Count

Figure 6.3.: Normalized relative total pressure $C_{pt,rel}$ at rotor exit [-] for baseline and reduced blade count rotor. Circumferentially mass- and time-averaged distribution (a) measured with 5HP, time-averaged contour diagrams in rotor relative frame of reference (FRAP) depicted in (b) and (c).

The lower relative total pressure at mid-span for the reduced blade count rotor is associated with the enhanced loss generation in the blade boundary layer. At 50 % span diffusion occurs, which provokes an adverse pressure gradient

on the blade suction side. The blade count reduction leads to an increased blade loading (similar stage loading for fewer blades) with more mass flow per rotor passage, which benefits the loss generation in the boundary layer and results in larger wake losses. This is demonstrated in the time-averaged contour diagrams in Figure 6.3, where at 25 % rotor pitch and 50 % blade span lower relative total pressure is found for the reduced blade count rotor. The zone **(2)** in Figure 6.3 is attributed to the tip passage vortex and tip trailing edge shed vortices which form at around 40 % rotor pitch and 70 % blade span a low relative total pressure region.
The clear distinction between the flow structures at this span-wise position is enabled by considering the streamwise vorticity in the rotor relative frame of reference which is provided in Figure 6.4. The positive streamwise feature indicated with **(I)** is the signature of the rotor hub passage vortex. For the reduced blade count rotor, the area of the vortex seems to be augmented in the passage. The combination of comparable vorticity levels with larger covered area suggests an increase in circulation and therefore strength of the vortex.

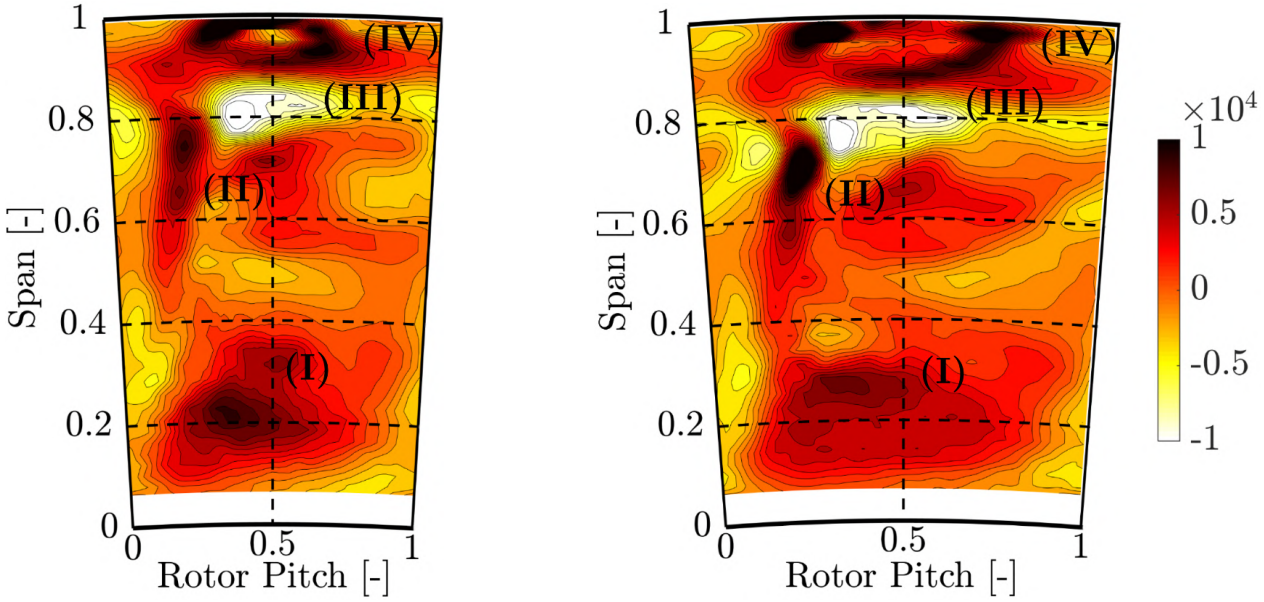

(a) Baseline **(b)** Reduced Blade Count

Figure 6.4.: Time-averaged streamwise vorticity Ω_S [Hz] in the rotor relative frame of reference for both rotor designs (FRAP)

The positive streamwise vorticity feature labeled with zone **(II)** is the signature of the tip trailing edge shed vortex, whereas the tip passage vortex is characterized by pronounced negative streamwise vorticity in zone **(III)**. Comparing the baseline and the reduced blade count rotor, the latter presents an enhanced positive streamwise vorticity for the tip trailing edge shed vortex by up to 88 %. The tip trailing edge shed vortex is associated with the radial outward migration of the rotor suction-side boundary layer and is therefore driven by the blade loading, which explains the higher levels for the reduced

blade count rotor. The negative streamwise vorticity levels for the tip passage vortex are comparable for both rotors; however, the reduced blade count rotor tends to have a more stretched vortex in the pitch-wise direction.
The stage efficiency penalty at the blade tip for the reduced blade count rotor is the result of the strong presence of the tip leakage vortices, which were indicated by the high positive streamwise vorticity in zone **(IV)** and was translated into the low relative total pressure region in zone **(3)** of Figure 6.3 (c). Specifically, for the reduced blade count rotor, the signature of the tip leakage vortices seemed to migrate radially downward to about 80 % span. In addition, two distinct high positive streamwise vorticity zones were present (97 % span) for the reduced blade count rotor. These zones had an up to 50 % higher positive streamwise vorticity than the ones of the baseline configuration. Since both rotor designs were unshrouded (with the same nominal tip gap), the tip leakage losses were mainly driven by the tip leakage flow over the blade tip, which was less turned and tended to roll up streamwise vortices, and secondly by the re-injection of the leakage flow into the main flow, which provoked intensive mixing. The tip leakage flow was driven by the pressure difference between the blade pressure and suction side. Due to the significant reduction in blade count, the blade loading close to the tip increases accordingly which benefits the tip leakage mass flow and therefore the formation of the tip leakage vortices. The presence of the squealer tip geometry for the reduced blade count rotor is not able to compensate for the consequences out of the blade loading increase at the tip.
In summary, this section shows the performance improvement of a reduced blade count rotor which is mainly attributed to a radial mass flow redistribution (and only a moderate reduction in stage loading) at specific span-wise positions without provoking an overweight of secondary flow losses that outweigh the benefits gained from the improved mass flow distribution. The presented aerodynamic results build a basis for the turbine noise investigation of both configurations.

6.1.2. Turbine Tonal Noise Investigation at the Rotor Exit

The investigation of noise-generating mechanisms in rotating machinery is typically linked to flow unsteadiness. Specifically, for relatively low-speed and sub-sonic turbomachines, the unsteadiness induced by the interaction of rotors and stators (blade passing) is one of the predominant sources. Therefore, the assessment of noise for the current turbine configurations is focused on the blade passing-induced noise. Since one of the drivers for pronounced blade passing-induced noise is the axial distance between rotors and stators [96], the investigation is performed first at the rotor exit where the axial distance between the rotor and second stator is about half of the one between the first

stator and rotor. The axial distances in percentage of the rotor axial chord between the blade rows can be found in Figure 2.2.
FRAP measurements were employed at the exit of the rotor. For each measurement point, a Fast Fourier Transformation was calculated when the probe yaw sensor is aligned to the mean flow direction. Subsequently, the pressure amplitude of the rotor blade passing frequency (RBPF) was extracted and converted into a normalized pressure amplitude induced by the blade passing. The pressure amplitude is normalized by the respective turbine inlet total pressure. In Figure 6.5 (a) and (b), the contour diagrams of the normalized blade passing pressure amplitude is depicted for one stator pitch and both rotor designs. The dashed inclined line in the figure represents the location of the second stator leading edge (LE S2). The plots reveal that blade passing amplitudes up to 3 % of the turbine inlet total pressure occur. The peak values of the blade passing-induced amplitudes are detected in close vicinity to the blade tip (above 90 % span), which is attributed to the rotor tip leakage vortex dynamics. The reduced blade count rotor shows additionally a strong presence of the blade passing within 10–40 % span and 50 % stator pitch as well as around 70–80 % span and 70 % stator pitch.
In order to better correlate the registered distribution of the blade passing pressure amplitude to the flow physics, Figure 6.5 (c) shows the absolute differential normalized pressure amplitude map for one stator pitch. The difference is shown with respect to the baseline rotor. Again, the dashed inclined line indicates the location of the second stator leading edge (LE S2). The map reveals the pitch-wise and radial location where the most pronounced increase in blade passing-induced pressure amplitudes occurs. Two zones are identified: one around 10–20 % blade span (50–70 % stator pitch) and one between 40–60 % span (30–70 % stator pitch). Both zones do not only show a radial extent but also are stretched pitch-wise. This implies that these features are modulated by the passing of the rotor. Furthermore, both zones show their local maxima at a certain pitch-wise location (around 60 % pitch), which does not coincide with the second stator leading edge location. The peak value of the absolute change for the zone close to the hub is 1.1 % of the turbine inlet total pressure, and the zone between 40–60 % span presents an increase of 0.9 % of the inlet total pressure. In close vicinity to the blade tip, an increased normalized pressure amplitude of up to 1 % of the inlet total pressure is detected for the reduced blade count rotor at around 90 % span and in pitch-wise direction around 50 % stator pitch.

As indicated in the blade row design section 2.2.3, the tip design of the reduced blade count rotor features a squealer tip geometry instead of a flat tip as for the baseline case. Therefore, the contribution of the geometrical change to noise production needs to be addressed. The tip clearance noise is separated into two mechanisms [83]. First, the unsteady interaction of the flow field in

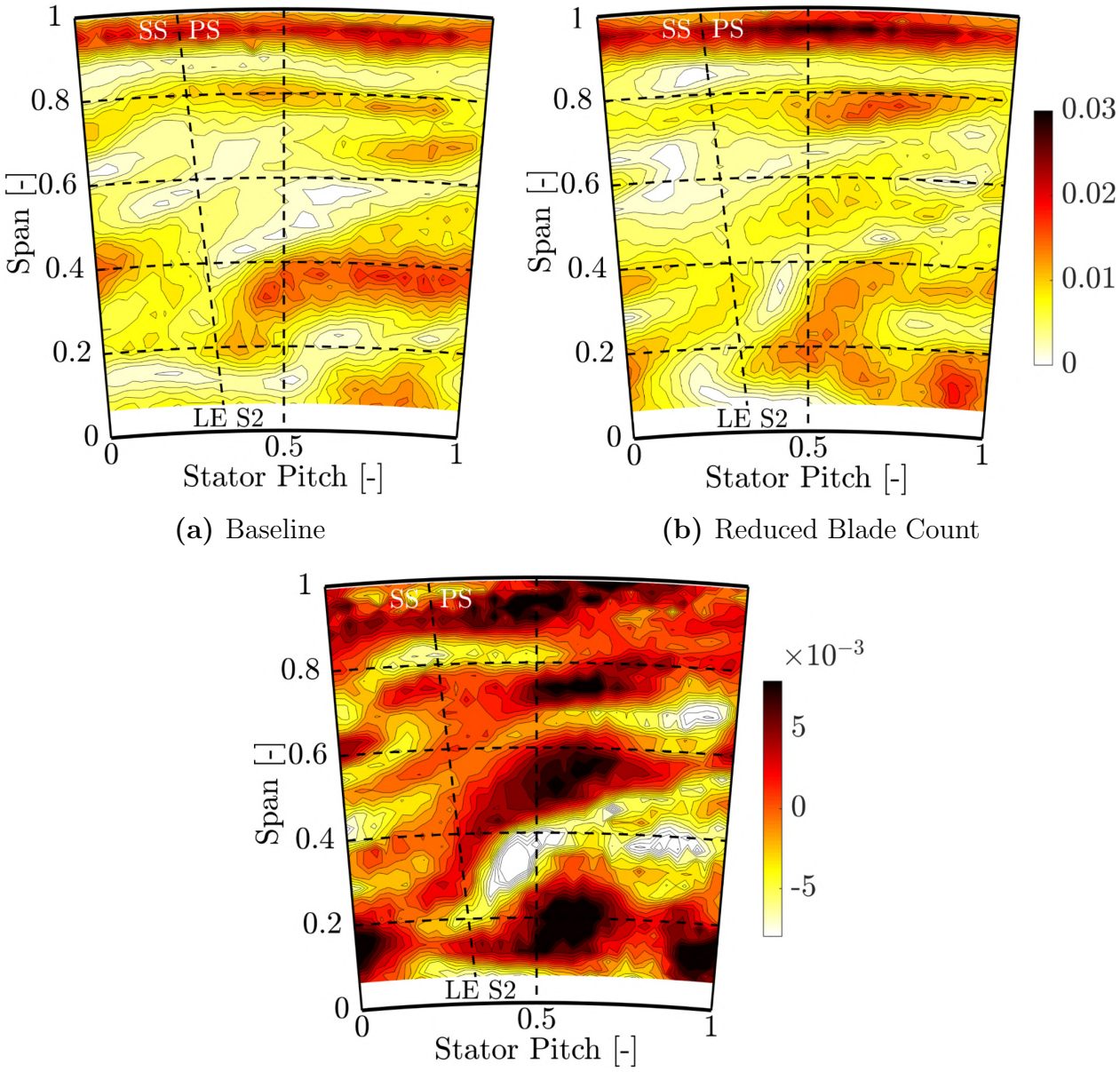

(a) Baseline

(b) Reduced Blade Count

(c) Difference (Reduced-Baseline)

Figure 6.5.: Normalized pressure amplitude of the blade passing frequency [-] in the absolute frame of reference and absolute difference [-] between the baseline and reduce blade count rotor (FRAP)

the vicinity of the tip with the tip surface which produces a broadband noise (rotor tip self-noise). Second, the downstream convection and interaction of the tip leakage vortex with the downstream stator which mainly contributes to the turbine tonal noise. Based on that, the main aspect to be considered for this study is the potential change or development of the tip leakage vortex. In a separate computational fluid dynamics (CFD) study where the blade tip geometry is altered (flat tip against squealer tip, for reduced blade count configuration), the total pressure losses at rotor exit induced by the tip leakage vortex are found to be only slightly increased (0.1 %) for the squealer tip which implies that the tip leakage vortex is not significantly strengthened. Based

on these moderate changes, the contribution of the squealer tip geometry with respect to the flat tip (with the same blade count) on the tonal noise production is estimated to be low based on the predictions. However, an experimental assessment is still to be performed and could not be conducted in the time frame of this thesis.

To understand the local changes in the blade passing-induced pressure amplitude at the rotor exit, the time-resolved flow field at the rotor exit needs to be analyzed. One approach to further investigate the findings of Figure 6.5 is to link the stronger presence of the rotor-stator interaction to the modulation of the flow structures coming from the rotor (and from the upstream stator) with the second stator. In Figure 6.6 (a) – (f), the time series of the streamwise vorticity at the rotor exit for the reduced blade count configuration is shown. The time scale is expressed as a fraction of the blade passing period T. To show the dynamics in more detail, the time series is limited to 40 % of the blade-passing period. The inclined dashed lines show the location of the downstream stator leading edge.
The secondary flow structure system **(I)**, previously presented in Figure 6.4, is indicated with a dashed white line consisting of the hub and tip passage vortices as well as the tip leakage vortices. However, the pronounced increase in blade passing pressure amplitude between 40–60 % span in Figure 6.5 (c) is associated with the vortex system highlighted in black dashed lines and indicated with **(II)**. This vortex system consists of two vortices with opposite senses of rotation. The negative vorticity region located closer to the hub end wall is anticipated to be the remnant of the first stator hub passage vortex, which is convected through the rotor passage on the suction side after being chopped by the rotor leading edge. The positive streamwise vorticity zone in **(II)** is expected to be the first stator hub trailing edge shed vortex, which again is convected through the rotor passage. A similar vortex dynamic was described in detail by Schneider et al. [172].
As shown in a previous study by Chaluvadi et al. [24], the remnant of the first stator hub passage vortex (which follows the suction side of the rotor) tends to radially migrate outwards over the rotor hub passage vortex. Similar behavior is found in the time sequence of the reduced blade count rotor flow field. As the rotor blade passing proceeds, the negative vorticity in zone **(II)** is continuously radially and pitch-wise displaced and with it the positive vorticity feature. At $t/T = 0.40$, the position of both features is within 40–60 % blade span and their streamwise vorticity are maximized. This process repeats for every rotor blade passing event which highlights the periodicity with respect to the rotor-stator interaction. The intensification of the streamwise vorticity with time by more than a factor of 3 is due to the interaction of the vortices with the downstream stator as the rotor blade passes. As the vortex system

indicated with **(II)** is accelerated in streamwise direction by the quick swing around the potential field of the downstream stator, the vortices are stretched in the streamwise direction, which increases the streamwise vorticity. Such vortex stretching was previously explained by Greitzer et al. [54]. A similar process of vorticity increase is also present for the other flow features. Part of it can be observed in the presented time series of the streamwise vorticity.
For instance, the rotor hub passage vortices, as well as the rotor tip passage vortices, undergo a similar increase in streamwise vorticity as they swing around the potential field of the second stator, which leads to the previously discussed increase in the blade passing pressure amplitude (Figure 6.5). When comparing the two turbine configuration, it is found that the baseline rotor exit flow field experiences similar changes in the streamwise vorticity, as described in the previous paragraphs. However, the peak negative and positive streamwise vorticity of zone **(II)** is enhanced for the reduced blade count rotor by about 9 % and 24 %, respectively. Also, the area covered by the two vortices was calculated using iso-surfaces of streamwise vorticity (2'000 Hz) to get a qualitative measure of circulation and, therefore, vortex strength. The circulation is found to be increased for the positive vorticity zone by about 40 %, and the negative one by 30 %, respectively. The time-resolved changes in vortex strength for the reduced blade count rotor is increased accordingly. This strengthening of the vortex is anticipated to be linked to the higher blade loading. The remnants of the first stator secondary flows follow the suction side of the rotor blade; since the blade loading is higher, also the relative Mach numbers on the suction side is increased which causes that the secondary flows are even more accelerated in the streamwise direction and therefore stretched which enhances the vorticity levels.
In this section, an attempt is made to link the local increase in blade passing pressure amplitude to the unsteady vortex dynamics of the 1.5-stage turbine configurations. Interestingly, the peak values in the pressure amplitude induced by the blade passing are predominantly provoked by the local vorticity fluctuations of the rotor passage vortices (including remnants of the first stator vortices), which are driven by the potential field interaction with the downstream stator. These periodic vorticity fluctuations inherently provoke local pressure fluctuations and therefore noise. By reducing the rotor blade count, the blade loading and hence the secondary flow structure strength is prone to be enhanced, which promotes the local increase in the blade passing-induced flow unsteadiness.

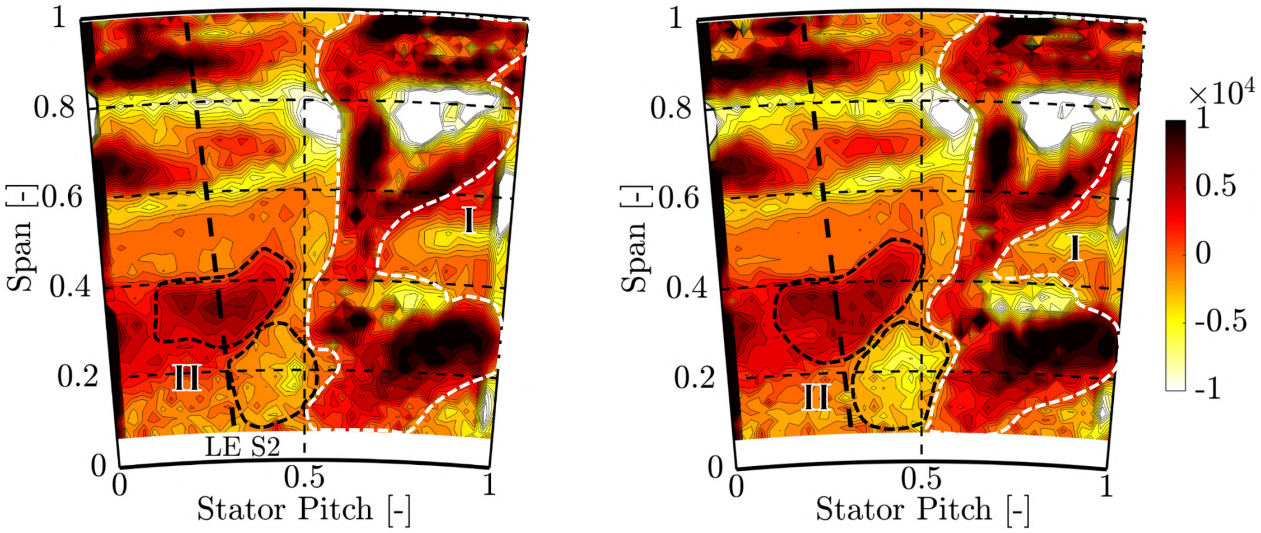

(a) $t/T = 0$ **(b)** $t/T = 0.05$

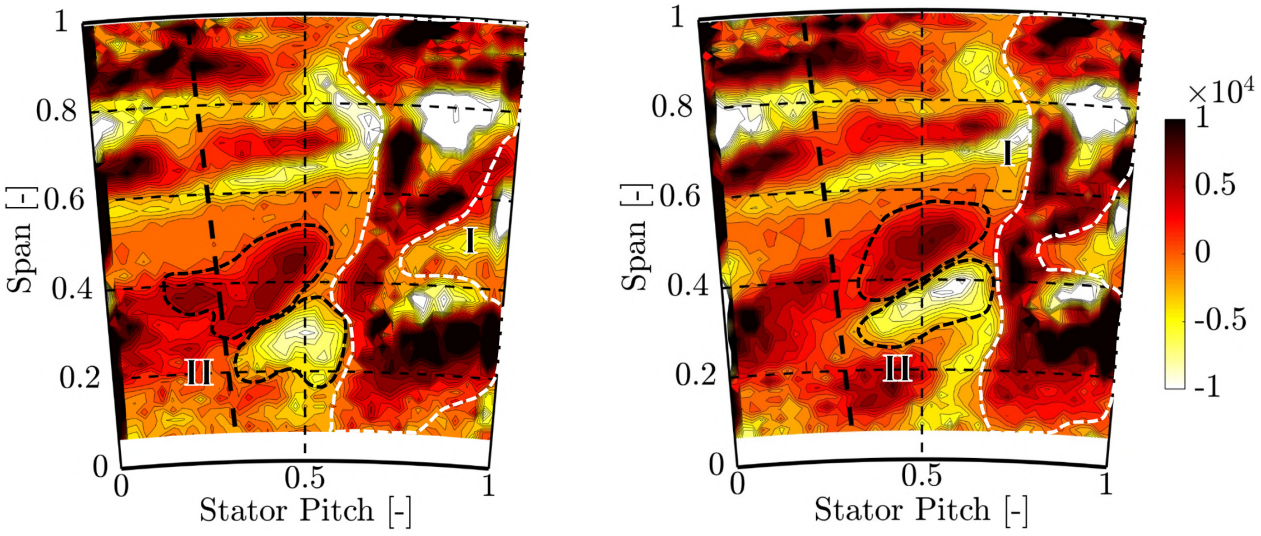

(c) $t/T = 0.10$ **(d)** $t/T = 0.20$

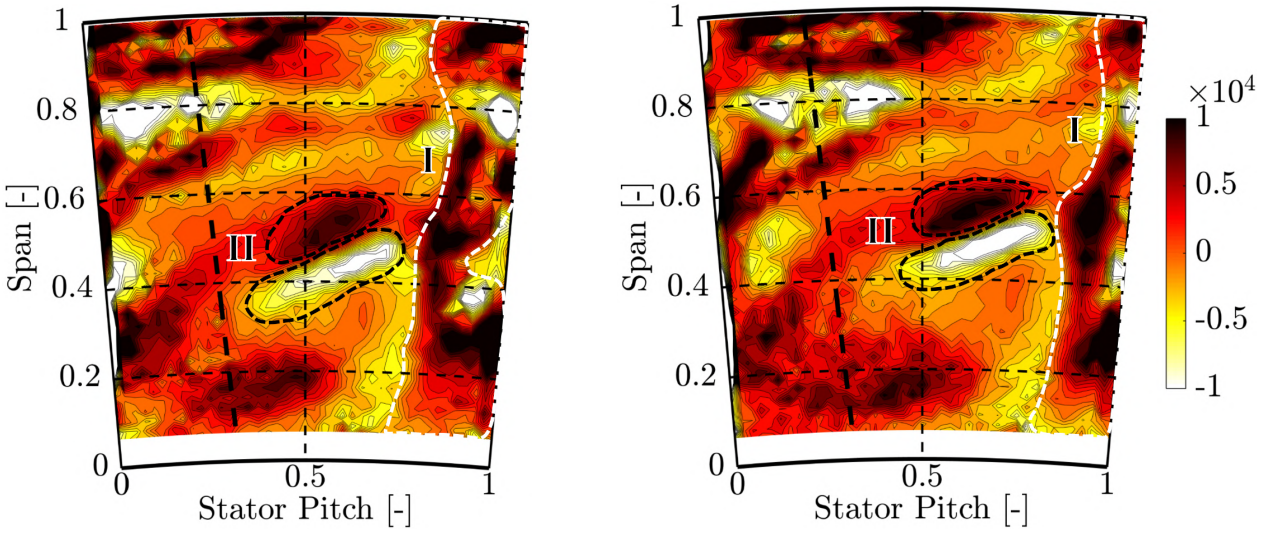

(e) $t/T = 0.30$ **(f)** $t/T = 0.40$

Figure 6.6.: Time series of streamwise vorticity Ω_S [Hz] at rotor exit for the reduced blade count rotor in the absolute frame of reference (FRAP)

6.1.3. Turbine Tonal Noise at the Second Stator Exit

The previous section has revealed a noise generating mechanism at the rotor exit. To assess the potential for this effect to propagate through the second stator, the analysis is complemented by time-resolved probe measurements at the exit of the second stator.

The flow field of the reduced blade count rotor at the second stator exit is illustrated by means of the time-averaged normalized absolute total pressure for one stator pitch in Figure 6.7 (a). The total pressure data are normalized by the respective turbine inlet total pressure. The dashed inclined line indicates the trailing edge of the second stator (TE S2). In the graph, two main regions of interest are identified. The dashed circle labeled with **(1)** covers the second stator hub passage vortex and the zone indicated with **(2)** is a region of accumulation of different flow structures including the ones from the upstream rotor. Rebholz et al. [152] found that the rotor tip secondary flows are able to migrate radially toward mid-span when traveling through the downstream stator and accumulate close to the suction side of the stator vane. Furthermore, part of the reduced total pressure in zone **(2)** is provoked by the wake of the second stator and by the tip secondary flow structures. In addition, it is found in the rotor exit flow field that the flow pitch angle of the rotor hub passage vortex is pointing toward the casing, which also indicates the tendency for part of this flow structure to migrate radially toward mid-span. The second stator exit flow field is therefore affected by its own secondary flows and the ones from the upstream rotor.

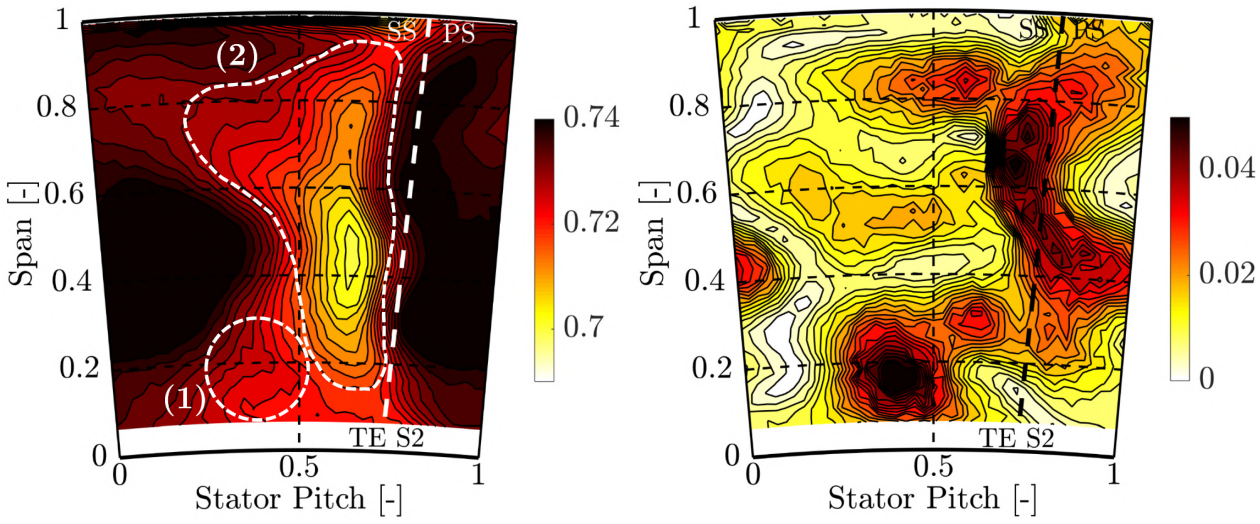

(a) Normalized Total Pressure [-]

(b) Normalized Blade Passing Pressure Amplitude [-]

Figure 6.7.: Time-averaged normalized total pressure C_{pt} at second stator exit for the reduced blade count rotor and normalized blade passing pressure amplitude (FRAP)

In Figure 6.7 (b), the normalized pressure amplitude of the blade passing

frequency is shown for the reduced blade count rotor at the second stator exit. The pressure information is normalized by the turbine inlet total pressure. In combination with the presented results of the normalized total pressure, one can better correlate the local changes of the pressure amplitude with the local appearance of the flow structures.
Overall, the whole flow field is characterized by a strong presence (1.5–2 % of the turbine inlet total pressure) of the blade passing-related pressure fluctuations. The most pronounced increase is found in the hub secondary flow region (around 40 % stator pitch and 15 % span) as well as in close vicinity to the second stator trailing edge region, which was previously labeled with zone **(2)**. Given the findings of the rotor exit assessment, the periodic strengthening of the secondary flow structures and the identified effect on the blade passing pressure amplitude also have an impact on the pressure amplitudes at the second stator exit. Due to the tendency for the accumulation of the rotor secondary flow structures around the mid-span region of the second stator exit and the potential interaction with the stator 2 originated flow structures, the blade passing related pressure amplitude might be even enhanced compared to the rotor exit.
Figure 6.8 (left) supports the statement by showing the pitch-wise averaged absolute change of the blade passing-induced pressure amplitude over the second stator for the reduced blade count rotor. An absolute increase of up to 1.7 % of the inlet total pressure is found at around 85 % span and up to 1.4 % in the mid-span region. The only reduction in the blade passing-induced pressure amplitude occurs above 90 % span (up to 1.5 % of the inlet total pressure) which implies that the second stator tip end wall flow features (sometimes referred as corner vortex) do not considerably interact with the rotor blade passing. The consequences of the reduction in blade count on the pressure intensity level at the second stator exit are illustrated in Figure 6.8 (right). The radial profile of the pressure intensity change reveals the significant increase for the reduced blade count configuration over the whole span. The peak intensity change of 13 dB is located at around 85 % span, and even at mid-span and close to the hub, changes up to 10 dB are detected. The given data highlight the detrimental effect of the blade count reduction on the turbine acoustic field.
Given the trend that, over the whole span, a higher blade passing-induced noise was measured for the reduced blade count rotor, the following aspects deserve mention: the rotor secondary flow structures were convected into the second stator passage where they periodically (with blade passing) interact and accumulate with the second stator originated flow structures. The periodic strengthening of the rotor secondary flow structures at the rotor exit, which was even found to be increased for the reduced blade count rotor, is one of the sources for the higher tonal noise at the stator 2 exit. In addition, the

pronounced span-wise increase of the blade passing-induced pressure amplitude over the second stator for the reduced blade count rotor (as shown in Figure 6.8 (left)), also suggests that the entire second stator flow field interacts strongly with the upstream rotor. In summary, this tells the reader that not only the flow structures coming from the rotor but the second stator flow field itself, which interacts with the rotor, drives the tonal noise level of the turbine configuration.

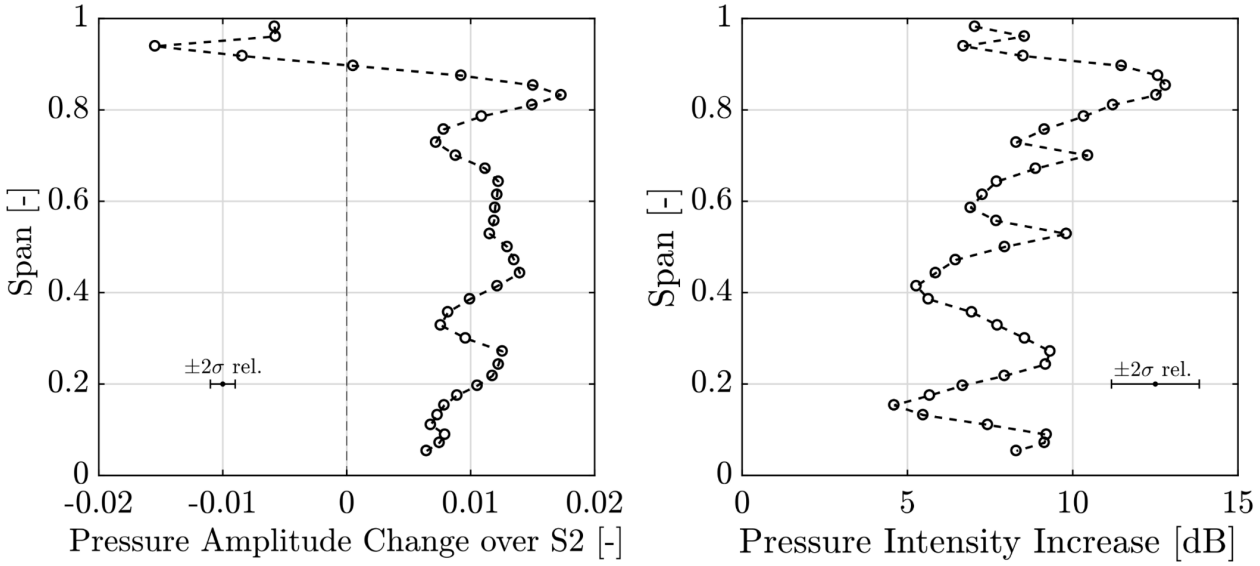

Figure 6.8.: Blade passing pressure amplitude change over second stator for the reduced blade count rotor (left). Span-wise pressure intensity increase for the blade passing frequency of the reduced blade count rotor relative to the baseline at stator 2 exit (right) measured with FRAP.

Overall, it can be summarized out of the extensive analysis of the reduced blade count rotor that the improvement in aerodynamic performance by 0.4 % points for a 22 % reduction in the number of rotor blades stays in conflict with an up to 13 dB higher turbine noise level compared with the baseline.

6.2. Aerodynamics of Optimized Rotor Blade Tip Designs

The previous section of this chapter addressed the impact of a substantial rotor blade count reduction on the aerodynamic and aeroacoustic characteristics of a turbine stage. Although the stage performance could be enhanced by means of a favorable mass flow and loading distribution, the strengthening of the secondary and tip leakage flows could not be avoided. Specifically, the near tip performance was found to be affected by the reduction in blade count (Figure 6.1). To further improve the aerodynamic performance of a reduced blade count rotor, the near tip flow field bears great potential for optimization. Therefore, a set of altered blade tip geometries is tested in a rainbow rotor

configuration featuring different design concepts. In the current section, the effect of the bare geometrical change of the blade tips on the aerodynamic performance and flow fields are investigated without having the additional impact of the ejected cooling flow at the tip. The coolant supply path from the upstream hub cavity into the blade cap plenum was sealed as explained in section 2.1.5 and schematically illustrated in Figure 2.7.

6.2.1. Aerodynamic Performance Overview

The analysis of the different tip designs, which are depicted in Figure 2.19, focuses firstly on the aerodynamic performance levels. As already mentioned in the experimental method chapter, the rainbow rotor configuration enables measuring different tip designs during the same test run. By employing fast-response probe measurements that can be triggered on individual blades, the respective flow quantities can be correlated to a specific blade tip design. Nevertheless, the aerodynamic performance cannot be readily determined as usual using a torque-based efficiency definition. Therefore, a temperature-based efficiency relationship, as introduced in Equation 2.37, is used, which includes the time-resolved temperature and pressure measurements of the fast-response entropy probe (FENT).
The resulting mass- and time-averaged temperature-based stage efficiency difference is presented in Figure 6.9. Note that efficiency is derived by triggering the FENT probe on the center blade tip of each design (three pitch-wise consecutive blade tips are equipped with one design, two guardian tips, and one center blade tip). Furthermore, the blade tips are not supplied with tip coolant ejection in order to allow for a fairer comparison between the designs with cooling holes and the Notch concept. In Figure 6.9 (left), the differential efficiency distribution is presented relating the stage efficiency data of each design to the one of the Reference (Figure 2.19 (b)). Positive values in the difference plot indicate that the respective design increases efficiency. The most significant changes are observed above 60 % blade span where the Optimized Squealer design presents improved efficiency levels of up to 0.98 % points at 80 % and 98 % span, respectively. Similar improvements are found for the Trench concept, close to the blade tip at 98 % span, the performance is enhanced by 0.9 % points and 0.6 % points at about 80 % span. Significant performance alteration is detected for the Notch concept. Between 60 % and 80 % span, the efficiency is improved up to 1.7 % points, whereas the benefits are compromised by the strong gradient in the radial efficiency distribution between 80 % and 100 % blade span. A local performance deterioration of up to 5.7 % points is measured. Below 50 % span, the different designs show comparably low fluctuations (±0.3 % points) around zero.
Furthermore, the radial efficiency distributions are mass- and radially averaged

such that the absolute integral changes in the temperature-based efficiency levels can be provided (Figure 6.9 (right)). The integral values are found to be positive for all three tip design concepts, where the largest improvement of 0.11 % points is detected for the Optimized Squealer. The Trench and Notch concept offer minor improvements for the stage efficiency by 0.06 % points and 0.03 % points, respectively.

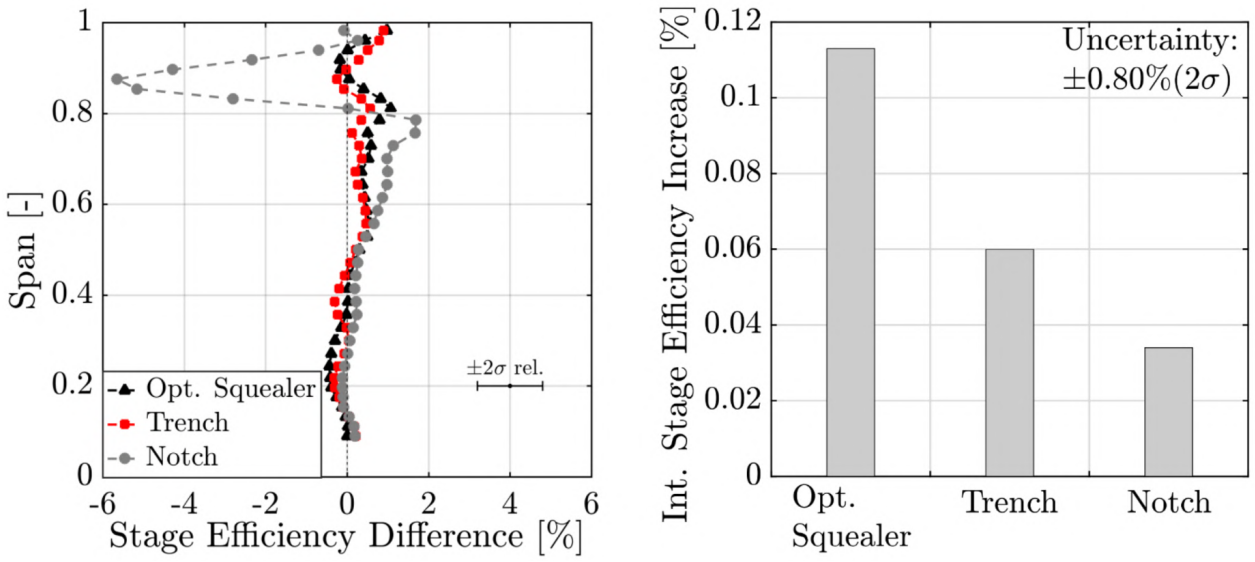

Figure 6.9.: Mass- and time-averaged temperature-based stage efficiency difference $\Delta\eta_{is}$ (left) and integral efficiency increase for each tip design (right) with respect to the Reference (FENT). No tip coolant ejection for all blade tip designs. Stage efficiency changes are given in percentage points.

Even though the Notch concept presents a strong performance penalty in the top 20 % span, the integral stage efficiency change is still positive. The only way to achieve such an outcome is if the mass flow toward the tip is substantially lower compared to the mid-span region. Hence, to confirm the identified trend, it is valuable to provide insight into the span-wise mass flow distribution. In Figure 6.10, the mass- and time-averaged flow coefficient radial distribution is provided for the three tip designs measured with FRAP. The main trend of the distribution shows that most of the mass flow is guided between 30 % and 70 % span. Toward the blade tip, the flow coefficient is substantially reduced by up to 36 %. In the mass-weighted efficiency calculation, the reduction in flow coefficient or the mass flow toward the tip leads to a lower sensitivity of the integral efficiency values with respect to the losses at the tip. Accordingly, the Notch concept benefits from the fact that at the span-wise location of highest efficiency deterioration, the lowest mass flow is present (at 85 % span). In contrast, the most pronounced performance increase is seen in the region where the mass flow is enhanced (73 % span). The explained effect, in turn, diminishes the effectiveness of the other designs as, for example, the performance distribution for the Optimized Squealer shows encouraging potential for a loss reduction toward the tip. Hence, this tip design would

benefit from a moderately higher flow coefficient at the tip. In summary, the presented mass flow distribution reduces the sensitivity of aerodynamic stage performance to changes at the blade tip, which is especially beneficial for the Notch concept that mainly improves the flow field below 80 %.

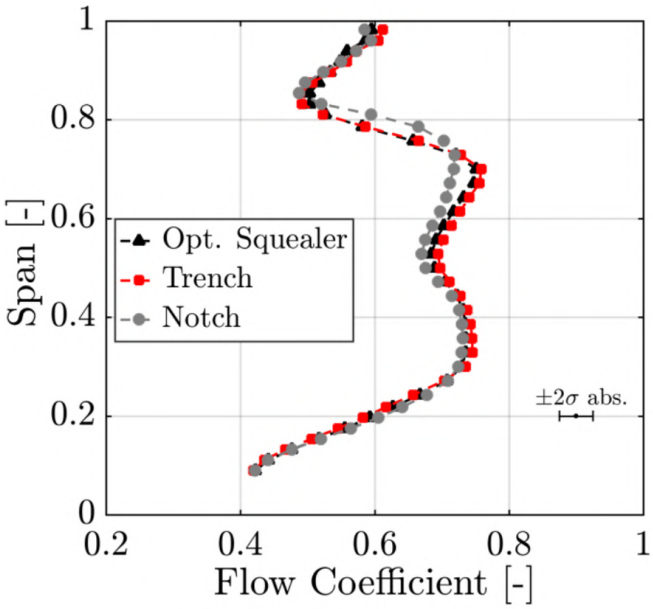

Figure 6.10.: Mass- and time-averaged flow coefficient for three blade tip designs (FRAP)

Additionally, it is of interest to study the impact of the blade tip variation on the 1.5-stage performance of the turbine configuration. It was previously shown in studies by Jenny [75] and Rebholz [151] that the rotor tip secondary flows tend to migrate radially inward when they are convected through the downstream stator passage. It is therefore likely that the variations in the rotor exit flow field are translated into changes at the second stator exit. In Figure 6.11, the temperature-based 1.5-stage efficiency difference is depicted. Again, the efficiency levels are related to the Reference tip design (Figure 2.19 (b)). The radial distribution of the 1.5-stage performance difference in Figure 6.11 (left) implies that most of the second stator flow field is altered by the different rotor blade tips. Depending on the tip design, the peak efficiencies are redistributed along the radial coordinate. The Optimized Squealer design presents an efficiency gain over most of the span, where local improvements of 0.7 % points (85 % span) and 0.4 % points (mid-span) are measured. The Trench concept provides the highest performance benefit of 1 % point at 76 % span, which is moderately compromised by penalties (0.2 % points) below 20 % span. The Notch design presents the largest span-wise gradients in the performance levels among the considered blade tips. The major improvements are detected in the span-wise coordinate range between 9 % and 27 % span with levels up to 0.8 % points. The most pronounced efficiency loss of 0.9 % points is probed at 40 % span.

The resulting absolute integral 1.5-stage efficiency gains are presented in Figure

6.11 (right). The Optimized Squealer design proves to be the superior design among the different tip concepts offering a performance gain of 0.30 % points. The Trench and Notch concept show a performance gain of 0.21 % points and 0.14 % points, respectively. The larger efficiency gains at the exit of the second stator compared to the rotor exit imply that minor improvements in the tip flow field at rotor exit are potentially translated into a doubled efficiency improvement at the exit of the turbine. A detailed flow field study is, however, required to understand the changes in more detail.

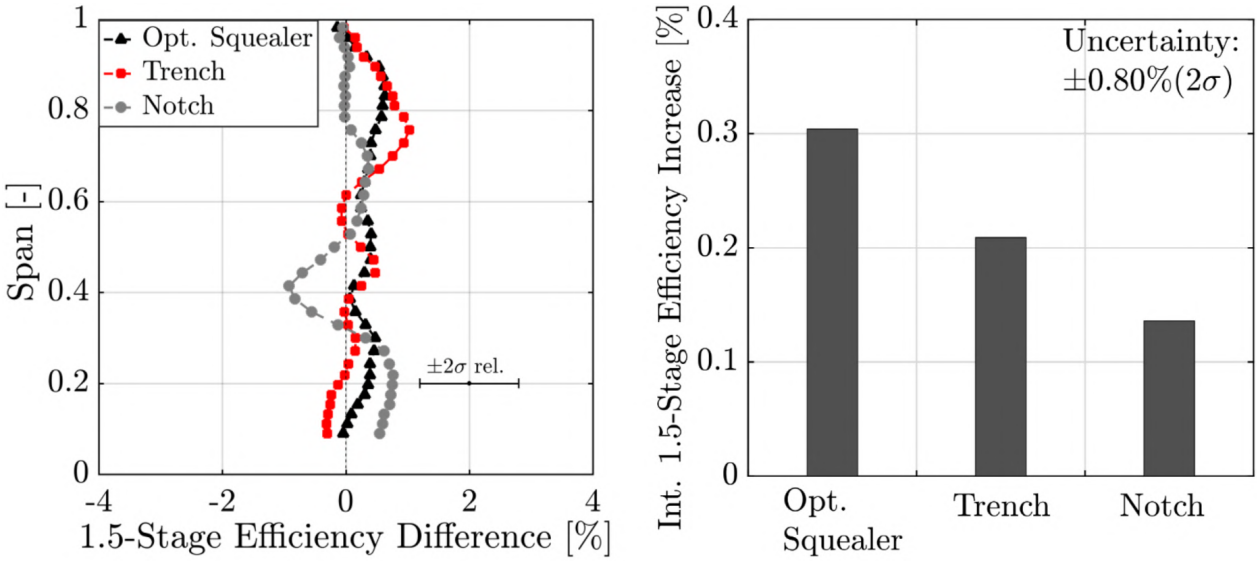

Figure 6.11.: Mass- and time-averaged temperature-based 1.5-stage efficiency difference $\Delta\eta_{is,1.5}$ (left) and integral 1.5-stage efficiency increase for each tip design (right) with respect to the Reference (FENT). No tip coolant ejection for all blade tip designs. Efficiency changes are given in percentage points.

6.2.2. Rotor Exit Flow Field Investigation

To support the aerodynamic performance assessment, a detailed flow field study was required to enhance confidence in the provided efficiency levels. First, the impact of the various tip designs on the rotor exit flow field was investigated. Similar to the performance assessment, the three different tip concepts were analyzed with respect to the Reference tip design illustrated in Figure 2.19 (b).

The impact of the novel blade tip geometries is well represented by the pitch-wise mass-averaged relative flow yaw angle distribution at the rotor exit (Figure 6.12). The radial profiles reveal that the flow for all tip designs is experiencing an under-turning effect in close vicinity to the blade tip (above 90 % span). Between 85 % and 70 % span, a substantial radial gradient in the relative yaw angle is detected, showing an up to 10° flow angle change within 15 % span. Such pronounced spatial gradients are typically associated with the presence of vortical structures that will be addressed throughout this section.

By comparing the different designs, it is helpful to study the differential yaw angle distribution with respect to the Reference tip which is depicted in Figure 6.12 (right). Positive values in the provided plot indicate lower relative flow yaw angles (reduced turning is anticipated), and negative ones suggest larger flow angles (increased turning). The Optimized Squealer offers a beneficial relative flow yaw angle distribution in most parts of the flow field. Around mid-span and between 60 % to 80 % span, an increase in the relative flow yaw angle of up to 0.5° and 0.7° is registered, respectively. Minor improvements of up to 0.3° are found above 90 % span. The improvements of the design are compromised by the reduced flow angles at around 83 % span where a reduced flow angle of up to 1.1° is found. The Trench concept follows the trend of the Optimized Squealer tip; however, it shows less turning around mid-span, which is indicated by the span-wise fluctuation around zero degrees. The Notch design provides the most substantial changes in the radial distribution of the relative flow yaw angle. A pronounced reduction of up to 3.9° in the flow angles with respect to the Reference design is detected at 80 % blade span. Contrary to that, the Notch concept offers a significant improvement of 2° within 60–80 % span.

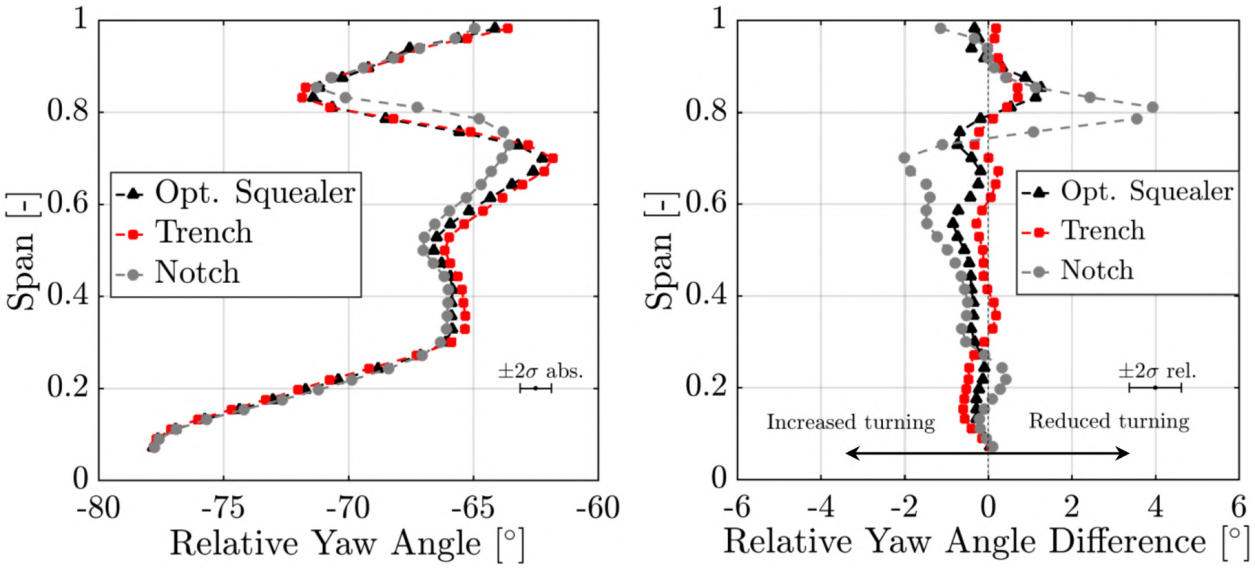

Figure 6.12.: Mass- and time-averaged relative flow yaw angle at rotor exit for different blade tip designs measured with FRAP. Absolute distribution (left) and difference with respect to Reference design (right).

In addition to the pitch-wise averaged results, the spatially resolved relative flow yaw angle is presented in Figure 6.13 for the various tip designs. The data are presented for the central blades of the individual designs. The most relevant flow features affected by the different blade tips are the region of pronounced under-turning close to the casing (95 % span, 0.4 rotor pitch), the over-turning region at 83 % span (0.6 rotor pitch) as well as the substantial under-turning zone between 60 % and 80 % span. The presence of the tip

leakage vortex reduces the relative flow yaw angle in the outermost radial zone. The region of increased flow angles at 83 % span is provoked by the interaction between the tip leakage and tip passage vortex. The under-turning effect between 60–80 % span is associated with the presence of the tip trailing edge shed vortex and part of the rotor wake. The distinction of the rotor flow structures is based on the streamwise vorticity contour diagrams presented in Figure 6.4 (b).

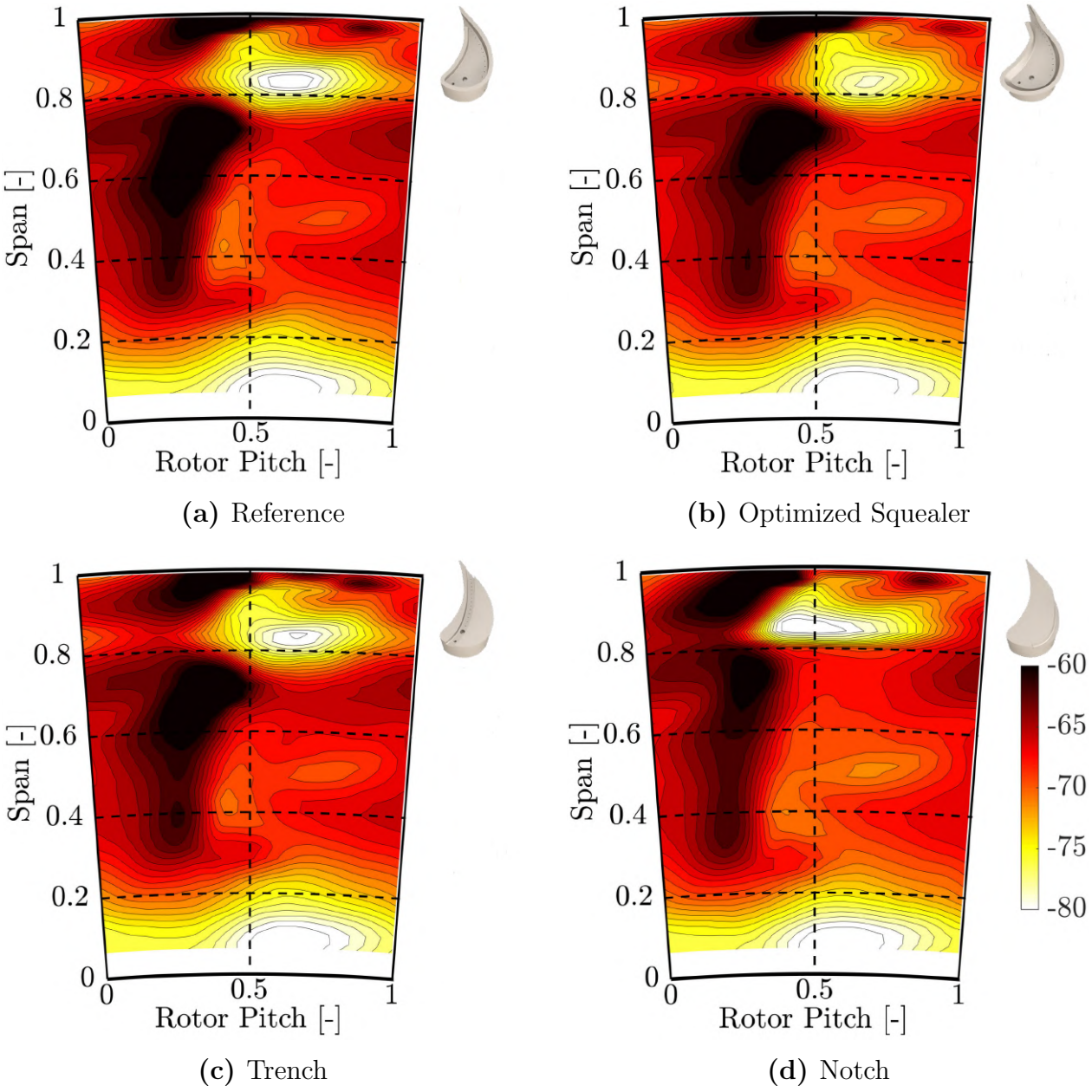

(a) Reference **(b)** Optimized Squealer

(c) Trench **(d)** Notch

Figure 6.13.: Time-averaged relative flow yaw angle [°] in the rotor relative frame of reference at rotor exit for different blade tip designs (FRAP)

The Optimized Squealer tip shows a maximum reduction of 3.5° of the over-turning of the flow at 83 % span compared to the Reference design. The extent of the tip trailing edge shed vortex seems to be reduced by the Optimized Squealer as well as for the Trench concept. The Notch tip offers the most

significant reduction of the tip trailing edge shed vortex-induced under-turning between 60–80 % span. On the downside, the tip leakage vortex region and its interaction with the tip passage vortex are strengthened and induces a larger extent of the under-turning and over-turning region in the top 20 % blade span. Based on the flow angle investigation, the altered regions are identified at the rotor exit which are affected by the blade tip variation. To underline the observed trends, other flow quantities are studied. To get a first indication of the change in aerodynamic losses, the normalized relative total pressure is considered. In Figure 6.14, the respective contour diagrams are depicted in the rotor relative frame of reference. The pressure data are normalized by the turbine inlet total pressure.

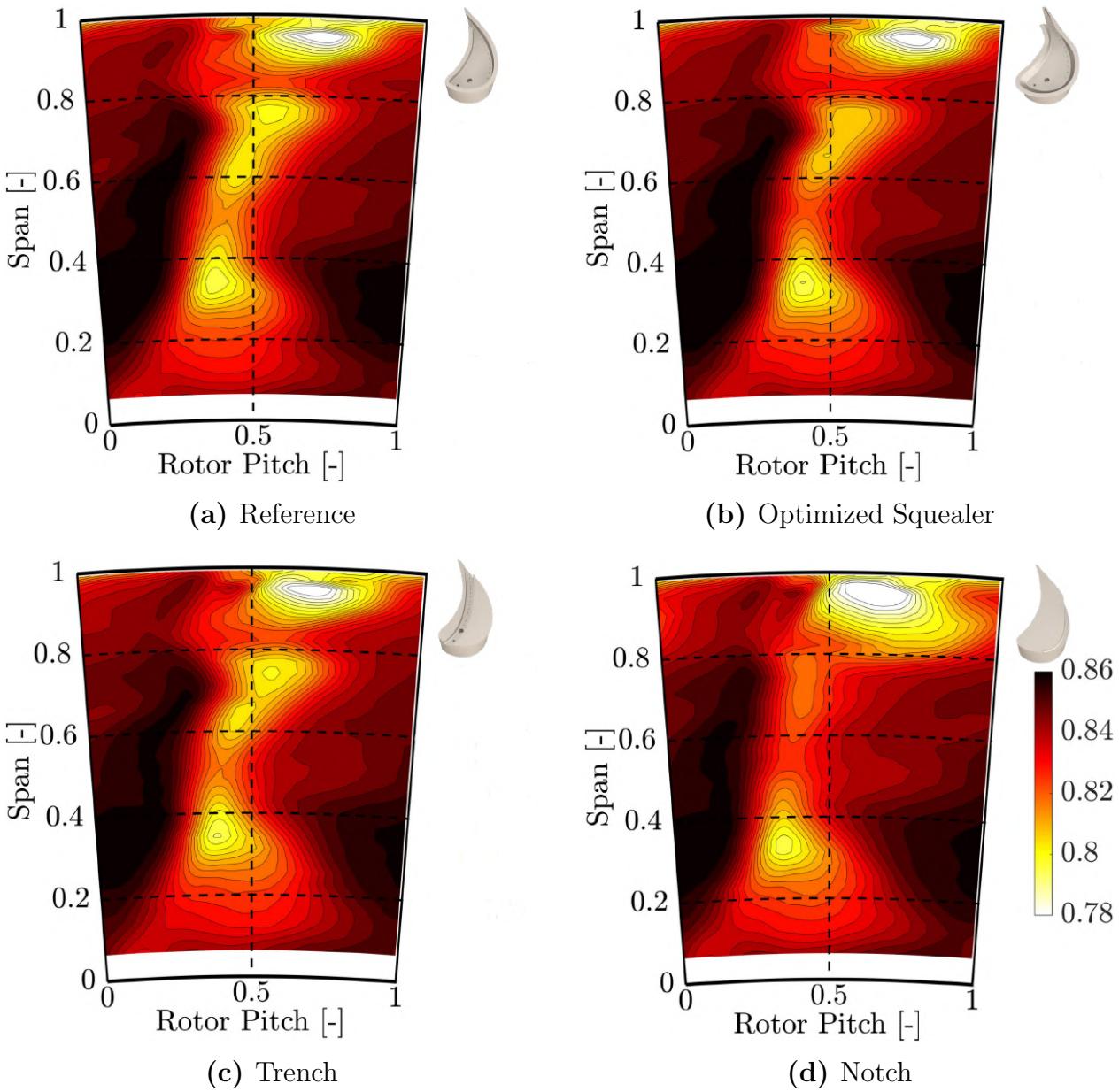

(a) Reference **(b)** Optimized Squealer

(c) Trench **(d)** Notch

Figure 6.14.: Time-averaged normalized relative total pressure $C_{pt,rel}$ [-] in the rotor relative frame of reference at rotor exit for different blade tip designs (FRAP)

The contour diagrams for the relative total pressure follow the trends identified for the relative flow yaw angles. Compared to the Reference, the Optimized Squealer tip presents reduced relative total pressure losses in the tip passage and trailing edge shed vortex between 60–80 % span, whereas a maximum increase in the pressure level of about 0.9 % is detected. The flow field region, which is dominated by the tip leakage vortex, is locally improved by 0.2 %. The Trench concept shows a minor improvement of about 0.1 % in the tip passage vortex and trailing edge shed vortex region. The tip leakage vortex region is only moderately affected, which agrees with the performance levels depicted in Figure 6.9. A substantial increase and larger extent of the tip leakage vortex at the top 20 % blade span are found for the Notch design. The tip trailing edge shed vortex region (60–80 % span, 0.45 rotor pitch), on the other hand, is significantly improved by more than 2 % compared to the Reference tip. It is anticipated that the benefits gained from the reduction of tip trailing edge shed vortex losses are compromised by the additional losses attributed to the tip leakage vortex.

Ultimately, the most appropriate aero-thermodynamic property to quantify the losses in a turbine flow is entropy [39]. The FENT enables the determination of the entropy rise with respect to the turbine inlet conditions. The respective levels are derived from the relationship provided in Equation 2.32. Figure 6.15 presents the contour diagrams of the entropy rise in the rotor relative frame of reference for the four different blade tip designs. From the contour levels, it is apparent that the largest contribution to the aerodynamic losses of the rotor passage is associated with the tip leakage vortex region, above 80 % span. The entropy levels are typically three times as high as the levels in the wake or tip trailing edge vortex region between 60–80 % span. The peak entropy levels in the tip leakage region of the Optimized Squealer design are moderately reduced by 0.8 % compared to the Reference tip. The tip trailing edge region is favorably affected by the design, presenting an entropy reduction up to 13 %. Within the same flow field region, the Trench design lowers the entropy levels by 4.5 %, whereas the tip leakage peak values are very comparable to the Reference and the Optimized Squealer. Similar to the trends presented for the relative flow yaw angle and the relative total pressure, the Notch concept shows the most pronounced change in the entropy levels in the tip trailing edge shed vortex region (60–80 % span) with a maximum local reduction of 44 % compared to the Reference design. Nevertheless, the tip leakage vortex region is area-wise increased and thereby occupies about 35 % more rotor passage area.
In summary, the local changes of the Optimized Squealer and the Trench tip design are judged to be moderate. For these two designs, the flow field region occupied by the tip trailing edge shed vortex is mostly affected and outside of

the respective measurement uncertainty. The rotor exit flow field associated with the Notch concept shows the largest sensitivity of the flow quantities, not only in magnitude but also in the appearance of the flow structures. The concept shows an encouraging potential to substantially reduce the tip trailing edge losses, but the benefits are almost outweighed by the increased tip leakage losses. The superior design out of the variety of concepts is judged to be the Optimized Squealer, as it improves the turning around mid-span and lowers the secondary flow losses within the tip passage and trailing edge shed vortex region.

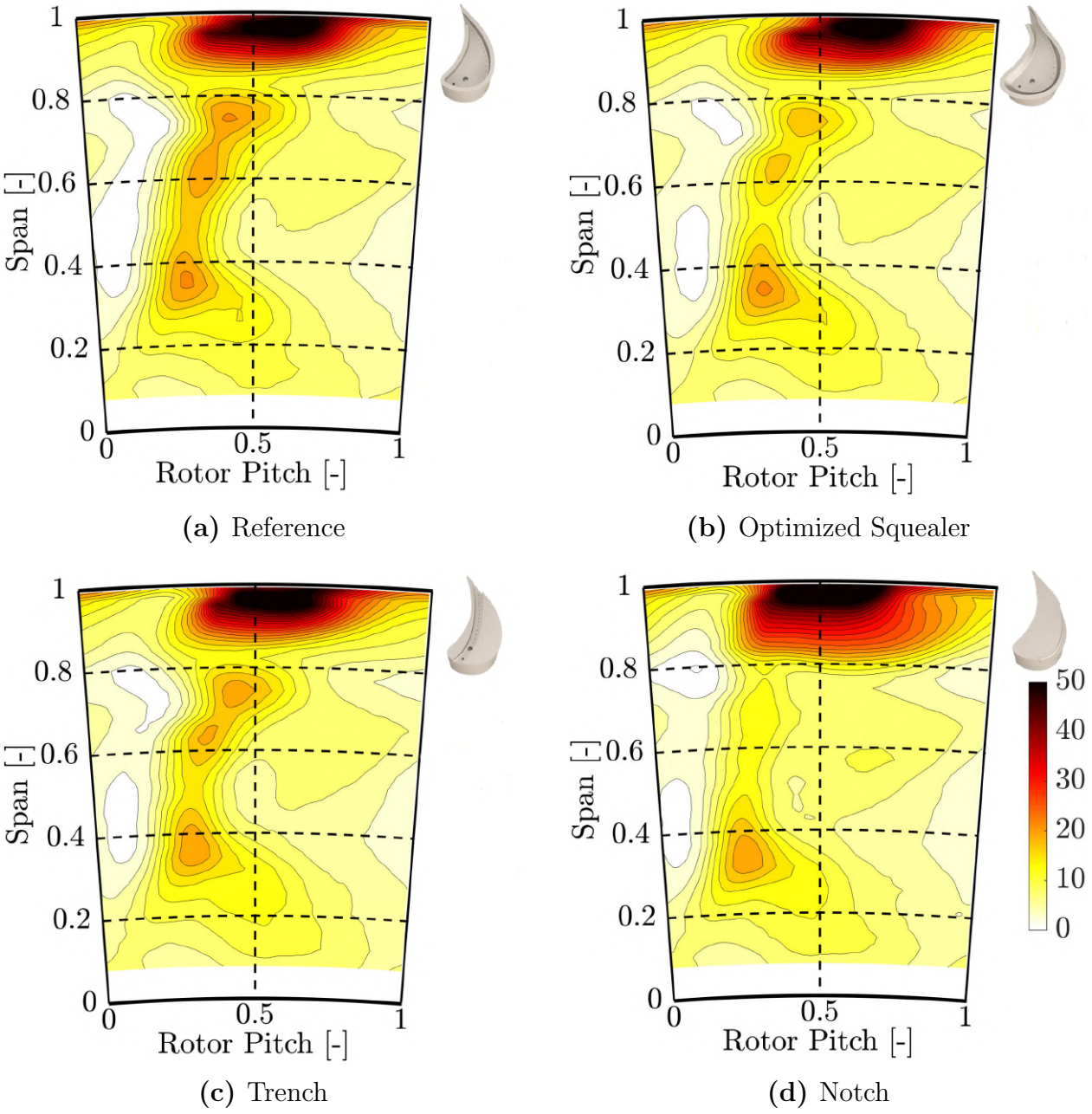

(a) Reference **(b)** Optimized Squealer

(c) Trench **(d)** Notch

Figure 6.15.: Time-averaged entropy rise Δs [J/kg/K] in the rotor relative frame of reference at rotor exit for different blade tip designs (FENT)

6.2.3. Second Stator Exit Flow Field Investigation

The aerodynamic performance alteration due to the different blade tip designs is found to be more pronounced for the 1.5-stage efficiency as for the stage consideration. The current section therefore strives to underline the detected performance changes using different flow quantities.
In order to provide some insight into the flow physics and the different flow field regimes, the absolute total pressure is probed at the exit of the second stator. Figure 6.16 depicts the contour diagram of the normalized total pressure in the absolute frame of reference for a one second stator pitch.

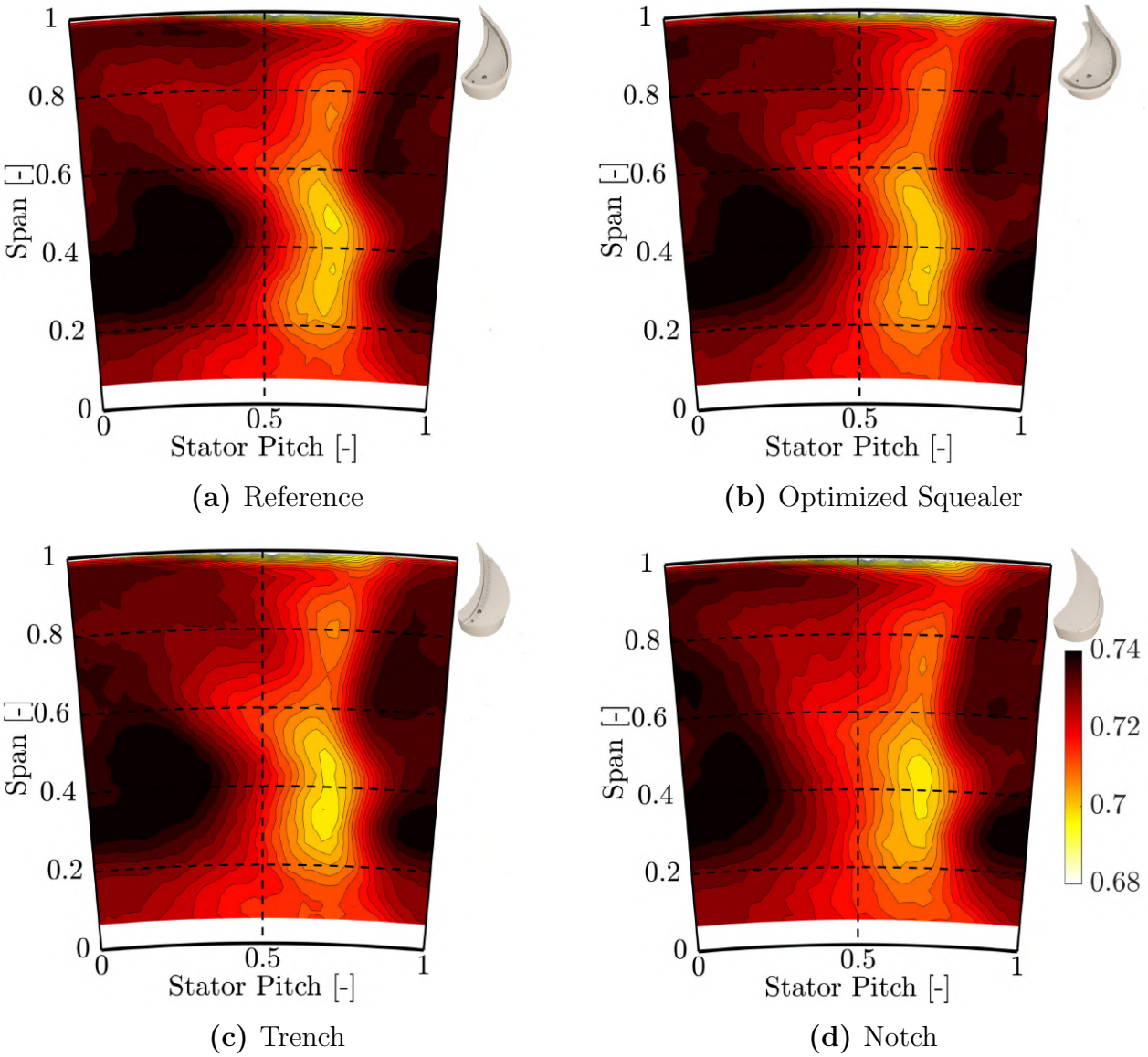

(a) Reference **(b)** Optimized Squealer

(c) Trench **(d)** Notch

Figure 6.16.: Time-averaged normalized total pressure C_{pt} [-] in the absolute frame of reference at stator 2 exit for different blade tip designs (FRAP)

All the contour diagrams have a radial feature in common which is characterized by a high total pressure deficit (0.55–0.7 stator pitch). As introduced in section 6.1.3, the total pressure losses are attributed to a variety of different secondary

flow structures from the upstream rotor and from the second stator itself. Part of the losses are associated with the second stator wake; the loss core found at about 40 % span and 0.7 stator pitch is altered by the different tip designs not only in magnitude but also in its shape. As the rotor tip secondary flows are found to have a tendency to migrate toward mid-span as they are convected through the downstream stator row, it is not excluded that the aforementioned loss core is affected by an altered rotor exit flow field. The span-wise variation becomes more obvious when presenting the pitch-wise averaged profiles. Figure 6.17 presents the circumferential mass-averaged profiles of the normalized total pressure at the exit of the second stator for the four tip designs. From the profiles, one can observe that most of the induced changes by the blade tips are within 20 % to 80 % span. The novel tip design concepts consistently show an enhanced total pressure for the span-wise coordinate range between 60–80 % span, where the maximum absolute increase in total pressure is 0.25 % for the Optimized Squealer and Trench concept relative to the Reference. The improvements are most likely attributed to the reduced losses found in the rotor tip trailing edge vortex (70–80 % span at rotor exit). The Notch design shows a pronounced loss region characterized by an absolute reduction in total pressure of up to 0.45 % at about 47 % span. The source of the pronounced loss core is not readily explained as multiple flow structures can strengthen the loss core as well as loss redistribution and incidence effects. As the flow coefficient (Figure 6.10) and the flow yaw angle (Figure 6.12) at the rotor exit are not substantially altered at 40–50 % blade span, the stator vane would need to be very sensitive to incidence variations, which is rather unlikely.

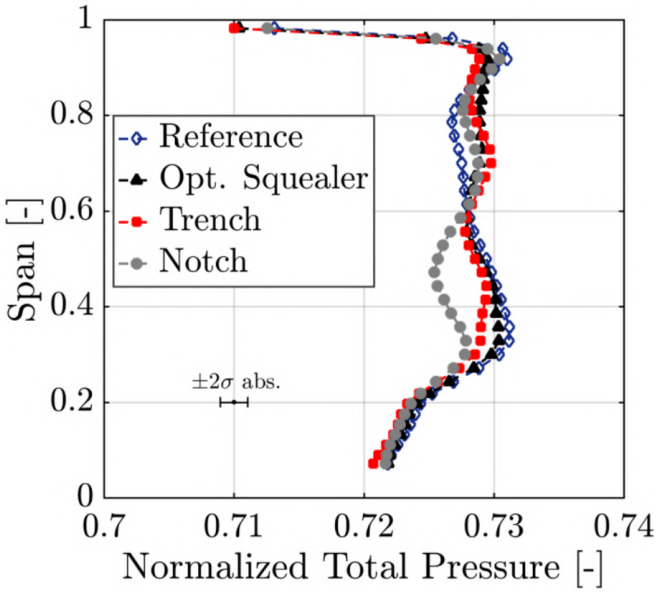

Figure 6.17.: Mass- and time-averaged normalized total pressure C_{pt} at stator 2 exit for different blade tip designs (FRAP)

To judge the potential to redistribute loss zones throughout the second stator passage, it is worth assessing the radial velocity at the exit of the rotor. In

Figure 6.18, contour diagrams of the normalized radial velocity in the rotor relative frame of reference are provided for the Reference tip design and the Notch concept. The velocity levels are normalized by the tangential speed of the rotor at the hub. The positive radial velocity regions indicate that the flow tends to migrate radially outward (white arrows), whereas the negative values suggest that the flow tends to go to the axis of the machine (black arrow). The flow structures that are mainly affected by the tip designs, such as the tip leakage and tip trailing edge shed vortex (60–80 % span and 0.3 stator pitch), present strong positive radial velocity levels indicating that the flow tends to migrate to the casing. It is therefore possible that part of the improvements for the Notch concept seen between 60–80 % span at stator 2 exit is related to the improvements at the rotor exit in the tip trailing edge vortex region. The pronounced loss region at 40 % span at stator 2 exit might be related to a higher radial momentum of the hub passage vortex at rotor exit (25 % span and 0.3 rotor pitch in Figure 6.18) which is, however, only moderately increased by 1.5 % for the Notch tip compared to the Reference. Therefore, a clear explanation for the Notch loss core at stator 2 exit is not given. The complexity of the flow field, which is characterized by the footprints of the flow structures from the upstream blade rows and the missing insight into the intra-row passage flow field, makes it challenging to elucidate the flow field behavior for the Notch concept at the exit of the second stator.

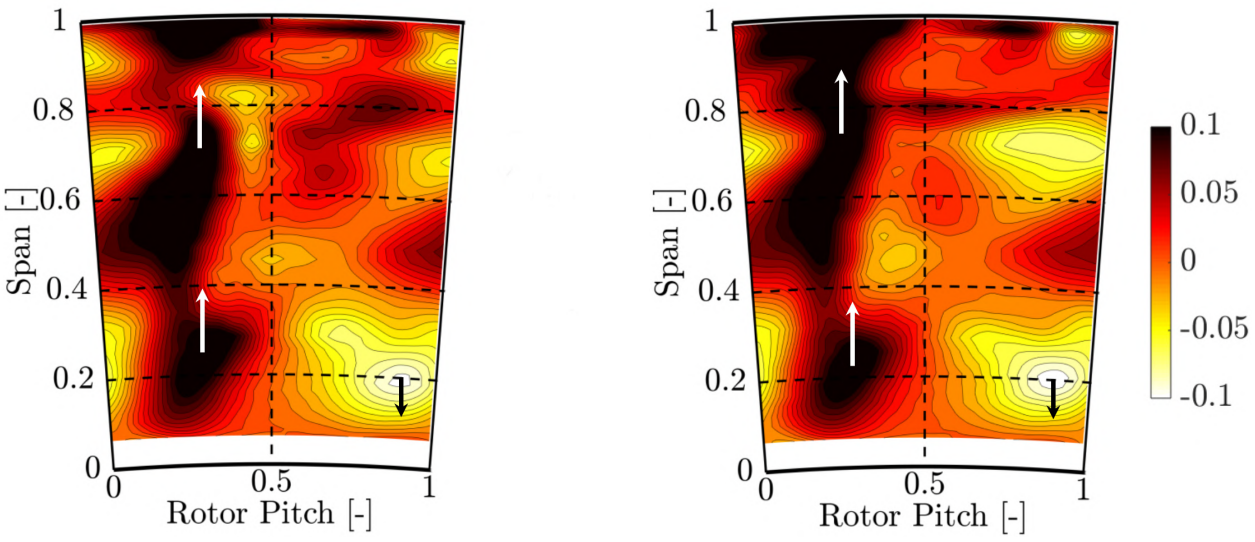

(a) Reference **(b)** Notch

Figure 6.18.: Time-averaged normalized radial velocity [-] in the rotor relative frame of reference at rotor exit for different blade tip designs (FRAP)

Nevertheless, the increased stator 2 losses for the Notch concept between 40–50 % span are confirmed by the entropy levels provided by the FENT probe. In Figure 6.19, the contour diagrams of the entropy rise with respect to the turbine inlet conditions are illustrated for the Reference and Notch design.

The radial feature that reduces the absolute total pressure (Figure 6.16) is also represented by increased entropy levels between 0.6–0.7 stator pitch. When carefully comparing the Reference design to the Notch concept, one can identify the larger pitch-wise extent of the loss zone around the mid-span region. The peak entropy values are comparable for the designs, but a larger occupied stator 2 passage area provokes to overall increase the losses at the specified span range.

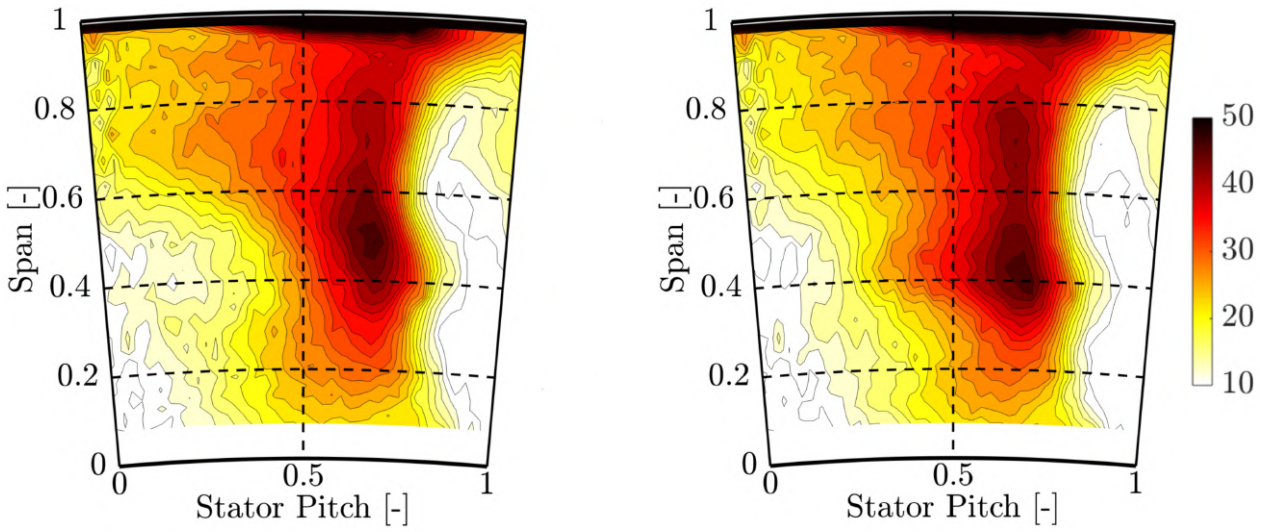

(a) Reference **(b)** Notch

Figure 6.19.: Time-averaged entropy rise Δs [J/kg/K] in the absolute frame of reference at stator 2 exit for two blade tip designs (FENT)

The FENT probe offers to resolve the entropy generation in time which could help to get more insight into the unsteady flow physics at the exit of the second stator. The time series of the unsteady entropy rise for the Notch tip design is therefore analyzed and depicted in Figure 6.20. The time-space is indicated as a fraction of the rotor blade passing period T. The effects that were identified are twofold. First, a patch of increased entropy is found at $t/T = 0.20$ which is highlighted by a black dashed surrounding line. This feature is intensified in amplitude as the blade passing proceeds and does not only show a cross-passage migration from pressure to suction side of the stator vane, but also a substantial radial downward migration toward 40–50 % span and contributes therefore to the increased loss zone that was found for the Notch concept. It is speculated that the feature is a tip passage feature of the second stator, which could also contain part of the rotor tip secondary flows such that the feature is strengthened if the rotor tip leakage or tip passage vortex strength is enhanced.
The second observed effect is related to the radial migration of a pronounced entropy feature at the tip end wall of the stator 2. The feature is indicated by a white dashed surrounding line in the Figures 6.20 (a) - (c).

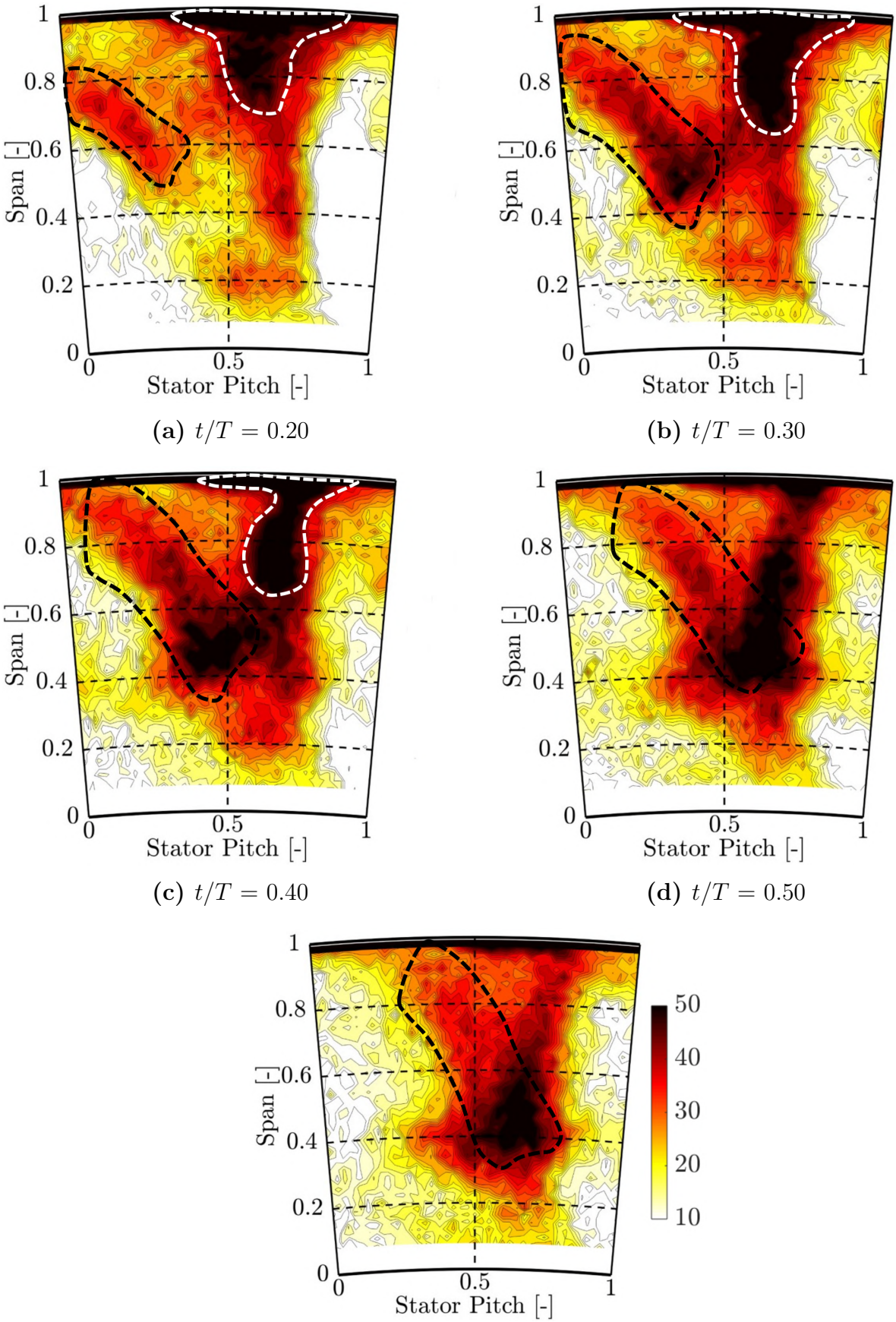

(a) $t/T = 0.20$ **(b)** $t/T = 0.30$

(c) $t/T = 0.40$ **(d)** $t/T = 0.50$

(e) $t/T = 0.60$

Figure 6.20.: Time series of entropy rise Δs [J/kg/K] at stator 2 exit for the Notch blade tip design in the absolute frame of reference (FENT)

As the blade passing proceeds, part of the feature is released from the second stator tip end wall and is reaching toward mid-span. The downward migration is almost radially and does not show a cross-passage migration, most likely since it is well aligned to the second stator trailing edge. It is assumed that the high entropy levels at the tip end wall which is found along the whole stator pitch at the top 5 % span, is fed by the incoming tip leakage and probably the tip passage vortex as they show to have a certain radial momentum toward the casing (Figure 6.18 (b)). Providing this set of data brings confidence into the statement that the loss region at the second stator exit, even around mid-span, can be altered by the incoming rotor tip secondary flow structures.

The previous sections have identified a superior tip design which is termed as the Optimized Squealer. The design reduces the tip trailing edge losses and improves the turning at mid-span, leading to an improvement of the stage efficiency of about 0.1 % points and 0.3 % points for the 1.5-stage efficiency, respectively. A Notch design shows the highest sensitivity of the flow structures at the rotor and second stator exit with respect to the geometrical change at the blade tip. It is furthermore anticipated that the strengthening of the rotor tip secondary flows and leakage flow is translated into increased losses at the exit of the second stator, even at mid-span.

6.2.4. Sensitivity of Tip Designs to Tip Coolant Ejection

The latest adaptation of the test rig enabled the provision of cooling air to the blade tips (section 2.1.5) which was ejected through an array of cooling and dust holes inside the squealer tip cavities as well as by a pattern of cooling holes on the blade pressure side (Figure 2.19). Besides the effect of cooling the blade tips, a performance improvement or deterioration could be expected from the tip ejection. In open literature, the statements of the impact of tip cooling ejection on aerodynamic performance are to some extent diverging, as the flow field dynamic is sensitive to the mass flow ratio, the tip gap size, the location of the ejection as well as to the tip geometry itself [150, 197].
The current section aims to provide a performance sensitivity of three out of four presented blade tip designs that feature the same cooling hole pattern on the blade pressure side and have some alteration of the cooling hole pattern in the squealer cavity (e.g., Reference against Trench concept). In the absence of cooling holes, the Notch concept is excluded from the analysis. For the current case, a maximum tip coolant ejection mass flow ratio of 0.4 % of the turbine mass flow (referenced to one rotor passage). Further details on additional non-dimensional quantities characterizing the tip coolant ejection can be found in Table 2.4. The performance sensitivity analysis is provided for the rotor exit plane, again where the temperature-based efficiency levels are considered

according to the relationship introduced in Equation 2.37. In Figure 6.21, the absolute mass- and time-averaged stage efficiency difference distribution and integral change are depicted. Identical to the previous study, the center blade of the individual design is considered for the investigation. Two terms were used for the analysis of the tip coolant ejection study. "Cooled" represents the case where the tip coolant supply in the rim seal hub cavity is open and a mass flow ratio of 0.4 % of rotor passage mass flow is supplied (Figure 2.7). The term "uncooled" means that the supply path is closed by installing a sealing plate in the hub cavity.
The radial profiles for the stage efficiency difference reveal that the performance is consistently improved for all supplied blade tip designs and most of the span when tip coolant is ejected. The span-wise regions where the most pronounced improvements are found are at 40 % span (up to 0.9 % points) and above 80 % span (up to 1.1 % points). The enhanced performance at 40 % span is anticipated to be partly related to the following effect: the difference of the bypass mass flow and the drum leakage flow is kept the same for the "cooled" and "uncooled" case. As the tip coolant flow is supplied from the hub cavity, part of the supplied bypass flow is going to the tip, and some share is injected into the main annulus as purge flow. When the supply path is closed for the "uncooled" condition only purging occurs which provokes that compared to the "cooled" case, the main annulus sees a moderately higher purge flow rate (+0.1 % of the turbine mass flow) which is translated into larger aerodynamic losses in the rotor hub passage vortex region at around 40 % span at the exit of the rotor.

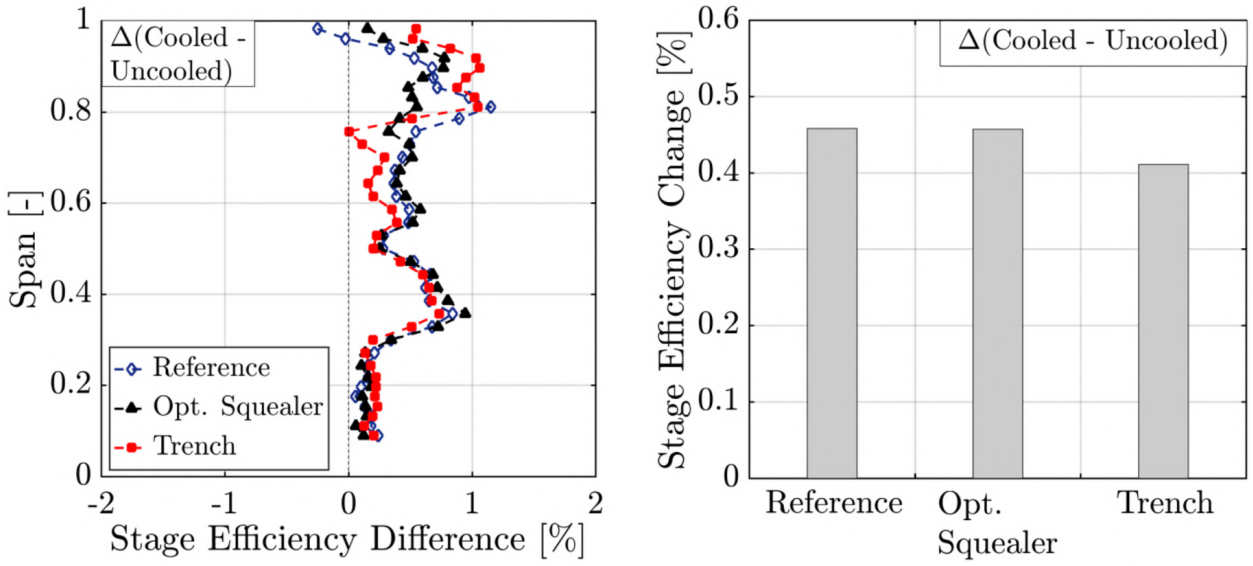

Figure 6.21.: Mass- and time-averaged temperature-based stage efficiency difference $\Delta\eta_{is}$ (left) and integral efficiency change for each tip design (right) in "cooled" (TR = 0.4 %) against "uncooled" mode (FENT). Stage efficiency changes are given in percentage points.

The substantial increase above 80 % span could be directly attributed to the

tip coolant ejection, which reduces the strength of the tip leakage vortex. However, this effect needs to be studied in more detail. The integral stage performance is measured to be increased for all considered tip designs by about 0.4 % points when tip coolant flow is present (Figure 6.21 (right)).
Since a temperature-based efficiency is used to derive the performance levels, it must be assessed whether part of the improvements is related to an artificial change in efficiency due to the purely lower temperature of the ejected cooling flow. Therefore, it is useful to decompose the stage efficiency into the total pressure and temperature variation. In Figure 6.22, the respective mass- and time-averaged flow quantities are depicted.

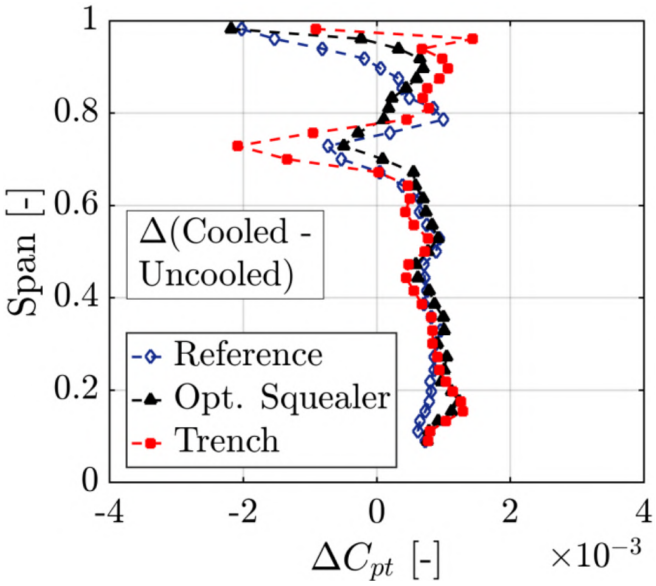

(a) Normalized Total Pressure Change

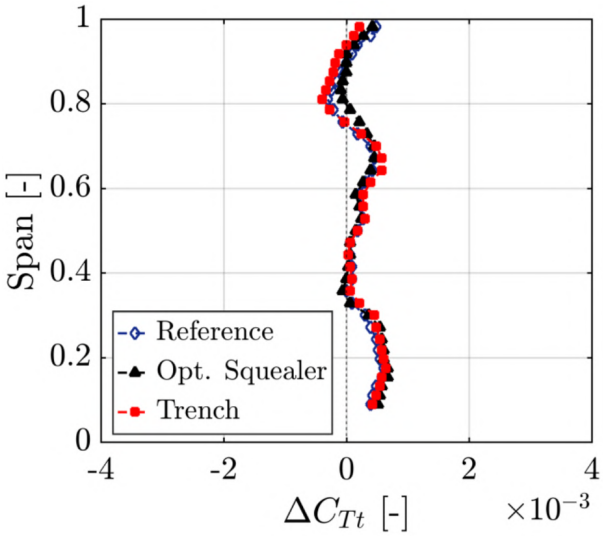

(b) Normalized Total Temperature Change

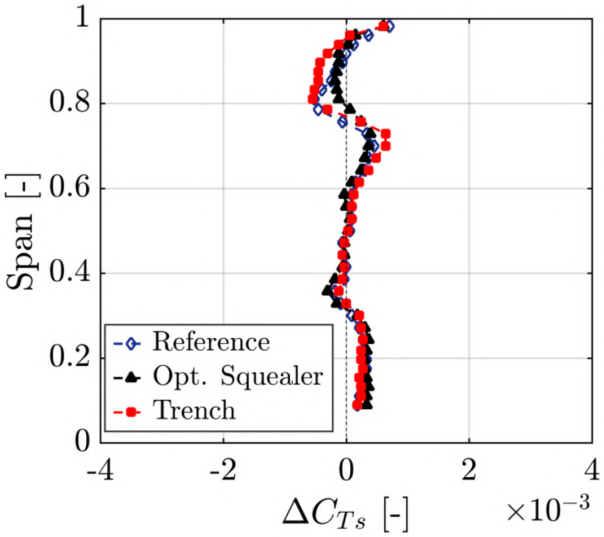

(c) Normalized Static Temperature Change

Figure 6.22.: Mass- and time-averaged total flow quantities and static temperature change at the exit of the rotor. Difference calculated between "cooled" and "uncooled" case (FENT).

For the most pronounced efficiency improvement at 80 % span, the following trends are observed for the total pressure and temperature: the total pressure is for most of the designs increased for tip coolant ejection at this span-wise location which can be interpreted as reduced pressure losses. On the other hand, the total- and static-temperature drop which could be either point toward an increased work extraction or the impact of the colder tip ejection flow. Between 60–80 % span, the trends can be related with higher confidence to the performance increase. For all the designs, the total pressure is increased at 65 % span, and the total temperature also increased. The only way efficiency can be improved is by having lower aerodynamic losses at this span position. However, the effective contribution of the tip coolant ejection to a potential performance increase cannot be accurately quantified, as the temperature drop across the stage is low. Small changes from the ejection of coolant air can substantially change the temperature-based efficiency. Therefore, the provided integral efficiency increase levels must be treated with great care.

6.3. Conclusions

Based on the analysis presented in the current chapter, it can be concluded that with advanced design optimization tools, the aerodynamic performance deficit due to a blade count reduction is compensated by improved rotor blade and tip geometries, which contribute to an overall higher engine efficiency, as the cooling requirements can be reduced because of a pure reduction in wetted surface for fewer blades. The encouraging results are, however, compromised by a significant increase in the turbine tonal noise provoked by the increased secondary flow strength.

The combination of a favorable mass flow redistribution along the span and moderate stage loading reduction can outweigh the performance deterioration induced by the reduction in blade count. The strengthening of the secondary flows provoked by the increased blade loading is, however, inherently given and cannot be suppressed. The evaluated stage efficiency increase for an improved rotor design with 22 % fewer blades is 0.4 % points, compared to a baseline configuration with identical stator rows and axial row spacing.

If the turbine noise emissions are of the highest importance to the designer, a blade count reduction must be implemented with great care. The enhanced secondary flow strength induced by the aforementioned blade loading increase and their interaction with the potential field of the downstream stator row provokes a substantial increase of the turbine tonal noise emissions by up to 13 dB. Accordingly, it is suggested that a blade count reduction should go along with a reevaluation of the axial row spacing with respect to the aeroacoustic excitation.

Using a modular rainbow rotor experimental setup in combination with fast-

response probe measurements, a set of four different rotor blade tip concepts was tested. Promising aerodynamic performance characteristics were identified. A CFD optimized squealer tip design with a non-uniform fence design that expands pitch-wise and upstream is found to be beneficial for stage and 1.5-stage performance improvements due to the tip leakage and tip passage vortex loss reduction. The overall additional gain of the stage performance was found to be 0.1 % points and 0.3 % points for the 1.5-stage consideration, respectively. A notch that follows the suction side of a flat tip is favorable for a substantial reduction of the tip trailing edge shed vortex but suffers from additional tip leakage losses in the top 20 % span. The strengthening of the tip leakage vortex promotes an increase in the aerodynamic losses even at the exit of the downstream stator row, which is induced by a complex cross-passage and radial migration of tip flow features throughout the stator row. It is therefore advisable to combine such a design with a leakage flow control setup (e.g., casing injection) to diminish the strength of the over-tip leakage flows.

7. Conclusions

In the present work, a combined experimental and numerical investigation of aerothermal characteristics of high-pressure turbines was performed. Extensive analysis of different turbine configurations facilitated the derivation of guidelines for the aerothermal design of advanced rim seal geometries and rotor blade tips to meet the challenges associated with substantial heat loads and extensive cooling requirements in modern high-pressure turbines. Experimental evidence is gained, conducting measurements in a one-and-a-half stage model axial turbine where specifically the effects of the rim seal – hub cavity space and near-blade tip flow region is systematically probed with respect to coolant and geometrical component variations. A unique dataset was acquired using miniature-size aerodynamic probes, wall-mounted fast-response pressure transducers, and a purpose-made hub cavity heat transfer measurement setup to experimentally analyze the aerodynamic and thermal characteristics of different rim seal geometries and blade tips. The test rig capabilities were successfully extended to provide reduced-temperature cooling flows and enable the modular integration of various blade tip designs in a rainbow rotor setup. The experimental assessment is complemented with extensive unsteady numerical modeling using an in-house developed, explicit unsteady Reynolds-averaged Navier–Stokes (RANS) solver.

7.1. Concluding Remarks and Contributions

The combined study of the aerothermal effects of different rim seal geometries and rotor tips under consideration of blade count reduction in model high-pressure turbines operated under different cooling flow rates leads to the following conclusions:

(1) **Significance and Prediction of Cavity Modes.** The low-frequency, non-synchronous flow structures (cavity modes) formed in the rim seal and hub cavity space are found to have a non-negligible impact on the aerothermal turbine characteristics and impose challenges on a broad range of turbine design aspects.

- The asynchronous flow perturbations found in the hub cavity need to be budgeted in the acoustic design of turbines. The pressure oscillations induced by the low-frequency modes are found to be in the order or

even exceed the originally dominating blade passing-induced fluctuations and are sensitive in their strength and frequency content to the rim seal purge flow. Consequently, these modes provoke an excitation of the aeroacoustic field in the low frequency range, which results in a peak pressure intensity increase of up to 18 dB at the source. The signature of the cavity-induced flow structures are found to radially migrate up to 30 % span of the main annulus and are convected by the hub secondary flows of the adjacent stator and downstream rotor, resulting in a noise increase in the low frequency band of up to 7 dB at turbine exit.

- The detected cavity modes provoke an additional pressure-induced hot gas ingestion mechanism which must be eliminated to provide sufficient sealing effectiveness of the rim seal. The low-frequency, asynchronous nature of the cavity modes is induced by rotating large scale low-pressure zones that provoke peaks in the ingress mass flow which clearly exceed those induced by the rotor leading-edge potential field.

Computationally expensive unsteady RANS calculations, including the vanes and blades of the main annulus, are capable of capturing the non-synchronous hub cavity modes.

- Full-annular unsteady calculations are required to accurately predict the non-synchronous excitation in the hub cavity. Sector models with a 1:1 pitch ratio fail to predict the hub cavity dynamics correctly when cavity modes are present, most likely due to the high-pass filter effect of the periodic boundary conditions, which limit the formation of the pressure waves inside the cavity.
- Multiple rotor revolutions have to be simulated (typically 4–5, coarse grid) to stabilize the dominating cavity mode pressure oscillations. It is advisable to perform a detailed sensitivity study on the unsteady solver parameters (number of time steps and sub-iterations) to provide accurate numerical results.
- For coarse full-annular meshes (in the order of 35 million nodes), the designer should expect an overprediction of the cavity mode pressure amplitude between 10–15 %.

(2) **Measures to Attenuate Cavity Modes.** Based on the extensive experimental assessment of the rim seal space, measures and geometrical concepts are identified to attenuate the signature of the hub cavity modes.

- High-rim seal purge flow rates that seal the cavity against ingress are favorable to completely eliminate the hub cavity-induced flow perturbations.

- The implementation of geometrical features right at the rim seal exit, for example, the "purge control features" presented in this work, which impart radial and circumferential momentum to the vented cavity fluid show encouraging attenuation potential (a factor of 2.5 reduction in cavity-mode pressure fluctuations). It is consequently anticipated that increasing the radial momentum of the cavity exiting fluid and reducing the shear layers at the interface between cavity and main annulus should be targeted to eliminate the modes.
- Overlap-type rim seals with rotor-sided sealing arms close to the exit of the cavity are superior to a simple angel-wing-type sealing arrangement, as they eliminate the hub cavity modes at a much lower purge flow rate, presumably due to the reduction in the upper cavity volume and the tendency to reduce the radial momentum of the ingestion flow.

(3) **Improved Rim Seal Design.** The aerodynamic performance deterioration due to the injection of purge flow could be reduced by integrating novel geometrical features, termed as "purge control features," right at the rim seal exit.

- The beneficial impact of the improved rim seal on the stage efficiency was determined to be 0.4 % points for nominal and high purge flow rates with respect to an already optimized turbine configuration. The sensitivity of the stage efficiency to purge flow was reduced by about 18 % when the features are installed, which improves the flexibility of the purge flow design range.
- Realignment of the cavity fluid with the main annulus flow and the reduction of tangential shear over the interface between hub cavity and main annulus are identified to be effective measures to enhance the turbine stage performance in the presence of purge flow.
- Imparting radial momentum by rotor-sided geometrical features installed at the exit of the rim seal is favorable to discourage the ingress mass flow from the main annulus. This design concept is expected to outperform conventional pre-swirl approaches that enhance only the tangential momentum of the cavity fluid at lower radial positions.

(4) **Hot Gas Ingestion and Hub Cavity Convective Heat Transfer.** A unique dataset is provided, quantifying the ingestion and convective heat transfer quantities for an engine-representative overlap-type rim seal for small integral changes in the rim-seal purge flow rates.

- The presented overlap-type rim seal is found to appropriately block the ingestion of main annulus fluid at high purge flow rates. Nevertheless, by gaining the last percentage points for highest adiabatic effectiveness,

the minor improvements are compromised by a relatively strong decrease in stage efficiency due to the linear decrease with purge flow. Therefore, the study encourages decreasing the sensitivity of the stage performance to purge flow in order to maximize the overall aerothermal performance of the turbine.

- Increasing the rim seal purge flow injection rate by 1 %, increases the local heat transfer coefficient on the rotor hub cavity wall by a factor of 2–3, which highlights the importance of the appropriate purge rate as a design parameter.
- It is inadvisable to use "free disk" empirical correlations to predict the local heat transfer coefficients for high cooling flow rates on the rotating cavity wall, as they are particularly sensitive to tuning parameters and were found to underpredict the convective heat transfer coefficient for high purge flow rates by up to 60 %. The correlation is more suitable (discrepancies ±20 %) for low- or net-zero purge flow rates.

(5) **Rotor Blade Count Reduction and Blade Tip Variation.** With advanced design optimization tools, the aerodynamic performance deterioration due to blade count reduction is compensated by improved rotor blade and tip geometries, contributing to an overall higher engine efficiency as cooling requirements are expected to drop (reduced wetted surface for fewer blades). The improvements in performance are compromised, however, by the substantial increase in turbine tonal noise caused by the strengthening and convection of secondary flows.

- A combination of a favorable mass flow redistribution and moderate stage loading reduction can outweigh the performance penalties associated with a substantial rotor blade count reduction. Nevertheless, the strengthening of the vortical structures due to the increase in blade loading cannot be suppressed. The identified absolute stage efficiency increase for an improved rotor design with a 22 % reduction in blade count is 0.4 % points in comparison to a baseline with more blades and identical stator rows and axial gaps.
- If the turbine noise emissions are of first-order concern, great care needs to be taken when the blade count is reduced. The elevated secondary flow strength induced by the inherent higher blade loading and their potential field interaction with the downstream stator row provokes a substantial increase in the aeroacoustic excitation at turbine exit in the order of 13 dB. It is therefore advised that a substantial blade count reduction should go along with a reevaluation of the axial row spacing.

- A set of four different rotor blade tip designs were successfully tested for a modular rainbow rotor setup in combination with fast-response

probe measurements, indicating their promising aerodynamic performance characteristics.

- A computational fluid dynamics (CFD)-optimized squealer tip design with a non-uniform fence design that pitch-wise and upstream expands is found to be beneficial for stage and 1.5-stage performance due to tip leakage and tip passage vortex loss reduction. The results highlight the capabilities of advanced optimization tools to improve the complex flow dynamics in the near tip region, thereby leading to an absolute increase of the stage (+0.1 % points) and 1.5-stage efficiency (+0.3 % points) relative to a reference tip design.
- A notch on the suction side of a flat tip is favorable for tip trailing-edge shed vortex loss reduction but suffers from the additional tip leakage losses in the top 20 % blade span. The strengthening of the tip leakage vortex also promotes an increase in aerodynamic losses at the exit of the downstream stator by a complex cross-passage and radial migration of tip flow features throughout the stator row. Therefore, an active leakage flow control at the tip might be required to gain a substantial performance increase for a notch design.

7.2. Summary

The current section offers a condensed overview of the topics addressed in the present thesis. The summary is provided topic-wise and in order of appearance throughout the thesis.

Non-Synchronous, Low-Frequency Hub Cavity Modes

The rim seal and hub cavity space are prone to establishing specific flow perturbations, often termed as “cavity modes,” which are not driven by the dominating dynamics of the main annulus of a turbine. The asynchronous flow excitation detected in this work, for an angel-wing-type rim seal by means of FRAP and wall-mounted pressure sensor measurements, exhibited low-frequency content (below the blade passing frequency) in the pressure frequency spectra. The amplitude of the pressure oscillations and the covered frequency band induced by the modes were found to be sensitive to the amount of injected rim seal purge flow. Depending on the purge flow rate, the frequency content was found to vary between 13–38 % of the rotor blade passing frequency, where the content shifted toward higher frequencies as the purge air rate was increased. At the highest purge flow rate (IR=1.2 %), the low-frequency modes were eliminated. Typically, the hub cavity modes provoked a band of elevated pressure amplitudes contrary to the purely geometrical

or tonal noise-induced perturbations. The signature of the identified modes was tracked by employing inter-row FRAP measurements. The measurements revealed that the footprint of the hub cavity modes penetrated up to 30 % span at the rotor inlet and were subsequently convected by the hub secondary flows through the rotor passage. Even though the pressure oscillations were attenuated throughout the turbine section, the resulting peak pressure intensity in the low frequency range was found to be increased by up to 7 dB at the exit of the turbine with respect to an operating condition where the modes were eliminated. Consequently, the significance of such modes for the aeroacoustic design of a turbine was demonstrated.

The capability of resolving such specific flow perturbations within the hub cavity by employing unsteady CFD simulations was investigated. One-stage, full-annular unsteady RANS calculations provided encouraging results underlining the potential to capture the specific flow dynamics in the hub cavity, even in the presence of purge flow. The pressure amplitudes of the hub cavity modes were overpredicted by about 10–15 %, most likely provoked by the coarse mesh. The computations were used to elucidate the essence of the cavity modes; it was found that the low-frequency content in the pressure field is induced by large-scale low-pressure zones that rotate with the rotor but at a fraction of its speed (89–91 % of the rotor rotational speed). The quality of the predictions enabled analysis of the importance of such low-pressure zones with respect to the ingestion of main annulus fluid into the rim seal and hub cavity space. The probing of the instantaneous ingestion mass flow showed that the cavity modes induce a pressure-driven ingestion mechanism, which provokes the entrainment of a considerable amount of fluid from the main annulus that exceeds the rotor potential field-induced ingestion.

Novel Rim Seal Design: Purge Control Features

To reduce the detrimental effect of injected rim seal purge flow on the aerodynamic performance of a turbine stage, a novel geometrical rim seal design concept, termed as “purge control features,” was extensively investigated by means of inter-row probe measurements. The features were installed right at exit of the rim seal space and are designed to impart radial and circumferential momentum to the exiting cavity and purge flow fluid aiming to reduce the mixing losses at the rotor inlet and counteract potential additional ingestion from the main annulus.

The aerodynamic probe measurements quantified the beneficial impact of the features on the stage performance of an already-optimized turbine configuration. The achieved absolute stage efficiency increase for nominal and high rim seal purge flow rates was determined to be 0.4 % points with respect to the baseline design without the geometrical features installed. The major

contributions to this improvement was found to be the reduction of the negative incidence at rotor inlet and the lowering of the tangential shear at rim seal interface, which are typically strengthened by the injection of purge flow into the main annulus. The reduction of the tangential shear layer and the associated increase in circumferential velocity was anticipated to influence the whole rotor inlet flow field, resulting in less total pressure deficit. The realignment of the cavity fluid to the main annulus flow was identified to diminish the rotor profile losses.

The study was complemented by a comparative assessment of the ingestion characteristics. An experimental comparison of the radial velocity component at the rim seal exit suggested that the purge control feature configuration does not compromise the improved stage efficiency levels with a substantial increase in the ingestion. Unsteady sector RANS calculations confirmed the experimental observations, highlighting that the amount of ingested mass flow is even moderately reduced compared to the baseline case.

The impact of such geometrical features on the strength of the hub cavity induced asynchronous low-frequency modes was quantified by FRAP measurements. The measurements reveal an unexpected improvement due to the installation of the purge control features with respect to the pressure perturbations in the cavity. A reduction of the cavity mode peak pressure amplitude by a factor of 2.5 was determined when the features were installed.

Ingestion and Hub Cavity Convective Heat Transfer

A combined study of the ingestion behavior and hub cavity convective heat transfer for an engine-representative overlap-type rim seal design was presented using a purpose-made, in-house developed measurement setup. The integration of a reduced-temperature secondary air system allowed for quantification of the effectiveness of the purge air to cool the stator- and rotor-sided cavity walls.

As the rim seal design was changed compared to a previous study in the thesis, an investigation of the main cavity dynamics was provided by an array of unsteady pressure transducers installed on the stator- and rotor-sided cavity walls. It was found that the overlap-type seal eliminates the asynchronous low-frequency excitation at a much lower purge flow rate (IR=0.2 %) compared to the simple angel-wing-type seal that was previously probed. Moderate-strength, low-frequency excitation was captured at the net zero rim seal purge flow rate and by determining the phase speed of the flow structures it was estimated that 26 low-pressure zones are rotating at 93 % of the rotor speed. Nevertheless, at the nominal and high purge flow injection rates, the dominating dynamics were the vane and blade passing frequency. Additionally, the time-resolved differential pressure measurements over the rotor-sided sealing arm implied

that at the highest considered purge flow rate (IR=1.2 %) a high sealing effectiveness is achieved, even when the potential field of the rotor tends to force the flow into the wheelspace.

A unique dataset was provided for the adiabatic effectiveness on the stator- and rotor-sided cavity wall for small steps in the rim seal purge flow injection rate. The results showed that adiabatic effectiveness is gradually increased as the amount of purge air is increased. The largest sensitivity of adiabatic effectiveness to purge flow was found in the zero to moderate purge flow rates (IR=0.0–0.6 %), where an increase of more than 25 % was detected. The sensitivity of the adiabatic effectiveness was compared to the stage efficiency deterioration, which was identified to be linearly dropping with purge flow (0.36 % points per percent purge flow injection rate). Consequently, the linear correlation of the stage efficiency with respect to purge flow helps in the lower purge flow band, as the gain in adiabatic effectiveness is relatively cheap. For the purge flow range above the design injection rate (IR=0.8 %), the addition of a few percentage points in the seal effectiveness is expensive with respect to aerodynamic performance.

By changing the thermal boundary conditions of the stator- and rotor-sided cavity walls, the convective heat transfer coefficient, and accordingly the Nusselt number, was derived. On the stator-sided wall below the rotor sealing arm, the change in convective heat transfer with purge flow was identified to be modest. Above the sealing arm, the Nusselt number dropped by about 53 % per percent purge flow injection rate, which was anticipated to be induced by the reduction in tangential flow velocity due to the purge air blockage effect. The rotor-sided cavity wall presented a substantial increase in the Nusselt number by a factor of 2 to 3 when the purge flow injection rate was increased by 1 %. Additionally, a tendency to reduce the convective heat transfer for larger radii was identified on the rotor wall for most of the purge flow rates. The trend is most likely induced by the growing thermal boundary layer.
An attempt was made to predict the measured convective heat transfer levels on the rotating wall by means of a “free disk” correlation. The variety and range of tuning parameters facilitated matching the distribution of the net zero purge flow rate (IR=0.0 %). However, for high purge flow injection rates, the distributions can be underpredicted by up to 60 %. Therefore, great care needs to be taken with such correlations as they can deviate substantially for high injection rates.

Rotor Blade Count Reduction and Tip Geometry Variation

To reduce cooling requirements and cut overall operational costs of a high-pressure turbine, a comparative study with respect to a substantial blade count reduction was performed. In the course of the analysis, it was found that

the expected aerodynamic performance drop due to the higher blade loading could be overcome by means of a favorable redistribution of mass flow and advanced non-axisymmetric end wall profiling. Nevertheless, the increased strength of most of the secondary flow features due to the reduction in blade count could not be suppressed. The absolute stage efficiency increase for an improved rotor design with a 22 % reduction in blade count was found to be 0.4 % points compared to a baseline turbine configuration with more blades and identical stator rows and axial row spacing.

However, the elevated secondary flow strength provoked by the inherent higher blade loading and the interaction of the flow structures with the potential field of the downstream stator row led to a substantial increase in tonal noise at the turbine exit. The resulting increase in turbine tonal noise was quantified to be up to 13 dB.

To further improve the stage performance and reduce the tip secondary flow strength, a set of four different blade tip geometries was extensively probed using a rainbow rotor design setup. A superior design was evaluated which is termed as the "Optimized Squealer," which is characterized by a non-uniform squealer fence design that expands pitch-wise and upstream. The integral performance benefit due to the integration of this tip design was found to be 0.1 % points for the stage efficiency and 0.3 % points for the 1.5-stage aerodynamic performance with respect to a reference squealer design. The manufacturing of a notch on the suction side of a flat tip is a moderate change to the tip design that substantially reduces the strength of the tip trailing edge shed vortex, but promotes additional losses in the tip leakage vortex such that the reduced complexity in design and manufacturing is to some degree compromised, especially since the leakage losses were found to promote additional aerodynamic losses at the exit of the turbine section due to a complex cross-passage and radial migration of the second stator tip flow structures.

7.3. Suggestions for Future Work

In the course of this work, novel design concepts, instrumentation setups, and data acquisition modules were successfully tested and implemented. Nevertheless, when extensively using hardware and diving into the topics, some details come into play which would benefit the further analysis of the respective fields. Therefore, the current section should provide a glance at what could be done in the future to provide further contributions.

Data Acquisition and Instrumentation

The usage of a modular, multipurpose telemetry system to provide measurement data in the rotating frame of reference substantially contributed to this work. To date, two factors offer the greatest potential to improve these modules:

(1) Temperature stability of the electronics: The sensitivity of the data acquisition modules to environmental temperature could be further reduced by using temperature-stable components (resistors, current source). This would eliminate a further calibration dimension and save time in the preparation of the experiments.

(2) WiFi communication: the WiFi connectivity between the telemetry modules and the receiving router inside the turbine drum could be improved, especially for long measurement days. Reducing the temperature sensitivity of the WiFi module on the telemetry system and an improved positioning of the receiving router antennas in the turbine drum space could contribute to the stability of the WiFi communication.

With respect to the turbine instrumentation, the results of the provided thesis suggest multiple extensions of the tools to capture specific flow dynamics and excitation. The impact of the asynchronous low-frequency modes formed in the hub cavity on the basic flow quantities such as yaw angle or total pressure could be quantified by using a four-sensor FRAP such that the virtual sensor mode could be excluded in the measurement procedure. In detail, the virtual four-sensor mode of the currently used 2-sensor FRAP does not allow derivation of such flow quantities: by rotating the probe, the phase information of the low-frequency modes is lost and thereby proper phase-locking of the quantities is not possible. By simultaneously acquiring all four sensors, this issue could be overcome. Additionally, it could be thought to use an externally generated trigger signal that matches the dominating frequency content of the previously found cavity mode.
Since part of the topics addressed in the current work are also related to the aeroacoustic excitation, it would be beneficial to install an array of stationary fast-response pressure probes at the exit of the turbine in order to be able to determine the modal decomposition of the acoustic field (radial and circumferential) and gain knowledge of the detailed contributions to the turbine noise.

Topic-Wise Suggestions

Non-Synchronous Hub Cavity Modes To further advance and gain knowledge of the formation of low-frequency asynchronous flow perturbations in

cavities, it is highly recommended to systematically change the rim seal design. The suggested design details to change are the seal gap and overlap, the volume ratio of the cavity compartments, and the blade count ratio between rotor and upstream stator. Furthermore, a quantification of the impact of the aerodynamic losses and performance could be done by using either a traversing four-sensor FRAP or conducting expensive, full-annular unsteady RANS calculations using a fine mesh.

Novel Rim Seal Design: Purge Control Features The presented novel rim seal design shows encouraging results for performance and ingestion characteristics. As the ingestion characteristics are determined numerically, it is suggested to confirm the findings by complementing the computations with a detailed experimental study comparably to the study performed for the overlap-type rim seal presented in this work.

Hub Cavity Convective Heat Transfer The amount of provided convective heat transfer data in the hub cavity is rarely found in open literature. It is therefore an appropriate database to compare with computational results to quantify the capabilities of modern CFD tools to predict the hub cavity heat transfer levels. Although the cavity walls were resolved by different positions of the sensing elements, it would be beneficial to increase the measurement data resolution, potentially by using optical measurement approaches (e.g., using optical fibers combined with a fast infrared camera and a thin-film heated carrier insert for rotor cavity wall measurements).

Blade Count Reduction and Tip Variation The rotor blade count reduction promoted tonal noise emissions due to the interaction of the secondary flows with the downstream blade row potential field. Consequently, an experimental study regarding the axial spacing between the rotor and the downstream stator would allow drawing conclusions on how much the axial gaps would need to be increased in order to compensate for the additional tonal noise contribution due to the higher blade loading.
The rainbow rotor study for different blade tip designs has revealed a superior design regarding the aerodynamic performance. In order to confirm the findings with improved measurement accuracy, a complementing set of aerodynamic probe measurements with a rotor setup that only consists of one tip design should be targeted so that performance data can be provided with a torque-based efficiency definition.
The recent advances at the Laboratory for Energy Conversion allow for the provision of heat transfer measurements at the blade tip using a quasi iso-energetic setup in combination with a fast-infrared camera. The complex measurement approach would enable to study the tip convective heat transfer

levels for the various presented blade tip geometries and could therefore provide a complementary dataset regarding the thermal performance of each design. Additionally, a set of high-quality CFD calculations that resolve the intra-row flow field (especially for the rotor) would contribute to the understanding of flow mechanisms induced by the various tip designs and would enable drawing further conclusions on potential design guidelines for rotor blade tips.

Bibliography

[1] R. S. Abhari and A. H. Epstein. An Experimental Study of Film Cooling in a Rotating Transonic Turbine. *Journal of Turbomachinery*, 116(1):63–70, 1994.

[2] R. S. Abhari, G. R. Guenette, A. H. Epstein, and M. B. Giles. Comparison of Time-Resolved Turbine Rotor Blade Heat Transfer Measurements and Numerical Calculations. *Journal of Turbomachinery*, 114(4):818–827, 1992.

[3] S. D. Abrahamson, J. K. Eaton, and D. J. Koga. The Flow Between Shrouded Co-Rotating Disks. *Physics of Fluids A: Fluid Dynamics*, 1(2):241–251, 1989.

[4] U.S. Energy Information Administration. U.S. Gulf Coast Kerosene - Type, Jet Fuel Spot Price. http://www.eia.gov/dnav/pet/, 2019.

[5] R. Bagnara. *High-Pressure Turbine Purge Flow Control Investigation using Unsteady CFD Simulations*. Master Thesis, ETH Zurich, Zurich, Switzerland, 2017.

[6] A. M. Basol. *Turbine Design Optimizations using High Fidelity CFD*. PhD Thesis, Diss. ETH No. 21559, Zurich, Switzerland, 2014.

[7] P. F. Beard, F. Gao, K. S. Chana, and J. Chew. Unsteady Flow Phenomena in Turbine Rim Seals. *Journal of Engineering for Gas Turbines and Power*, 139(3):032501–032501–10, 2016.

[8] T. Behr. *Control of Rotor Tip Leakage and Secondary Flow by Casing Air Injection in Unshrouded Axial Turbines*. PhD Thesis, Diss. ETH No. 17283, Zurich, Switzerland, 2007.

[9] T. Behr, A. I. Kalfas, and R. S. Abhari. Unsteady Flow Physics and Performance of a One-and 1/2-Stage Unshrouded High Work Turbine. *Journal of Turbomachinery*, 129(2):348–359, 2007.

[10] T. Behr, L. Porreca, T. Mokulys, A. I. Kalfas, and R. S. Abhari. Multistage Aspects and Unsteady Flow Effects of Stator and Rotor Clocking in an Axial Turbine with Low Aspect Ratio Blading. *Journal of Turbomachinery-Transactions of the ASME*, 128(1):11–22, 2006.

[11] R. A. Berg, C. S. Tan, Z. Ding, G. Laskowski, P. Palafox, and R. Miorini. Experimental and Analytical Assessment of Cavity Modes in a Gas Turbine Wheelspace. *Journal of Engineering for Gas Turbines and Power*, 140(6):062502–062502–11, 2018.

[12] A. Binder, W. Forster, K. Mach, and H. Rogge. Unsteady Flow Interaction Caused by Stator Secondary Vortices in a Turbine Rotor. *Journal of Turbomachinery-Transactions of the ASME*, 109(2):251–257, 1987.

[13] J. P. Bindon. The Measurement and Formation of Tip Clearance Loss. *Journal of Turbomachinery of the ASME*, 111(3):257–263, 1989.

[14] H. M. Blackburn and J. M. Lopez. Modulated Waves in a Periodically Driven Annular Cavity. *Journal of Fluid Mechanics*, 667:336–357, 2011.

[15] T. C. Booth, P. R. Dodge, and H. K. Hepworth. Rotor-Tip Leakage: Part I - Basic Methodology. *Journal of Engineering for Power*, 104(1):154–161, 1982.

[16] I. Bosdas, M. Mansour, A. I. Kalfas, and R. S. Abhari. Experimental Methods for Performance and Reliability of Steam and Gas Turbines. In *Proceedings of the 1st Global Power and Propulsion Forum, GPPF-2017-88*, Zurich, 2017.

[17] J. Boudet, N. J. Hills, and J. W. Chew. Numerical Simulation of the Flow Interaction Between Turbine Main Annulus and Disc Cavities. In *Proceedings of the ASME Turbo Expo, GT2006-90307*, Barcelona, 2006.

[18] BP. Bp Energy Outlook. https://www.bp.com/content/dam/bp-country/de-ch/PDF/Energy-Outlook-2018-edition-Booklet.pdf, 2018.

[19] K. W. Bushell. A Survey of Low Velocity and Coaxial Jet Noise with Application to Prediction. *Journal of Sound and Vibration*, 17(2):271–282, 1971.

[20] C. Camci, D. Dey, and L. Kavurmacioglu. Aerodynamics of Tip Leakage Flows Near Partial Squealer Rims in an Axial Flow Turbine Stage. *Journal of Turbomachinery*, 127(1):14–24, 2005.

[21] M. Cames, J. Graichen, A. Siemons, and V. Cook. Emission reduction targets for international aviation and shipping. In *Policy Department A: economic and scientific policy*, European Parliament Directorate general for internal policies, 2015.

[22] C. Cao, J. W. Chew, P. R. Millington, and S. I. Hogg. Interaction of Rim Seal and Annulus Flows in an Axial Flow Turbine. *Journal of Engineering for Gas Turbines and Power*, 126(4):786–793, 2004.

[23] B. C. Cernat, M. Pátý, C. De Maesschalck, and S. Lavagnoli. Experimental and Numerical Investigation of Optimized Blade Tip Shapes - Part I: Turbine Rainbow Rotor Testing and Numerical Methods. *Journal of Turbomachinery*, 141(1):011006–011006–13, 2018.

[24] V. S. P. Chaluvadi, A. I. Kalfas, M. R. Banieghbal, H. P. Hodson, and J. D. Denton. Blade-Row Interaction in a High-Pressure Turbine. *Journal of Propulsion and Power*, 17(4):892–901, 2001.

[25] V. S. P. Chaluvadi, A. I. Kalfas, and H. P. Hodson. Vortex Transport and Blade Interactions in High Pressure Turbines. *Journal of Turbomachinery-Transactions of the ASME*, 126(3):395–406, 2004.

[26] G. Chen, W. Dawes, and H. Hodson. *Numerical and Experimental Investigation of Turbine Tip Gap Flow*. Joint Propulsion Conferences. American Institute of Aeronautics and Astronautics, 1993.

[27] J. W. Chew. A Theoretical Study of Ingress for Shrouded Rotating Disk Systems with Radial Outflow. *Journal of Turbomachinery*, 113(1):91–97, 1991.

[28] J. W. Chew, S. Dadkhah, and A. B. Turner. Rim Sealing of Rotor-Stator Wheelspaces in the Absence of External Flow. *Journal of Turbomachinery-Transactions of the ASME*, 114(2):433–438, 1992.

[29] J. W. Chew, T. Green, and A. B. Turner. Rim Sealing of Rotor-Stator Wheelspaces in the Presence of External Flow. In *Proceedings of the ASME Turbo Expo, 94-GT-126*, The Hague, 1994.

[30] M. Chilla, H. Hodson, and D. Newman. Unsteady Interaction Between Annulus and Turbine Rim Seal Flows. *Journal of Turbomachinery*, (44748):1359–1370, 2012.

[31] M. Chilla, H. P. Hodson, G. Pullan, and D. Newman. High-pressure turbine rim seal design for increased efficiency. In *Proceedings of the ASME Turbo Expo, GT2016-57495*, Seoul, 2016.

[32] E. Couch, J. Christophel, E. Hohlfeld, K. A. Thole, and F. J. Cunha. Comparison of Measurements and Predictions for Blowing from a Turbine Blade Tip. *Journal of Propulsion and Power*, 21(2):335–343, 2005.

[33] N. A. Cumpsty. *Compressor Aerodynamics*. Longman, 1989.

[34] N. A. Cumpsty and J. H. Horlock. Averaging Nonuniform Flow for a Purpose. *Journal of Turbomachinery*, 128(1):120–129, 2005.

[35] O. Czarny, H. Iacovides, and B. E. Launder. Precessing Vortex Structures in Turbulent Flow within Rotor-Stator Disc Cavities. *Flow, Turbulence and Combustion*, 69(1):51–61, 2002.

[36] S. Dadkhah, A. B. Turner, and J. W. Chew. Performance of Radial Clearance Rim Seals in Upstream and Downstream Rotor-Stator wheelspaces. *Journal of Turbomachinery-Transactions of the ASME*, 114(2):439–445, 1992.

[37] C. De Maesschalck, S. Lavagnoli, G. Paniagua, T. Verstraete, R. Olive, and P. Picot. Heterogeneous Optimization Strategies for Carved and Squealer-Like Turbine Blade Tips. *Journal of Turbomachinery*, 138(12):121011–121011–12, 2016.

[38] C. D. Dean. On the Necessity of Unsteady Flow in Fluid Machines. *Journal of Basic Engineering -Transactions of the ASME*, 81(1):24–28, 1959.

[39] J. D. Denton. Loss Mechanisms in Turbomachines. *Journal of Turbomachinery-Transactions of the ASME*, 115(4):621–656, 1993.

[40] D. Dey. *Tip Desensitization in an Axial Turbine*. PhD Thesis, PhD Thesis Pennsylvania State University, Pennsylvania, United States of America, 2001.

[41] D. Dey and C. Camci. Aerodynamic Tip Desensitization of an Axial Turbine Rotor using Tip Platform Extensions. In *Proceedings of the ASME Turbo Expo, 2001-GT-0484*, volume V001T03A069, New Orleans, 2001.

[42] M. G. Dunn and C. W. Haldeman. Time-Averaged Heat Flux for a Recessed Tip, Lip, and Platform of a Transonic Turbine Blade. *Journal of Turbomachinery*, 122(4):692–698, 2000.

[43] M. G. Dunn, C. W. Haldeman, R. S. Abhari, and M. L. McMillan. Influence of Vane/Blade Spacing on the Heat Flux for a Transonic Turbine. *Journal of Turbomachinery*, 122(4):684–691, 2000.

[44] DuPont. DuPont Kapton Summary of Properties. https://www.dupont.com/content/dam/dupont/products-and-services/membranes-and-films/polyimde-films, 2019.

[45] A. H. Epstein, G. R. Guenette, R. J. G. Norton, and C. Yuzhang. High-Frequency Response Heat-Flux Gauge. *Review of Scientific Instruments*, 57(4):639–649, 1986.

[46] C. Faustmann, S. Zerobin, S. Bauinger, A. Marn, F. Heitmeir, and E. Göttlich. Turbine Noise Reduction: Axial Spacing and Embedded Design. In *Proceedings of the ASME Turbo Expo, GT2015-43565*, Montreal, 2015.

[47] J. Gier and S. Ardey. On the Impact of Blade Count Reduction on Aerodynamic Performance and Loss Generation in a Three-Stage LP Turbine. In *Proceedings of the ASME Turbo Expo, GT2001-0197*, volume V003T01A071, New Orleans, 2001.

[48] J. Gier, B. Stubert, B. Brouillet, and L. de Vito. Interaction of Shroud Leakage Flow and Main Flow in a Three-Stage LP Turbine. *Journal of Turbomachinery*, 127(4):649–658, 2003.

[49] S. Girgis, E. Vlasic, J.-P. Lavoie, and S. H. Moustapha. The Effect of Secondary Air Injection on the Performance of a Transonic Turbine Stage. In *Proceedings of the ASME Turbo Expo, GT-2002-30340*, Amsterdam, 2002.

[50] V. V. Golubev and H. M. Atassi. Acoustic-Vorticity Waves in Swirling Flows. *Journal of Sound and Vibration*, 209(2):203–222, 1998.

[51] C. Gossweiler. *Sonden und Messsystem für schnelle aerodynamische Strömungsmessung mit piezoresistiven Druckgebern.* PhD Thesis, Diss. ETH No. 10253, Zurich, Switzerland, 1993.

[52] D. L. Graber, W. A. Daniels, and B. V. Johnson. *Disk Pumping-Test. Air Force Wright Aeronautical Laboratories.* 1987.

[53] D. G. Gregory-Smith, C. P. Graves, and J. A. Walsh. Growth of Secondary Losses and Vorticity in an Axial Turbine Cascade. *Journal of Turbomachinery-Transactions of the ASME*, 110(1):1–8, 1988.

[54] E. M. Greitzer, C. S. Tan, and M. B. Graf. *Internal Flow: Concepts and Applications.* Cambridge Engine Technology Series. Cambridge University Press, Cambridge, 2004.

[55] K. Hamabe and K. Ishida. Rim Seal Experiments and Analysis of a Rotor-Stator System with Nonaxisymmetric Main Flow. In *Proceedings of the Internation Gas Turbine and Aeroengine Congress, 92-GT-160*, Cologne, 1992.

[56] D. D. Hänni. *Full-Annular Unsteady RANS Simulation of the Rotor Upstream Hub Cavity.* Master Thesis, ETH Zurich, Zurich, Switzerland, 2015.

[57] D. D. Hänni, R. Schädler, A. I. Kalfas, R. S. Abhari, G. Schmid, E. Lutum, and N. Lecoq. Purge flow effects on rotor hub endwall heat transfer with extended endwall contouring into the disk cavity. *Journal of the Global Power and Propulsion Society*, 3:555–568, 2019.

[58] S. Harrison. The Influence of Blade Lean on Turbine Losses. *Journal of Turbomachinery-Transactions of the ASME*, 114(1):184–190, 1992.

[59] N. W. Harvey. Aerothermal Implications of Shroudless and Shrouded Blades. In *von Karman Institute Lecture Series on Turbine Balde Tip Design and Tip Clearance*, 2004.

[60] N. W. Harvey and K. Ramsden. A Computational Study of a Novel Turbine Rotor Partial Shroud. *Journal of Turbomachinery*, 123(3):534–543, 2000.

[61] R. T. Haslam and E. L. Chappell. The Measurement of the Temperature of a Flowing Gas. *Industrial & Engineering Chemistry*, 17(4):402–408, 1925.

[62] W. R. Hawthorne. Secondary Circulation in Fluid Flow. *Proceedings of the Royal Society of London. Series A, Mathematical and Physical Sciences*, 206(1086):374–387, 1951.

[63] W. R. Hawthorne. Rotational Flow Through Cascades. *Journal of Mech. and Appl. Math*, 3, 1955.

[64] N. J. Hills, J. W. Chew, and A. B. Turner. Computational and Mathematical Modeling of Turbine Rim Seal Ingestion. *Journal of Turbomachinery*, 124(2):306–315, 2002.

[65] M. P. Hodak. *Quantification of Fourth Generation Kapton Heat Flux Gauge Calibration Performance*. Master Thesis, The Ohio State University, Columbus Ohio, United States of America, 2010.

[66] H. P. Hodson and W. N. Dawes. On the Interpretation of Measured Profile Losses in Unsteady Wake-Turbine Blade Interaction Studies. *Journal of Turbomachinery-Transactions of the ASME*, 120(2):276–284, 1998.

[67] E. M. Hohlfeld, J. R. Christophel, E. L. Couch, and K. A. Thole. Predictions of cooling from dirt purge holes along the tip of a turbine blade. In *Proceedings of the ASME Turbo Expo, GT2003-38251*, Atlanta, 2003.

[68] International Energy Agency IEA. *World Energy Outlook 2015*. ., ISBN 978-92-64-24366-8, 1st edition, 2015.

[69] International Energy Agency IEA. Renewables 2018 - Executive Summary. http://webstore.iea.org/market-report-series-renewables-2018, 2018.

[70] International Energy Agency IEA. World Energy Outlook 2018 - Executive Summary. http://webstore.iea.org/world-energy-outlook-2018, 2018.

[71] International Air Transport Association. Technology road map 2013. http://www.iata.org/whatwedo/environment/Documents/technology-roadmap-2013.pdf, 2013.

[72] ISO. *Guide to the Expression of Uncertainty in Measurement (GUM)*. International Organisation for Standardisation (Geneva, Switzerland), ISBN 92-67-1011889, 1st edition, 1993.

[73] R. Jakoby, T. Zierer, K. Lindblad, J. Larsson, L. deVito, D. E. Bohn, J. Funcke, and A. Decker. Numerical Simulation of the Unsteady Flow Field in an Axial Gas Turbine Rim Seal Configuration. In *Proceedings of the ASME Turbo Expo, GT2004-53829*, Vienna, 2004.

[74] A. Jameson, W. Schmidt, and E. L. I. Turkel. *Numerical Solution of the Euler Equations by Finite Volume Methods using Runge Kutta Time Stepping Schemes*. Fluid Dynamics and Co-located Conferences. American Institute of Aeronautics and Astronautics, 1981.

[75] P. Jenny. *Interaction Mechanisms Between Rim Seal Purge Flow and Profiled End Walls in a Low-Pressure Turbine*. PhD Thesis, Diss. ETH No. 20429, Zurich, Switzerland, 2012.

[76] P. Jenny, R. S. Abhari, M. G. Rose, M. Brettschneider, K. Engel, and J. Gier. Unsteady Rotor Hub Passage Vortex Behavior in the Presence of Purge Flow in an Axial Low Pressure Turbine. *Journal of Turbomachinery*, 135(5):051022–051022–9, 2013.

[77] B. Johnson, G. Mack, R. Paolillo, and W. Daniels. *Turbine Rim Seal Gas Path Flow Ingestion Mechanisms*. Joint Propulsion Conferences. American Institute of Aeronautics and Astronautics, 1994.

[78] J. B. Johnson. Thermal Agitation of Electricity in Conductors. *Physical Review*, 32(1):97–109, 1928.

[79] S. Julien, J. Lefrancois, G. Dumas, G. Boutet-Blais, S. Lapointe, J. F. Caron, and R. Marini. Simulations of Flow Ingestion and Related Structures in a Turbine Disk Cavity. In *Proceedings of the ASME Turbo Expo, GT2010-22729*, Glasgow, 2010.

[80] C. E. Kachel and J. D. Denton. Experimental and Numerical Investigation of the Unsteady Surface Pressure in a Three-Stage Model of an Axial High Pressure Turbine. *Journal of Turbomachinery of the ASME*, 128(2):261–272, 2004.

[81] I. Kaiser and J. P. Bindon. The Effect of Tip Clearance on the Development of Loss Behind a Rotor and a Subsequent Nozzle. In *Proceedings of the ASME Turbo Expo, 97-GT-053*, volume V001T03A0111, Orlando, 1997.

[82] Ch. Kasper, M. G. Rose, S. Staudacher, and J. Gier. A Study of Unsteady Secondary Flow in a Water Flow Axial Turbine Model. In *Proceedings of the ASME Turbo Expo, GT2008-50239*, 2008.

[83] M. R. Khorrami, F. Li, and M. Choudhari. Novel Approach for Reducing Rotor Tip-Clearance-Induced Noise in Turbofan Engines. *AIAA Journal*, 40(8):1518–1528, 2002.

[84] Y. W. Kim, J. P. Downs, F. O. Soechting, W. Abdel-Messeh, G. D. Steuber, and S. Tanrikut. Darryl E. Metzger Memorial Session Paper: A Summary of the Cooled Turbine Blade Tip Heat Transfer and Film Effectiveness Investigations Performed by Dr. D. E. Metzger. *Journal of Turbomachinery*, 117(1):1–11, 1995.

[85] K. Knobloch, L. Neuhaus, F. Bake, P. Gaetani, and G. Persico. Experimental Assessment of Noise Generation and Transmission in a High-Pressure Transonic Turbine Stage. *Journal of Turbomachinery*, 139(10):101006–101006–12, 2017.

[86] N. Kobayashi, M. Matsumato, and M. Shizuya. An Experimental Investigation of a Gas-Turbine Disk Cooling System. *Journal of Engineering for Gas Turbines and Power-Transactions of the ASME*, 106(1):136–141, 1984.

[87] S. Krebietke. *Full-Annular Numerical Investigation of Tip Shroud Cavity Flows*. Master Thesis, ETH Zurich, Zurich, Switzerland, 2014.

[88] P. Kupferschmied. *Zur Methodik zeitaufgelöster Messungen mit Strömungssonden in Verdichtern und Turbinen*. PhD Thesis, Diss. ETH No. 12474, Zurich, Switzerland, 1998.

[89] J. S. Kwak and J. C. Han. Heat Transfer Coefficients and Film Cooling Effectiveness on the Squealer Tip of a Gas Turbine Blade. *Journal of Turbomachinery*, 125(4):648–657, 2003.

[90] K. Kyprianidis. Future Aero Engine Designs: An Evolving Vision. 2011.

[91] L. S. Langston. Secondary Flows in Axial Turbines - A Review. *Heat Transfer in Gas Turbine Systems, Annals of the New York Academy of Siences*, 934(1):11–26, 2001.

[92] S. Lavagnoli, C. De Maesschalck, and V. Andreoli. Design Considerations for Tip Clearance Control and Measurement on a Turbine Rainbow Rotor With Multiple Blade Tip Geometries. *Journal of Engineering for Gas Turbines and Power*, 139(4):042603–042603–10, 2016.

[93] S. Lazzi Gazzini, R. Schädler, A. I. Kalfas, and R. S. Abhari. Infrared Thermography with Non-Uniform Heat Flux Boundary Conditions on the Rotor Endwall of an Axial Turbine. *Measurement Science and Technology*, 28(2):025901, 2016.

[94] S. Lazzi Gazzini, R. Schädler, A. I. Kalfas, R. S. Abhari, S. Hohenstein, G. Schmid, and E. Lutum. Effect of Purge Air on Rotor Endwall Heat Transfer of an Axial Turbine. *Journal of the Global Power and Propulsion Society*, 1:211–223, 2017.

[95] C. Lenherr. *High Temperature Fast Response Aeordynamic Probe*. PhD Thesis, Diss. ETH No. 19367, Zurich, Switzerland, 2011.

[96] M. V. Lowson. Theoretical Analysis of Compressor Noise. *The Journal of the Acoustical Society of America*, 47(1B):371–385, 1970.

[97] J. M. Owen and R. H. Roger. *Flow and Heat Transfer in Rotating-Disc Systems. Volume I - Rotor-Stator Systems*, volume 90. 1989.

[98] M. Mansour. *A 48kHz Bandwidth, 1.8mm Diameter Entropy Probe for Aerothermal Loss Measurements in Turbomachinery Flows*. PhD Thesis, Diss. ETH No. 18087, Zurich, Switzerland, 2009.

[99] M. Mansour, N. Chokani, A. I. Kalfas, and R. S. Abhari. Time-resolved Entropy Measurements Using a Fast Response Entropy Probe. *Measurement Science and Technology*, 19(11), 2008.

[100] M. Mansour, N. Chokani, A. I. Kalfas, and R. S. Abhari. Unsteady Entropy Measurements in a High Speed Radial Compressor. *Journal of Engineering for Gas Turbines and Power*, 130(2), 2008.

[101] M. Mansour, P. Rebholz, A. I. Kalfas, and R. S. Abhari. An On-Board Wireless Multi-Sensor Measurement System for Rotating Turbomachinery Application. In *Proceedings of the International Gas Turbine Congress 2015*, Tokyo, 2015.

[102] R. Marini and S. Girgis. The Effect of Blade Leading Edge Platform Shape on Upstream Disk Cavity to Mainstream Flow Interaction of a High-Pressure Turbine Stage. In *Proceedings of the ASME Turbo Expo, GT2007-27429*, Montreal, 2007.

[103] R. M. Mathison, C. W. Haldeman, and M. G. Dunn. Aerodynamics and Heat Transfer for a Cooled One and One-Half Stage High-Pressure Turbine - part II: Influence of Inlet Temperature Profile on Blade Row and Shroud. *Journal of Turbomachinery*, 134(1):011007–011007–8, 2011.

[104] R. M. Mathison, C. W. Haldeman, and M. G. Dunn. Heat Transfer for the Blade of a Cooled Stage and One-Half High-Pressure Turbine - Part I: Influence of Cooling Variation. *Journal of Turbomachinery*, 134(3):031014–031014–12, 2011.

[105] T. Matsunuma. Unsteady Flow Field of an Axial-Flow Turbine Rotor at a Low Reynolds Number. *Journal of Turbomachinery-Transactions of the ASME*, 129(2):360–371, 2007.

[106] M. Matter. *Characterization and Deployment of a Wireless Multi-Sensor Measurement System for Turbomachinery Application.* Master Thesis, ETH Zurich, Zurich, Switzerland, 2015.

[107] R. E. Mayle. The 1991 IGTI Scholar Lecture: The Role of Laminar-Turbulent Transition in Gas Turbine Engines. *Journal of Turbomachinery*, 113(4):509–536, 1991.

[108] C. McLean, C. Camci, and B. Glezer. Mainstream Aerodynamic Effects Due to Wheelspace Coolant Injection in a High-Pressure Turbine Stage: Part I - Aerodynamic Measurements in the Stationary Frame. *Journal of Turbomachinery-Transactions of the ASME*, 123(4):687–696, 2001.

[109] C. McLean, C. Camci, and B. Glezer. Mainstream Aerodynamic Effects Due to Wheelspace Coolant Injection in a High-Pressure Turbine Stage: Part II - Aerodynamic Measurements in the Rotational Frame. *Journal of Turbomachinery-Transactions of the ASME*, 123(4):697–703, 2001.

[110] D. E. Metzger and D. E. Larson. Use of Melting Point Surface Coatings for Local Convection Heat Transfer Measurements in Rectangular Channel Flows with 90-deg Turns. *Journal of Heat Transfer*, 108(1):48–54, 1986.

[111] D. E. Metzger, W. J. Mathis, and L. D. Grochowsky. Jet Cooling at the Rim of a Rotating Disk. *Journal of Engineering for Power*, 101(1):68–72, 1979.

[112] R. N. Meyer. The Effect of Wakes on the Transient Pressure and Velocity Distribution in Turbomachines. *Journal of Basic Engineering -Transactions of the ASME*, 80(1):1544–1552, 1958.

[113] A. V. Mirzamoghadam, G. Heitland, and K. M. Hosseini. The Effect of Annulus Performance Parameters on Rotor-Stator Cavity Sealing Flow. In *Proceedings of the ASME Turbo Expo, GT2009-59380*, Orlando, 2009.

[114] A. V. Mirzamoghadam, G. Heitland, M. C. Morris, J. Smokte, M. Malak, and J. Howe. 3D CFD Ingestion Evaluation of a High Pressure Turbine Rim Seal Disk Cavity. In *Proceedings of the ASME Turbo Expo, GT2008-50531*, Berlin, 2008.

[115] B. Mischo, T. Behr, and R. S. Abhari. Flow Physics and Profiling of Recessed Blade Tips: Impact on Performance and Heat Load. *Journal of Turbomachinery*, 130(2):021008–021008–8, 2008.

[116] B. Mischo, A. Burdet, and R. S. Abhari. Influence of Stator-Rotor Interaction on the Aerothermal Performance of Recess Blade Tips. *Journal of Turbomachinery*, 133(1):011023–011023–11, 2010.

[117] R. J. Moffat. Describing the Uncertainties in Experimental Results. *Experimental Thermal and Fluid Science*, 1(1):3–17, 1988.

[118] R. J. Moffat. What's New in Convective Heat Transfer? *International Journal of Heat and Fluid Flow*, 19(2):90–101, 1998.

[119] J. Moore and R. Adhye. Secondary Flows and Losses Downstream of a Turbine Cascade. *Journal of Engineering for Gas Turbines and Power-Transactions of the ASME*, 107(4):961–968, 1985.

[120] S. H. Moustapha, G. J. Paron, and J. H. T. Wade. Secondary Flows in Cascades of Highly Loaded Turbine Blades. *Journal of Engineering for Gas Turbines and Power-Transactions of the ASME*, 107(4):1031–1038, 1985.

[121] MTU. GP7000 high-pressure turbine blades and vanes. http://www.mtu.de/fileadmin/EN/7_News_Media/1_Press/3_Press_kits/Paris_Air_Show_2015/Fotos/GP7000_high_pressure_turbine_blades_and_vanes.jpg, 2015.

[122] R. H. Ni. *A Multiple Grid Scheme for Solving the Euler Equations*. Fluid Dynamics and Co-located Conferences. American Institute of Aeronautics and Astronautics, 1981.

[123] J. B. Nickol, R. M. Mathison, and M. G. Dunn. Heat-Flux Measurements for a Realistic Cooling Hole Pattern With Multiple Flow Conditions. *Journal of Turbomachinery*, 136(3):031010–031010–8, 2013.

[124] J. B. Nickol, R. M. Mathison, M. F. Malak, R. Rana, and J. S. Liu. Time-Resolved Heat Transfer and Surface Pressure Measurements for a Fully Cooled Transonic Turbine Stage. *Journal of Turbomachinery*, 137(9):091009–091009–11, 2015.

[125] Institute of Virtual Manufacturing (IVP) at ETH Zurich. http://www.ivp.ethz.ch/en/infrastructure/tensile-test, 2019.

[126] T. S. D. O'Mahoney, N. J. Hills, J. W. Chew, and T. Scanlon. Large-Eddy Simulation of Rim Seal Ingestion. In *Proceedings of the ASME Turbo Expo, GT2010-22962*, Glasgow, 2010.

[127] J. H. P. Ong, R. J. Miller, and S. Uchida. The Effect of Coolant Injection on the Endwall Flow of a High Pressure Turbine. In *Proceedings of the ASME Turbo Expo, GT2006-91060*, Barcelona, 2006.

[128] J. M. Owen. Prediction of Ingestion Through Turbine Rim Seals - Part I: Rotationally Induced Ingress. *Journal of Turbomachinery*, 133(3):031005–031005–9, 2010.

[129] J. M. Owen. Prediction of Ingestion Through Turbine Rim Seals - Part II: Externally Induced and Combined Ingress. *Journal of Turbomachinery*, 133(3):031006–031006–9, 2010.

[130] G. Paniagua, R. Denos, and S. Almeida. Effect of the Hub Endwall Cavity Flow on the Flow-Field of a Transonic High-Pressure Turbine. *Journal of Turbomachinery-Transactions of the ASME*, 126(4):578–586, 2004.

[131] I. Papagiannis. *Unsteady Steam Turbine Optimization using High Fidelity CFD*. PhD Thesis, Diss. ETH No. 25781, Zurich, Switzerland, 2019.

[132] R. Parker and J. F. Watson. Interaction Effects Between Blade Rows in Turbomachines. *Proc. of I.Mech.E*, 186(21), 1972.

[133] M. Pátý, B. C. Cernat, C. De Maesschalck, and S. Lavagnoli. Experimental and Numerical Investigation of Optimized Blade Tip Shapes - Part II: Tip Flow Analysis and Loss Mechanisms. *Journal of Turbomachinery*, 141(1):011007–011007–13, 2018.

[134] A. Perdichizzi and V. Dossena. Incidence Angle and Pitch-Chord Effects on Secondary Flows Downstream of a Turbine Cascade. *Journal of Turbomachinery*, 115(3):383–391, 1993.

[135] A. Pfau, J. Schlienger, A. I. Kalfas, and R. S. Abhari. Virtual Four Sensor Fast Response Aerodynamic Probe (FRAP). In *The 16th Symposium on Measuring Techniques in Cascades and Turbomachines*, Cambridge, UK, 2002.

[136] A. Pfau, J. Schlienger, A. I. Kalfas, and R. S. Abhari. Unsteady, 3-Dimensional Flow Measurement Using a Miniature Virtual 4 Sensor Fast Response Aerodynamic Probe (FRAP). In *Proceedings of the ASME Turbo Expo, GT2003-38128*, Atlanta, 2003.

[137] A. Pfau, M. Treiber, M. Sell, and G. Gyarmathy. Flow Interaction From the Exit Cavity of an Axial Turbine Blade Row Labyrinth Seal. *Journal of Turbomachinery*, 123(2):342–352, 2000.

[138] U. P. Phadke and J. M. Owen. Aerodynamic Aspects of the Sealing of Gas-Turbine Rotor-Stator Systems: Part 1: The Behavior of Simple Shrouded Rotating-Disk Systems in a Quiescent Environment. *International Journal of Heat and Fluid Flow*, 9(2):98–105, 1988.

[139] U. P. Phadke and J. M. Owen. Aerodynamic Aspects of the Sealing of Gas-Turbine Rotor-Stator Systems: Part 2: The Performance of Simple Seals in a Quasi-Axisymmetric External Flow. *International Journal of Heat and Fluid Flow*, 9(2):106–112, 1988.

[140] U. P. Phadke and J. M. Owen. Aerodynamic Aspects of the Sealing of Gas-Turbine Rotor-Stator Systems: Part 3: The Effect of Nonaxisymmetric External Flow on Seal Performance. *International Journal of Heat and Fluid Flow*, 9(2):113–117, 1988.

[141] V. Pinilla, J. P. Solano, G. Paniagua, and R. J. Anthony. Adiabatic Wall Temperature Evaluation in a High Speed Turbine. *Journal of Heat Transfer*, 134(9):091601–091601–9, 2012.

[142] I. Popović and H. P. Hodson. Aerothermal Impact of the Interaction Between Hub Leakage and Mainstream Flows in Highly-Loaded High Pressure Turbine Blades. *Journal of Turbomachinery*, 135(6):061014–061014–11, 2013.

[143] I. Popović and H. P. Hodson. The Effects of a Parametric Variation of the Rim Seal Geometry on the Interaction Between Hub Leakage and Mainstream Flows in High Pressure Turbines. *Journal of Engineering for Gas Turbines and Power*, 135(11):112501–112501–11, 2013.

[144] I. Popović and H. P. Hodson. Improving Turbine Stage Efficiency and Sealing Effectiveness Through Modifications of the Rim Seal Geometry. *Journal of Turbomachinery*, 135(6):061016–061016–10, 2013.

[145] L. Porreca. *Aerothermal Optimization of Partially Shrouded Axial Turbines*. PhD Thesis, Diss. ETH No. 17138, Zurich, Switzerland, 2007.

[146] L. Porreca, M. Hollenstein, A. I. Kalfas, and R. S. Abhari. Turbulence Measurements and Analysis in a Multistage Axial Turbine. *Journal of Propulsion and Power*, 23(1):227–234, 2007.

[147] G. Qureshi, M. H. Nguyen, N. R. Saad, and R. N. Tadros. Heat Transfer Measurements for Rotating Turbine Discs. In *Proceedings of the Internation Gas Turbine and Aeroengine Congress, 89-GT-236*, Toronto, 1989.

[148] M. A. Raheem. *Improvement of Transonic Low Pressure Steam Turbine using High Performance Computation*. PhD Thesis, Diss. ETH No. 25646, Zurich, Switzerland, 2019.

[149] N. M. Rao and C. Camci. Axial Turbine Tip Desensitization by Injection from a Tip Trench: Part 1 - Effect of Injection Mass Flow Rate. In *Proceedings of the ASME Turbo Expo, GT2004-53256*, Vienna, 2004.

[150] N. M. Rao and C. Camci. Axial Turbine Tip Desensitization by Injection from a Tip Trench: Part 2 - Leakage Flow Sensitivity to Injection Location. In *Proceedings of the ASME Turbo Expo, GT2004-53258*, Vienna, 2004.

[151] P. S. Rebholz. *Aeromechanical Challenges of Shrouded Low Pressure Turbines for Geared Turbofan Engines*. PhD Thesis, Diss. ETH No. 24212, Zurich, Switzerland, 2017.

[152] P. S. Rebholz, R. S. Abhari, A. I. Kalfas, and C. Zscherp. Tip-Shroud Cutbacks in a Low-Pressure Gas Turbine Stage. *Journal of Propulsion and Power*, 32(5):1077–1086, 2016.

[153] Patrick S. Rebholz, Simon Krebietke, Reza S. Abhari, and Anestis I. Kalfas. Turbine Aerodynamic Low-Frequency Oscillation and Noise Reduction Using Partial Shrouds. *Journal of Propulsion and Power*, 32(5):1067–1076, 2016.

[154] K. Regina. *High-Pressure Turbines with Novel Airfoils and End Walls Operating under Engine Representative Aero-Thermodynamic Effects*. PhD Thesis, Diss. ETH No. 22633, Zurich, Switzerland, 2015.

[155] K. Regina, A. I. Kalfas, and R. S. Abhari. Experimental Investigation of Purge Flow Effects on a High Pressure Turbine Stage. *Journal of Turbomachinery*, 137(4):041006–041006–8, 2014.

[156] K. Regina, A. I. Kalfas, R. S. Abhari, A. Lohaus, S. Voelker, and T. auf dem Kampe. Aerodynamic Robustness of End Wall Contouring Against Rim Seal Purge Flow. In *Proceedings of the ASME Turbo Expo, GT2014-26007*, Düsseldorf, 2014.

[157] K. Reid, J. Denton, G. Pullan, E. Curtis, and J. Longley. The Effect of Stator-Rotor Hub Sealing Flow on the Mainstream Aerodynamics of a Turbine. In *Proceedings of the ASME Turbo Expo, GT-2006-90838*, Barcelona, 2006.

[158] E. Reshad. *Power Supply for Turbine Shaft Onboard Electronics*. Bachelor Thesis, ETH Zurich, Zurich, Switzerland, 2013.

[159] M. Rezasoltani, K. Lu, M. T. Schobeiri, and J. Han. A Combined Experimental and Numerical Study of the Turbine Blade Tip Film Cooling Effectiveness Under Rotation Condition. *Journal of Turbomachinery*, 137(5):051009–051009–12, 2015.

[160] Rolls-Royce. *The Jet Engine*. 5th edition, 2015.

[161] M. Rose, P. Schuepbach, and M. Mansour. The Thermodynamics of Wake Blade Interaction in Axial Flow Turbines: Combined Experimental and Computational Study. *Journal of Turbomachinery*, 135(3):031015–031015–10, 2013.

[162] M. G. Rose. *Unsteady Flows in Axial Turbines*. Verlag im Internet GmbH, dissertation.de, Institut fuer Luftfahrtantriebe (ILA), Stuttgart Universtity, 2011.

[163] M. G. Rose and N. W. Harvey. Turbomachinery Wakes: Differential Work and Mixing Losses. *Journal of Turbomachinery-Transactions of the ASME*, 122(1):68–77, 2000.

[164] B. Rosić, J. D. Denton, and E. M. Curtis. The Influence of Shroud and Cavity Geometry on Turbine Performance: An Experimental and Computational Study - Part I: Shroud Geometry. *Journal of Turbomachinery*, 130(4):041001–041001–10, 2008.

[165] B. Rosić, J. D. Denton, E. M. Curtis, and A. T. Peterson. The Influence of Shroud and Cavity Geometry on Turbine Performance: An Experimental and Computational Study - Part II: Exit Cavity Geometry. *Journal of Turbomachinery*, 130(4):041002–041002–10, 2008.

[166] R. P. Roy, J. Feng, D. Narzary, and R. E. Paolillo. Experiment on Gas Ingestion Through Axial-Flow Turbine Rim Seals. *Journal of Engineering for Gas Turbines and Power*, 127(3):573–582, 2005.

[167] R. P. Roy, G. Xu, and J. Feng. A Study of Convective Heat Transfer in a Model Rotor-Stator Disk Cavity. *Journal of Turbomachinery*, 123(3):621–632, 2001.

[168] R. P. Roy, G. Xu, J. Feng, and S. Kang. Pressure Field and Main-Stream Gas Ingestion in a Rotor-Stator Disk Cavity. In *Proceedings of the ASME Turbo Expo, 2001-GT-0564*, New Orleans, 2001.

[169] C. M. Sangan, O. J. Pountney, K. Zhou, M. Wilson, J. M. Owen, and G. D. Lock. Experimental Measurements of Ingestion Through Turbine Rim Seals - Part I: Externally Induced Ingress. *Journal of Turbomachinery*, 135(2):021012–021012–10, 2012.

[170] J. Schlienger. *Evolution of Unsteady Secondary Flows in a Multistage Shrouded Axial Turbine*. PhD Thesis, Diss. ETH No. 15230, Zurich, Switzerland, 2003.

[171] J. Schlienger, A. I. Kalfas, and R. S. Abhari. Vortex-Wake-Blade Interaction in a Shrouded Axial Turbine. *Journal of Turbomachinery*, 127(4):699–707, 2005.

[172] C. M. Schneider, D. Schrack, M. Kuerner, M. G. Rose, S. Staudacher, Y. Guendogdu, and U. Freygang. On the Unsteady Formation of Secondary Flow Inside a Rotating Turbine Blade Passage. *Journal of Turbomachinery*, 136(6):061004–061004–10, 2013.

[173] P. Schuepbach. *Influence of Rim Seal Purge Flow on the Performance of an End Wall Profiled Axial Turbine*. PhD Thesis, Diss. ETH No. 18458, Zurich, Switzerland, 2009.

[174] P. Schuepbach, R. S. Abhari, M. G. Rose, T. Germain, I. Raab, and J. Gier. Improving Efficiency of a High Work Turbine Using Nonaxisymmetric Endwalls - Part II: Time-Resolved Flow Physics. *Journal of Turbomachinery*, 132(2):021008–021008–10, 2010.

[175] P. Schuepbach, M. G. Rose, R. S. Abhari, T. Germain, I. Raab, and J. Gier. Effects of Suction and Injection Purge-Flow on the Secondary Flow Structures of a High-Work Turbine. *Journal of Turbomachinery-Transactions of the ASME*, 132(2), 2010.

[176] P. Schuepbach, M. G. Rose, R. S. Abhari, and J. Gier. Influence of Rim Seal Flow on the Performance of an Endwall-Profiled Axial Turbine. *Journal of Turbomachinery-Transactions of the ASME*, 133(1), 2011.

[177] P. Schuler, K. Dullenkopf, and H. J. Bauer. Investigation of the Influence of Different Rim Seal Geometries in a Low-Pressure Turbine. In *Proceedings of the ASME Turbo Expo, GT2011-45682*, Vancouver, 2011.

[178] P. Schuler, W. Kurz, K. Dullenkopf, and H. J. Bauer. The Influence of Different Rim Seal Geometries on Hot-Gas Ingestion and Total Pressure Loss in a Low-Pressure Turbine. In *Proceedings of the ASME Turbo Expo, GT2010-22205*, Glasgow, 2010.

[179] M. Sell, J. Schlienger, A. Pfau, M. Treiber, and R. S. Abhari. The 2-Stage Axial Turbine Test Facility *LISA*. In *Proceedings of the ASME Turbo Expo, 2001-GT-0492*, New Orleans, 2001.

[180] E. Serre, E. Crespo Del Arco, and P. Bontoux. Annular and Spiral Patterns in Flows Between Rotating and Stationary Discs. *Journal of Fluid Mechanics*, 434:65–100, 2001.

[181] O. P. Sharma, T. L. Butler, H. D. Joslyn, and R. P. Dring. 3-Dimensional Unsteady-Flow in an Axial-Flow Turbine. *Journal of Propulsion and Power*, 1(1):29–38, 1985.

[182] C. H. Sieverding. Recent Progress in the Understanding of Basic Aspects of Secondary Flows in Turbine Blade Passages. *Journal of Engineering for Gas Turbines and Power-Transactions of the ASME*, 107(2):248–257, 1985.

[183] C. H. Sieverding and P. Van den Bosche. The Use of Coloured Smoke to Visualize Secondary Flows in a Turbine Blade cascade. *Journal of Fluid Mechanics*, 134:85–89, 1983.

[184] H. B. Squire and K. G. Winter. The Secondary Flow in Cascade of Airfoils in a Nonuniform Stream. *Journal Aeronautical Sciences*, 18(4):271–277, 1951.

[185] W. Traupel. *Thermische Turbomaschinen, Band I, Thermodynamisch-stroemungstechnische Berechnung*. Springer-Verlag, Berlin [etc.], 3rd edition, 1988.

[186] J. M. Tyler and T. G. Sofrin. Axial Flow Compressor Noise Studies. In *This paper received the 1961 Manly Memorial Award*. SAE International, 1962.

[187] A. Vipluv. *Experimental Investigation of the Influence of Flow Structure on Compound Angled Film Cooling Performance.* PhD Thesis, Diss. ETH No. 18714, Zurich, Switzerland, 2009.

[188] J. A. Walsh and D. G. Gregory-Smith. The Effect of Inlet Skew on Secondary Flows and Losses in a Turbine Cascade. *IMechE*, C275/87, 1987.

[189] C. Z. Wang, S. P. Mathiyalagan, B. V. Johnson, J. A. Glahn, and D. F. Cloud. Rim Seal Ingestion in a Turbine Stage From 360 Degree Time-Dependent Numerical Simulations. *Journal of Turbomachinery*, 136(3):031007–031007–12, 2013.

[190] C. Warren and H. T. Strahle. *Fan Noise and Control: Turbine Noise Generation, Reduction, and Prediction.* Progress in Astronautics and Aeronautics. American Institute of Aeronautics and Astronautics, 1976.

[191] M .M. Weaver, J. R. Moselle, M .G. Dunn, and G. R. Guenette. *Reduction of Data from Heat-Flux Gauges - A Documentation of the MIT ACQ Code and an Adaptation to Single-Sided Gauges.* 1994.

[192] D. C. Wilcox. Reassessment of the Scale-Determining Equation for Advanced Turbulence Models. *AIAA Journal*, 26(11):1299–1310, 1988.

[193] D. C. Wisler. The Technical and Economical Relevance of Understanding Blade Row Interaction Effects in Turbomachinery. In *Blade Row Interference Effects in Axial Turbomachinery Stages*, volume VKI LS 1998-02, 1998.

[194] World Bank. Air Transport, Passengers Carried in the year 2017. http://data.worldbank.org/indicator/is.air.psgr, 2017.

[195] A. Yamamoto. Production and Development of Secondary Flows and Losses in Two Types of Straight Turbine Cascades: Part I - A Stator Case. *Journal of Turbomachinery-Transactions of the ASME*, 109(2):186–193, 1987.

[196] A. Yamamoto. Production and Development of Secondary Flows and Losses in Two Types of Straight Turbine Cascades: Part II - A Rotor Case. *Journal of Turbomachinery-Transactions of the ASME*, 109(2):194–200, 1987.

[197] C. Zhou and H. Hodson. The Tip Leakage Flow of an Unshrouded High Pressure Turbine Blade With Tip Cooling. *Journal of Turbomachinery*, 133(4):041028–041028–12, 2011.

[198] C. Zhou, H. Hodson, I. Tibbott, and M. Stokes. Effects of Winglet Geometry on the Aerodynamic Performance of Tip Leakage Flow in a Turbine Cascade. *Journal of Turbomachinery*, 135(5):051009–051009–10, 2013.

[199] M. B. Zlatinov, C. Sooi Tan, M. Montgomery, T. Islam, and M. Harris. Turbine Hub and Shroud Sealing Flow Loss Mechanisms. *Journal of Turbomachinery*, 134(6):061027–061027–12, 2012.

A. Nomenclature

Symbols

A	area	[m^2]
BR	blowing ratio	[-]
c_{ax}	axial chord (rotor, stator)	[m]
c_p	specific heat	[J/kg/K]
C_p	normalized pressure	[-]
C_T	normalized temperature	[-]
D	cooling hole diameter	[m]
DR	density ratio	[-]
f	frequency	[Hz]
h	convective heat transfer coefficient	[W/(m^2 K)]
i	incidence angle	[°]
I	momentum flux ratio	[-]
IR	rim seal purge flow injection rate	[%]
K	calibration sensitivity coefficients	[-]
k	coefficients of calibration polynomial	[-]
k	uncertainty coverage factor	[-]
k	thermal conductivity	[W/(m K)]
M	torque	[Nm]
M	Mach number	[-]
N	rotational speed	[rpm]
$\dot{m}$	mass flow	[kg/s]
p	pressure	[Pa]
$\overline{p}$	time-averaged pressure part	[Pa]
p'	random pressure part	[Pa]
$\tilde{p}$	periodic pressure part	[Pa]
$\dot{q}''$	heat flux	[W/m^2]
R	gas constant	[J/kg/K]
Re	Reynolds number	[-]
r	radial coordinate	[m]
s	entropy	[J/kg/K]
T	temperature	[K]
T	blade passing period	[s]
t	time	[s]

TR	tip mass flow ratio	[%]
U	blade speed	[m/s]
U	voltage	[V]
V	absolute flow velocity	[m/s]
W	relative flow velocity	[m/s]
x	axial coordinate	[m]
y^+	non-dimensional wall distance	[-]

Greek

γ	pitch angle	[°]
δ	measurement uncertainty	
Δ	change in quantity	
ε	sealing effectiveness	[-]
η	efficiency	[-]
θ	circumferential coordinate	[rad]
κ	ratio of specific heats	[-]
Π	compressor / turbine pressure ratio	[-]
ρ	density	[kg/m^3]
σ	standard uncertainty	
φ	yaw angle	[°]
ω	angular velocity	[1/s]
Ω	vorticity	[1/s]
ϕ	flow coefficient	[-]
μ	laminar viscosity	[Pa·s]
ψ	stage loading coefficient	[-]
Ψ	circulation	[m^2/s]
χ	mass-averaged quantity	

Subscripts

ad	adiabatic
atm	atmospheric
c	coolant flow
cav / cavity	flow quantity in rim seal cavity
conv	convective
DC	direct current
ex	row exit
i	velocity component index
in	turbine inlet
is	isentropic

j	velocity component index
main	main flow quantity
r	radial coordinate
red	reduced flow quantity
ref	reference quantiy
rel	relative frame
s	static flow quantity
S	streamwise
t	stagnation flow quantity
tt	total-to-total
x	axial coordinate
γ	pitch angle
θ	circumferential coordinate
φ	yaw angle
1.5	total-to-static 1.5 stages
∞	undisturbed flow / main flow

Abbreviations

Blisk	blade integrated disk
CFD	computational fluid dynamics
CFL	Courant-Friedrichs-Lewy number
DAQ	data acquisition
EXP	measured data
FENT	fast entropy probe
FEM	finite element method
FRAP	fast response aerodynamic probe
GPU	gaphics processing unit
GUM	guide of uncertainty in measurements
HPV	hub passage vortex
LEC	Laboratory for Energy Conversation
LDA	laser Doppler anemometry
MEMS	micro-electro-mechanical system
PEEK	polyetheretherketone
PIV	particle image velocimetry
PT100	platinum resistance thermometer
R	rotor blade row
RBPF	rotor blade passing frequency
rms	root mean square
S1	first stator
S2	second stator
SD	secure digital (memory card)
SLM	selective laser melting

TSFC	thrust specific fuel consumption
VPF	vane passing frequency
4HP	four hole probe
5HP	five hole probe

B. List of Publications

Journal Publications

Schädler, R., Hänni, D. D., Kalfas, A. I., Abhari, R. S., Schmid, G., Lutum, E., Schneider, C. "Noise Characteristics of a Reduced Blade Count Rotor with Improved Stage Efficiency", 2019, Journal of the Global Power and Propulsion Society. 3: 653–667. https://doi.org/10.33737/jgpps/112303

Schädler, R., Kalfas, A. I., Abhari, R. S., Schmid, G., auf dem Kampe, T., Prabhu, S. B. "Novel High-Pressure Turbine Purge Control Features for Increased Stage Efficiency", 2017, Journal of the Global Power and Propulsion Society. 1: 113-128. https://doi.org/10.22261/68MK5V

Schädler, R., Kalfas, A. I., Abhari, R. S., Schmid, G., Voelker, S. "Modulation and Radial Migration of Turbine Hub Cavity Modes by the Rim Seal Purge Flow", ASME Journal of Turbomachinery, 2016, 139(1):011011-011011-10. https://doi.org/10.1115/1.4034416

Hänni, D. D., Schädler, R., Kalfas, A. I., Abhari, R. S., Schmid, G., Lutum, E., Lecoq, N. "Purge Flow Effects on Rotor Hub Endwall Heat Transfer with Extended Endwall Contouring into the Disk Cavity", 2019, Journal of the Global Power and Propulsion Society. 3: 555-568. https://doi.org/10.22261/JGPPS.KBBD71

Lazzi Gazzini, S., Schädler, R., Kalfas, A. I., Abhari, R. S., Hohenstein, S., Schmid, G., Lutum, E. "Effect of Purge Air on Rotor Endwall Heat Transfer of an Axial Turbine", 2017, Journal of the Global Power and Propulsion Society. 1: 211-223. https://doi.org/10.22261/F29ZWY

Lazzi Gazzini, S., Schädler, R., Kalfas, A. I., Abhari, R. S. "Infrared Thermography with Non-Uniform Heat Flux Boundary Conditions on the Rotor Endwall of an Axial Turbine", 2017, Measurement Science and Technology 28 (2): 25901. https://doi.org/10.1088/1361-6501/aa5174

Conference Contributions

Schädler, R., Hänni, D. D., Kalfas, A. I., Abhari, R. S., Schmid, G., Lutum, E., Schneider, C. "Noise Characteristics of a Reduced Blade Count Rotor with Improved Stage Efficiency", Global Power and Propulsion Technical Conference 2019, Zurich, Switzerland, Proceedings of the Global Power and Propulsion Forum, GPPS-TC-2019-0037.

Schädler, R., Kalfas, A. I., Abhari, R. S., Schmid, G., auf dem Kampe, T., Prabhu, S. B. "Novel High-Pressure Turbine Purge Control Features for Increased Stage Efficiency", Global Power and Propulsion Forum GPPF, 2017, Zurich, Switzerland, Proceedings of the 1st Global Power and Propulsion Forum, GPPF-2017-92.

Schädler R., Kalfas A. I., Abhari R. S., Schmid G., Voelker S. "Modulation and Radial Migration of Turbine Hub Cavity Modes by the Rim Seal Purge Flow", ASME Turbo Expo, 2016, Seoul, South Korea: Power for Land, Sea, and Air, Volume 2B: Turbomachinery: V02BT38A025.

Hänni, D. D., Schädler, R., Kalfas, A. I., Abhari, R. S. "Variable Blade Tip Geometry Inserts for Combined Aerothermal Measurements for Bladed Disk Rotors", Global Power and Propulsion Technical Conference 2019, Beijing, China, Proceedings of the Global Power and Propulsion Forum, GPPS-BJ-2019-0013.

Hänni, D. D., Schädler, R., Kalfas, A. I., Abhari, R. S., Schmid, G., Lutum, E., Lecoq, N. "Purge Flow Effects on Rotor Hub Endwall Heat Transfer with Extended Endwall Contouring into the Disk Cavity", Global Power and Propulsion Technical Conference 2019, Zurich, Switzerland, Proceedings of the Global Power and Propulsion Forum, GPPS-TC-2019-0014.

Lazzi Gazzini, S., Schädler, R., Kalfas, A. I., Abhari, R. S., Hohenstein, S., Schmid, G., Lutum, E. "Effect of Purge Air on Rotor Endwall Heat Transfer of an Axial Turbine", Global Power and Propulsion Forum GPPF, 2017, Zurich, Switzerland, Proceedings of the 1st Global Power and Propulsion Forum, GPPF-2017-95.